SANDIA REPORT
SAND2022-4187
Printed April 2022

Sandia National Laboratories

Tritium Fires: Simulation and Safety Assessment

Alexander L. Brown, Randy C. Shurtz, Lynelle K. Takahashi, Eric N. Coker, John C. Hewson, Michael L. Hobbs

Prepared by
Sandia National Laboratories
Albuquerque, New Mexico
87185 and Livermore,
California 94550

Issued by Sandia National Laboratories, operated for the United States Department of Energy by National Technology & Engineering Solutions of Sandia, LLC.

Available to DOE and DOE contractors from
U.S. Department of Energy
Office of Scientific and Technical Information
P.O. Box 62
Oak Ridge, TN 37831

Telephone: (865) 576-8401
Facsimile: (865) 576-5728
E-Mail: reports@osti.gov
Online ordering: http://www.osti.gov/scitech

Available to the public from
U.S. Department of Commerce
National Technical Information Service
5301 Shawnee Rd
Alexandria, VA 22312

Telephone: (800) 553-6847
Facsimile: (703) 605-6900
E-Mail: orders@ntis.gov
Online order: https://classic.ntis.gov/help/order-methods/

ABSTRACT

This is the Sandia report from a joint NSRD project between Sandia National Labs and Savannah River National Labs. The project involved development of simulation tools and data intended to be useful for tritium operations safety assessment. Tritium is a synthetic isotope of hydrogen that has a limited lifetime, and it is found at many tritium facilities in the form of elemental gas (T_2). The most serious risk of reasonable probability in an accident scenario is when the tritium is released and reacts with oxygen to form a water molecule, which is subsequently absorbed into the human body. This tritium oxide is more readily absorbed by the body and therefore represents a limiting factor for safety analysis. The abnormal condition of a fire may result in conversion of the safer T_2 inventory to the more hazardous oxidized form. It is this risk that tends to govern the safety protocols. Tritium fire datasets do not exist, so prescriptive safety guidance is largely conservative and reliant on means other than testing to formulate guidelines. This can have a consequence in terms of expensive and/or unnecessary mitigation design, handling protocols, and operational activities. This issue can be addressed through added studies on the behavior of tritium under representative conditions. Due to the hazards associated with the tests, this is being approached mainly from a modeling and simulation standpoint and surrogate testing. This study largely establishes the capability to generate simulation predictions with sufficiently credible characteristics to be accepted for safety guidelines as a surrogate for actual data through a variety of testing and modeling activities.

ACKNOWLEDGEMENTS

Jeff Brewer and Ben Zeidman have been project manager at Sandia handling liaison work with the NSRD program office. This work is funded under the DOE office of Nuclear Safety's Nuclear Safety Research and Development (NSR&D) program. This work was performed under a collaborative project with Matt Kesterson, James Laurinat, and Adrian Mistreanu at Savannah River National Laboratory (SRNL). We gratefully acknowledge the peer reviews of Jeff Engerer, Russ Jarek, Rick Karnesky, Andrew Kurzawski, Josh McConnell, Heather Richard, Clark Snow, Ethan Zepper, and Xiaowang Zhou. Additional programmatic support was provided by Raj Tandon.

CONTENTS

LIST OF FIGURES

LIST OF TABLES

This page left blank

ACRONYMS AND DEFINITIONS

Abbreviation	Definition
AFT	Adiabatic Flame Temperature
ANSI	American National Standards Institute
ARF	Airborne release fraction
BC	Boundary condition
CEA	Chemical equilibrium with applications
CF	Conversion Fraction
CFD	Computational fluid dynamics
CJ	Chapman-Jouguet
CVE	Constant Volume Explosion
CVFEM	Control volume finite element mechanics
DIPPR	Design Institute for Physical Properties
EDC	Eddy dissipation concept
FLAME	Fire laboratory for accreditation of modeling by experiment
DC	Dose Coefficient
DOE	Department of Energy
HC	Hazard Category
ISF	Ignition Safety Factor
GC	Gas chromatograph
HVAC	Heating, ventilation, and air conditioning
ISO	International Organization for Standardization
JANAF	Joint Army Navy Air Force
LES	Large eddy simulation
LFL	Lower Flammability Limit
LOC	Level Of Concern
MaCFP	Measurement and computation of fire phenomena
MFC	Mass flow controller
NASA	National Aeronautics and Space Administration
NFPA	National Fire Protection Association
NG	Neutron Generator
NGF	Neutron Generator Facility
NIST	National Institute of Standards and Technology
NOAA	National Oceanographic and Atmospheric Administration
OBT	Organically Bound Tritium

Abbreviation	Definition
ORNL	Oak Ridge National Laboratory
OSHA	Occupational Safety and Health Administration
PIV	Particle image velocimetry
PLIF	Planar laser induced fluorescence
PMMA	Polymethylmethacrylate
RANS	Reynolds averaged Navier-Stokes
RF	Respirable fraction
RMS	Root-mean-squared
SCCM	Standard cubic centimeters per minute
SNL	Sandia National Laboratories
SRNL	Savannah River National Lab
STC	Special Tritium Compound
STD	Standard deviation
TCV	Tritium Containment Vessels
TFG	Tritium Focus Group
TFNS	Temporally filtered Navier-Stokes

1. INTRODUCTION

Tritium is a radioactive isotope of hydrogen that has roughly three times the mass of hydrogen. It has a half-life of 12.3 years (DOE-STD-1129), and upon decay it releases a low energy beta particle and produces ^{3}He. The low energy beta decay product has too low of a kinetic energy to pose a hazard to the human body through external exposure; therefore, the radiological hazards result purely from tritium that has been taken into the body (i.e. via inhalation, skin absorption, ingestion).

At Sandia National Laboratories (SNL), tritium is used in the production of Neutron Generators (NGs). Sandia National Laboratories' Neutron Generator Facility (SNL-NGF) typically maintains its tritium inventory in gaseous form within bottles or in uranium hydride beds. Some tritium at the SNL-NGF is also temporarily maintained as tritiated water adsorbed onto molecular sieve beds as part of the tritium capture system, which is used to minimize tritium emissions to the environment. Tritium on such sieve beds are considered waste and are retained until ready for disposal. Incidental amounts of tritium may take on other forms such as organically bound tritium (OBT) or other special tritium compounds (STCs), but generation of these forms is intentionally minimized for safety reasons.

With respect to the size of its tritium inventory, the SNL-NGF is one of the smaller tritium facilities within the DOE complex. Given the inventory threshold quantities outlined in DOE-STD-1027-2018, the SNL-NGF is currently designated as a radiological facility, with a maximum permissible inventory of 1.6 g or 16,000 Ci of tritium. If the facility's tritium inventory ever exceeds the threshold quantity, the SNL-NGF could potentially transition to a Hazard Category 3 (HC3) facility. Under the current standard, an inventory between 1.6 g and 30 g would make the initial categorization of the SNL-NGF a HC3 facility, while an inventory over 30 g would make its initial categorization a Hazard Category (HC2) facility. HC3 facilities are considered to have "potential for significant localized consequences" (i.e. 10 rem exposure at 30 meters from the release point), while HC2 facilities have the "potential for significant on-site consequences" (i.e. 1 rem exposure at 100 meters away from point of release, DOE-STD-1027-2018).

DOE-STD-1027 defines the initial screening hazard category threshold quantities for all radionuclides. It does so by doing a simple calculation using conservative (worst case) estimates to gauge the hazards posed by the radioisotopes in a facility's inventory. The calculations include factors such as airborne release fractions (ARF, how much can release into the air), respirable fractions (RF, how much of what is released can be taken into the human body) and dose coefficients (DC, how detrimental the radioisotope is for the human body). Each factor is assumed to take a conservative value representative of a bounding accident scenario to ensure that the worst case is used to determine a facility's initial hazard categorization. The more hazardous the radioactive isotope, the lower the threshold quantities are before a facility becomes HC3 or HC2.

Historically, tritium has been a notable exception to the standard methodology of DOE-STD-1027. In the table of threshold quantities for each radioisotope, there is an asterisk next to tritium, which reads:

"At the recommendation of the Tritium Focus Group, the HC-2 and HC-3 tritium threshold values were provided by the Tritium Focus Group (TFG) and are not calculated using the methodology in this Standard."

The 1992 revision of DOE-STD-1027 elaborated further, stating that:

"the Category 3 tritium threshold value has been increased from 1.0E+03 Ci and 1.0E-01 grams to 1.6E+04 Ci and 1.6E+00 grams, consistent with the methodology of EPA used for the other nuclides."

Without the exception, the threshold quantity for tritium HC3 facilities would have been 0.1 grams, and the SNL-NGF initial hazard categorization would have been as a HC3 facility.

Having tritium as an exception to the DOE-STD-1027 formalism recognizes that tritium is unique among radionuclides. As a radioisotope of hydrogen, tritium can evolve in many different ways, taking on forms spanning all three fundamental phases of matter: tritium can permeate solid metals or substitute hydrogen atoms in polymer materials; it can be present as a liquid (e.g. tritiated water or oils); it can also oxidize to form tritiated water vapor, or remain a molecular gas (e.g. T_2). This complexity inevitably complicates the safety analysis for tritium, since ARF, RF and DC factors can vary many orders of magnitude depending on which form the tritium takes. For example, the DC for tritiated water vapor is 10,000 times higher than that for T_2 gas (DOE-STD-1129), and the RF for tritiated particulates is several orders of magnitude lower than that for T_2 gas (DOE-STD-3010).

The diversity of tritium forms and the fact that tritium can change forms over the course of an accident makes reasonable bounding safety analysis difficult. It is impossible to properly account for this level of complexity with the current simple formalism in DOE-STD-1027, yet efforts are being made to make the treatment of tritium more consistent with that of other radionuclides. In a presentation made at the 2018 Tritium Focus Group meeting, a presentation from Oak Ridge National Laboratory (ORNL) communicated the Department of Energy's (DOE's) intent to update the calculations in DOE-STD-1027 and to eliminate the special exception made for tritium (Walker, 2018). This proposal, or something similar to it, will likely be adopted in the next revision of DOE-STD-1027 unless a technical justification can be made to the contrary.

In the initial ORNL proposal for calculating the threshold for HC3 facilities, it was proposed that the dose coefficient (DC) should be that of OBT, the ARF should be 0.5 (or 1, if 0.5 could not be adequately justified), and the RF should be 1, since the gaseous form is readily inhaled. For the HC2 threshold quantity calculation, it was proposed that the DC should be that of tritide particulate, and ARF and RF should similarly be set to 1 as for tritium gas (T_2). These assumed values for the ARF, RF and DC factors and some other changes resulted in a 66% decrease in the HC3 threshold (a greater decrease would be realized if the 0.5 RF could not be justified), and a 89.6% decrease in the current HC2 threshold.

ORNL's proposed approach to conservatively bound the tritium hazard at a given facility acknowledged that tritium can evolve into various forms that disperse and interact with the human body very differently, since it borrows ARF, RF and DC values for different forms of tritium; however, this approach also grossly overestimates the hazards of a facility's tritium inventory by multiplying worst case factors corresponding to different forms of tritium, ignoring branching ratios and physical constraints. Due to the wide range of values in the ARF, RF and DC values for different forms of tritium, ignoring the branching ratios results in a hazard analysis that compounds conservatisms to an extreme degree. Such conservatism, if adopted, could raise the apparent hazard categorization of several DOE tritium facilities, substantially increasing facility operational costs without any true added safety benefit.

In order to make the threshold quantity calculation more appropriately bounding for tritium hazards while maintaining worker and public safety, the ability to account for the evolution of tritium forms for a given accident scenario must be improved. In addition to ARF, RF and DC, an additional factor, a conversion fraction (CF) is proposed to better account for branching ratios of tritium.

Inherently in the ORNL analysis, the CF was assumed to be 1 (i.e. 100% conversion) to OBT. For the SNL-NGF (and for most other tritium facilities), much of the tritium inventory is stored as either a gas (specifically, T_2) or on tritide beds, both of which can release T_2 gas. It is unclear what kind of accident scenario would result in appreciable OBT generation (i.e. CF is inherently low and not bounding). More feasible, however, is that the tritium (either from T_2 in containment vessels or desorbed from metal tritide beds) could release as T_2 gas and subsequently oxidize in air. This consideration, plus the fact that tritiated water vapor has a DC of the same order as that of OBT (ICRP 119, 2012), make T_2 oxidation in a fire an accident scenario of primary concern.

Since the DC for tritiated water vapor is much greater than for T_2 gas, facility-wide accidents involving fires or explosions are generally the default scenarios of greatest concern for overall facility hazard categorization. When considering such a fire scenario, a CF of 1 for T_2-to-water conversion is indeed bounding for cases where a tritium source is directly in a fire; yet this assumption is extremely conservative if used for a facility average given the conditions relevant to tritium use and storage at most facilities. At the SNL-NGF, 100% inventory conversion to tritiated water vapor is effectively impossible; the magnitude of the accident needed for complete release and conversion of the entire tritium inventory would likely need to be so large as to render radiological hazards to surrounding personnel irrelevant.

For more appropriate CF values to be applied to safety analyses, quantitative data are needed. Due to the characteristics of its tritium inventory, a facility average CF for the tritium at SNL-NGF is likely much less than 1, an assumption that is also likely applicable to several other tritium facilities. Arguments for a CF<1, while reasonable in principle, are based on qualitative knowledge of the norms of tritium operations and stored inventory; it is difficult in the absence of direct evidence to define what a more reasonable bounding CF value should be. Tritium accidents involving fires are rare (one known case is documented by Jensen and Martin, 1988), and experiments that examine T_2 to water conversion are inherently difficult and dangerous. The unfortunate result is a dearth of tritium conversion data for release conditions of relevance and a general tendency to adopt a CF of 1 for all cases.

In the absence of specific data for tritium, information from hydrogen literature is frequently used conservatively to approximate tritium behavior in fires, yet the gas storage conditions described in most hydrogen literature typically involves much higher quantities and pressures than what is remotely relevant to the SNL-NGF tritium inventory and most other tritium facilities. Because of the high pressures and quantities of concern in the hydrogen community, dangers from explosions and propagating flames are naturally a concern that are considered by safety analysts; however, for most tritium facilities, the quantities of tritium are frequently far below the threshold where these phenomena are significant concerns.

Of greater practical concern is the more gradual conversion of T_2 to tritiated water vapor from a nearby sustained fire. For most tritium facilities, storage of tritium under low pressures (moderate to sub-atmospheric) and relatively low quantities compared to hydrogen (<50 g) are the norm, therefore oxidation with T_2 concentrations below the flammability limit in air is likely. Unfortunately, these conditions also constitute the kinetic regime where hydrogen oxidation data are poorly characterized.

The aim of this work is to develop and validate a modeling and simulation approach to examine the behavior of tritium releases in close proximity to fires under a wide range of starting conditions. Simulations have the advantage of being able to sample a wider range of accident scenarios without the radiological hazards of working with the radioisotope. Starting conditions are chosen such that

tritium pressures and quantities are more relevant to SNL-NGF and most tritium facilities, which will greatly improve bounding estimates of tritium hazards at these facilities.

Given the distributed nature of the tritium inventory at SNL-NGF, individual tritium sources will have some spatial distribution function with respect to fire sources in a facility-wide accident scenario. This work therefore focuses on developing modeling capabilities for the dispersion and reaction (oxidation) of small quantities of tritium in proximity to a fire, varying multiple scenario-specific parameters. The modeling examines how factors such as distance from fire, hydrogen isotope kinetic effects, scenario geometry, temperature and fire intensity (thermal power output) might impact the overall tritium CF for a tritium facility like the SNL-NGF. These results represent the first close examination of water conversion fractions for tritium released under conditions of relevance to most tritium facilities. It is the hope of the authors that this work will serve as a foundation to illustrate the utility of applying more sophisticated tools (i.e. detailed modeling and simulation) to evaluate tritium hazards and to enable more educated decisions in balancing risk and safety.

1.1. Organization

This report is organized in five main chapters that serve as independent studies and have been each, except Chapter 2, presented at conferences as papers in other forms. These chapters tend to be longer and include more information than the corresponding conference papers, as the paper size limitations required reduction of presented material. In the case of Chapter 5, there were a significant number of follow-on simulations added to the original study, effectively doubling the size of the simulation matrix for this report.

The chapters are of varying relevance to the direct problem introduced above and are each notably different in their applicability to the problem of tritium fires. Chapter 2 addresses the explosion hazard for tritium under common use conditions and help characterize the threshold above which the hazard is credible. Chapter 3 is a foundational study needed to address the lack of commonly available thermodynamic and transport properties for tritium and related gases. The study is largely based on extrapolating isotopic behaviors from existing data and is based on methodologies that have been historically presented and characterized for other isotopes. Chapter 4 is less related to the direct problem of tritium fires and deals with the simulation accuracy of a turbulent buoyant helium plume using a CFD model. Relevancy to this work is through the credibility found in the validation exercise that is used to quantify the accuracy of the model to the challenging dataset. Chapter 5 employs the model and the property data to assess a variety of scenarios involving a tritium release in a room outside the fire. The room and fire were selected conformal to the ISO-9705 standard to provide results for a fire that is largely considered representative for testing the fire safety of construction materials. Chapter 6 tests were ongoing during most activities relating to the prior chapters. The tests provide a surrogate (^{1}H, ^{2}H) basis for an approximate tritium (3H) reaction kinetic model in an environment that is representative of expected conditions relevant to non-pressurized storage releases.

Overall conclusions from the technical chapters are summarized in Chapter 7. An appendix was added to capture some of the extraneous information developed in the process of producing the chapters. This is content not believed significant to the body of the chapters, but with possible relevance to better expose the work done and described in the main chapters.

2. THE EFFECT OF SCALE ON HYDROGEN ISOTOPE HAZARDS

Many DOE tritium facilities maintain some inventory of elemental tritium gas (T_2, HT, DT). The quantities and pressures of tritium gas at these facilities can vary widely, but at many facilities tritium inventories are maintained at moderate pressures (on the order of one to a few atm), at sub-atmospheric pressures, and/or in extremely limited quantities. As examples of the limited tritium quantities in question, current radiological and HC3 tritium facility inventories may not exceed 1.6 g and 30 g, respectively (DOE-STD-1027-2018). In practical terms, these quantities correspond to approximately 6 and 112 standard liters, respectively, substantially less than the approximately 6000 standard liters of H_2 gas in a typical 1A gas cylinder. These strict inventory limits are due to tritium's potential radiological hazards, which are 10,000 times higher when the released T_2 converts to tritiated water vapor (T_2O or HTO; DOE-STD-1129).

Due to the higher hazard of tritium in water vapor form, the degree of oxidation of released elemental tritium gas in fire accident scenarios is a primary concern for tritium safety analyses. When estimating the T_2-to-water conversion fraction (CF), it is commonly assumed that tritium will have similar CFs as H_2 when subjected to fires or ignition sources. While this is true in theory due to the chemical similarity of H_2 and T_2, the gas quantities and pressures of concern at tritium facilities are considerably different from those examined in the safety literature for hydrogen explosions and deflagrations. It is therefore important for accuracy and cost management to gauge whether some of the same accident scenarios of greatest concern to H_2 safety remain relevant to tritium safety.

Tritium safety programs often rely heavily on data from the hydrogen safety literature despite the large differences in quantities and pressure due to the lack of data on tritium oxidation in fire scenarios. As a result, it is not uncommon to see the assumption that all released elemental tritium converts to water vapor (CF = 1), which reflects an inherent presumption of high pressures and high quantities of gas (with the accompanying higher risk for large explosive plumes, self-propagating flames and/or the possibility of sustained, directional flow into a fire). It is postulated that the CF for tritium in fire scenarios, with the lower quantities and pressures of relevance, differs considerably from those for the same accidents involving high quantities and pressures of H_2; limited facility inventories of elemental tritium tend to result in smaller and shorter release events, thereby resulting in overall lower T_2 concentrations in air. Similarly, lower pressure tritium gases tend to release slower and therefore have a lower likelihood of producing a flammable T_2-air mixture at any given point in space or time. This in turn lowers both the risk for ignition and the value of the final CF. At many DOE tritium facilities, T_2 inventories are so low that the tritium is unable to sustain a flame upon release, thus requiring other sources of flammable material to provide the heat required to react.

Despite these qualitative arguments, the fact remains that in principle, both H_2 and T_2 can undergo rapid oxidation reactions given the proper conditions. It is therefore necessary to concretely demonstrate that such conditions cannot be met for most DOE tritium facilities (non-HC2). In this section, deflagration and explosion events for reasonable tritium storage conditions are evaluated to determine whether such events can reasonably occur and whether their potential magnitude could propagate facility damage that could cause tritium in other areas of a facility to be released. TIGER, an equilibrium code developed at Sandia National Laboratories (Hobbs et al., 2014), is applied to two theoretical accident hazard scenarios frequently discussed in hydrogen safety literature: (1) explosive oxidation of T_2 gas released in air and (2) confined ignition of T_2 gas, examined for both sea level and higher elevations (Albuquerque, NM, about 5000 feet above sea level). The analyses are performed using the JCZS3 database (Hobbs et al., 2018), which uses piecewise specific heat fits

to numerous species like the National Aeronautics and Space Administration (NASA) program, CEA (Chemical Equilibrium with Applications). Equilibrium codes like TIGER find the lowest energy state for a given suite of reactants and potential products. The results reflect a reaction that has gone to an idealized completion based on minimization of the Gibbs Free Energy for the gases. Overpressures are predicted by knowing the initial reactant composition, initial energy, volume, and potential products. This is referred to as an "explosion" calculation in TIGER. The results provide a means to conceptually bound the behavior and resulting hazards expected for elemental tritium gas under common storage conditions relevant to DOE tritium facilities.

2.1. Explosive Oxidation of Elemental Tritium Gas in Air

Hydrogen/air explosions can cause major facility damage, worker injury or death. However, at most tritium facilities, T_2 gas inventories are stored in comparatively smaller quantities and lower pressures. In this analysis, equilibrium calculations with the TIGER code are used to provide a high-level bounding analysis that illustrates the relevant hazards for different tritium storage conditions.

When considering T_2 releasing into room air in a fire scenario, frequently the tritium safety analyst's main concern will be whether the lower flammability limit (LFL) is exceeded, which helps establish the possibility of a rapid oxidation event (deflagration, which is often referred to as an explosion if there is a moderate overpressure event). While more destructive forms of hydrogen explosions (rapid oxidation events) are also potential events of concern in hydrogen safety, the hydrogen detonation limits (19% to 57%) are much narrower than the flammability limits required for deflagration events (4% to 74%). As this analysis will show, most DOE tritium facilities have insufficient quantity and/or pressures to create a significant flammable or explosive T_2-air mixture, even in the most ideal situations. This major difference may be difficult to conceptualize for those who are used to thinking about hydrogen safety, but it is important to understand in order to identify the tritium accident scenarios that pose the greatest practical hazards. Because tritium's radiological hazard is largely determined by the fraction of material that oxidizes and the exact mechanism involved is of secondary importance, we focus our analysis on the lower flammability limit. To bound the explosive damage potential of the tritium inventory, it is assumed that a shock occurs even for the ignition of gas concentrations below 19 mole %; however the reader should keep in mind that safety analysis based on flammability limits is very conservative with respect to the most destructive events possible (Shapiro and Moffette, 1957).

To begin this exercise, we first consider a very small tritium lab space containing multiple vessels of T_2 gas. The total T_2 inventory of these vessels is allowed to vary. In order to analyze the behavior of this T_2 upon release into room air, the behavior of an equivalent molar quantity of H_2 is examined. H_2 gas is thus used as a surrogate for T_2 by assuming that the thermodynamics are the same. The results from Chapter 3 suggest that this is an adequate assumption for tritium because the property differences for H_2 versus T_2 are 1.7% for combustion enthalpy and 0.1% for Gibbs Free Energy (the minimized objective in the TIGER equilibrium code) at the adiabatic flame temperature (AFT) of about 2400 K, which is applicable to the higher temperatures relevant to this analysis. The H_2 gas is assumed to release into a dry air mixture consisting of 78%:21%:1% molar percentages of N_2:O_2:Ar to form an H_2-air mixture. T_2 and H_2 are assumed to have the same molar reactivity despite their differing molecular weights. Similar molar reactivity implies that calculated quantities such as the adiabatic flame temperature are the same for identical molar concentrations of T_2. This assumption is supported by Gray *et al.* (1970) who measured similar adiabatic flame temperatures for hydrogen isotopes.

After release, the gas is assumed to homogeneously mix with the air within a fixed volume before being subjected to an ignition source. The calculations assume that the flammability limits of tritium (T_2) in air are similar to the flammability limits for hydrogen (H_2) in air, with an LFL of 4 mole %. This assumption is conservative for tritium since the LFL for T_2 is expected to be higher, on the order of 6.6% (Cadwallader and Petti, 2002). The LFL is the lowest concentration of fuel (*e.g.*, H_2 or T_2) wherein an external ignition source (*e.g.*, light switch) will propagate a flame, resulting in the rapid oxidation of potentially significant quantities of the available H_2 gas. Mixtures below the LFL will not ignite even with a substantial ignition source such as a static discharge or an arc from a mechanical light switch. The case where a sub-LFL T_2-air mixture is exposed to a sustained, externally fueled flame is considered separately in Chapter 5. Note that 4% constitutes a conservative LFL even for protium because it is derived from observations of flame propagation in the upward direction favored by buoyancy; higher LFL limits are observed for horizontal and downward directions (Shapiro and Moffette, 1957). The LFL in the most conservative upward direction does not vary significantly with temperature and pressure near ambient conditions (Shapiro and Moffette, 1957), so no additional conservatism is needed to account for these environmental factors.

Table 2-1 contains the results of the TIGER calculations with some additional metrics in a standardized scenario. In order to assign a number to assess the relative risk of an ignition event for different scenarios, two volumes are considered: the volume at which 4 mole % of T_2 is achieved after release from an idealized point source and assuming homogeneous mixing ("Volume for LFL" in Table 2-1), and the volume of a standard room with dimensions 12 ft (Length) x 8 ft (Width) x 8 ft (Height), which corresponds to 21.75 m^3 ("Room Volume" in Table 2-1). The "Volume for LFL" in Table 2-1 increases with the quantity of T_2 released. The "Room Volume" corresponds to the room size for a standard room fire, as defined in ISO-9705. Note that the same room volume is used for the simulations in Chapter 5. The ratio of the two volumes yields an ignition safety factor (ISF) for the given T_2 amount released within the "standard room" size, from which the likelihood of an ignition event may be deduced. In practical terms, an ISF≤1 indicates that an ignition event is likely, while an ISF > 1 indicates that ignition is unlikely due to greater dilution of the T_2 to below the LFL. The ISF for each examined quantity of tritium is inherently conservative since the standard room size considered is very small for a tritium lab space, and the safety factor will increase proportionally with the room volume (i.e., doubling the room volume in question will double the safety factor). Additional factors that would tend to increase the ISF are neglected, such as the presence of air leak paths in and out of the room and partial releases of inventories (*i.e.,* release fraction < 1). As such, the ISFs suggested by the equilibrium results should be viewed as a worst-case evaluation, limited only by the boundary condition imposed by the size of the tritium inventory in question and the physics of the problem. Improved (tighter) thresholds of safety may be obtained through more detailed analyses of more realistic scenarios.

Another way to think about the ignition safety factor is to take the ISF ≤1 as an indicator that an ignition source provided anywhere within that volume is likely to be effective in causing a deflagration event. For a volume with an ignition safety factor >>1, an ignition source located randomly within the volume is unlikely to be effective; effective ignition would only occur if the ignitor happens to be located within a poorly mixed sub-volume with a local ignition safety factor ≤1 (i.e., near the source of the hydrogen release). The LFL volumes and spherical radii in Table 2-1 below indicate that at least 40 grams of tritium must be released for an ignition source at 1 meter to have a high effectiveness probability (scaled to 1 m radius as 30 g × [1 m/ 0.91 m]^3). In this scenario, a high probability of ignition at 1 meter is only applicable if the ignition source operates in a narrow window of time before the released hydrogen can dissipate further into the room and beyond. Note

that for facilities with ISF >> 1, this distance and time window will decrease rapidly relative to the value in Table 2-1 once the finite spatial distribution of tritium is accounted for, even if the containment vessels are housed within the same room. Furthermore, the possibility of attaining patches of gas above the LFL at all is essentially zero for low-pressure and sub-atmospheric T_2 sources with sub-catastrophic containment failure (*i.e.,* a gradual rather than instantaneous release of the gas). Thus, the distance and time window of concern in even the worst possible (and extremely idealized) case is narrow, making ignition for these inventory levels highly unlikely. The spherical LFL radii and the corresponding ISFs in Table 2-1 lose quantitative accuracy as safety metrics in the special case of a high-momentum jet of hydrogen released from a pressurized source, but even for this case (resembling the more traditional safety concerns for hydrogen) the metrics in Table 2-1 remain valid for volumes and distances large enough for most of the jet momentum to dissipate.

Table 2-1. Equilibrium calculation of AFT, Chapman-Jouguet (CJ), and Constant Volume Explosion (CVE) states in various rooms at 298 K and 1 atm

	1.6 g T_2 in small room[a]	30 g T_2 in small room[a]	222.5 g T_2 in small room[a]	30 g T_2 in large room[b]
Room Volume, m^3	21.75	21.75	21.75	43.49
Dry air, moles[c]	889.5	889.5	889.5	1779
Mass of T_2, g	1.6	30	222.5	30
Moles of T_2, moles	0.2667	5.000	37.08	5.000
Room T_2 Concentration, mole%	0.03	0.56	4.0	0.28
Volume for LFL, m^3	0.2	3.1	23.4	3.1
Radius of LFL Spherical Volume, m	0.34	0.91	1.77	0.91
Ignition safety factor (ISF)	133	7	1	14
Ignition Likelihood	Unlikely[d,e]	Unlikely[d,e]	Likely[f]	Unlikely[d,e]
AFT at 1 atm, K	300[e]	344[e]	628	321[e]
Shock Velocity, km/s[f]	0.39[e,g]	0.53[e,g]	0.91[g]	0.47 [e,g]
Shock Temperature, K[f]	312[e,g]	401[e,g]	850[g]	358[e,g]
Shock Pressure, (P-Po) psig[f]	2.2[e,g]	11.3[e,g]	50.2[g]	7.2[e,g]
CVE Pressure, (P-Po) psig	0.2[e]	3.2[e]	21.4	1.6[e]
CVE Temperature, K	302[e]	363[e]	745	331[e]

[a] The small room is 12 ft (length) × 8 ft (width) × 8 ft (height)

[b] The large room is twice as large as the small room 2×(12 ft × 8 ft × 8 ft)

[c] Calculated using standard dry air at 1.18 kg/m^3 and a molecular weight of 28.85 g / mol

[d] The Ignition Likelihoods in green are zero probability events that are beyond extremely unlikely (BEU), significantly below LFL, or kinetically restrained.

[e] An ignition event resulting in a high CF is extremely unlikely with an ISF> 0.5 (Shapiro and Moffette, 1957, Thompson et al. 1988). However, 100% conversion is assumed regardless of probability for illustrating the worst-case damage scenario.

[f] The Ignition Likelihood in red is a probable event that might occur with a sufficient ignition source.

[g] Shock calculations are determined using conservations of mass, momentum and energy with the one-dimensional Chapman-Jouguet equations (Fickett et al., 1979). Such shock conditions will not be feasible in real scenarios until the LFL reaches 19 mole %.

If the H_2-air mixture ignites, 100% conversion is conservatively assumed to gauge the maximum damage consequences of an ignition event. This is not to suggest that 100% conversion is likely or expected; the risk of any ignition event decreases as the average T_2 concentration in the room decreases, and the risk of an event with 100% conversion becomes extremely unlikely in cases when the average concentration in the room is significantly below the LFL. Nevertheless, the physical parameters for an explosion event with CF=1 are calculated and presented in Table 2-1 (see the lower cells in gray) to illustrate the physical limit for the inventory's damage potential based on an idealized equilibrium approximation.

Figure 2-1 shows a graphical representation of the data from Table 2-1. The ISF and the average concentration of T_2 in air are based on the standard room size, which is conservatively small. Note that the ISF and concentration should be scaled appropriately with the actual room size and inventory size in question. The graphic is not meant to suggest that all facilities with 222.5 g of tritium or more pose high deflagration or explosion hazards.

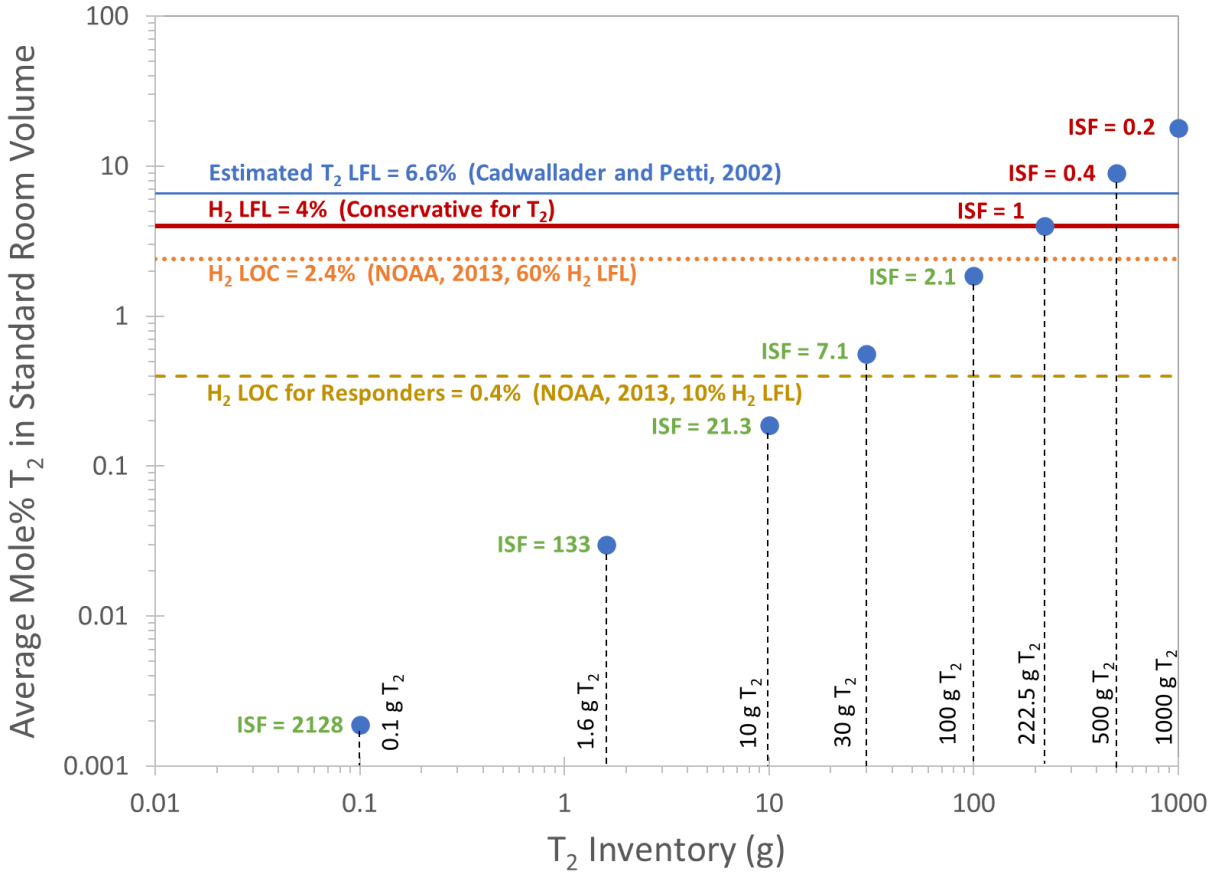

Figure 2-1. Visual representation of the ISO-9705 standard room T_2 concentrations and ignition safety factors (ISFs) from Table 2-1, including additional quantities of T_2.

2.1.1. Analysis for Radiological Facilities (< 1.6 g Tritium)

Table 2-1 and Figure 2-1 show the results of the TIGER calculations. For current radiological facilities (1.6 g of T_2 or below), the ignition safety factor is 133 (or higher). This value illustrates that even if one assumes that (1) all of a radiological facility's tritium is in gaseous form, (2) all of the facility's tritium is consolidated to a single point, (3) the room used for storage is very small, (4) 4% is conservatively used as the LFL for tritium, and (5) all of the tritium is instantaneously released (a poor assumption for low pressure tritium sources) from a single point source, the explosion and deflagration risk is very low. Another way to conceptualize the risk is to consider that at equilibrium, the concentration in the room would be 0.03 mole %. This average concentration, even if one were concerned about local ignition due to concentration patchiness, is well below any level of concern (LOC) for flammability (defined as 60% of LFL by NOAA), or even the extra-conservative 10% of LFL (0.4 mole %) used by responders (NOAA, 2013). If one assumes

homogeneous mixing as the gas expands from its idealized singular and instantaneous point of release, the concentration decreases below the LFL beyond a sphere of radius 0.34 m (~1.1 feet). Given the conservatisms used in the calculation, this small length scale points to very low likelihood of a rapid oxidation event being triggered, short of all the inventory being directly released into a sustained, externally fueled fire. All of these considerations suggest that tritium-fueled explosions and deflagrations are not major concerns at tritium radiological facilities.

The risk for delayed ignition in a radiological facility is similarly unlikely. A simple calculation using the ISO-9705 standard room dimensions with the assumption that the light hydrogen isotopes concentrate near the ceiling suggests that in the worst-case scenario, a flammable mixture from a release of 1.6 grams would require all released tritium to be collected to within less than 1 inch of the ceiling. Such an idealized flammable layer is likely to be significantly less than 1 inch thick in any real radiological facility, depending on the room dimensions, T_2 distribution throughout the facility, and presence of ventilation or other leak paths. Given all the conservatisms of this analysis and the dispersing action of diffusion and ambient air movement, it is unlikely that an enriched ceiling layer could form and be maintained to pose a significant ignition risk from tritium at radiological facilities. For the case with a pre-existing fire in the room, the simulations in Chapter 5 indicate that hydrogen isotopes that encounter the plume of hot gas near the ceiling are converted to water, but most of the released hydrogen avoids this hot region entirely and eventually leaves the room, resulting in a conversion fraction CF << 1. A series of follow-up simulations are planned to study whether ceiling enrichment up to the minimum ignition concentration (LFL) is likely to occur in scenarios where there is no fire in the room to drive mixing. It is worth noting that flame quenching occurs for thin layers of nominally flammable gas mixtures adjacent to a surface such as a ceiling that can absorb thermal energy (Shapiro and Moffette, 1957; Turns, 2000; Lefebvre and Ballal, 2010). Thus, concentrations somewhat higher than the LFL are required for a flame to propagate and achieve a high conversion fraction; the quenching behavior depends on the fuel (hydrogen isotope), layer thickness, and the thermal properties of the ceiling material.

Having established the low risk of an ignition event at a tritium radiological facility, we can next consider the potential impacts of this very improbable explosion. The purpose of this analysis is to determine whether it is possible for a fraction of a radiological facility's inventory to ignite and cause explosive damage to the surrounding facility such that tritium stored in other areas of a facility could be released. If, despite all of the conservative assumptions (1-5 above), the mixture were to somehow ignite and convert all 1.6 g of T_2 to water vapor, then the resulting rapid energy release would result in an overpressure (also called the Constant Volume Explosion Pressure or "CVE Pressure") of only 0.2 psig in the standard room. Based on this overpressure, the work of Baker et al. (Baker et al., 1992) and the damage approximations of Kinney and Graham (1985) would suggest that this event would be capable of only minor damage (for reference, glass shatters at an overpressure of 1 psi). This bounding calculation thus demonstrates that any fraction of tritium at a radiological facility does not on its own pose an explosion hazard of sufficient magnitude to induce the release of tritium in other areas of the facility.

Note that although 100% conversion is assumed for the purpose of evaluating potential structural impacts, the risk of achieving a high oxidation fraction after ignition decreases rapidly as the ignition safety factor increases, which is not explicitly reflected in Table 2-1. Hydrogen flammability studies have shown that combustion efficiency does not approach 100% for hydrogen concentrations lower than about 8% (Thompson et al., 1988) to 10% (Shapiro and Moffette, 1957), which implies low conversion fractions (CF between 0.3 and 0.7) for ISF > 0.5 or even ISF > 0.4. This suggests a reduced radiological hazard for deflagration events near the LFL that this analysis does not take

credit for (another conservatism). The following statement from Shapiro and Moffette (1957) provides a good description of behavior near the LFL:

> "When mixtures having compositions close to flammability limits are ignited a ring of flame is formed which breaks up into balls of flame that travel to the top of the test vessel. Only a fraction of the hydrogen is burned in these cases. …A 5.6% hydrogen mixture, for example, will only burn about 50% of the H_2, and complete combustion will not occur until the percentage of hydrogen is increased to 10%."

At this point it is worth reiterating that many tritium facilities store elemental tritium gas at near-atmospheric to sub-atmospheric pressures. With low-pressure tritium sources, the T_2 will tend to release slowly due to the lack of a positive pressure differential forcing the release. As a result, even when considering dynamic, non-equilibrium releases, the relevance of local high concentration patchiness is suspect, and the possibility of ignition becomes even more remote. With these considerations in mind, ignition events can be seen to have low relevance at radiological facilities unless H_2, D_2 or other flammables are stored with the T_2 in significant quantities. Note that for the current discussion, tritium mixtures containing H_2 and D_2 are not considered explicitly, but the behavior of isotopic mixtures may be deduced by replacing the row labeled "Moles of T_2" in Table 2-1 with "Total moles of H_2, D_2, and T_2". It should also be noted that various organizations like the National Fire Protection Association (NFPA), Occupational Safety and Health Administration (OSHA) and the American National Standards Institute (ANSI) have their own standards to mitigate risks from other flammable gases such as H_2 and D_2 (ANSI/AIHA Z9.5, NFPA 45, NFPA 91).

In summary, for facilities with <1.6 g of tritium, explosions and propagating tritium-fueled flames are not a relevant bounding hazard scenario for the overall facility inventory; with a very conservative ignition safety factor of 133 or more, the risk of an ignition event is low even in the most ideal circumstances, and the possibility of an event leading to near 100% conversion is even more remote. Ignition safety factors for an actual tritium facility are likely much higher than 133 due to the larger size of typical tritium lab spaces and the true, finite spatial distribution of the tritium inventory. Accumulation of flammable concentrations of tritium at the ceiling over time, even assuming the conservatively sized "standard" storage room, is not a concern at radiological facilities. If an event were to somehow convert 100% of tritium at a radiological facility, the resulting pressure wave would be insufficient to propagate widescale major facility damage that could release gases in other areas. Thus, tritium explosions and deflagrations at radiological facilities are of very low probability and low consequence. Rather than explosions or deflagrations, at radiological facilities it is more relevant to think of elemental tritium converting to water vapor in a fire environment under sub-LFL concentrations in air, a scenario that is discussed in more detail in Chapter 5.

2.1.2. Analysis for Hazard Category 3 Facilities (1.6 g - 30 g Tritium)

Similar analysis for a facility with a maximum of 30 g of T_2 (the threshold quantity for a tritium HC2 facility) in Table 1 shows that with an ignition safety factor of 7 or more and using the same conservative assumptions discussed for radiological facilities above, the risk of triggering a rapid oxidation event remains low. Assuming homogeneous mixing, the average molar T_2 concentration in the small standard room is 0.56%, which is on par with the aforementioned conservative 0.4% LOC concentration used by responders for hydrogen (this is below the 0.66% LOC that would be obtained from the tritium LFL estimated by Cadwallader and Petti, 2002). However, if one considers that facilities with large tritium inventories will have larger storage rooms, even a modest 2x increase to the room size brings the average T_2 concentration to 0.27 mole %, well below even this most

conservative LOC intended for entry of responders into a room with patchy concentrations of flammable gas (implicitly a scenario with a pressurized source). Another way to conceptualize the low hazard is to consider the fact that the 4% LFL threshold is reached when 30 g of tritium expands to fill a volume of 3.1 m^3, corresponding to a sphere of radius 0.91 m. Beyond a distance of this magnitude from the point of release, the released tritium dilutes to concentrations incapable of ignition or flame propagation. Any partitioning of the inventory into different containers, even within the same room, would decrease this distance by effectively diluting the T_2 concentration at the initial time of release. These calculations, despite their conservative starting assumptions, again illustrate that tritium-fueled explosions and deflagrations are unlikely to be the bounding hazard scenario at tritium HC3 facilities.

Having established the low risk of an ignition event at a tritium HC3 facility, we can again examine the potential consequences of an unlikely explosion or deflagration. As was discussed previously, the risk of achieving a high oxidation fraction after an ignition event decreases rapidly with increasing safety factor (combustion efficiency drops rapidly for hydrogen concentrations below 8% in air with low moisture, Thompson et al., 1988, corresponding to ISF > 0.5). Nevertheless, we consider the unlikely case of the mixture igniting and achieving 100% conversion to water vapor for worst-case damage estimates. The resulting rapid energy release from such an event would result in an overpressure ("CVE Pressure" in Table 2-1) of 3.2 psig within the small standard room. Any partitioning of the tritium inventory in different rooms would decrease the severity of an ignition event, but rather than assume how the tritium inventory is distributed within the hypothetical facility, we consider the reasonable and more easily generalizable assumption that the tritium is stored in a room with 2x the standard room volume. This conservative increase in the room size due to the larger inventory housed within results in an overpressure of 1.6 psig. We consider 2.8 psi to be an appropriate "major facility damage threshold" based on the range of specific impulse and overpressures resulting in "minor structural damage", as outlined by Baker, et. al. (Baker et al, 1992), and the damage approximations of Kinney and Graham (1985). The 1.6 psig overpressure for 30 g of tritium suggests that only minor facility damage would be expected to occur in the worst-case scenario at a HC3 facility. Thus, we again conclude that in this case the tritium inventory by itself will not generate facility damage capable of releasing tritium stored in other facility areas. As before, tritium mixtures containing H_2 and D_2 are not considered explicitly in the calculations, but the behavior of isotopic mixtures may be deduced by replacing the "Moles of T_2" row in Table 1 with "Total moles of H_2, D_2, and T_2".

In summary, with an ignition safety factor of 7 or more, the T_2 gas inventory at HC3 tritium facilities also pose a low explosion and deflagration risk. The elemental tritium gas in an HC3 facility is unlikely on its own to result in damage that propagates throughout the facility unless H_2, D_2 or other flammables are added in close proximity and significant quantities. Ignition safety factors for an HC 3 tritium facility are likely much higher than 7 due to the larger size of tritium lab spaces with larger inventories and the finite spatial distribution of the tritium inventory. Even if an event were to somehow convert 100% of tritium at an HC3 facility, the resulting pressure wave in anything larger than a very small room would be insufficient to cause major facility damage capable of releasing tritium stored in other areas of a facility. This analysis demonstrates that explosions and deflagrations, barring direct immersion in a fire, are not relevant concerns for HC3 facilities; rather, as with radiological facilities, it is more relevant to think of elemental tritium converting to water vapor in a fire environment from sub-LFL concentrations in air as a bounding hazard for HC3 facility inventories, a scenario examined in Chapter 5.

2.1.3. Analysis for Hazard Category 2 Facilities (> 30 g Tritium)

For HC2 facilities, which have greater than 30 g of tritium, it is more challenging to make a blanket statement to characterize the tritium hazards due to the wide range of inventories that this category encompasses. Whether explosions or deflagrations are major concerns for a HC2 facility will depend on a number of site-specific factors. For the small standard room examined in Table 2-1 (very conservative), the average concentration will exceed 4% at tritium quantities above 222.5 g. For HC2 facilities with closer to 30 g of tritium, the risk of deflagrations or explosions remains remote. However, as the safety factor approaches 1, the occurrence of ignition becomes likely.

When evaluating this wide range of possibilities, it is important to remember that the calculations in Table 2-1 involve many conservative assumptions. As was described in the earlier discussion of HC3 facilities, the size of the rooms used to store tritium tend to increase with the inventory. Rooms storing large quantities of tritium gas at HC2 facilities can become quite large, and the ignition safety factor scales with the size of the room in question. Larger facilities have more potential for gas dilution and pressure wave dissipation before encountering a structure. Thus, both the likelihood of an ignition event and the severity of the consequences for an ignition event on the facility structure will likely differ greatly from the values in Table 2-1. As was also mentioned earlier, the finite physical distribution of T_2 containers in relation to other flammables is a very important mitigating factor to consider in a facility's tritium safety analyses, as this inherently dilutes the starting T_2 concentration distribution upon release. Storage conditions can also impact the explosion risk since low pressure gas will tend to release to the room air slower in the case of a leaking containment vessel, resulting in lower T_2 concentration in air at any location or point in time. Depending on the size of the inventory and the nature of the facility, it is possible for leaked tritium to accumulate over time near the ceiling, potentially posing a delayed ignition risk. Each of these factors should be considered when interpreting the results in Table 2-1.

2.1.4. Summary

This simple equilibrium analysis illustrates that for radiological or HC3 tritium facilities, the tritium quantities are extremely limited and essentially preclude explosion or propagating flames as a valid oxidation mechanism of concern for any significant fraction of T_2 inventory. Slower conversion mechanisms such as sub-LFL conversion in proximity to a sustained external fire, simulated in Chapter 5 and test evaluated in Chapter 6, are of greater practical concern. Even in a worst-case scenario, the energy released from the rapid oxidation of the T_2 alone is insufficient to propagate facility damage of a magnitude required to liberate more tritium in other areas of the facility. These statements also hold true for some HC2 facilities with smaller tritium inventories. However, a general statement regarding HC2 facilities is more difficult to make due to the wide range of facility inventories encompassed by this category. The likelihood and degree of the hazards at a given HC2 facility will depend on the specific nature of a facility's inventory (such as T_2 quantities, storage pressures, and spatial distribution), the size of the facility, and the co-localization of tritium with hydrogen, deuterium and/or other flammables. Ignition safety factors for different T_2 quantities and room sizes may be deduced by appropriate scaling of the white rows in Table 2-1.

The equilibrium calculations show that the hazards for tritium at DOE facilities can vary widely depending on the specific nature of the inventory and its storage facility. However, with simple conservative assumptions it can be seen that for most tritium facilities it is erroneous to automatically equate tritium hazards with those of hydrogen. Given the drastic difference in quantity and pressure compared to hydrogen storage applications, the dominant oxidation mechanisms relevant for hydrogen accidents do not pose the greatest conversion hazards for

radiological, HC3 and even some smaller HC2 facilities. This concept of scale should be carefully considered in tritium safety analyses.

2.2. Confined Ignition of Elemental Tritium Gas (i.e., Leaking Containment Vessel)

Deflagrations of released elemental tritium gas that is initially under low-pressure storage conditions and/or low quantities will typically result in conversion significantly less than 100% since tritium concentrations in air are typically well below the lower flammability limit. This scenario is examined in detail in Chapter 5. However, one common consideration in hydrogen safety literature is that some confinement may occur, permitting the released H_2 to accumulate or persist at concentrations within the wide flammability range of 4% to 75%. Thus, deflagrations under confined or semiconfined conditions are a reasonable safety concern that must also be considered for tritium. Because the T_2 quantities in question are often very small, confinement scenarios with the highest impact (i.e., prior to the dissipation of significant fractions of the released T_2 to below the LFL) for most tritium facilities must happen near the point of release. The original gas container may provide the means to retain partial confinement in certain accident scenarios (i.e., a non-catastrophic containment breach), and the container is by definition within the immediate vicinity of the gas in every case. For this reason, confined oxidation of T_2 within a (non-catastrophically compromised) leaking containment vessel is considered here.

For this analysis, the vessels are assumed to be initially stored with sub-atmospheric pressures of H_2 gas. Tritium gas is commonly transported in Tritium Containment Vessels (TCVs) that are filled with near-atmospheric to sub-atmospheric pressures of elemental tritium gas (and occasionally other hydrogen isotopes). As the gas is used, the pressure will decrease. The negative-pressure T_2 storage cylinder is assumed to be compromised non-catastrophically (i.e., the hydrogen isotopes are assumed to remain more or less confined in the original container volume while air gradually enters the vessel), in such a way as to form a confined and potentially ignitable gas mixture. Note that this is not necessarily expected to be a common failure mode that applies to every container within a dispersed facility inventory; nevertheless, the original container is a potential source of partial confinement and is considered as a potential worst case for a confined T_2 and air mixture. Ignition of the T_2-air mixture would result in the formation of some tritium oxide and the release of energy, the latter of which would cause an internal pressure increase that would actively drive the rapid release of some fraction of the bottle's reacted contents through the leak orifice.

Table 2-2. TIGER simulation results for bottles stored at Sandia (0.85 atm air pressure). Results assume that all gas in the container prior to air ingress was H_2.

Starting Hydrogen Partial Pressure (atm*100)	30	35	40	45	50	55	60	65	70	75	80	85
Air Ingress Partial Pressure (atm*100)	55	50	45	40	35	30	25	20	15	10	5	0
Adiabatic Flame Temperature (K)	2165.5	2020.7	1869.2	1712.5	1551.0	1385.0	1214.3	1038.5	857.8	676.0	525.6	298.0
Ending Mole% H2	12.2	21.2	30.0	38.6	46.9	55.0	63.0	70.7	78.3	85.5	91.5	100.0
Ending Mole% H2O	27.8	25.0	22.3	19.6	16.9	14.3	11.8	9.3	6.9	4.6	2.6	0.0
Ending Mole% N2	59.2	53.2	47.3	41.5	35.9	30.4	25.0	19.8	14.7	9.6	3.6	0.0
Tfinal/Tinitial	7.27	6.78	6.27	5.75	5.20	4.65	4.07	3.48	2.88	2.27	1.76	1.00
Fraction of gas (includes air) expelled (ARF)	0.86	0.85	0.84	0.83	0.81	0.78	0.75	0.71	0.65	0.56	0.43	0.00
Fraction Converted to water vapor (CF)	0.69	0.54	0.43	0.34	0.27	0.21	0.16	0.12	0.08	0.05	0.03	0.00
Fraction Expelled & Converted to water vapor	0.60	0.46	0.36	0.28	0.21	0.16	0.12	0.08	0.05	0.03	0.01	0.00

The TIGER commands for the 0.3 atm H_2 partial pressure is **com,h2,0.3,air,0.55,mole** followed by **aft,p,0.85**

Table 2-2 shows the TIGER simulation results for various starting T_2 bottle pressures at Sandia National Laboratories, where the atmospheric pressure is lower than 1 atm due to the higher

elevation. The top row shows the starting pressure of the initial hydrogen isotopes mixture inside the container. The second row shows the partial pressure of air that flows into the vessel such that the bottle pressure equilibrates to local atmospheric pressure (0.85 atm). Similar calculations were performed for bottles stored closer to sea level (1 atm air pressure) in Table 2-3. The adiabatic flame temperatures from Table 2-2 and Table 2-3 are plotted in Figure 2-2.

Table 2-3. TIGER simulation results for bottles stored at sea level (1 atm air pressure). Results assume that all gas in the container prior to air ingress was H2.

Starting Hydrogen Partial Pressure (atm*100)	30	35	40	45	50	55	60	65	70	75	80	85
Air Ingress Partial Pressure (atm*100)	70	65	60	55	50	45	40	35	30	25	20	15
Adiabatic Flame Temperature (K)	2276.2	2165.6	2043.7	1917.2	1786.8	1652.9	1515.6	1374.8	1230.3	1081.8	929.6	774.9
Ending Mole% H2	4.1	11.8	19.4	27.0	34.3	41.5	48.5	55.4	62.2	68.8	75.3	81.6
Ending Mole% H2O	30.2	28.0	25.6	23.2	20.9	18.6	16.4	14.2	12.0	9.9	7.9	5.9
Ending Mole% N2	64.7	59.5	54.4	49.3	44.4	39.5	34.8	30.1	25.6	21.1	16.7	12.4
Tfinal/Tinitial	7.64	7.27	6.86	6.43	6.00	5.55	5.09	4.61	4.13	3.63	3.12	2.60
Fraction of gas (includes air) expelled (ARF)	0.87	0.86	0.85	0.84	0.83	0.82	0.80	0.78	0.76	0.72	0.68	0.62
Fraction Converted to water vapor (CF)	0.88	0.70	0.57	0.46	0.38	0.31	0.25	0.20	0.16	0.13	0.09	0.07
Fraction Expelled & Converted to water vapor	0.77	0.61	0.49	0.39	0.32	0.25	0.20	0.16	0.12	0.09	0.06	0.04

The TIGER commands for the 0.3 atm H_2 partial pressure is **com,h2,0.3,air,0.70,mole** followed by **aft,p,1**

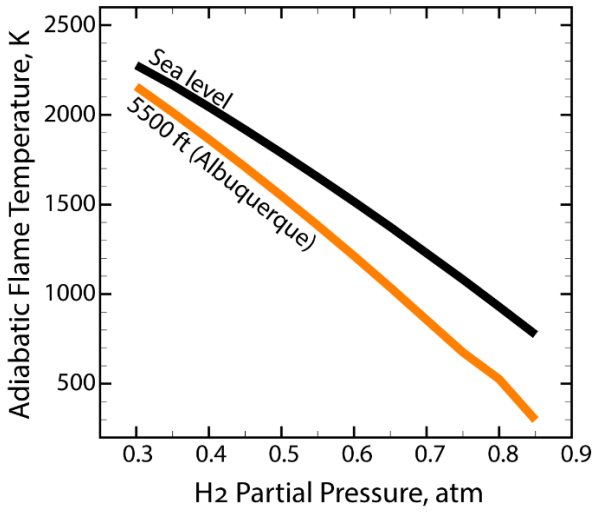

Figure 2-2. Adiabatic flame temperatures from Table 2-2 and Table 2-3.

The degree of air ingress is assumed to be dependent on the original container gas pressure, such that the T_2 + air total pressure inside the containment vessel prior to ignition equilibrates to the local atmospheric pressure. Ignition is then assumed to occur by some mechanism (a conservative assumption), and the reaction is assumed to proceed to the extent permitted by the amount of oxygen available. The gaseous reaction products are assumed to equilibrate, from which a conversion fraction (CF) can be determined. The fraction of material that is released (i.e., airborne release fraction, ARF) is then determined by assuming that pressure equilibrium between the inside and outside of the containment vessel is re-established at local atmospheric pressure.

Table 2-2 and Table 2-3 summarize the results for the confined combustion reaction under various starting pressures. When interpreting these simulation results for tritium applications, the starting hydrogen partial pressure row should be interpreted to be the total pressure of all hydrogen isotopes (H_2, HD, HT, D_2, DT, T_2, or any mixture thereof). This is because the presence of H_2 and D_2 will impact the ARF and CF of the co-localized tritium. The ARF (Table 2-2 and Table 2-3, row 8) and CF (Table 2-2 and Table 2-3, row 9) are shown individually as well as their product (Table 2-2 and Table 2-3, row 10). Due to the nature of the accident under consideration, the ARF and CF are

coupled together. The product of the two is the most reflective measure of the relative radiological hazard posed by the different starting conditions in this accident scenario. Since the dose coefficient (DC) of tritiated water vapor is 10,000 times greater than that for elemental tritium gas, it is the tritium that both converts to tritiated water vapor and escapes containment that dominates the radiological hazards; while some residual T_2 is released in most of the conditions considered, the hazard of the released T_2 is negligible compared to that of the released tritiated water vapor, and tritiated water vapor that remains contained is not a radiological hazard within a reasonable time window of concern.

As an example of how to interpret the data in Table 2-2 and Table 2-3, consider a T_2 vessel in Albuquerque, NM with a starting pressure of 0.55 atm (Table 2-2, column 7). 0.3 atmospheres of air will be driven into the vessel due to the pressure difference between the bottle interior and the surrounding air (the air is assumed to not be depleted of O_2). Since air contains only ~21% O_2 under normal conditions, the pre-ignition gas mixture is ~0.55 atm T2 and ~0.06 atm O_2, and any combustion reaction of the T_2 gas in the confined volume of the vessel will be O_2 limited. Conservatively assuming reaction goes to completion, the ratio between the final (post-ignition) and initial (ambient) gas temperature ($T_{final}/T_{initial}$) in the vessel is 4.65. From the ideal gas law, this temperature change will result in an internal pressure increase which will provide the driving force for the vessel to expel 78% of its contents (i.e., ARF=0.78); however, <21% of its tritium contents is expected to have reacted to form tritiated water vapor (i.e., CF=0.21).

When weighing the results from the TIGER equilibrium calculations in this section, it is worth mentioning that:

- ARF and CF values are not independent of each other, and they vary differently with the starting storage condition.
- Given the sub-atmospheric starting pressures, none of the pressures generated by the combustion reaction were capable of completely destroying the bottles (i.e., ARF < 1 for all starting T2 gas pressures examined). Tritium is known to be incompatible with organic materials and is stored in metal containers for this reason.
- It is difficult to identify an effective ignition source that would operate inside a closed metal container using only the materials and structures present in such a design; the metallic walls would tend to preclude sparks in the interior. Most plausible confined ignition scenarios are destructive on the level of a large collision or engulfment of the container in a fire, either of which may negate the unique features of the confined ignition scenario.
- For gases stored very close to atmospheric pressure, the T_2 combustion reaction in this confined ignition scenario is O_2 limited. In an environment with a widespread building fire, O_2 may be partially depleted from the surrounding air, which would tend to reduce the CF and ARF values from those listed in Table 2-2 and Table 2-3.
- The flammability limits of H_2 gas spans 4% to 75% in air at 1 atmosphere. The equilibrium calculations assume that the reaction occurs in all cases regardless of whether the starting gas mixture falls within the flammability limits. Furthermore, the lower flammability limit of T_2 tends to be higher than that for H_2 (Cadwallader 2002).
- For the described confined ignition scenario to come into play, the tritium gas vessels must first be compromised. Although the mechanism by which that initial leak is formed has not been considered here, the generation of semi-confined reaction conditions in all tritium gas

vessels in a facility is not probable given their finite spatial distribution. Some fraction of vessels may also remain intact (ARF = CF = 0) and some may undergo unconfined release, in which case, the analysis from Chapter 5 of this report is more applicable.

- If the elemental T_2 gas is mixed with other H_2 isotopologues (which are also flammable), then these other H_2 isotopologues will also react with the available oxygen. In oxygen-limiting scenarios, this would tend to further reduce the fraction of the T_2 that converts to HTO compared to the values in Table 2-1.
- ARFs and CFs in Tables 3 and 4 would be reduced further if T_2 were diluted with any inert gases such as N_2 or Ar.
- The ARF*CF product is higher for containers that have lower starting total pressures. Lower starting pressures such as 0.3 atm are reflective of partially spent gas bottles. A lower fraction of the tritium inventory is contained in vessels with lower pressures. Thus, when considering a facility-wide average, the most conservative ARF*CF value in Tables 3 and 4 may not be the most relevant. TCVs with the most T2 gas (near 1 atm), have the smallest CF and ARF values.

2.2.1. Summary

Given the finite spatial distribution of tritium vessels within a tritium facility and the robustness of the containers, the confined ignition scenario considered here is not necessarily believed to be a common failure mode, but it illustrates the complex interplay between pressure, quantity, and the resulting ARF and CF values. Indeed, it is difficult to identify an effective ignition source that would operate inside a closed metal container using only the materials and structures present in such a design; the metallic walls would tend to preclude sparks in the interior. While bottles with the lowest sub-atmospheric pressures in this scenario would tend to pose the greatest hazard when considering the fraction of T_2 that converts to tritiated water vapor, these bottles also inherently house a smaller quantity of tritium (they are depleted), while sub-atmospheric bottles that contain larger tritium quantities pose lower hazards. This would suggest that when considering a facility-wide average T_2-to-tritiated water CF, this confined ignition scenario is not a likely bounding case. For this reason, the conversion of released T_2 gas under sub-LFL concentrations in air are carefully considered in Chapter 5.

This page left blank

3. HYDROGEN ISOTOPE PROPERTIES

This chapter describes a compilation of thermodynamic and transport properties required to model the isotopes of hydrogen using computational fluid dynamics (CFD). This work was initially presented at the 12th US National Combustion Institute Meeting, and the content of this chapter is from a paper that was produced for this meeting (Shurtz et al., 2021). This work addresses a key uncertainty relative to modeling tritium, which is that property data are largely unavailable due to the scarcity and the lack of common studies with tritium as a fluid. An accepted methodology is followed to deduce appropriate property information that largely consists of projecting the trend of the particular property of interest using measurements of the more common protium (^{1}H) and deuterium (^{2}H) isotopes.

3.1. Introduction

In order to assess the safety properties of radioactive tritium release in a fire scenario via computational fluid dynamics (CFD) modeling, thermodynamic and transport properties are required for isotopes of hydrogen (H_2, D_2, and T_2) and their oxidized water derivatives (H_2O, D_2O, T_2O, and mixed-isotope combinations). Ideally, isotope effects should also be considered for oxidation kinetics, but consideration of these is beyond the scope of this paper. The expected trend for hydrogen diffusing in air from a leaking container is that lighter isotopes will diffuse faster, which means molecules composed of the protium isotope (^{1}H) should disperse throughout the available volume more rapidly than their isotopologues containing tritium (^{3}H or T). In a hydrogen leak scenario with a fire in the room, some portion of the protium may also reach a location hot enough to react with oxygen sooner than would be the case with an equivalent tritium leak. The degree of conversion of radioactive molecular tritium T_2 ($^3H_2$) to T_2O (^3H_2O) in such a scenario is an important safety consideration because T_2O is assimilated by the human body far more readily than T_2 (DOE-STD-1129-2015).

To our knowledge no attempt has been made to quantify differences between behavior of tritium and protium using distinct properties in a CFD model of a credible fire scenario. This work evaluates and summarizes properties selected for implementation in CFD simulations of fires with a nearby hydrogen isotope source, appropriate for evaluating safety-relevant differences in behavior arising from a tritium release event (T_2) with respect to a protium release event (H_2). Since very few properties have been measured and released publicly for tritium, estimates have been made for tritium properties based on known trends for protium and deuterium (^{2}H or D).

The properties assembled in this work are intended for fire simulations in SIERRA/Fuego (2019a, 2019b), which is an in-house CFD code developed and maintained at Sandia National Laboratories. Thermodynamic and transport properties for chemical species in Fuego are supplied using a Cantera-style ".xml" file (Goodwin et al. 2021); the types of parameters reported in this work are thus constrained in terms of the forms of the equations used to calculate properties. The CFD simulation results of a tritium fire scenario utilizing the properties that are the subject of this work are presented in Chapter 5.

3.2. Thermodynamic Properties

Thermodynamic properties used in SIERRA/Fuego are derived from coefficients developed by NASA for chemical equilibrium calculations. These take the form of either the legacy 7-parameter model (McBride et al. 1993) or the extended 9-parameter model (McBride et al. 2002), either of which typically occurs in two temperature ranges. The 7-parameter model for properties of ideal

gases at atmospheric pressure (1 bar) consists of a fourth-order polynomial for heat capacity with appropriate integral expressions for enthalpy and entropy (McBride 1993):

$$\frac{c_p^0(T)}{R} = a_0 + a_1 T + a_2 T^2 + a_3 T^3 + a_4 T^4 \quad 3\text{-}1$$

$$\frac{h^0(T)}{RT} = a_0 + \frac{a_1}{2} T + \frac{a_2}{3} T^2 + \frac{a_3}{4} T^3 + \frac{a_4}{5} T^4 + \frac{a_5}{T} \quad 3\text{-}2$$

$$\frac{s^0(T)}{R} = a_0 \ln(T) + a_1 T + \frac{a_2}{2} T^2 + \frac{a_3}{3} T^3 + \frac{a_4}{4} T^4 + a_6 \quad 3\text{-}3$$

The most recent version of the NASA chemical equilibrium code CEA adopts two additional coefficients to allow the heat capacity to be modeled with non-polynomial terms (McBride 2002). To reduce confusion, different letters have been used in this representation of the coefficients for the two versions of the NASA thermodynamic curve fits. The 9-parameter model is:

$$\frac{c_p^0(T)}{R} = b_0 T^{-2} + b_1 T^{-1} + b_2 + b_3 T + b_4 T^2 + b_5 T^3 + b_6 T^4 \quad 3\text{-}4$$

$$\frac{h^0(T)}{RT} = -b_0 T^{-2} + b_1 \frac{\ln(T)}{T} + b_2 + \frac{b_3}{2} T + \frac{b_4}{3} T^2 + \frac{b_5}{4} T^3 + \frac{b_6}{5} T^4 + \frac{b_7}{T} \quad 3\text{-}5$$

$$\frac{s^0(T)}{R} = -\frac{b_0}{2} T^{-2} - b_1 T^{-1} + b_2 \ln(T) + b_3 T + \frac{b_4}{2} T^2 + \frac{b_5}{3} T^3 + \frac{b_6}{4} T^4 + b_8 \quad 3\text{-}6$$

The NASA curve-fits for the 7-parameter model (Equations 3-1 through 3-3 with coefficients in Table 3-1) and the 9-parameter model (Equations 3-4 through 3-6 with coefficients in

Table 3-2) considered in this study are of essentially identical quality with respect to the NIST-JANAF Thermochemical Tables (Chase 1998), which are taken as authoritative values in this work. An entropy comparison between the two models shown in Figure 3-1 for H_2O demonstrates the comparable quality of the two models. The two NASA models differ from each other by at most 0.02% from 298.15 K to 3000 K, and the maximum deviation from the JANAF tables is 0.17% at 3000 K. These very small differences for H_2O entropy in Figure 3-1 are typical of entropies and enthalpies for D_2O, H_2, and D_2 using either of the NASA models. Enthalpies of formation for isotopes of molecular hydrogen at 298.15 K are zero by definition; calculations using the NASA models for H_2 and D_2 yield values on the order of 10^{-5} at 298.15 K, which is acceptably close to zero. The temperature range shown in Figure 3-1 is sufficient for most combustion modeling because the adiabatic flame temperature of H_2 in air is close to 2500 K. Hence,

Table 3-2 omits a third temperature range provided above 6000 K for protium and deuterium isotopologues of H_2 and H (McBride 2002).

The existing NASA coefficients for H_2, D_2, H_2O, and D_2O are used directly in this work. Estimated properties for compounds containing tritium are defined in terms of coefficient adjustments from the corresponding deuterated compounds. The newer 9-parameter model (Equations 3-4 through 3-6,

Table 3-2, from McBride 2002) was used to derive coefficient offsets reported in this paper. However, the near-perfect agreement with the 7-parameter model (Equations 3-1 through 3-3, Table 3-1, from McBride 1993) indicates that the same offsets may be applied to the analogous coefficients in either model. As the 7-parameter model was already in use for other species in our simulations,

the simpler 7-parameter model was applied in our CFD calculations in Chapter 5 with coefficients from Table 3-1 plus the tritium isotopologue coefficients in Table 3-3 that are calculated in this work. Table 3-4 presents similar information for tritium compounds using the 9-parameter model (McBride 2002).

Table 3-1. NASA thermodynamic coefficients for H and D, 7-parameter model (McBride 1993, Equations 3-1 to 3-3)

	H_2	D_2	H_2O	D_2O
	Min Temp = 200 K, Max Temp = 1000 K	**Min Temp = 200 K, Max Temp = 1000 K**	**Min Temp = 200 K, Max Temp = 1000 K**	**Min Temp = 300 K, Max Temp = 1000 K**
a_0	2.344331120E+00	3.495469740E+00	4.198640560E+00	3.854113100E+00
a_1	7.980520750E-03	2.583481590E-04	-2.036434100E-03	1.471228800E-04
a_2	-1.947815100E-05	-1.317625020E-06	6.520402110E-06	3.006900600E-06
a_3	2.015720940E-08	2.429120180E-09	-5.487970620E-09	-1.774762800E-09
a_4	-7.376117610E-12	-1.059824980E-12	1.771978170E-12	2.301886200E-13
a_5	-9.179351730E+02	-1.046315800E+03	-3.029372670E+04	-3.115165100E+04
a_6	6.830102380E-01	-2.519053850E+00	-8.490322080E-01	1.733419840E+00
	Min Temp = 1000 K, Max Temp = 6000 K	**Min Temp = 1000 K, Max Temp = 6000 K**	**Min Temp = 1000 K, Max Temp = 6000 K**	**Min Temp = 1000 K, Max Temp = 5000 K**
a_0	2.932865790E+00	2.730689290E+00	2.677037870E+00	2.726459500E+00
a_1	8.266079670E-04	1.480047810E-03	2.973183290E-03	3.984517300E-03
a_2	-1.464023350E-07	-4.793148480E-07	-7.737696900E-07	-1.493262600E-06
a_3	1.541003590E-11	7.894962740E-11	9.443366890E-11	2.634977200E-10
a_4	-6.888044320E-16	-4.883808230E-15	-4.269009590E-15	-1.764955700E-14
a_5	-8.130655970E+02	-7.952675040E+02	-2.988589380E+04	-3.090263800E+04
a_6	-1.024328870E+00	1.642662430E+00	6.882555710E+00	7.318201340E+00

Table 3-1 continued, for Equations 3-1 to 3-3

	H	D
	Min Temp = 200 K, Max Temp = 1000 K	**Min Temp = 200 K, Max Temp = 1000 K**
a_0	2.500000000E+00	2.500000000E+00
a_1	0.000000000E+00	0.000000000E+00
a_2	0.000000000E+00	0.000000000E+00
a_3	0.000000000E+00	0.000000000E+00
a_4	0.000000000E+00	0.000000000E+00
a_5	2.547365990E+04	2.592125960E+04
a_6	-4.466828530E-01	5.917158270E-01
	Min Temp = 1000 K, Max Temp = 6000 K	**Min Temp = 1000 K, Max Temp = 6000 K**
a_0	2.500002860E+00	2.500000000E+00
a_1	-5.653342140E-09	0.000000000E+00
a_2	3.632517230E-12	0.000000000E+00
a_3	-9.199497200E-16	0.000000000E+00
a_4	7.952607460E-20	0.000000000E+00
a_5	2.547365890E+04	2.592125960E+04
a_6	-4.466984940E-01	5.917158270E-01

Table 3-2. NASA thermodynamic coefficients for H and D, 9-parameter model (McBride 2002, Equations 3-4 to 3-6)

	H_2	D_2	H_2O	D_2O
	Min Temp = 200 K, Max Temp = 1000 K	**Min Temp = 200 K, Max Temp = 1000 K**	**Min Temp = 200 K, Max Temp = 1000 K**	**Min Temp = 200 K, Max Temp = 1000 K**
b_0	4.078323210E+04	2.125790482E+04	-3.947960830E+04	6.958278470E+03
b_1	-8.009186040E+02	-2.996945907E+02	5.755731020E+02	-1.280889437E+01
b_2	8.214702010E+00	5.130314980E+00	9.317826530E-01	3.595878870E+00
b_3	-1.269714457E-02	-4.172970890E-03	7.222712860E-03	1.502093683E-03
b_4	1.753605076E-05	5.014345720E-06	-7.342557370E-06	3.594675050E-07
b_5	-1.202860270E-08	-2.126389969E-09	4.955043490E-09	5.340417200E-10
b_6	3.368093490E-12	2.386536969E-13	-1.336933246E-12	-5.181941270E-13
b_7	2.682484665E+03	3.944985900E+02	-3.303974310E+04	-3.101944566E+04
b_8	-3.043788844E+01	-1.164191209E+01	1.724205775E+01	2.895556576E+00
	Min Temp = 1000 K, Max Temp = 6000 K	**Min Temp = 1000 K, Max Temp = 6000 K**	**Min Temp = 1000 K, Max Temp = 6000 K**	**Min Temp = 1000 K, Max Temp = 6000 K**
b_0	5.608128010E+05	8.215168560E+05	1.034972096E+06	1.544193253E+06
b_1	-8.371504740E+02	-2.365623159E+03	-2.412698562E+03	-5.474238900E+03
b_2	2.975364532E+00	5.342974510E+00	4.646110780E+00	1.017542424E+01
b_3	1.252249124E-03	6.928145990E-05	2.291998307E-03	-9.619415540E-04
b_4	-3.740716190E-07	-8.523671020E-08	-6.836830480E-07	2.036545675E-07
b_5	5.936625200E-11	2.456447415E-11	9.426468930E-11	-2.050566442E-11
b_6	-3.606994100E-15	-1.960597698E-15	-4.822380530E-15	8.510770690E-16
b_7	5.339824410E+03	1.434214587E+04	-1.384286509E+04	2.983248980E+03
b_8	-2.202774769E+00	-1.712600356E+01	-7.978148510E+00	-4.465011570E+01

Table 3-2 continued, for Equations 3-4 to 3-6

	H	D
	Min Temp = 200 K, Max Temp = 1000 K	**Min Temp = 200 K, Max Temp = 1000 K**
b_0	0.000000000E+00	0.000000000E+00
b_1	0.000000000E+00	0.000000000E+00
b_2	2.500000000E+00	2.500000000E+00
b_3	0.000000000E+00	0.000000000E+00
b_4	0.000000000E+00	0.000000000E+00
b_5	0.000000000E+00	0.000000000E+00
b_6	0.000000000E+00	0.000000000E+00
b_7	2.547370801E+04	2.592128700E+04
b_8	-4.466828530E-01	5.917143380E-01
	Min Temp = 1000 K, Max Temp = 6000 K	**Min Temp = 1000 K, Max Temp = 6000 K**
b_0	6.078774250E+01	6.050019210E+01
b_1	-1.819354417E-01	-1.810766064E-01
b_2	2.500211817E+00	2.500210817E+00
b_3	-1.226512864E-07	-1.220711706E-07
b_4	3.732876330E-11	3.715172170E-11
b_5	-5.687744560E-15	-5.660680210E-15
b_6	3.410210197E-19	3.393920393E-19
b_7	2.547486398E+04	2.592243752E+04
b_8	-4.481917770E-01	5.902125370E-01

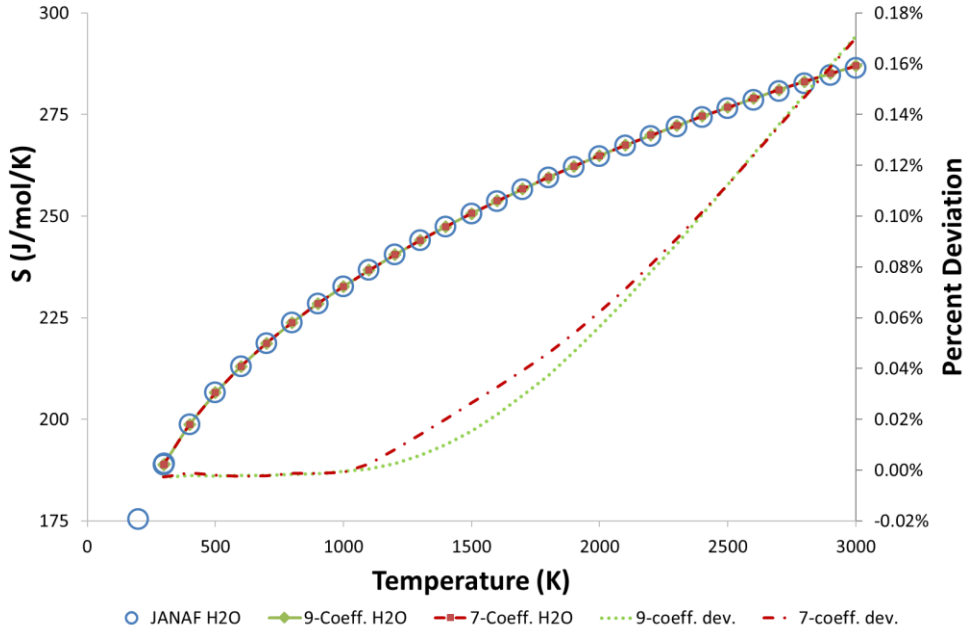

Figure 3-1. Entropy Comparison for H_2O models (McBride 1993, 2002) with respect to NIST-JANAF Tables (Chase 1998).

Table 3-3. 7-parameter thermodynamic coefficients (Equations 3-1 to 3-3) from this work for tritium species; *asterisks designate coefficients differing from deuterium isotopologues in Table 3-1

	T_2	T_2O	T
	Min Temp = 200 K, Max Temp = 1000 K	**Min Temp = 300 K, Max Temp = 1000 K**	**Min Temp = 200 K, Max Temp = 1000 K**
a_0	3.495469740E+00	4.009745100E+00*	2.500000000E+00
a_1	2.583481590E-04	1.471228800E-04	0.000000000E+00
a_2	-1.317625020E-06	3.006900600E-06	0.000000000E+00
a_3	2.429120180E-09	-1.774762800E-09	0.000000000E+00
a_4	-1.059824980E-12	2.301886200E-13	0.000000000E+00
a_5	-1.046315800E+03	-3.161854700E+04*	2.613474181E+04*
a_6	-1.18790409E+00*	1.733419840E+00	1.396607672E+00*
	Min Temp = 1000 K, Max Temp = 6000 K	**Min Temp = 1000 K, Max Temp = 5000 K**	**Min Temp = 1000 K, Max Temp = 6000 K**
a_0	2.730689290E+00	2.882091500E+00*	2.500000000E+00
a_1	1.480047810E-03	3.984517300E-03	0.000000000E+00
a_2	-4.793148480E-07	-1.493262600E-06	0.000000000E+00
a_3	7.894962740E-11	2.634977200E-10	0.000000000E+00
a_4	-4.883808230E-15	-1.764955700E-14	0.000000000E+00
a_5	-7.952675040E+02	-3.136953400E+04*	2.613474181E+04*
a_6	2.97381219E+00*	7.318201340E+00	1.396607672E+00*

Table 3-4. 9-parameter thermodynamic coefficients (Equations 3-4 to 3-6) from this work for tritium species; *asterisks designate coefficients differing from deuterium isotopologues in Table 3-2

	T_2	T_2O	T
	Min Temp = 200 K, Max Temp = 1000 K	**Min Temp = 200 K, Max Temp = 1000 K**	**Min Temp = 200 K, Max Temp = 1000 K**
b_0	2.125790482E+04	6.958278470E+03	0.000000000E+00
b_1	-2.996945907E+02	-1.280889437E+01	0.000000000E+00
b_2	5.130314980E+00	3.751510829E+00*	2.500000000E+00
b_3	-4.172970890E-03	1.502093683E-03	0.000000000E+00
b_4	5.014345720E-06	3.594675050E-07	0.000000000E+00
b_5	-2.126389969E-09	5.340417200E-10	0.000000000E+00
b_6	2.386536969E-13	-5.181941270E-13	0.000000000E+00
b_7	3.944985900E+02	-3.148634154E+04*	2.613476921E+04*
b_8	-1.031076233E+01*	2.895556576E+00	1.396606183E+00*
	Min Temp = 1000 K, Max Temp = 6000 K	**Min Temp = 1000 K, Max Temp = 6000 K**	**Min Temp = 1000 K, Max Temp = 6000 K**
b_0	8.215168560E+05	1.544193253E+06	6.050019210E+01
b_1	-2.365623159E+03	-5.474238900E+03	-1.810766064E-01
b_2	5.342974510E+00	1.033105620E+01*	2.500210817E+00
b_3	6.928145990E-05	-9.619415540E-04	-1.220711706E-07
b_4	-8.523671020E-08	2.036545675E-07	3.715172170E-11
b_5	2.456447415E-11	-2.050566442E-11	-5.660680210E-15
b_6	-1.960597698E-15	8.510770690E-16	3.393920393E-19
b_7	1.434214587E+04	2.516353104E+03*	2.613591973E+04*
b_8	-1.579485380E+01*	-4.465011570E+01	1.395104382E+00*

3.2.1. Enthalpy

The enthalpy coefficients for tritium species summarized in Table 3-3 and Table 3-4 are defined in this section. The corresponding coefficient differences for tritium-containing species with respect to their deuterium isotopologues are summarized in Table 3-5, which indicates that constant offsets were made in some cases to heat capacity (C_p), enthalpy (H) and/or entropy (S). Enthalpy shifts in the middle column of Table 3-5 were deduced from distinct enthalpies of dissociation reported by Greenwood and Earnshaw (1997) at standard temperature and pressure for molecular protium, deuterium and tritium (parenthetical values listed in Table 3-6). Table 3-6 indicates that these dissociation enthalpies are defined as the reverse of the standard formation reaction. The slopes of the molar formation enthalpies shown in Figure 3-2 imply constant and equivalent molar heat capacities for all three atomic isotopes. This is expected for the atomic species because they do not have rotational or vibrational degrees of freedom; the C_p column for atomic tritium in Table 3-5 is defined to be zero. Larger and non-constant heat capacities are expected for polyatomic molecules. The reported difference between the deuterium and tritium bond energies was applied to estimate a shift of +213.48221 in the constant enthalpy coefficient for formation of atomic tritium with respect to the deuterium coefficients (a_5 or b_7, as indicated in Table 3-5).

Table 3-5. Thermodynamic coefficient adjustments for tritium species with respect to the parameters for the analogous deuterium species; these were used to calculated terms with asterisks in Table 3-3 and Table 3-4.

Molecule	Change in a_0 or b_2 (linear C_p offset)	Change in a_5 or b_7 (H offset)	Change in a_6 or b_8 (S offset)
T_2O	0.15563196	-466.8959	0
T_2	0	0	1.33114976
T	0	213.48221	0.80489184

Table 3-6. Isotope properties used to estimate thermodynamic properties for T_2 and T_2O from NASA (McBride 2002); parenthetical values are reference bond strengths from (Greenwood and Earnshaw 1997) and terms with asterisks are extrapolations from this work.

Molecule	Molecular Mass (g/mol)	Reaction	Reaction Enthalpy (kJ/mol at 298.15 K)	Percent Isotopic Enthalpy Variation: (D/H -1) or (T/H-1)
H_2	2.0157	$H_2 \rightarrow 2H$	436.0 (435.88)	N/A
D_2	4.0282	$D_2 \rightarrow 2D$	443.44 (443.35)	1.71%
T_2	6.0321	$T_2 \rightarrow 2T$	447.0 (446.9)	2.53%
H_2O	18.0151	$2H + O \rightarrow H_2O$	-927.00	N/A
D_2O	20.0276	$2D + O \rightarrow D_2O$	-941.83	1.6%
T_2O	22.0315	$2T + O \rightarrow T_2O$	-948.87*	2.36%*

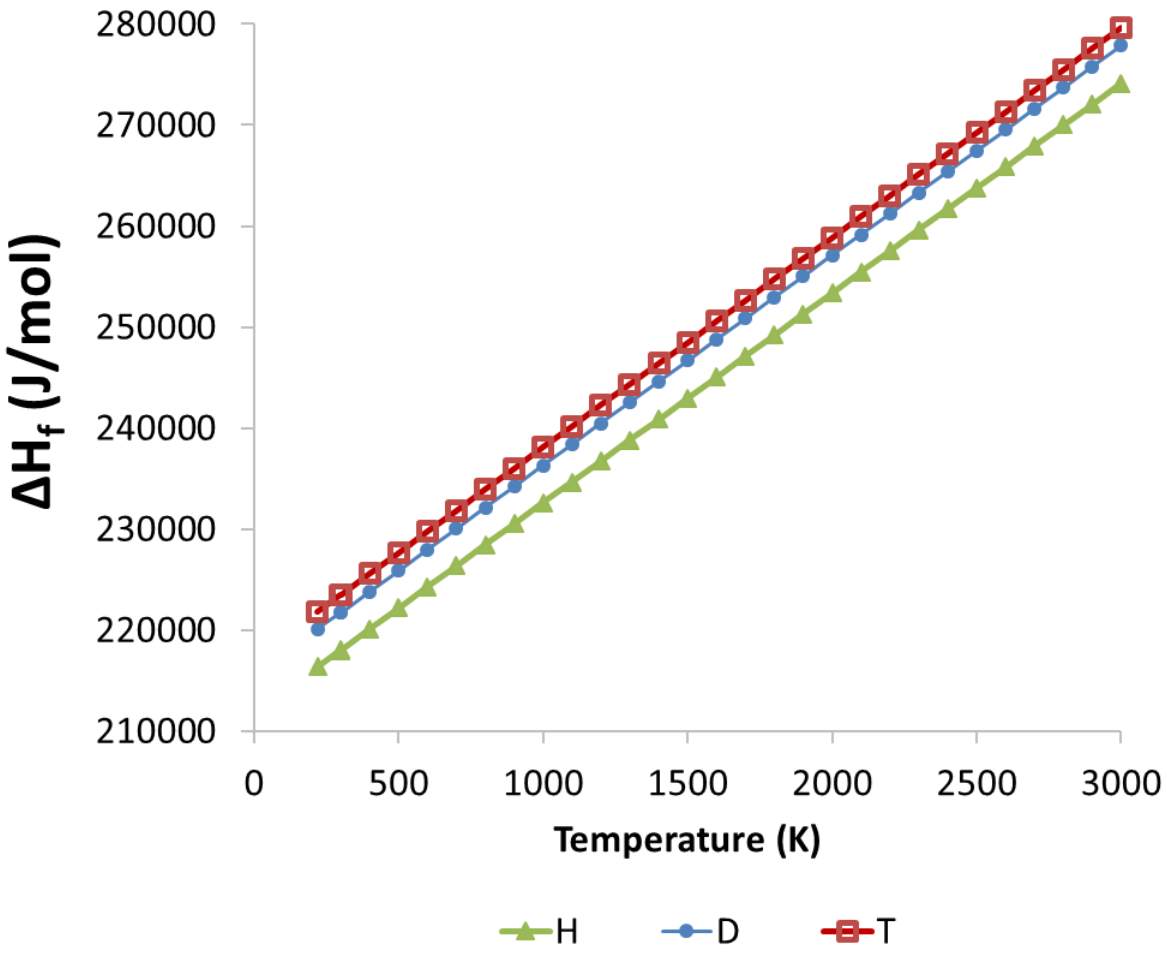

Figure 3-2. Enthalpies of formation for isotopes of atomic hydrogen (T from this work, H and D from McBride 2002)

Enthalpies of formation for pure molecular species are defined to be zero at 298.15 K for all isotopes; all isotopes of molecular hydrogen are normalized by this convention to have similar formation enthalpies at conditions that deviate from standard temperature and pressure. Figure 3-3 shows that the formation enthalpy of D_2 exceeds H_2 by only 4% at 3000 K, and the incremental difference from D_2 to T_2 is expected to be smaller. Consequently, the full set of D_2 enthalpy coefficients are recommended as a satisfactory approximation for T_2 without modification. Therefore, the first two coefficient shifts for T_2 in Table 3-5 are defined to be zero.

Given the scarcity of data on tritium bond strengths with respect to other hydrogen isotopes, the isotopic trends for H-H bond strengths from (Greenwood and Earnshaw 1997) were extrapolated to H-O bonds. The last column in Table 3-6 notes the percent isotopic enthalpy variation, which is defined here as the deviation of the reaction enthalpy with heavier hydrogen isotopes from the same reaction in a system that contains only the protium isotope. The ratio of these isotopic enthalpy variations for dissociation of T_2 with respect to D_2 is (2.53/1.71) = 1.48. This ratio was multiplied by the 1.6% isotopic enthalpy variation for formation of deuterated water (D_2O, as calculated from NASA enthalpies, McBride 2002) to obtain 2.36% isotopic enthalpy variation for formation of tritiated water (T_2O) from the atomic elements. This extrapolation was used to calculate the last

reaction enthalpy of -948.87 kJ/mol in Table 3-6, which was then used to define an offset of 3496.2 J/mol for T_2O formation enthalpy (from T_2 and O_2) with respect to D_2O formation at 298.15 K. While not ideal, this extrapolation is the best that could be done with the information available; the method described here of scaling isotopic reaction enthalpy variations prevents the extrapolations from becoming excessive.

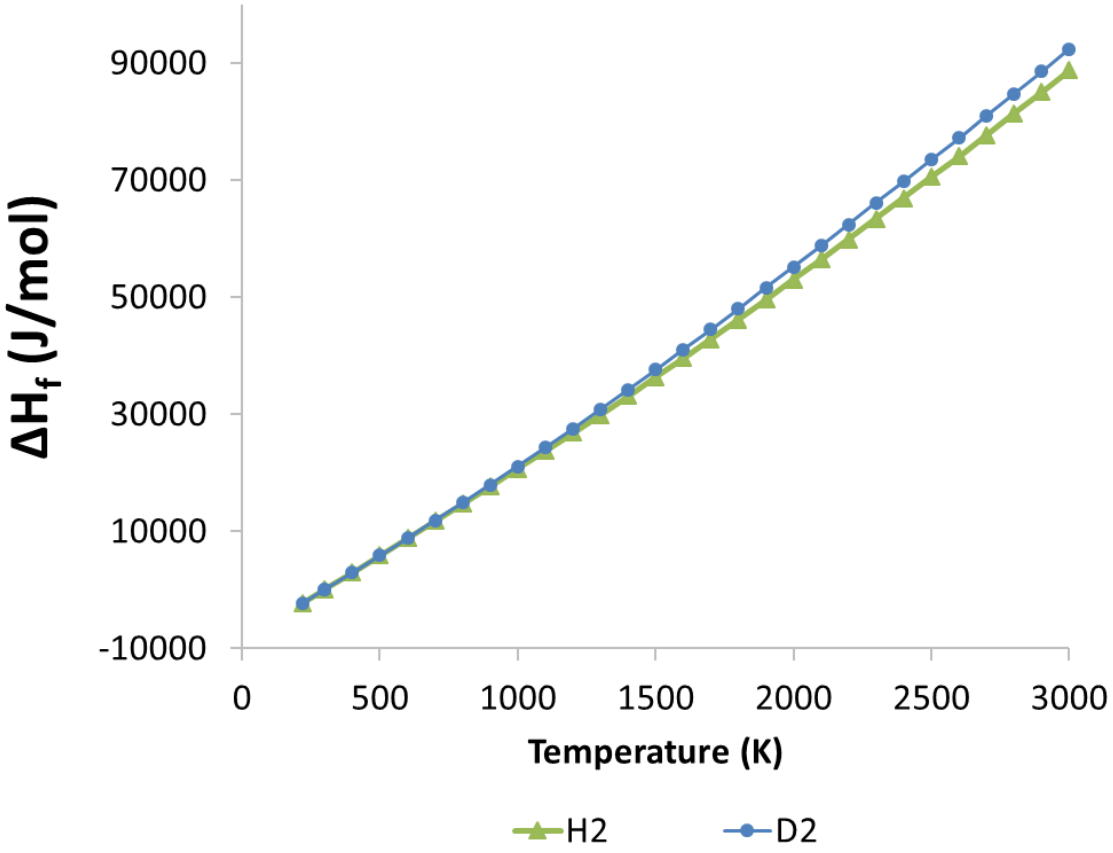

Figure 3-3. Enthalpies of formation for isotopes of molecular hydrogen (McBride 2002); T_2 is assumed to have formation enthalpy equivalent to D_2 in this work.

The enthalpy of formation of T_2O at 298.15 K and 1 atm calculated from the last line of Table 3-6 is -25.2706 kJ/mol, which is 3496.2 J/mol less than D_2O. Although the enthalpy is thus defined at the lowest temperature of interest, behavior at higher temperatures still requires guidance from the trend of the normal and deuterated water. Comparison of the formation enthalpies of H_2O and D_2O in Figure 3-4 suggests that differences between the isotopologues of water become less important at high temperatures because the enthalpy curves converge and cross near 2800 K (McBride 2002). As there are three constituent modes of heat capacity for water (translational, vibrational, and rotational), this observation may be explained if one of these modes is a weaker function of the constituent hydrogen isotope mass and becomes dominant at high temperature. The coefficient adjustments for T_2O in Table 3-5 include contributions from the linear heat capacity term (increase a_0 or b_2 by 0.1556and the enthalpy offset term (decrease a_5 or b_7 by 466.9) that simultaneously satisfy the enthalpy shift of -3496.2 J/mol at 298.15 K with respect to D_2O and an assumed crossover point of 3000 K (above the highest temperature of interest for our simulations). This approach enforces a trend for T_2O that is similar to H_2O and D_2O in Figure 3-4.

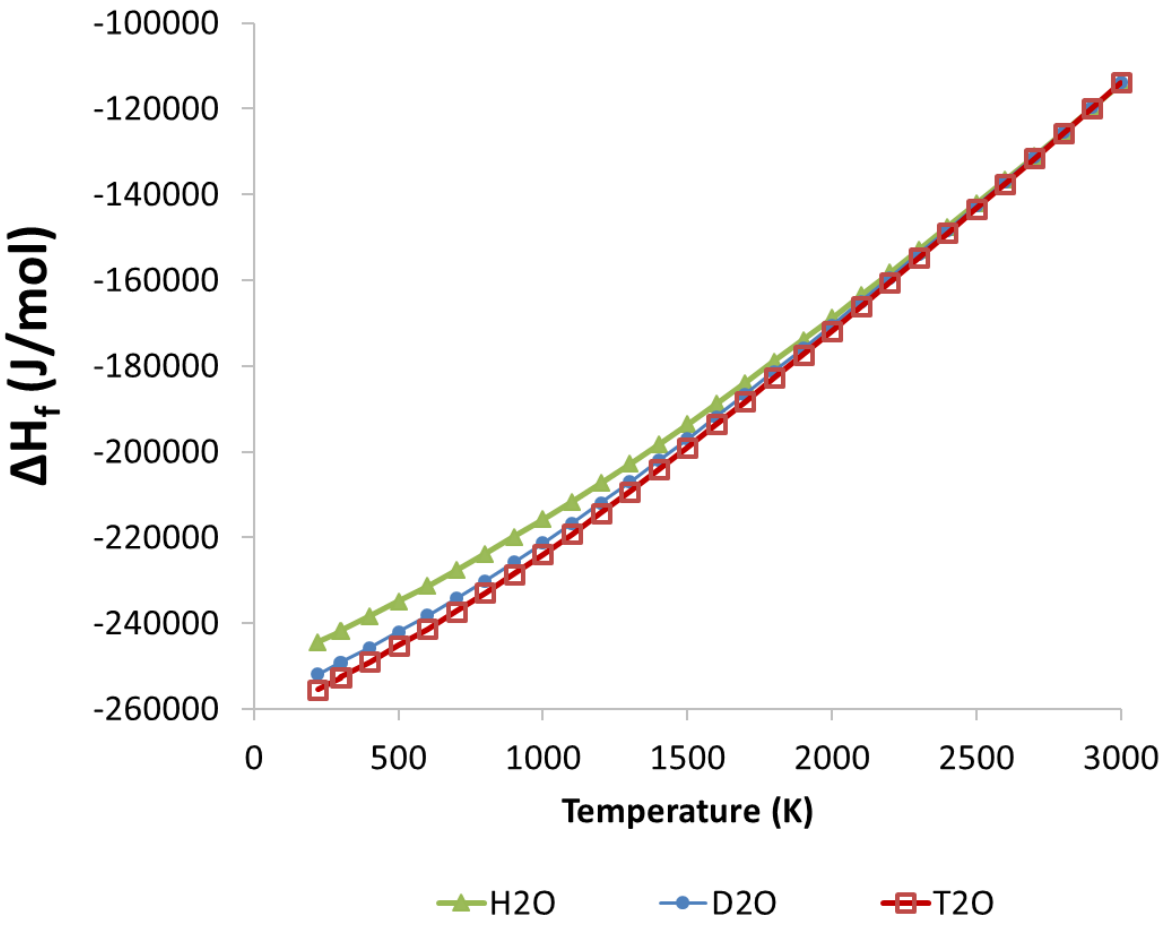

Figure 3-4. Enthalpies of formation for water with different hydrogen isotopes (T_2O from this work, H_2O and D_2O from McBride 2002)

Additional parameter adjustments for the tritium-containing species could be pursued if more data were available to justify subtle changes in the curvature of the formation enthalpies or deviations from the trends of the other isotopologues. However, such data are not available, and the tritium enthalpies defined in this section are sufficient to enable the intended simulation capabilities. Figure 3-5 shows the oxidation enthalpies that result from the adjustments described above ($H_2 + 0.5\ O_2 \rightarrow H_2O$). These are lower heating values because water products are assumed to occur as vapor. The oxidation enthalpy of molecular tritium is only moderately lower than that of deuterium, and is calculated to be nearly constant above 1000 K. If an intersection temperature higher than 3000 K were chosen for D_2O and T_2O to define high-temperature formation enthalpy for T_2O, the enthalpy difference between oxidation of T_2 versus D_2 in Figure 3-5 would persist to higher temperatures, but this would not have a significant effect on the simulations these properties are intended for. Figure 3-3 suggests that a small increase in the heat capacity of T_2 with respect to D_2 could be anticipated at high temperatures, but more data would be needed to provide an estimate the magnitude. Such a change would make the high-temperature slope of tritium combustion enthalpy shown in Figure 3-5 more similar to deuterium combustion, so the slight enthalpy increase shown for tritium combustion at higher temperatures may not be real.

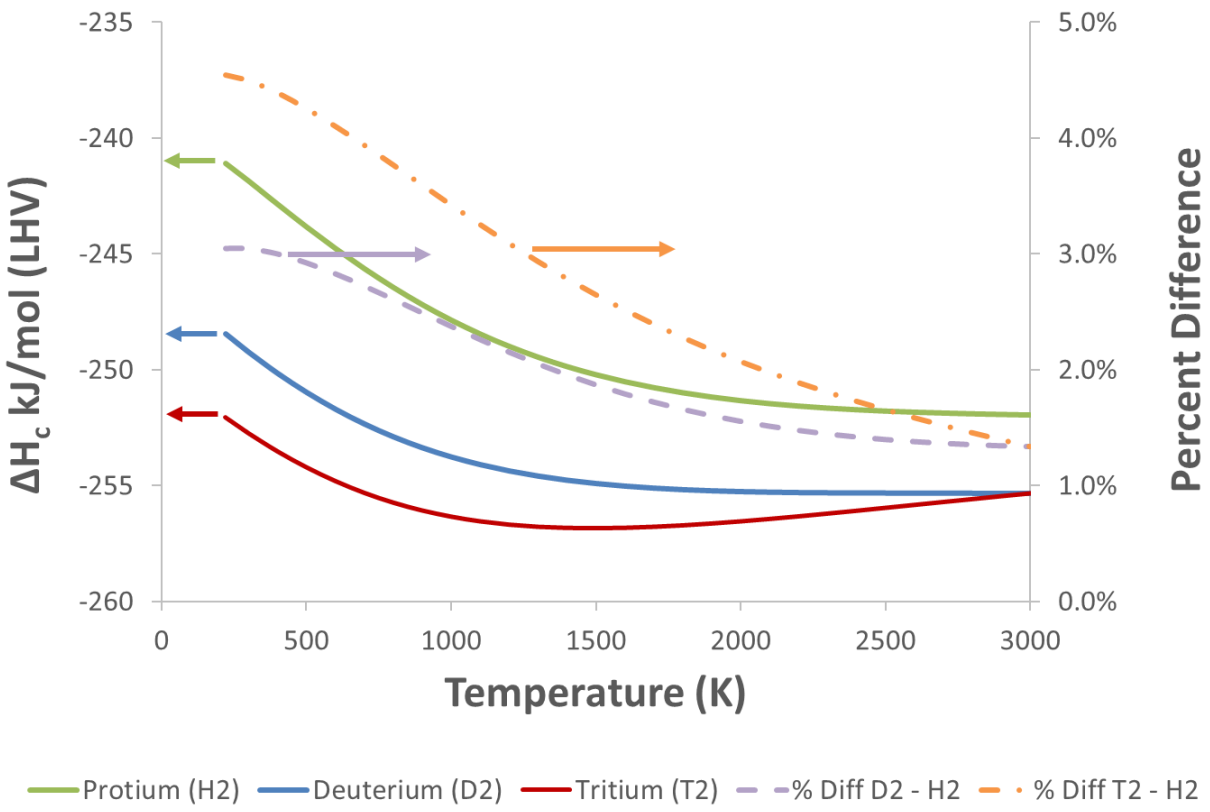

Figure 3-5. Combustion enthalpies (solid lines) of different hydrogen isotopes and the percent difference from hydrogen combustion enthalpy (dashed lines for D_2 and T_2)

3.2.2. Entropy

The formation enthalpy correlations (Equations 3-2 and 3-5) in the case of protium and deuterium species originate from enthalpy measurements from calorimetry (typically heats of reaction and heat capacities) (McBride 1993, 2002, Chase 1998). For tritium species, this work uses deuterium enthalpy coefficients with adjustments to maintain high-temperature trends from the protium and deuterium isotopologues. Given that enthalpy and entropy share functional relationships with heat capacity, the entropy correlations (Equations 3-3 and 3-6) inherit the parameters discussed in the previous section; only one parameter (an integration constant designated as a_6 or b_8) is uniquely designated for entropy. Proper entropy trends should also be considered, especially for cases where reversible reactions are involved. Reverse rate constants are calculated from a forward rate constant and an equilibrium constant that is derived from Gibbs free energy of reaction, which is defined as $\Delta G = \Delta H - T\Delta S$.

Figure 3-6 shows that the entropy for T_2O with no additional parameter adjustments beyond the C_p offset indicated in Table 3-5 (applied to the shared parameter a_0 or b_2) has a trend that is consistent with respect to D_2O and H_2O (the H offset applied to a_5 or b_7 is unique to enthalpy). The smaller difference between T_2O and D_2O compared to D_2O and H_2O is expected, since the percent difference in mass between the pairs of isotopologues follows a similar trend. If the enthalpy crossover point for T_2O and D_2O is defined to be a temperature higher than the assumed 3000 K, the difference between T_2O and D_2O entropies would be reduced for all temperatures with respect

to Figure 3-6 because the adjusted heat capacity coefficient is shared between the enthalpy and entropy correlations. Figure 3-6 suggests that no adjustment to the assumed enthalpy crossover point is needed to improve the entropy trend until some form of high-temperature data becomes available to define a better assumption.

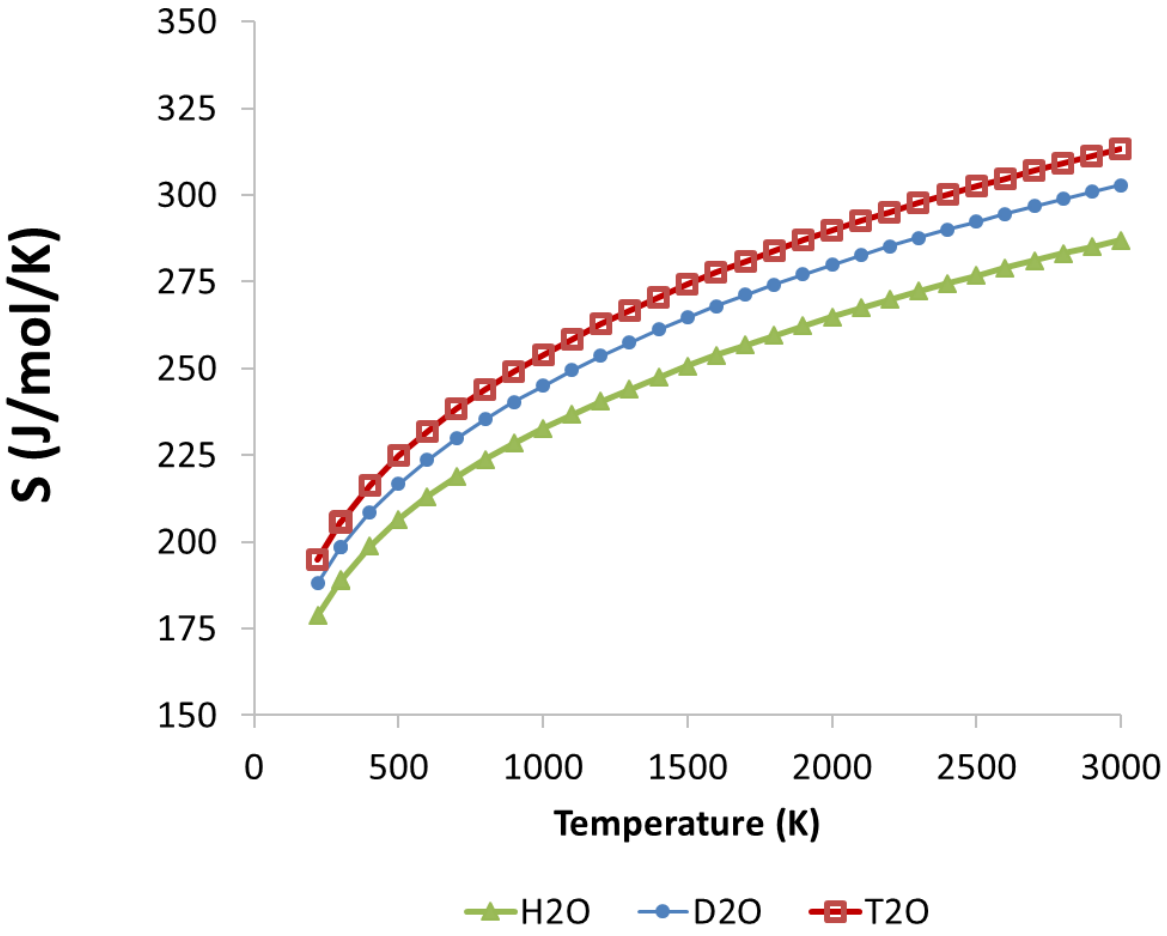

Figure 3-6. Entropies for water with different hydrogen isotopes (T_2O from this work, H_2O and D_2O from McBride 2002)

The entropies and ratios of entropy differences for isotopologues of water at 298.15 K from Figure 3-6 are listed at the top of Table 3-7, which shows the resulting percent isotopic entropy variation for T_2O with respect to H_2O in bold. In a manner analogous to the enthalpy trend extrapolation shown in Table 3-6, we used the isotopic entropy variation trend from water species in Table 3-7 to adjust the unique entropy offset term for other tritium-containing species. The ratio between the isotopic entropy variations for T_2O and D_2O in Table 3-7 is 8.94/5.04 = 1.78; this value was multiplied by the D_2 and D entries in Table 3-7 to estimate the isotopic entropy variation for T_2 and T and hence the entropy at 298.15 K. Implementing these extrapolated entropy trends via the entropy offset coefficient (a_6 or b_8 as shown in Table 3-5) does not affect enthalpies or heat capacities described in the previous section. The temperature-dependent entropies for atomic and molecular tritium resulting from these procedures are shown in Figure 3-7. These extrapolations in the entropy trends should be revisited if appropriate data become available, but they are unlikely to have a strong effect on the results of the intended CFD applications (see Chapter 5).

Table 3-7. Isotope properties from (McBride 2002) used to estimate entropies for tritium species; *asterisks designate extrapolations from this work used to specify entropy coefficients a_6 or b_8

Molecule	Entropy (kJ/mol/K at 298.15 K)	Percent Isotopic Entropy Variation at 298.15 K: (D/H -1) or (T/H-1)
H_2O	155.8	N/A
D_2O	198.3	5.04%
T_2O	205.7	**8.94%**
H_2	130.7	N/A
D_2	145.0	10.93%
T_2	156.0*	19.40%*
H	114.7	N/A
D	123.4	7.53%
T	130.0*	13.36%*

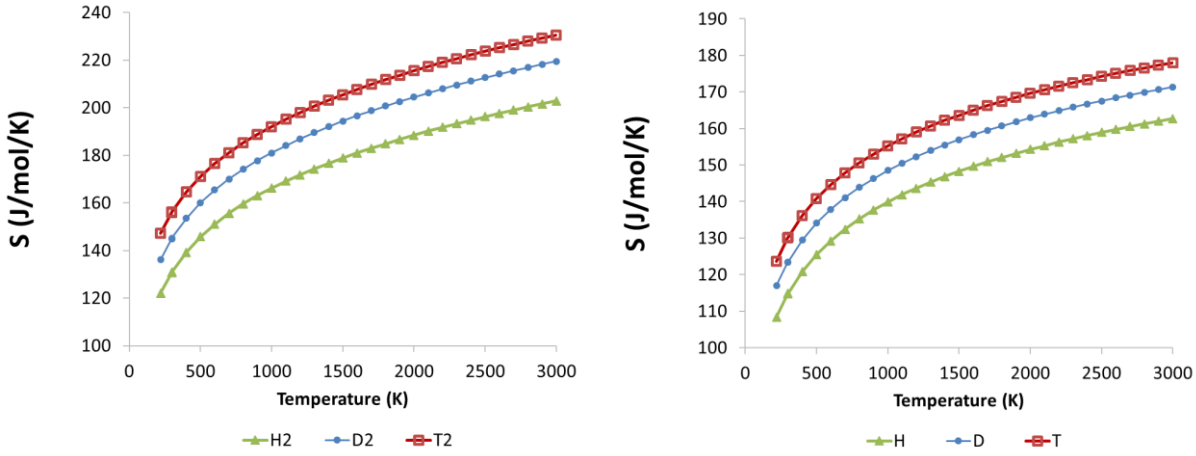

Figure 3-7. Entropies for isotopes of molecular and atomic hydrogen (McBride 2002), including tritium estimates from this work.

3.3. Transport Properties

SIERRA/Fuego (2019a, 2019b) utilizes the Cantera format (Goodwin et al., 2021) for transport properties, which was originally developed for the CHEMKIN package TRANLIB (Kee et al. 1986). Transport properties include molecular viscosity, thermal conductivity, and binary diffusivities. In practice, viscosities are the principal source of reference measurements for the main parameters that are common to all three properties. Thermal conductivities are not explicitly considered in this work due to lack of data for comparison and because the equations for thermal conductivity utilize the same parameters as viscosity (Kee 1986, Bird et al. 2002). Also, gas-phase thermal conductivity differences for isotopologues of hydrogen and water are not expected to affect simulations investigating oxidation of hydrogen isotopes in trace quantities documented in Chapter 5. Of the three transport properties, diffusivities are expected to have the most direct effect on mixing-limited oxidation of hydrogen, so diffusivities are also included in the comparisons in this section.

Viscosities calculated from parameters in the Cantera ".xml" files are expressed in terms of Chapman-Enskog theory with two or three parameters, depending on whether the properties are derived from a Lennard-Jones potential (for nonpolar molecules) or a Stockmayer potential (for polar molecules). These parameters are the Lennard-Jones collision diameter σ_k, the Lennard-Jones

potential well depth ε_k, and the dipole moment μ_k for polar molecules such as water. The equation for viscosity for nonpolar molecules is (Bird 2002)

$$\eta_k = \frac{5}{16}\frac{\sqrt{\pi M_k \kappa_b T}}{\pi \sigma_k^2 \Omega^{(2,2)^*}} = 2.6693 \times 10^{-5}\frac{\sqrt{M_k T}}{\sigma_k^2 \Omega^{(2,2)^*}} \quad 3\text{-}7$$

where the first form includes the Boltzmann constant κ_b and the simplified final form yields viscosities in g/cm/s with absolute temperature in K, molecular weight M_k in g/mol, and σ_k in Angstroms. The collision integral $\Omega^{(2,2)^*}$ is tabulated in terms of a reduced temperature and a reduced dipole moment (Monchick and Mason 1961), which are

$$T^* = \frac{\kappa_b T}{\varepsilon_k} \quad 3\text{-}8$$

$$\delta^* = \frac{1}{2}\frac{\mu_k^2}{\varepsilon_k \sigma_k^3} = 3622.0\frac{\mu_k^2}{\left(\frac{\varepsilon_k}{\kappa_b}\right)\sigma_k^3} \quad 3\text{-}9$$

The Lennard-Jones or Stockmayer potential well depth is typically normalized by Boltzmann's constant as ε_k/κ_b for tabulation, with units of Kelvin (Bird 2002, Monchick 1961). The right-hand expression for the reduced dipole moment is valid with the dipole moment in units of Debye and the other units as indicated above. Equation 3-7 shows that the viscosity is expected to scale with the square root of molecular weight; this is the simplest expression of isotopic effect if the other parameters do not change.

Thermal conductivity is calculated from the same parameters as viscosity, along with a rotational relaxation collision number Z_{rot} (Kee 1986). The thermal conductivity equations used in Cantera are somewhat lengthy and are not presented in this work. However, it has been noted that hydrogen thermal conductivity is not very sensitive to the value of this parameter (Assael et al. 1986). For water with different hydrogen isotopes, Z_{rot} was found to differ moderately with isotope type only at temperatures below ~600 K (Matsunaga and Nagashima 1983). Given that thermal conductivity is unlikely to be an important driver of behavior in our simulations of tritium release and oxidation (Chapter 5), potential variations in Z_{rot} with isotopic mass are neglected for the purpose of this work; the default values of Z_{rot} for H_2 and H_2O (Kee 1986) are used for their isotopologues.

Binary diffusivities are evaluated as (Kee 1986, Bird 2002):

$$D_{jk} = \frac{3}{16}\frac{\sqrt{2\pi(\kappa_b T)^3/m_{jk}}}{P\pi\sigma_{jk}^2\Omega^{(1,1)^*}} = 1.8583 \times 10^{-3}\sqrt{T^3\left(\frac{1}{M_j}+\frac{1}{M_k}\right)}\frac{1}{P\sigma_{jk}^2\Omega^{(1,1)^*}} \quad 3\text{-}10$$

The simplified version of the expression on the right yields diffusivities in cm^2/s when pressure is expressed in atmospheres. The term m_{jk} on the left is defined as the inverse of the term in parentheses on the right, and the subscripts j and k are indices for different constituents of a gas mixture. The $\Omega^{(1,1)^*}$ collision integral used for diffusivities is different from the $\Omega^{(2,2)^*}$ collision integral used for viscosities and thermal conductivities, but both types are generally available in similar references (Bird 2002, Monchick 1961).

For diffusion of a polar species in a nonpolar species, calculation of σ_{jk} requires a tabulated polarizability parameter designated as a_n for the nonpolar molecule. The evaluation of binary properties for polar-polar or nonpolar-nonpolar interactions require the following equations (Kee 1986):

$$\frac{\varepsilon_{jk}}{\kappa_b} = \sqrt{\frac{\varepsilon_j}{\kappa_b}\frac{\varepsilon_k}{\kappa_b}} \tag{3-11}$$

$$\sigma_{jk} = \frac{1}{2}\left(\sigma_j + \sigma_k\right) \tag{3-12}$$

$$\mu_{jk}^2 = \mu_j \mu_k \tag{3-13}$$

For a polar molecule *p* interacting with a nonpolar molecule *n*, the following relations are used (*p* and *n* are similar to *j* and *k*, but more specific in terms of the type of molecule):

$$\frac{\varepsilon_{np}}{\kappa_b} = \sqrt{\frac{\varepsilon_n}{\kappa_b}\frac{\varepsilon_p}{\kappa_b}} \tag{3-14}$$

$$\sigma_{np} = \frac{1}{2}\left(\sigma_n + \sigma_p\right)\xi^{-\frac{1}{6}} \tag{3-15}$$

$$\mu_{np}^2 = 0 \tag{3-16}$$

$$\xi = 1 + \frac{1}{4}\alpha_n^* \mu_p^* \sqrt{\frac{\varepsilon_p}{\varepsilon_n}} \tag{3-17}$$

$$\alpha_n^* = \frac{\alpha_n}{\sigma_n^3} \tag{3-18}$$

$$\mu_p^* = \frac{\mu_n}{\sqrt{\varepsilon_p \sigma_p^3}} \tag{3-19}$$

In either the polar-nonpolar or nonpolar-nonpolar case, the collision integral lookup requires a binary reduced temperature:

$$T_{jk}^* = \frac{\kappa_b T}{\varepsilon_{jk}} \tag{3-20}$$

For a study with water diffusivity in air and CO_2 using different isotopes of hydrogen, it was observed that the predicted binary diffusivities agreed with experiments within the expected measurement error, and the predicted ratio of water diffusivities for different isotopes approached the limiting value expected for the assumption of identical Lennard-Jones parameters at high temperatures (Matsunaga 1983). Therefore, the explicit molecular weight dependence shown in Equation 3-10 is assumed to dominate over other isotopic effects related to differences in the remaining parameters. The molecular weight effect in Equation 3-10 yields much larger isotopic diffusivity differences for hydrogen isotopes in air compared to differences in diffusivities of water isotopes in air.

For Fick's law diffusion calculations in Fuego (in regions with laminar or stagnant flow), mixture diffusivities are used, which are defined as pseudo-binary diffusivities for each species as if the

remainder of the mixture were a single species (Goodwin 2021, Bird et al. 1960, Fairbanks and Wilke 1950, Mitchell 1980):

$$D_{j,mix} = \frac{1 - y_j}{\sum_{\substack{k=1,\\ k \neq j}}^{Species} \frac{y_k}{D_{jk}}} \quad 3\text{-}21$$

where y represents mole fractions and D represents binary or pseudo-binary diffusivities.

Although Fuego can invoke Cantera to calculate binary and mixture diffusivities as specified in the equations above, a simpler option is to specify a universal mixture diffusivity D_{mix} via the Schmidt number Sc, the gas density ρ and the mixture viscosity μ_{mix} (Goodwin 2021, Bird 2002, Wilke 1950, Buddenberg and Wilke 1949):

$$D_{mix} = \frac{\mu_{mix}}{\rho Sc} \quad 3\text{-}22$$

$$\mu_{mix} = \sum_{\alpha=1}^{Species} \frac{y_\alpha \mu_\alpha}{\sum_{\beta=1}^{Species} y_\beta \Phi_{\alpha\beta}} \quad 3\text{-}23$$

$$\Phi_{\alpha\beta} = \frac{\left(1 + \sqrt{\frac{\mu_\alpha}{\mu_\beta}} \sqrt{\frac{M_\beta}{M_\alpha}}\right)^2}{\sqrt{8\left(1 + \frac{M_\alpha}{M_\beta}\right)}} \quad 3\text{-}24$$

Note that all $\Phi_{\beta\beta} = \Phi_{aa} = 1$ (summations in Equation 3-23 include interactions between the same species, unlike Equation 3-21). Using the mixture diffusivity as specified in Equation 3-22 for diffusion calculations causes all variation in species diffusion rates to be attributed to concentration differences, with no differential effect of species mobility.

3.3.1. Viscosity and Diffusivity for Isotopes of H_2

Figure 3-8 shows how predictions of molecular hydrogen viscosity from TRANLIB (Kee 1986) (e.g., the equations presented in the previous section) and other correlations from literature (Assael et al., 1986, Svehla 1995, DIPPR 2010) compare to data for normal hydrogen (molecular protium, DIPPR 2010). All the correlations are comparable below about 1000 K, and the correlations based on Lennard-Jones parameters yield lower predictions at higher temperatures compared to the NASA correlation (Svehla 1995). The TRANLIB parameters (Kee 1986) yield results consistent with the Assael parameters with the same functional form (Assael 1986), so either of these parameter sets are expected to yield lower viscosities and thermal conductivities with higher binary diffusivities at high temperatures compared to the NASA or DIPPR correlations (which are closer to the DIPPR database measurements at 1000 K). Revised Lennard-Jones parameters could be sought to obtain better agreement with the NASA or DIPPR correlations if more data become available above 1000 K to justify the change. The trend towards slightly higher viscosities at higher temperatures in the NASA correlation (Svehla 1995) was derived from corresponding states theory (Bird 2002).

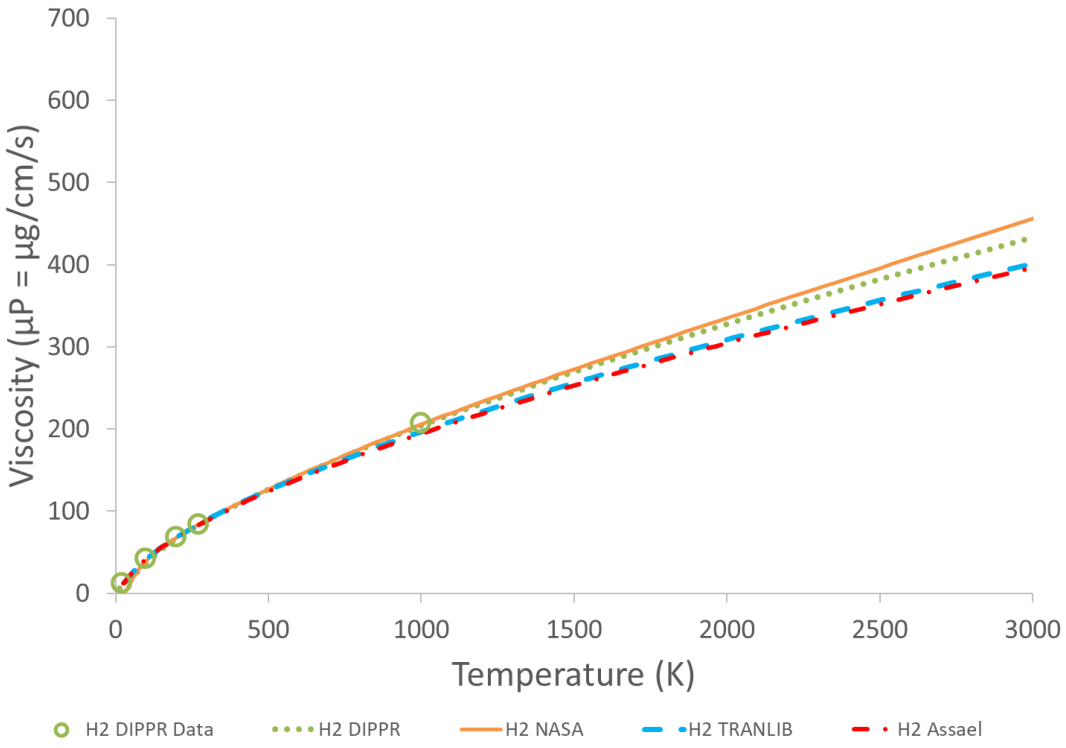

Figure 3-8. Predicted viscosities (lines, Assael 1986, Svehla 1995, DIPPR 2010) of molecular protium (H_2) at the low-density limit (atmospheric pressure) compared to measurements (open circles, DIPPR 2010).

A molecular weight scaling exponent of 0.5 (as in Equation 3-7) was found to adequately describe scaling between measured viscosities of molecular protium and deuterium within 1% between 250 K and 350 K (Assael et al. 1987). This molecular weight scaling exponent of 0.5 was estimated to be accurate within 4% at higher temperatures up to 2200 K (Assael 1987). This scaling was also used by NASA for predictions of deuterium viscosity from protium, although the functional form of the final correlation differed from the equations shown here (Svehla 1995). Since the agreement with viscosity data in Figure 3-8 at temperatures below 1000 K is acceptable for all correlations considered and this temperature range is representative of the unreacted state, we recommend the TRANLIB parameters (Kee 1986) shown in Table 3-8 as appropriate for all isotopes of molecular hydrogen. As noted above, the additional parameters needed for calculations of thermal conductivities and binary diffusivities appear to be substantially independent of isotope mass and/or have a negligible effect on the calculated properties of the different isotopes of hydrogen. The range of expected viscosities for isotopes of molecular hydrogen is shown in Figure 3-9.

Table 3-8. Transport parameters recommended for oxygen, nitrogen and isotopes of molecular hydrogen [10]

Molecule	M_k (g/mol)	ε_k/κ_b (K)	σ_k (Angstroms)	μ_k (Debye)	α_k (Angstroms^3)	Z_{rot} (at 298 K)
H_2	2.0157	38.0	2.92	0	0.79	280
D_2	4.0282	38.0	2.92	0	0.79	280
T_2	6.0321	38.0	2.92	0	0.79	280
O_2	31.998	107.4	3.458	0	1.6	3.8
N_2	28.014	97.53	3.621	0	1.76	4.0

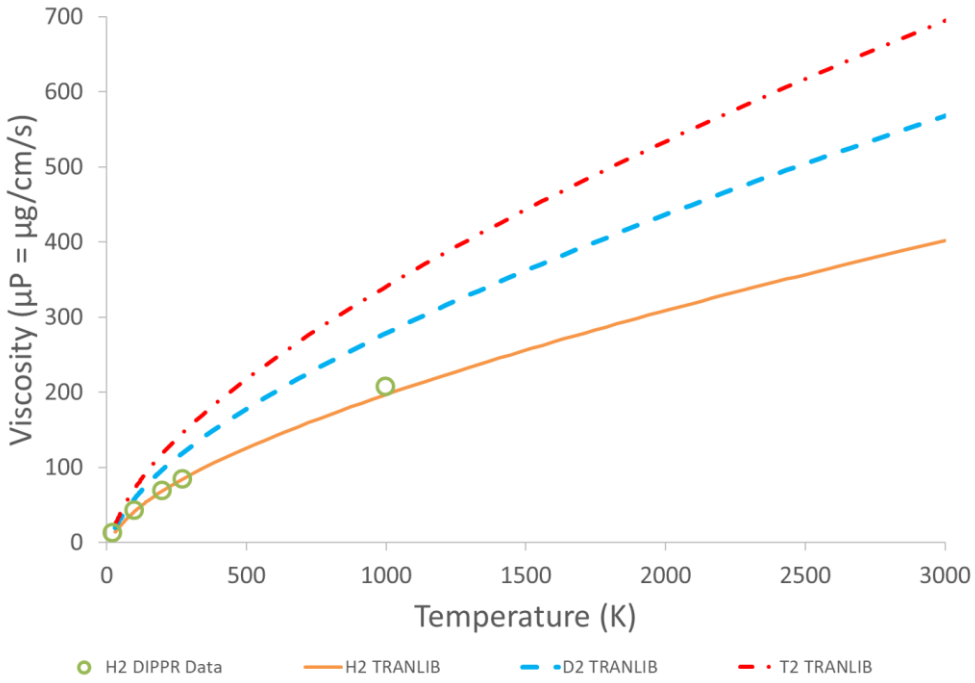

Figure 3-9. Correlated viscosities of molecular hydrogen isotopes at the low-density limit (e.g. atmospheric pressure) compared to molecular protium measurements (Kee 1986, DIPPR 2010).

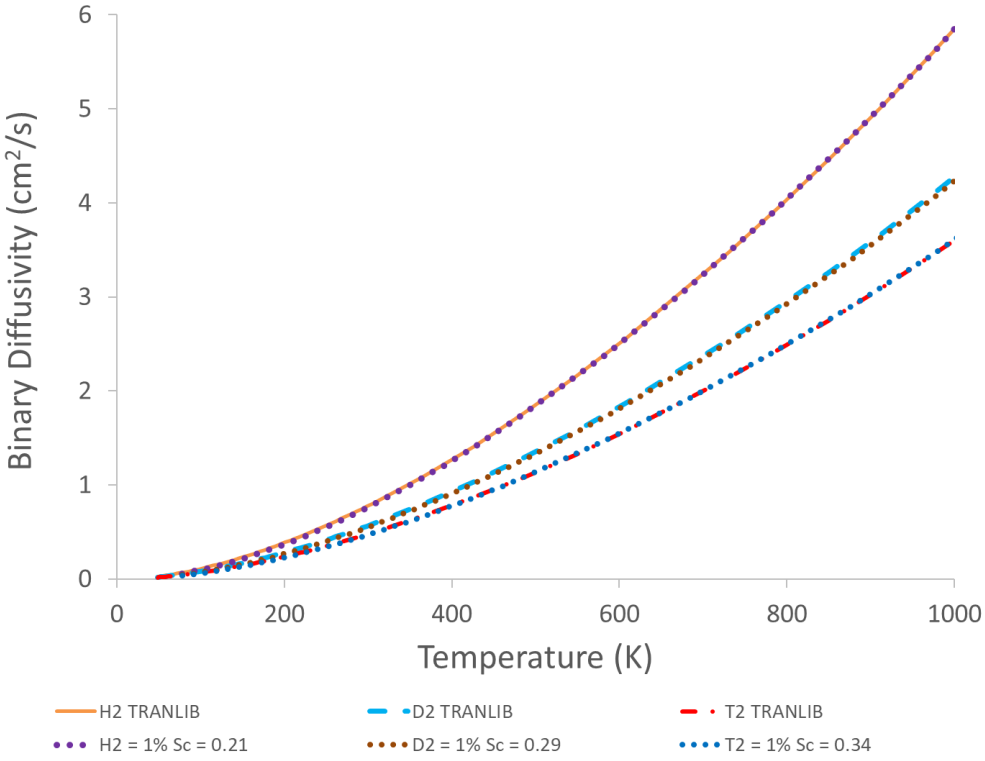

Figure 3-10. Calculated diffusivities from Equation 3-10 (Kee 1986) for molecular hydrogen isotopes in nitrogen at atmospheric pressure compared to diffusivities derived from Schmidt numbers (Equation 3-22) with 1% hydrogen.

Predicted diffusivities of hydrogen isotopes in nitrogen from Equation 3-10 are shown in Figure 3-10. The temperature scale is restricted to 1000 K because the lower temperatures are of more interest to predict transport of the hydrogen reactant prior to reaction in air. Figure 3-10 shows that the largest difference in diffusivities occurs between protium and deuterium, with a more modest decrease in the transition from deuterium to tritium. This is consistent with trends in the other properties considered in this study. Figure 3-10 also includes diffusivities predicted from Schmidt numbers (Equation 3-22), which vary with composition as indicated in Equations 3-23 and 3-24. The diffusivities from Schmidt numbers in Figure 3-10 all assume a hydrogen isotope concentration of 1% by volume in nitrogen. At this concentration, Schmidt numbers of 0.21 for H_2, 0.29 for D_2, and 0.34 for T_2 are required to match the corresponding diffusivities from Equation 3-10.

Figure 3-11 compares the calculated diffusivities from Equation 3-10 to diffusivities from Equation 3-22 using hydrogen concentrations of 50% rather than 1%. Figure 3-11a uses the same Schmidt numbers as Figure 3-10; the concentration change increases the calculated tritium diffusivity to the point that it is consistent with the protium diffusivity from Equation 3-10 while maintaining similar differences between the properties for different isotopes. Figure 3-11b demonstrates that a uniform Schmidt number yields very little difference between diffusivities for different isotopes. The results for the different isotopes shown in Figure 3-10 would have been visually indistinguishable if this approach with identical Schmidt numbers had been used with 1% hydrogen.

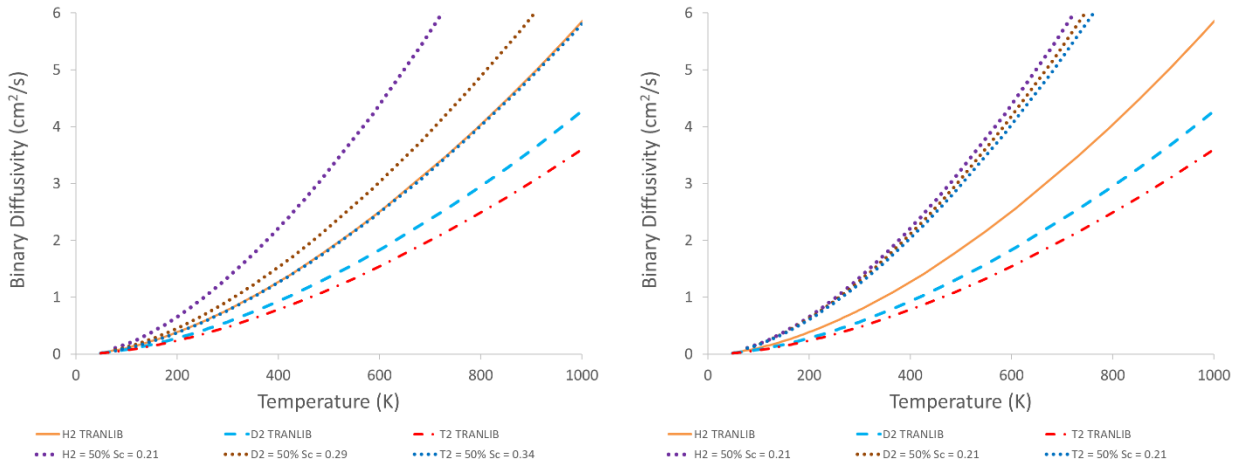

Figure 3-11. Diffusivity comparison as in Figure 3-10, but with 50% hydrogen in nitrogen (left), and uniform Schmidt numbers (right).

3.3.2. Viscosity and Diffusivity for Isotopes of H_2O

Equation 3-7 with a molecular weight exponent of 0.5 was originally developed for nonpolar molecules; more attention is required for polar water molecules. When the parameters for normal water from TRANLIB (Kee 1986) are used with all the isotopes of hydrogen, the TRANLIB viscosities shown in Figure 3-12 demonstrate the trend that would occur if the molecular weight dependence is represented by an exponent of 0.5.

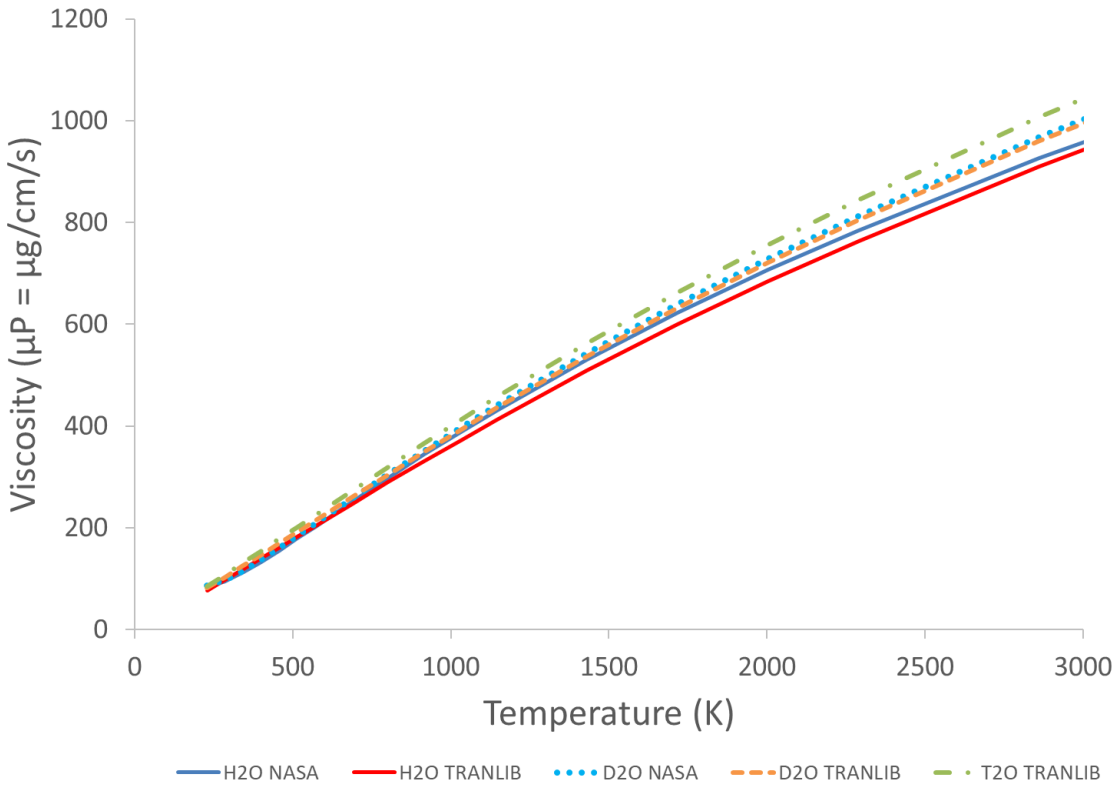

Figure 3-12. Viscosities of water vapor at the low-density limit (e.g. atmospheric pressure) as predicted from TRANLIB (Kee 1986) and NASA (Svehla 1995) correlations.

NASA has produced curve-fits of transport properties for H_2, D_2, H_2O, and D_2O (Svehla 1995). The NASA correlations are specified as empirical curve-fits for individual species rather than molecular potentials, so they do not extrapolate directly to T_2O. Some discrepancies become apparent when the NASA viscosity correlations are plotted in Figure 3-12. First, the TRANLIB prediction of normal water viscosity is lower than the NASA prediction. The same is true for deuterated water, but the difference in this case is minimal. This means that the NASA correlations predict a smaller isotope effect for water than is assumed for the TRANLIB calculations (molecular weight exponent of 0.5).

A closer look at the correlations for H_2O in the temperature range where data are available (DIPPR 2010) in Figure 3-13 shows that the NASA correlations [20] provide a better match for experimental viscosities of normal water (with protium only) compared to the TRANLIB correlations (Kee 1986). The maximum deviation magnitude for the NASA correlation is 1.8% with respect to the measurements, and the average deviation magnitude is 0.3%. The TRANLIB correlation yields a maximum deviation magnitude of 7.3%, with an average deviation magnitude of 2.8% from measurements.

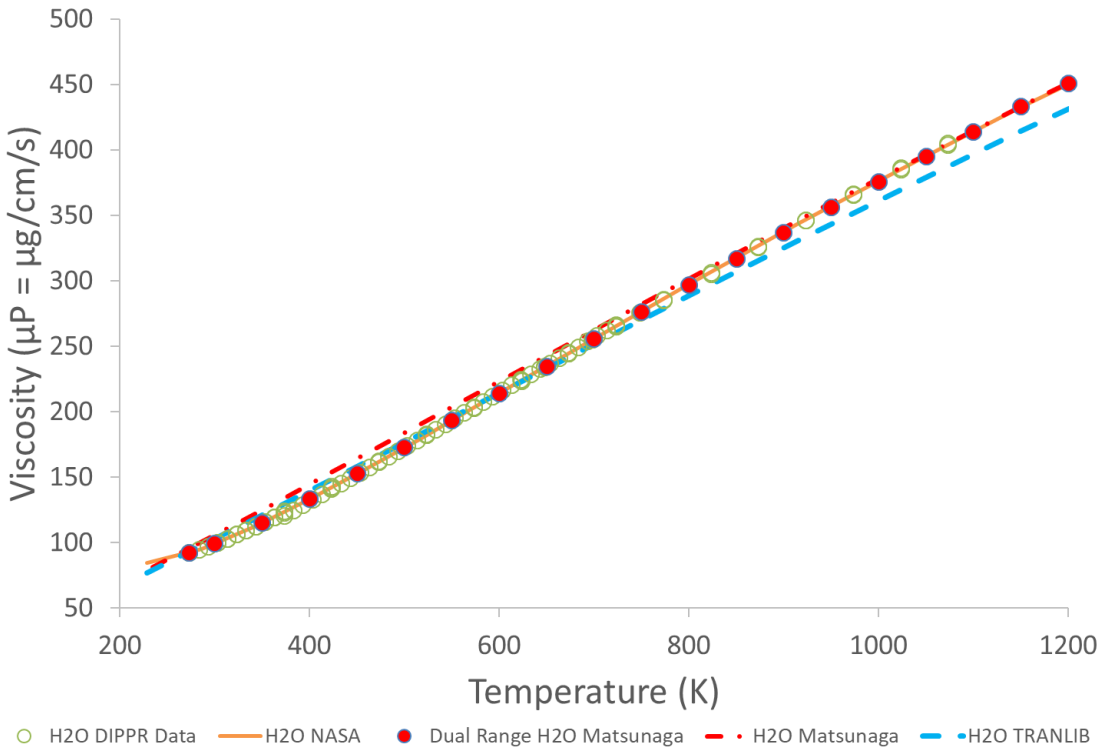

Figure 3-13. Water vapor viscosity predictions (Kee 1986, Matsunaga 1983, Svehla 1995) compared to atmospheric pressure measurements (DIPPR 2010)

The NASA correlation is principally based on the study of Matsunaga and Nagashima (1983), who produced correlations for two temperatures ranges. The upper temperature Matsunaga correlation between 1100 K and 2000 K uses the same type of (12-6-3) Stockmayer potential parameters that are used in Fuego, Cantera, and TRANLIB. A different functional form was chosen to produce a better fit of experimental viscosities available in the lower temperature range (Matsunaga 1983), which is the basis for the low-temperature NASA correlation. The difference between the red line and the red points in Figure 3-13 shows that the high-temperature Matsunaga correlation over-estimates viscosity data for water vapor when extrapolated to low temperatures, whereas the dual-range Matsunaga correlation matches the available viscosity data at low temperatures. At ~700 K the TRANLIB predictions and the high-temperature Matsunaga correlation have similar deviations from viscosity measurements (about 2% in opposite directions). At higher temperatures, TRANLIB under-estimates measurements with increasing error (average of 3%), while the high-temperature Matsunaga predictions improve at higher temperatures (average of 1%). TRANLIB predictions are better than the extrapolated high-temperature Matsunaga correlation between about 400 K and 700 K (average deviation of 1% versus 4%), and also below 400 K (average of 4% versus 8%).

Matsunaga and Nagashima (1983) indicate that the (12-6-3) Stockmayer potential cannot fit data for water over the full temperature range; the polarity of water has more temperature dependence than can be modeled with this form between 273.15 K and 2000 K. However, they also demonstrated parameters for D_2O and developed a very reasonable estimate for T_2O properties. They noted that the high-temperature correlations maintain consistent isotopic trends when extrapolated to lower temperatures, and Figure 3-13 shows that the predictions for water viscosity below 700 K are still quite reasonable (within 6% of the measurements on average).

Figure 3-14 shows the high-temperature Matsunaga correlations (Matsunaga 1983) for H_2O, D_2O, and T_2O compared to H_2O from TRANLIB (Kee 1986) and DIPPR data for H_2O (DIPPR 2010). The TRANLIB parameters are recommended for H_2O in our application because they yield better predictions of the DIPPR data below 700 K and have been used in a wide variety of simulation scenarios historically where we would like to maintain comparability. We recommend adopting the high-temperature parameters from (Matsunaga 1983) for the other isotopes of hydrogen (D_2O, and T_2O). This combination of recommended parameters listed in Table 3-9 may over-estimate the property differences between H_2O and the two forms of heavy water. In cases where greater consistency is desired in terms of the expected trends between the isotopologues of water, the alternate H_2O parameters from Table 3-9 may be used with a minor loss in H_2O accuracy below 700 K (all properties from Matsunaga). The parameters from (Matsunaga 1983) in Table 3-9 include ε_k/κ_b, σ_k, and μ_k. The parameters a_k and Z_{rot} (298 K) are assumed to be the same as water in the TRANLIB library (Kee 1986).

Table 3-9. Transport parameters recommended* for water with different hydrogen isotopes (Kee 1986, Matsunaga 1983)

Molecule	M_k (g/mol)	ε_k/κ_b (K)	σ_k (Angstroms)	μ_k (Debye)	α_k (Angstroms^3)	Z_{rot} (298 K)
H_2O (Kee 1986)*	18.0151	572.4	2.605	1.844	0	4
D_2O (Matsunaga 1983)*	20.0276	422	2.706	1.861	0	4
T_2O (Matsunaga 1983)*	22.0315	381	2.816	1.877	0	4
Alternate H_2O (Matsunaga 1983)	18.0151	470	2.595	1.844	0	4

The predicted binary diffusivities of water with different hydrogen isotopes in nitrogen are shown in Figure 3-15. The property differences for water isotopes are much smaller than the property differences for hydrogen isotopes because the oxygen atom provides an inert mass that is substantially larger than hydrogen, and also because the effect of mass has been reduced by altering the Lennard-Jones parameters (Matsunaga 1983). The H_2O diffusivity from the TRANLIB parameters (Kee 1986) in Figure 3-15 is comparable to the calculation using the alternate Matsunaga parameters.

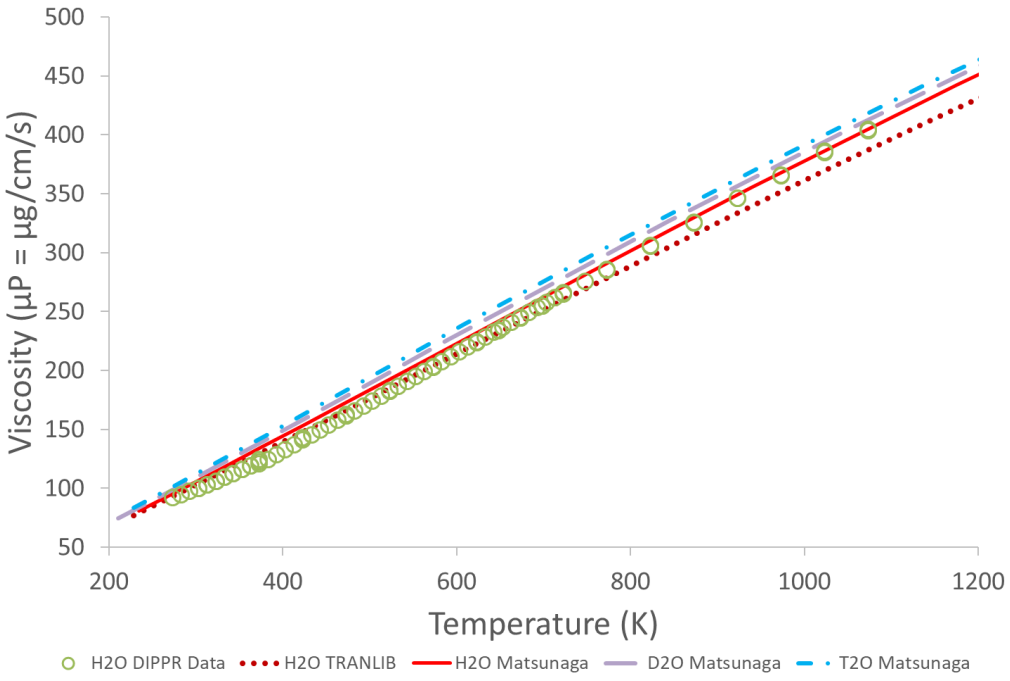

Figure 3-14. Water vapor viscosity predictions and data with different hydrogen isotopes (Kee 1986, Matsunaga 1983, DIPPR 2010)

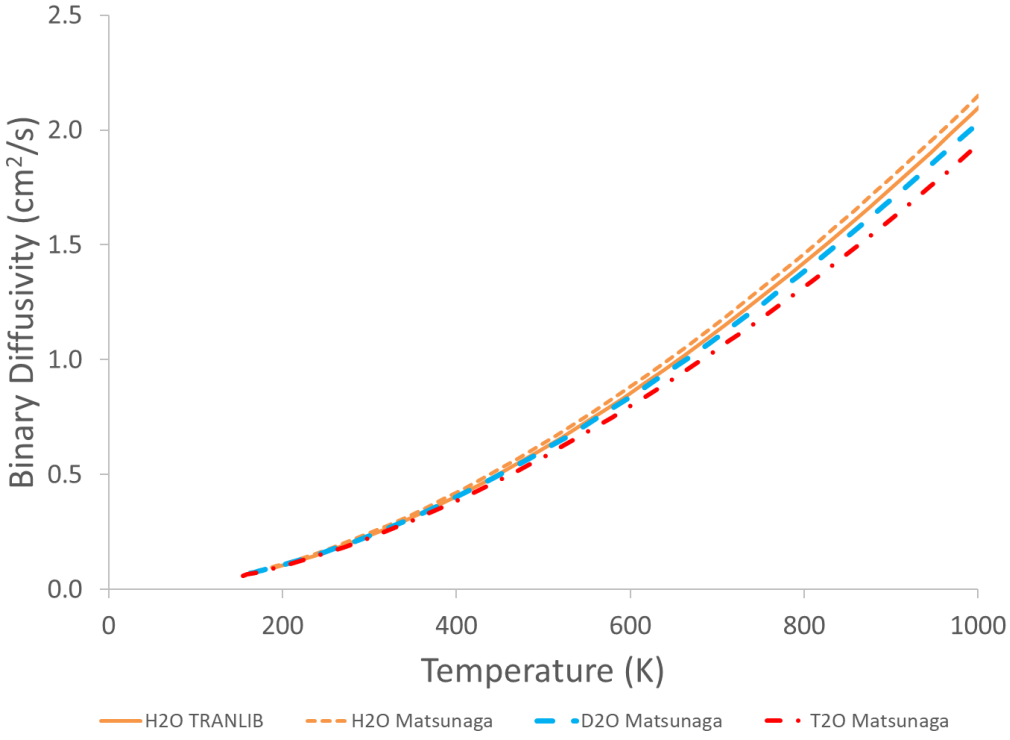

Figure 3-15. Calculated diffusivities of water isotopes in nitrogen at atmospheric pressure (Kee 1986, Matsunaga 1983)

Figure 3-16 shows that for 1% water in nitrogen, the most appropriate Schmidt numbers at high temperatures are approximately 0.58 for protium, 0.61 for deuterium, and 0.64 for tritium. The curvature of the water diffusivities with increasing temperature calculated from Schmidt numbers (Equation 3-10) is less than the molecular diffusivity from Equation 3-22, which causes the Schmidt number approach to overestimate the diffusivity at low temperatures. This discrepancy in behavior for the different models is likely due to the absence of polarity terms in the Schmidt number approach.

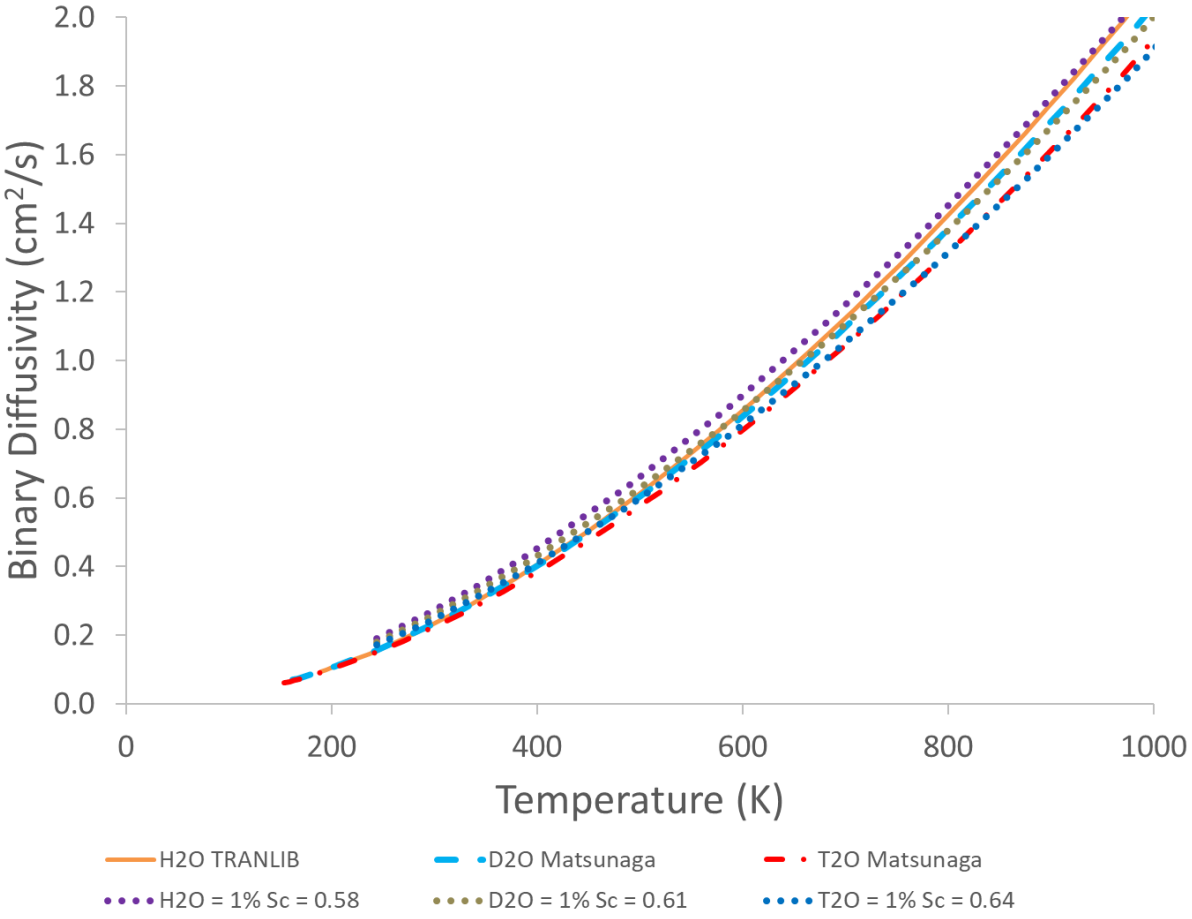

Figure 3-16. Diffusivities of water isotopes in nitrogen at atmospheric pressure (Kee 1986, Matsunaga 1983) compared to the Schmidt number approach (Goodwin 2021, Bird 2002, Wilke 1950, Buddenberg 1949).

3.4. Conclusions

A planned set of CFD simulations requires chemical property sets that distinguish between isotopes of hydrogen that may be released in a fire scenario. The functional forms required for Sandia's SIERRA/Fuego code are consistent with Cantera-style inputs. Accordingly, a suite of thermodynamic properties has been assembled from prior literature to enable computational simulations of systems that include isotopes of molecular hydrogen and their fully oxidized water forms. For the tritium isotope (^{3}H), the thermodynamic properties were estimated in this work based on the trends between the other hydrogen isotopes, namely protium (^{1}H) and deuterium (^{2}H). The thermodynamic properties reported in this work include formation enthalpies, heat capacities, and

entropies. These are reported in terms of a 7-parameter model (Table 3-1 and Table 3-3) and a 9-parameter model (

Table 3-2 and Table 3-4) that are both in common use for chemical equilibrium and CFD calculations.

A suite of transport properties was also reviewed for use in simulations including isotopes of molecular hydrogen and their fully oxidized water forms. A literature study for properties of molecular hydrogen isotopes indicated that the explicit molecular weight dependence in the Cantera/TRANLIB equations is adequate to describe isotopic properties variations for viscosity, thermal conductivity, and diffusivity. Therefore, the default TRANLIB parameters for H_2 were recommended for all hydrogen isotopes in this work, as summarized in Table 3-8. Viscosities calculated from the H_2 parameters compare favorably with viscosity measurements of molecular protium as well as published correlations for hydrogen viscosity utilizing alternate functional forms. It was found that a common simplified species transport model for CFD applications may require different Schmidt numbers for each isotopologue of H_2 (see Figure 3-10)

Literature regarding transport properties of the hydrogen isotopologues of water was also evaluated, and evidence was found for additional isotope mass effects on transport properties for these highly polar molecules. Accordingly, distinct parameter sets from literature are recommended in Table 3-9 to calculate transport properties for H_2O, D_2O and T_2O. Viscosities calculated from the H_2O parameters compare favorably with viscosity measurements of normal water as well as published correlations for water viscosity utilizing alternate functional forms. The simplified model for diffusion of H_2O isotopologues did not require as wide a range of Schmidt numbers as was the case for isotopes of H_2 (see Figure 3-16).

This page left blank

4. HELIUM PLUME VALIDATION

The fire science community has been participating in a workshop series known as Measurement and Computation of Fire Phenomena (MaCFP) that is aimed at identifying and promoting solutions to accuracy and quality assurance problems for fire modeling tools (Brown et al., 2018). A working group involves participants from around the globe, and has focused on simulating a series of high-quality tests. The first two workshops included comparisons to a large-scale helium plume dataset. The second activity coincided with the tritium project, and since there is a need to validate the ability of the code to diffuse a lighter-than-air substance in turbulent air for the tritium work, this project was leveraged to accomplish some of the validation work.

Validation is one of the key aspects of credibility that goes into modeling and simulation tools. It involves the comparison of predictions to experimental data in a way that characterizes the accuracy of the simulation tool. While it may mean different things to different people, in the context of computational simulations, we look for validation to almost always involves a direct comparison of a measured result to a model prediction. More sophisticated validation can provide the simulation results with the credibility necessary to rely upon the model results for critical decision making. This may include quantitative understanding of the margins of uncertainty, or characterization of the accuracy for a given problem.

Validation is not normally a one-time effort, especially for complex models used on an array of different problems. One should seek validation as close to the intended application as is reasonably feasible given the various constraints of the effort. A tool such as a fire simulation CFD code has a wide variety of use cases, and the success in one case is not necessarily a predictor of success in another because the regimes of applicability of the constituent models change from case to case.

In validation for complex problems it is often helpful to perform the activity by breaking down or simplifying components of the problem and isolating particular parts of the model that can be individually characterized for accuracy. This approach allows the accuracy of the components to be assessed and is helpful for strategic development to apply resources to the problem with the greatest error or sensitivity.

Fires normally involve atmospheric pressures including fuel and air. These react, creating normally carbon dioxide and water vapor as the major products of combustion. The reactions are heavily exothermic, resulting in heat given off in the proximity of the reactions (flames). Flame temperatures are typically in the 1000-2000K range, and since the temperature of the products is high, the density of the flame is significantly lower than the surrounding air. With fires, the fuel is normally on the ground, and the fire plume accelerates buoyantly above the fuel. The presence of a low-density flame below higher density atmospheric air is a classical condition for forming instabilities. This is known as the Rayleigh-Taylor instability, when a higher density fluid is initially above a lower density fluid. This condition results in buoyant acceleration of the fluids as they seek a more stable equilibrium exchanging relative positions with each other. This also forms eddies, and augments mixing. When, for instance, a low-density flame is accelerating vertically against a high-density air to its side, this also constitutes a classical shear-driven instability condition known as the Kelvin-Helmholtz instability. This involves fluids of different densities with a velocity variation at the interface. Instabilities are sources for turbulence, and challenge models due to the resolution requirements to resolve the behavior, and due to the complex nature of turbulent models used in computational models.

The helium plume exhibits many of the conditions lending to flow complexity in a fire without adding in the challenges of flame dynamics, high-heat, thermal radiation, soot formation, etc., which

complicate the ability to extract relevant data from fire tests. The helium plume scenario represents an excellent simplified surrogate to test the accuracy of simulation tools under some representative conditions of relatively high complexity. It resembles a pool fire, much like a fire from a fuel spill on a flat surface.

For hydrogen releases and hydrogen fires, the helium plume is also a step away from full relevancy, but due to the existence of the dataset and the proximity of the scenario to the physical regime of interest, the helium plume dataset is a good test of a code's accuracy under relevant and representative conditions. The transport physics for lighter than air gas species are tested, including the accuracy of the turbulent behavior induced by the buoyant motion. Further, the entrainment of released hydrogen into a separate fire depends on the mixing of the surroundings into the plume. This mixing of the surroundings into a buoyant plume is the focus of the physics assessment in the helium plume.

4.1. Introduction

In the interest of validating buoyant turbulent mixing for fire codes, a test campaign was conducted at Sandia's FLAME facility (O'Hern et al., 2005). A 1-m diameter diffuser was located part way up in the facility to introduce helium into otherwise calm air. A shroud around the diffuser mimicked a ground condition. A light flow was induced from below to allow the plume to draw air and simulate a semi-infinite condition. The test involved planar laser induced fluorescence (PLIF) for species concentrations, and particle image velocimetry (PIV) for velocities. The plume was ostensibly axi-symmetric, though the test was conducted in a rectangular enclosure. The test resulted in a plane of data for velocity and concentration that includes temporal statistics as well as mean vector and scalar quantities. The data were primarily reported in the 1-m region directly above the diffuser. While the plane suggested some degree of symmetry, it was not perfect, and represents an uncertainty in the system.

The facility was well characterized for flow accuracy prior to testing. Pitot and hot wire velocity probes were used to scan over the flow surfaces to characterize the uniformity of the inflow boundaries. Boundaries consisted of honeycomb flow channels that induce a pressure drop across the inflow surface and help to eliminate any pressure and/or eddy effects in the inflow conditions. The historical reports may be examined for further details on the accuracy of the test conditions (Blanchat, 2001).

The particular case of the helium plume lacks certain complicating physics of interest to fire modeling. It is missing radiation, reactions, soot, and the rest of the physics that accompany these phenomena. It is a good problem for validation because it includes much of what is important. It is fully turbulent (≈1 m source characteristic scale) with density gradients and mixing. It is also amenable to optical diagnostics, as the plume is transparent. The diagnostics were able to illuminate a center-plane with a laser sheet and detect with reasonable accuracy and signal to noise the behavior of the plume. This included PIV measurements for velocity and PLIF measurements for concentration. While this is not the perfect dataset for fire model validation, it is one of the better ones because it is of relevant scale, has high-quality data, and provides relatively high levels of detail for quality model comparisons.

4.2. Methods

This study involves comparisons between SIERRA/Fuego and the measured data from O'Hern et al. (2005). The 1-meter diameter diffuser sourced the helium into the domain where a plane of PLIF

provided a measure concentration, and PIV provided a measure of velocity. The primary parameter of study with the simulation tool is the mesh resolution. There are a number of parameters of uncertainty with respect to modeling tools, some of which are not part of the present study. All material properties have uncertainty, and there are geometric uncertainties that are neglected in this effort. The mesh resolution was selected as a key parameter for study due to the points outlined in the prior section. Added resolution is increasingly able to resolve the instabilities, which is suspected of lending to some of the larger inaccuracies of the modeling. The role of this is important to fire modeling efforts. Fire models are often used in under-resolved conditions, and it is significant to benchmark the effect on accuracy of the use of an under-resolved prediction to model a complex flow problem.

4.2.1. Simulation Tool

SIERRA/Fuego (2019a, 2019b) is a low-Mach reacting flow module in the Thermal/Fluids suite of simulation tools. The code was designed with a focus on being able to predict the heat transfer to objects in fires. This effort used Version 4.54.2 for all simulations. A user manual and a theory manual are both available publications detailing the specifics of the CFD theory and implementation. The code is massively parallel and uses a variety of unstructured elements. A differentiating factor in SIERRA/Fuego is that the code is finite element based instead of a more traditional control volume formulation. A control volume finite element formulation (CVFEM) is used to access some of the more traditional features of a control-volume-based model.

A variety of models are available for most of the physics relevant for a fire prediction, allowing a model form assessment with each prediction. In this particular case, the KSGS LES formulation was used, with light upwinding (factor 0.02) and no under-relaxation. The conservation equations are solved in a segregated manner sequentially with an outer non-linear loop to insure consistency among the conservation equations. The non-linear iteration was cycled 5 times within a timestep to allow for convergence of the solution within each timestep. The mixture state was modeled using a mixture fraction model and constitutive models for the air and helium streams were formulated from a thermodynamics database using a mixture rule for non-binary mixtures. The mixture fraction is linear in the composition varying from air to the helium source with unity Lewis numbers assumed. The unity Lewis number assumption is not generally appropriate for helium-air mixtures, but in fully turbulent flows differential diffusion effects tend to be small (Kerstein, A.R., M.A. Cremer, and P.A. McMurtry, 1995).

Simulations were run for eight seconds to allow the initial conditions to develop towards steady state, after which the Favre averaged parameters were accumulated for another 15 seconds. This averaging process repeated, and for the coarsest cases a second 15 second average was obtained and observed to be adequately similar to the first.

4.2.2. Geometry

Figure 4-1 shows an image with dimensions for a subsequent test to the tests performed following the helium plume effort. The facility and stand are all consistent with the helium plume tests. The top of the pedestal and the lack of a circular shroud are the differences between this geometry figure and the geometry of the tests. The documentation of the tests should be consulted for the best description of configuration.

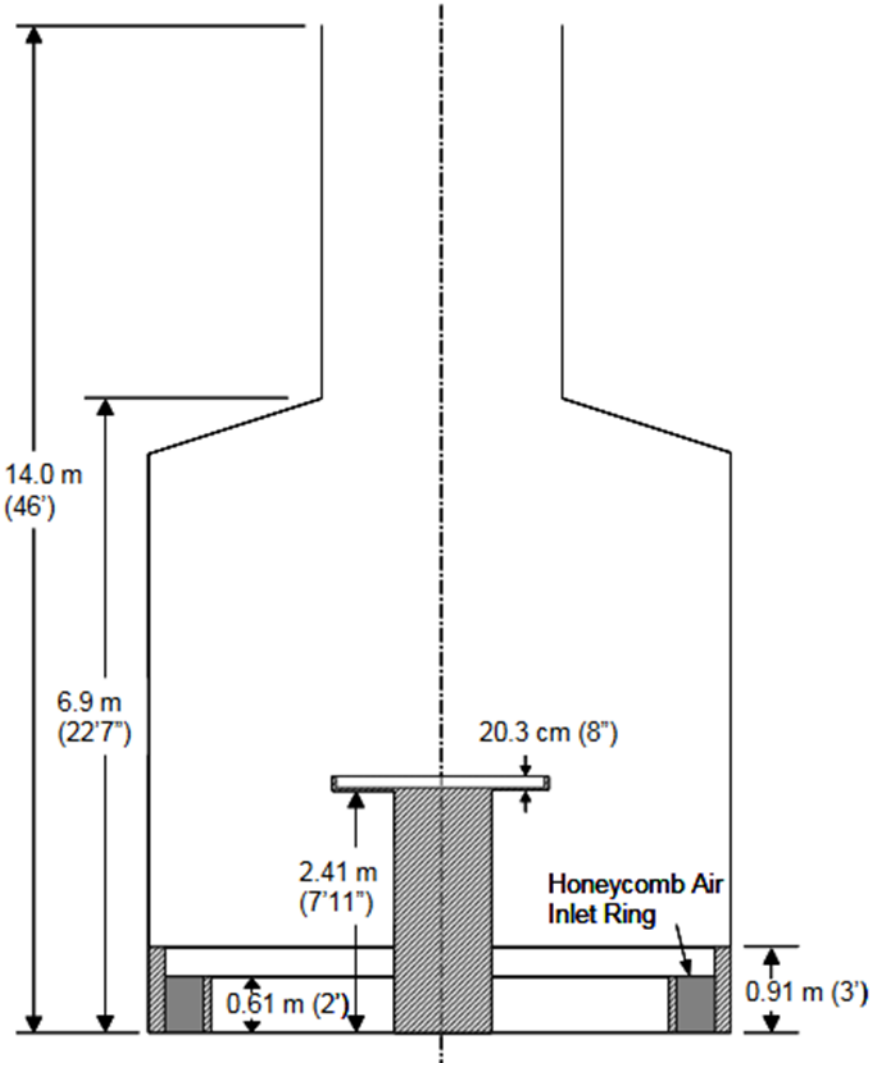

Figure 4-1. An illustration of the FLAME facility configured for a pool fire test

4.2.3. Diffuser Model

The inlet condition was difficult to model for a CFD code. The diffuser consisted of a honeycomb layer with a total thickness of 10.2 cm and 0.3 cm cells at the interface with the domain. The experimental assumption was that the diffuser would create a pressure drop and reduce or eliminate the influence of the domain behavior on the inflow boundary condition. In reality, this assumption is difficult to verify. To model this condition in the simulations, a porous region was assigned below the level of the honeycomb to induce a pressure drop. The flow was allowed to penetrate into the diffuser, but the porous model would function as the honeycomb to induce a pressure drop and to inhibit flow conditions above the diffuser from propagating down into the inflow region. A pressure perturbation above the inlet might propagate into the honeycomb, but the channels would inhibit significant propagation of that disturbance. The inflow condition is consistent with this interpretation of the inflow boundary. Initial simulations omitting the porous region exhibited poor quantitative and qualitative comparisons to the experimental data low in the plume. This motivated the porous assumption illustrated in Figure 4-2. The gas volume fraction was 1.0 at the z-height of

0.0. Below this, the porosity was decreased until a 0.80 gas volume fraction at -0.01 m. Below that, the gas volume fraction was constant.

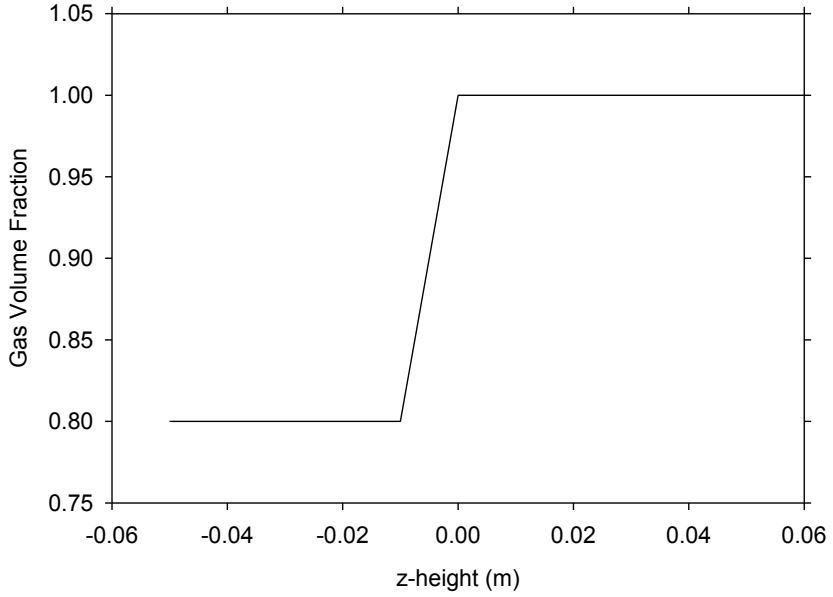

Figure 4-2. The gas volume fraction applied to the inlet condition

This inflow condition was arrived at empirically, by examining the predicted planar flow and comparing the contours to experimental results. Note that the coarsest (R4; look ahead to Table 4-1 for mesh details) mesh lacked nodes in the transition region between the maximum and minimum gas volume fraction, so the variation appeared more as a step function for that coarse simulation prediction. The magnitude of the gas volume fraction was the main parameter adjusted to achieve the final condition used for all the subsequently described simulations (unless otherwise noted). Figure 4-3 shows a comparison of data and simulation results for the R6 mesh. The most notable variations from the data were in the centerline mass fraction, the vertical velocity at the centerline, and the radial velocity recirculation zones. Contours are all spaced identically in the images, and the images were manually sized to be approximately similar.

Figure 4-4 shows planar images of the variety of assumptions evaluated on the R5 mesh prior to selection of the final simulation inlet conditions. The best simulations involved a domain that extended 2.5 cm below the nominal inlet plane, and a porous approximation for the flow in the honeycomb diffuser of the inlet. Figure results suggest a moderate to high degree of sensitivity of the predicted results to the inflow boundary condition assumption. For the greatest porous drag imposed on the inflow at the right side of Figure 4-4 some recirculation regions develop near the plume center over the inflow; this flow separation is not observed to any noticeable extent in the measurements. As less porous drag is imposed on the inflow moving from right to left in Figure 4-4 this recirculation region disappears but for the greatest porosities the flow accelerates too rapidly in the vertical direction with little mixing. This change in the recirculation region and the change in the degree of turbulent mixing evident in the flow suggests that the modeling of the inlet diffuser affects the near-source shear stresses. The inlet flow condition that produces the correct Reynolds stresses is most likely the one that performs optimally. The intermediate case with 80% porosity is selected

here to represent the appropriate amount of inflow damping. The calibrated inlet produces the results most closely resembling the data and are therefore used for all subsequent simulations.

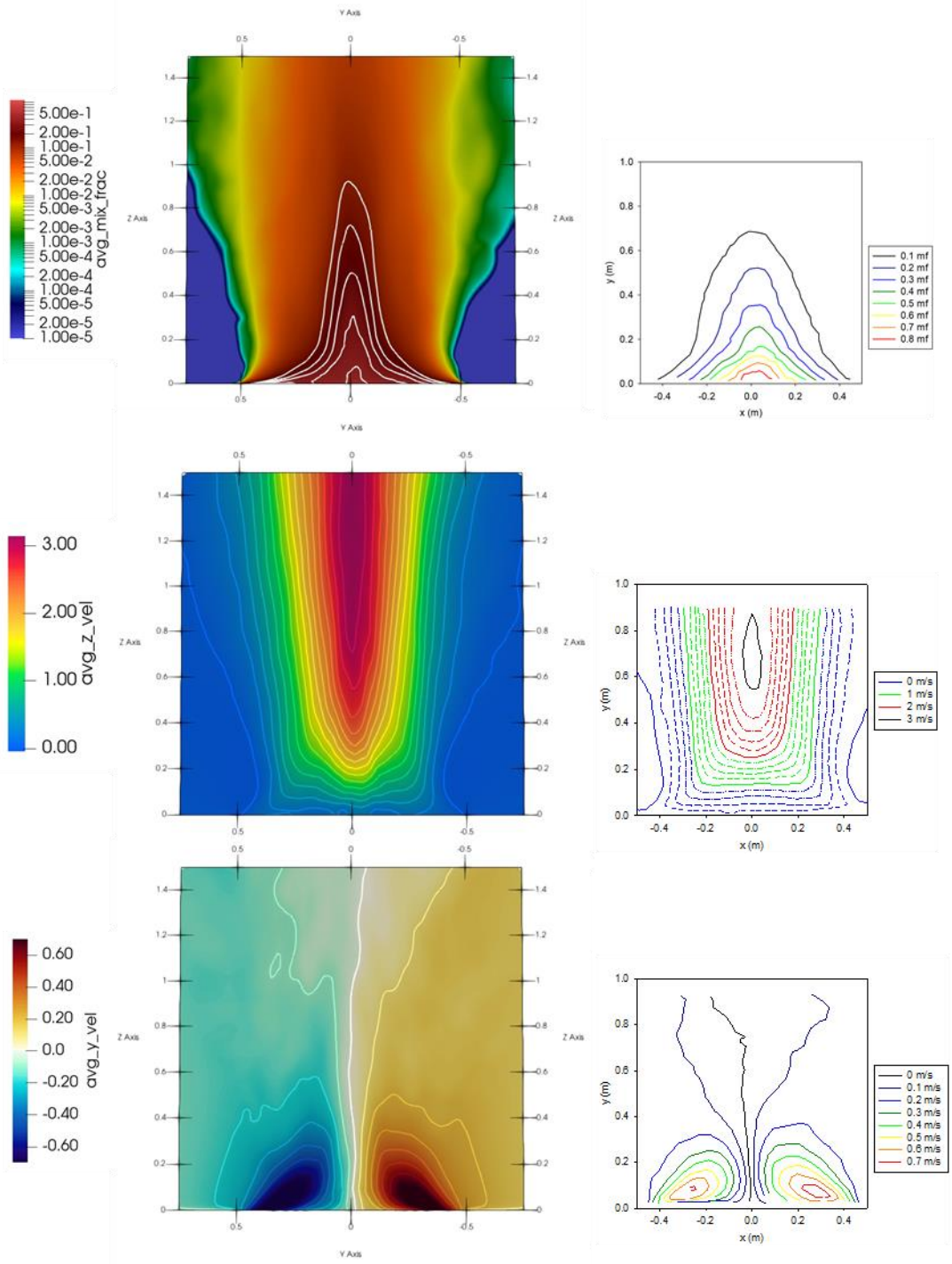

Figure 4-3. The R6 simulation results (left) with calibrated inlet compared to the planar data from the tests (right) for mixture fraction (top), vertical velocity (middle), and radial velocity (bottom)

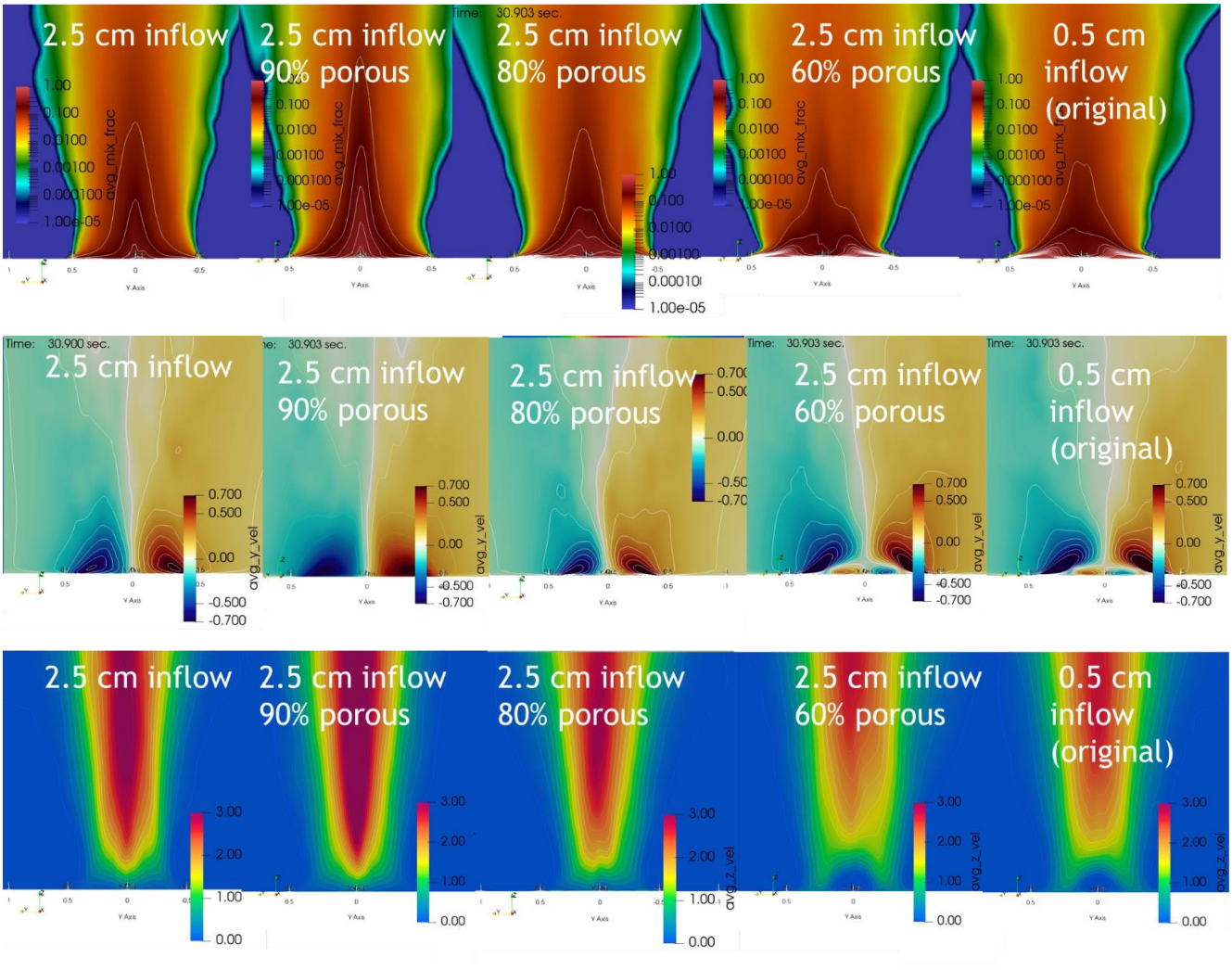

Figure 4-4. The R5 planar results with a variety of inlet assumptions for mixture fraction (top), radial velocity (middle), and vertical velocity (bottom)

4.2.4. Simulation Parameters

The domain selected for this simulation series was a 9 m high, 5.82 m diameter cylindrical mesh, as illustrated in Figure 4-5. This image shows a cut-away of the coarse (R4) mesh. The computational domain is smaller than the full FLAME facility, which presumes that the domain was successful in achieving a semi-infinite condition with respect to the plume. The bottom air inlet was not modeled in favor of a shroud plane simplified air inlet (blue in Figure 4-5) that was functional in the velocity with distance. The lateral extent was inside that of the facility walls as well as the internal cylindrical shroud. The vertical dimension was significantly higher than what might be construed as the facility roof, or the constriction to the exhaust, which was neglected here. The simulations in this way are more representative of an open plume. The effect of the upper structure of the facility on the flow in the measurement region is not well established, but at this point assumed negligible.

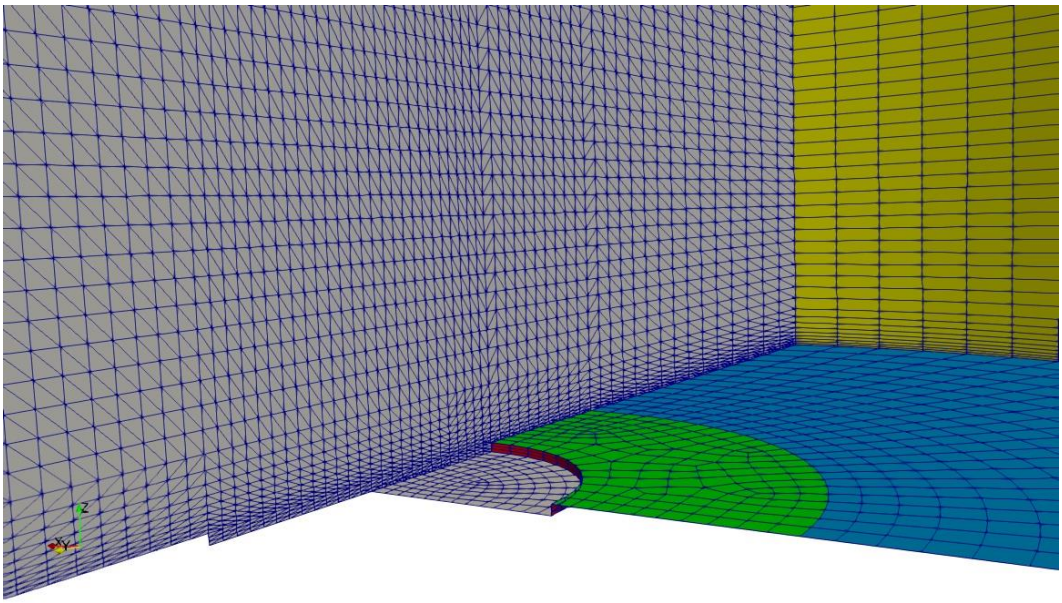

Figure 4-5. The coarse (R4) He plume mesh

Other meshes were used, which included progressive refinement of the baseline mesh. This means that each hexahedral element was split into N equal intervals, where N varied from 0 for the baseline case up to 4 for the finest case run in this effort. A finer mesh existed, but due to resource limitations was not run to completion. Figure 4-6 shows a graphical representation of the mesh characteristics, while Table 4-1 gives the values corresponding to the mesh parameters. Resolution is referenced to the pan region and is characterized by the z- and y-fine dimensions. The z-fine (vertical) value is representative of the length scales of the mesh along the boundary, while the x- and/or y-fine (radial) parameter is more representative of the resolution in the bulk region where data and simulation results are primarily compared.

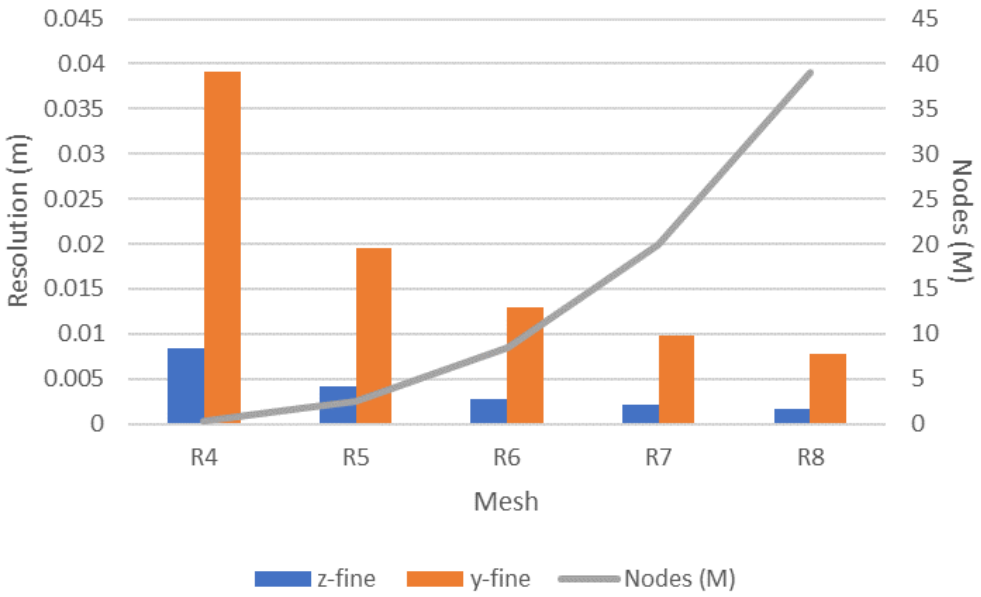

Figure 4-6. Meshes for the He plume study

Table 4-1. Detailed mesh parameters for the He study

	z-fine	y-fine	Nodes (M)	Split Intervals	Radial Nodes
R4	0.00833	0.039	0.3125	1	13
R5	0.00417	0.020	2.5	2	25
R6	0.00278	0.013	8.44	3	38
R7	0.00208	0.009	20.0	4	51
R8	0.00167	0.008	39.0	5	63

Included here as well are images of the R8 predicted dynamics. Figure 4-7 shows a volume rendering of the species mass fraction. Resolution is expressed in the fingering of the instabilities at the base of the plume. Lower resolution predictions exhibited fewer features in this region of the flow. Figure 4-8 is another visualization of the plume showing iso-contours of the Q-criterion colored by velocity magnitude, instantaneous velocity vectors colored by magnitude, and mixture fraction on a logarithmic scale. These serve to illustrate the complexity of the dynamics from the simulations that are not as obvious in most of the rest of the work in this section, which focuses on the mean and RMS values of the results, and not the instantaneous behavior.

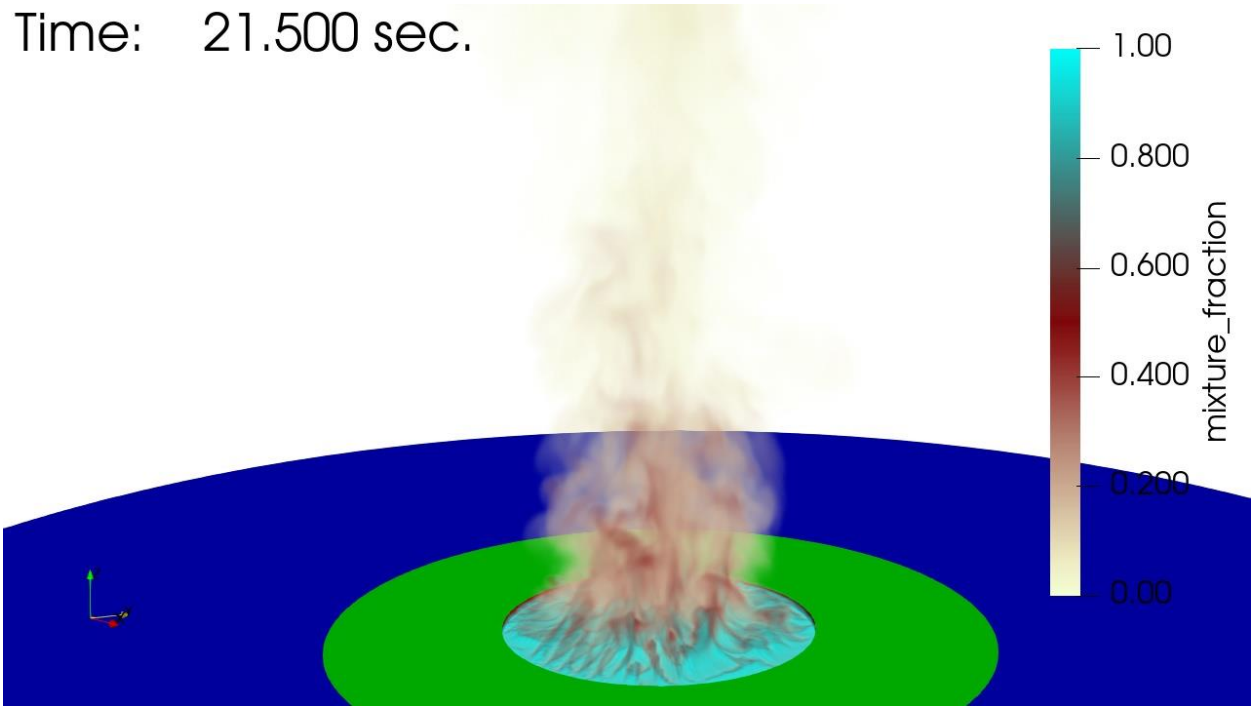

Figure 4-7. A volume rendered image from the R8 simulation

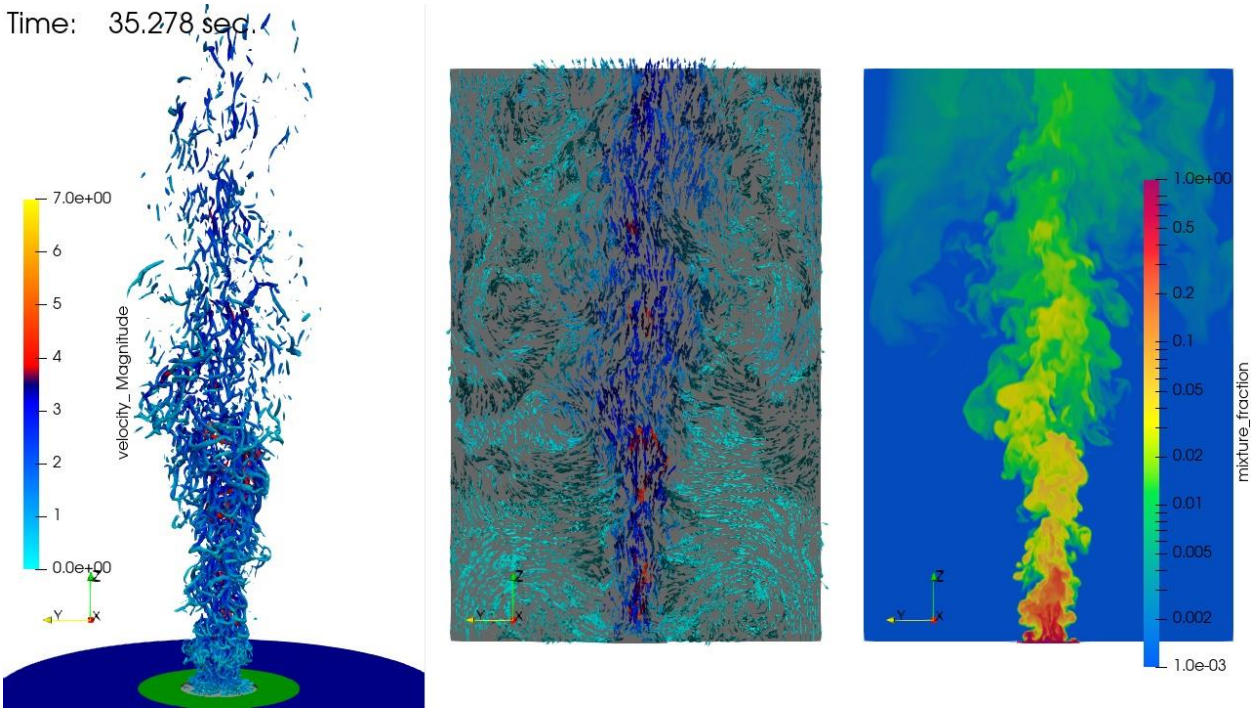

Figure 4-8. Images from the R8 simulation, Q-criterion (left), velocity vectors (center), and mass fraction (right)

4.3. Results

For the MaCFP effort, the predictions of velocity, concentration, and RMS of these were compared to data along radial lines at a number of fixed heights. The first sub-section illustrates those results. The next sub-section details a quantitative comparison with the data, which is illustrated using two different mathematical comparison metrics. The third sub-section touches on the puffing frequency, which was reported during the experiments.

4.3.1. Line Comparisons

A common notation is used for the plots in this section. The corresponding legend is found in Figure 4-9. Data are represented with a circle at each data point with solid lines through each point and a solid black line. The highest resolution predictions (R8) are shown with a long blue dashed line. The lowest resolution (R4) is gray with a double small dash pair.

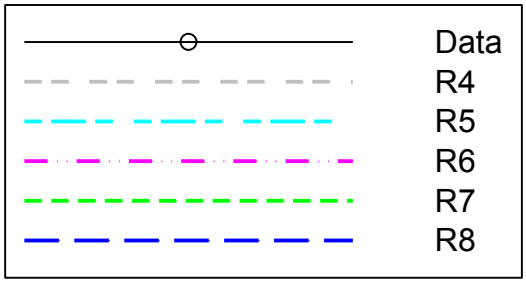

Figure 4-9. Standard legend for comparison line plots

The vertical component of velocity here is termed the W velocity, and involves the highest magnitude velocities from the test, as motion is primarily vertical. Figure 4-10 through Figure 4-12 show predictions at 0.2, 0.4, and 0.6 m heights. There is an obvious improvement in the results, with R4 predictions clearly deviating from the data, and the progressive refinement results showing trending towards the data. The highest level of refinement (R8) gives a very good approximation of the data, and are with few exceptions trending with the data.

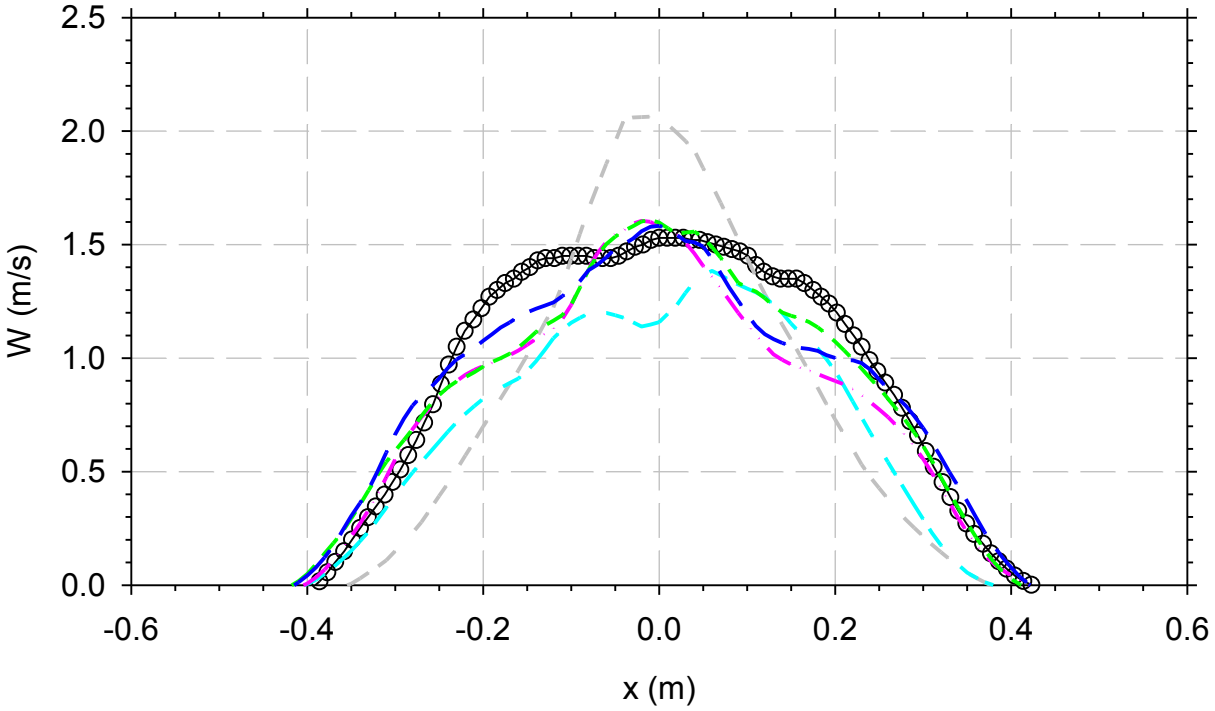

Figure 4-10. W-Velocity comparisons at 0.2 m above the diffuser

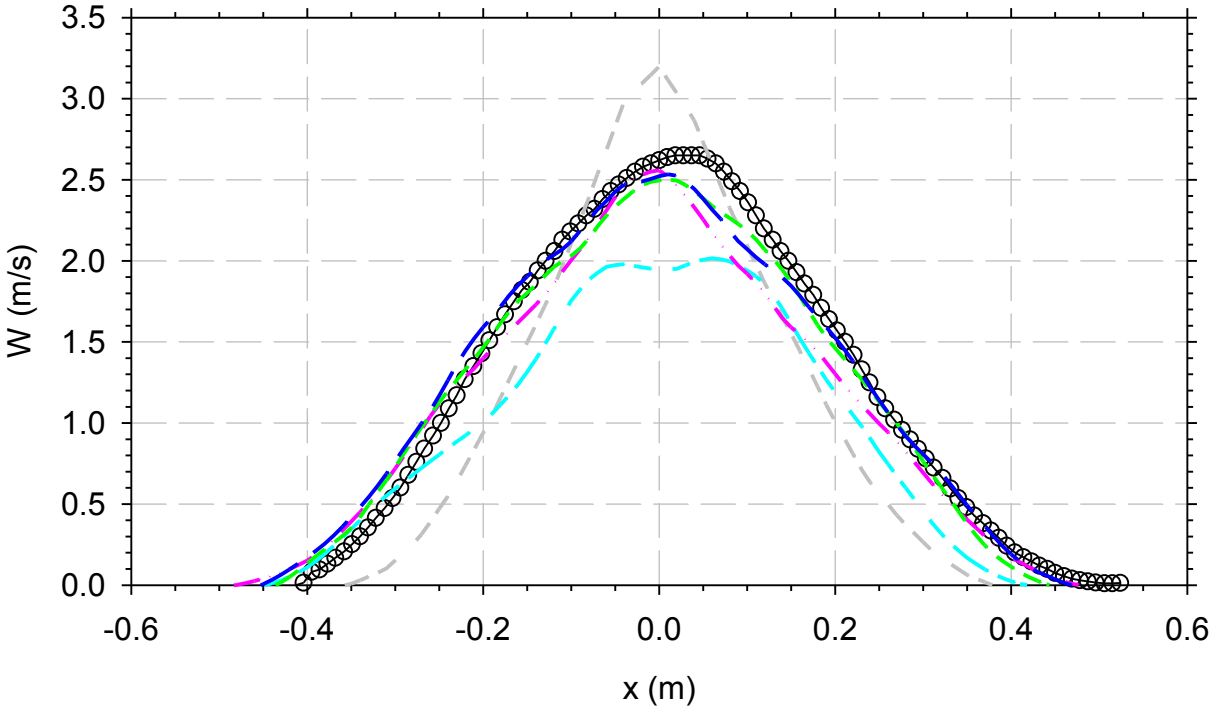

Figure 4-11. W-Velocity comparisons at 0.4 m above the diffuser

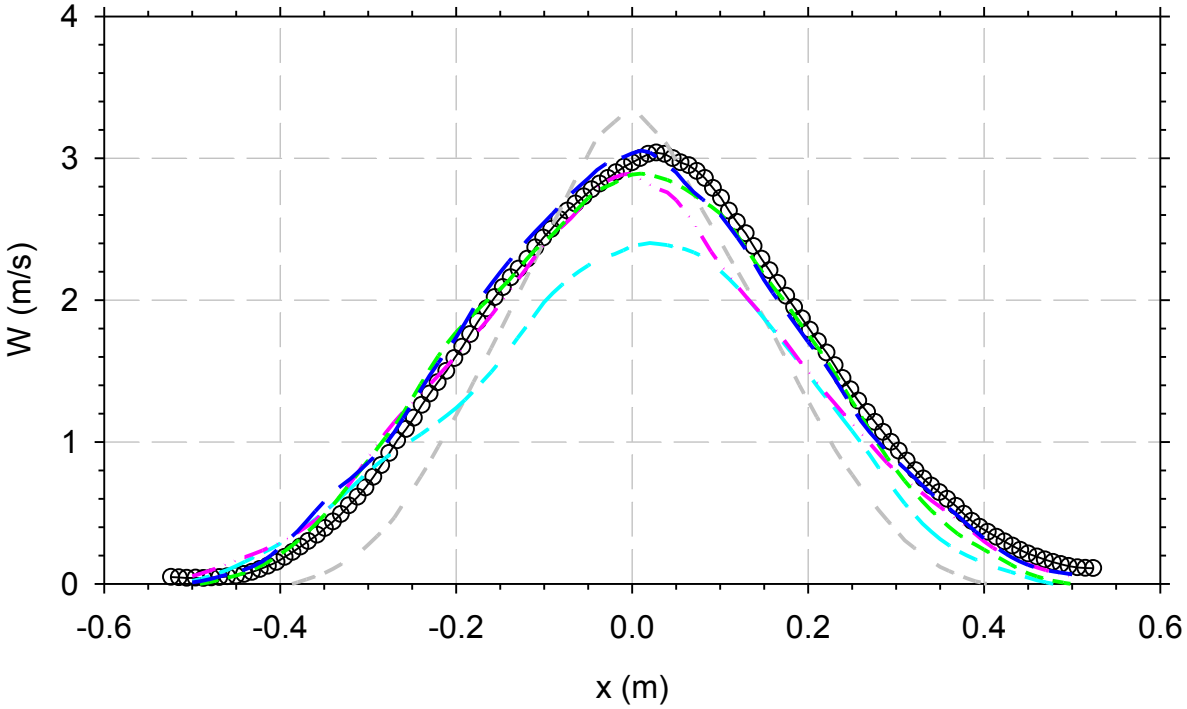

Figure 4-12. W-Velocity comparisons at 0.6 m above the diffuser

The radial component of the velocity is the U-velocity, and results are shown in Figure 4-13 through Figure 4-15. It is important to keep in mind that the geometry is ostensibly symmetric, and the data and models should exhibit corresponding behavior. For the most part, the models do this well, however a moderately large example of the data lacking symmetry is found in the data in Figure 4-14 where +/- 0.4 m data differ significantly. Major trends are well predicted; however, inflection points tend to be different between the models and data.

Note the difference in the magnitude of the U-velocity compared with the figures in the prior section. The magnitude of velocity is about an order of magnitude higher for the vertical velocity. Were these plotted on a similar scale, the U-velocity comparisons might appear much more accurate when compared with the data.

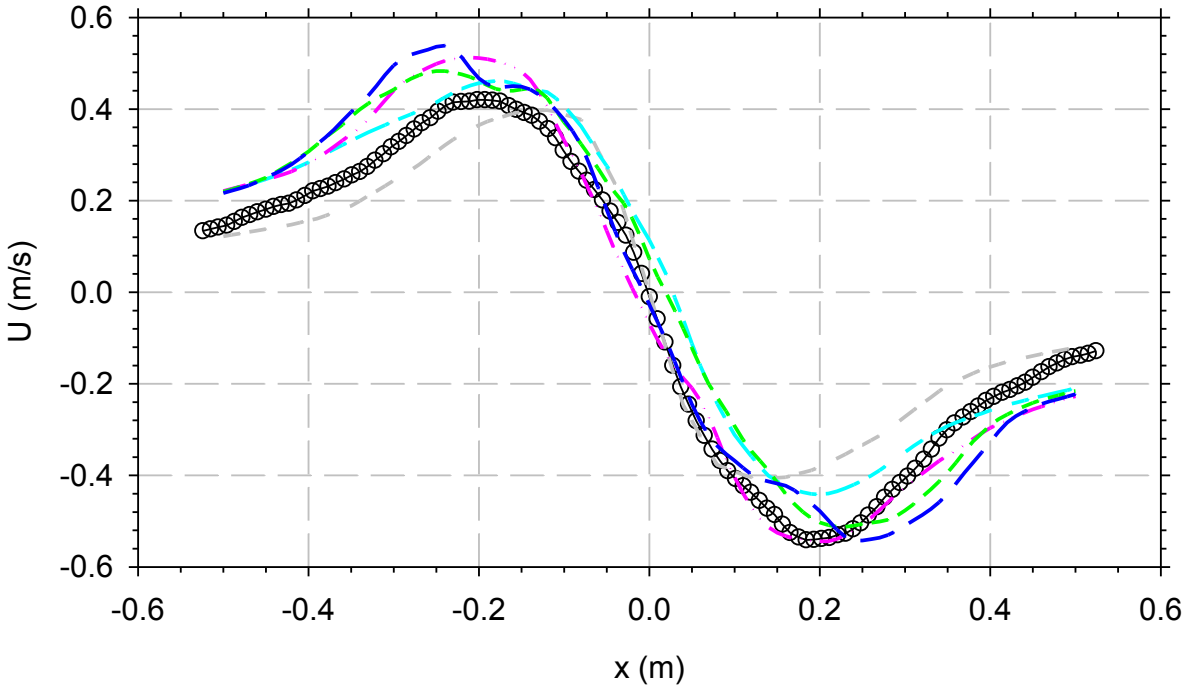

Figure 4-13. U-Velocity comparisons at 0.2 m above the diffuser

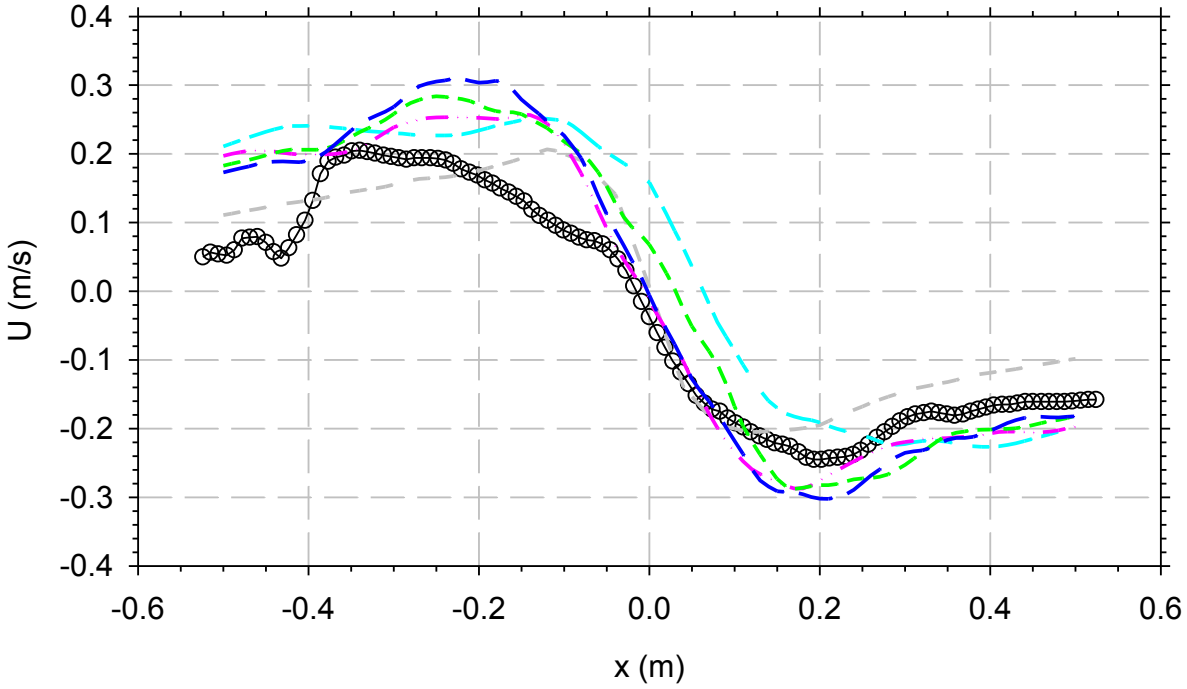

Figure 4-14. U-Velocity comparisons at 0.4 m above the diffuser

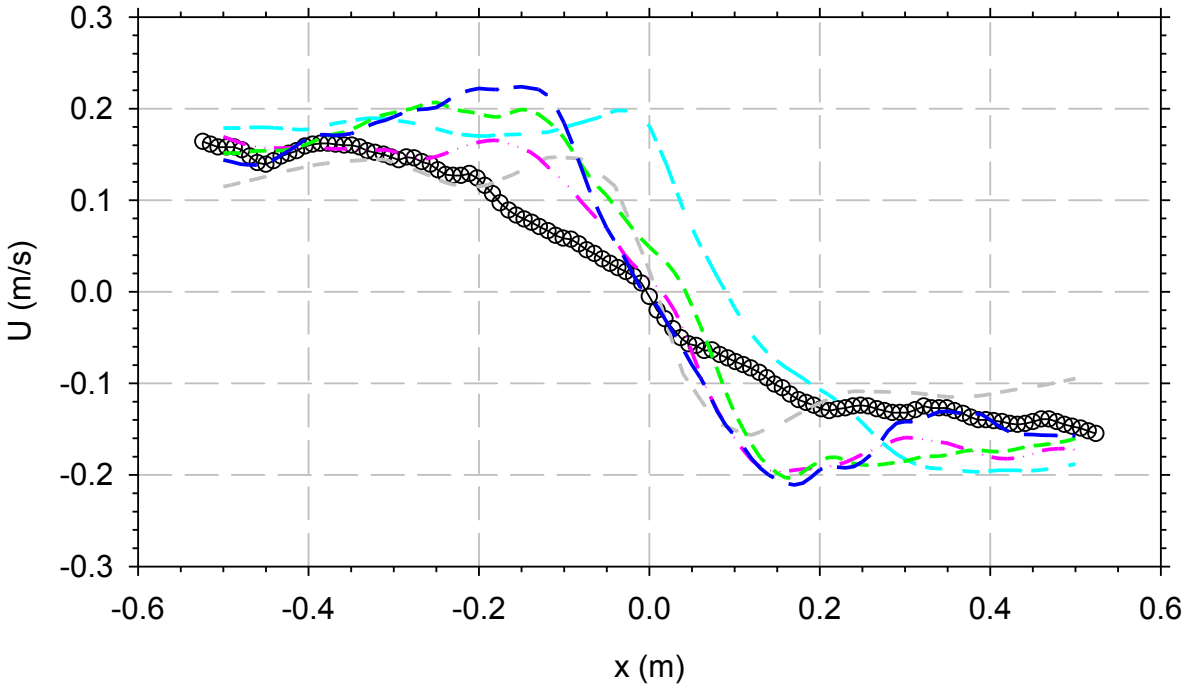

Figure 4-15. U-Velocity comparisons at 0.6 m above the diffuser

Figure 4-16 through Figure 4-18 show mass fraction comparisons. The data tend to be higher than the models at low (0.2 m) levels, and pretty accurate at intermediate heights (0.4 m). At the highest

elevation, data tend lower than the model. This elevation bias is somewhat surprising, as there is not a similar velocity offset that would tend to suggest an advective source for the differences. Further, the radial entrainment velocity predictions in the previous set of Figure 4-13 through Figure 4-15 generally suggest greater entrainment in the predictions. We expect this would tend to increase the dilution and spreading of the plume mass fraction more than in the measurements, but the opposite appears in this set of figures. This might be suggestive of some diffusional bias, but it could have its source in other variabilities. Note also that the peak data are slightly skewed in the positive-x direction, whereas the model predictions tend to be symmetric. The breadth of the peaks is reasonably predicted, which suggests the effect causing the discrepancy is center-line dominant.

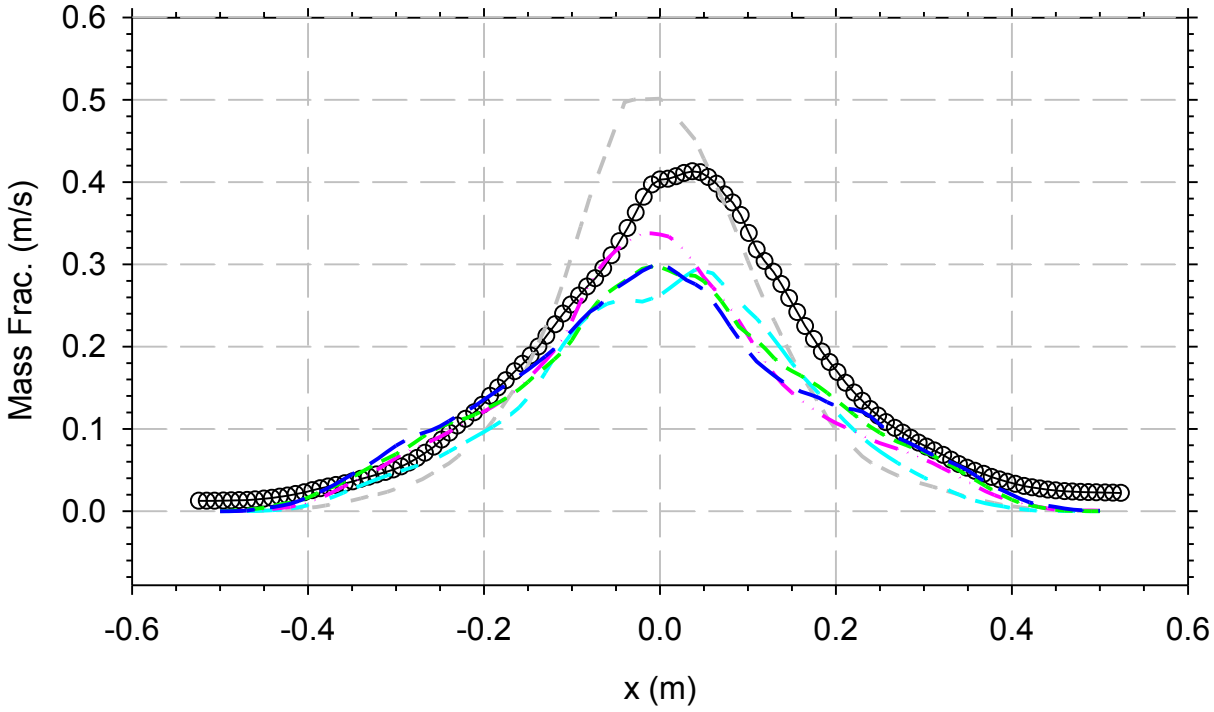

Figure 4-16. Mass fraction comparisons at 0.2 m above the diffuser

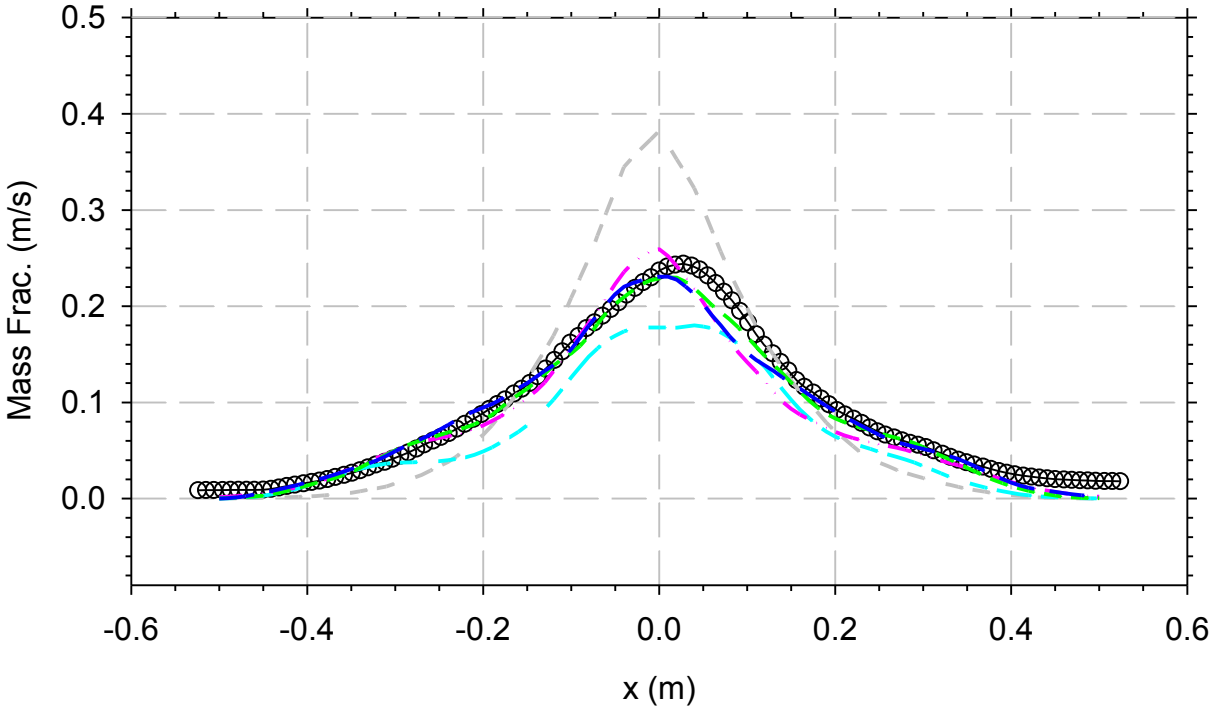

Figure 4-17. Mass fraction comparisons at 0.4 m above the diffuser

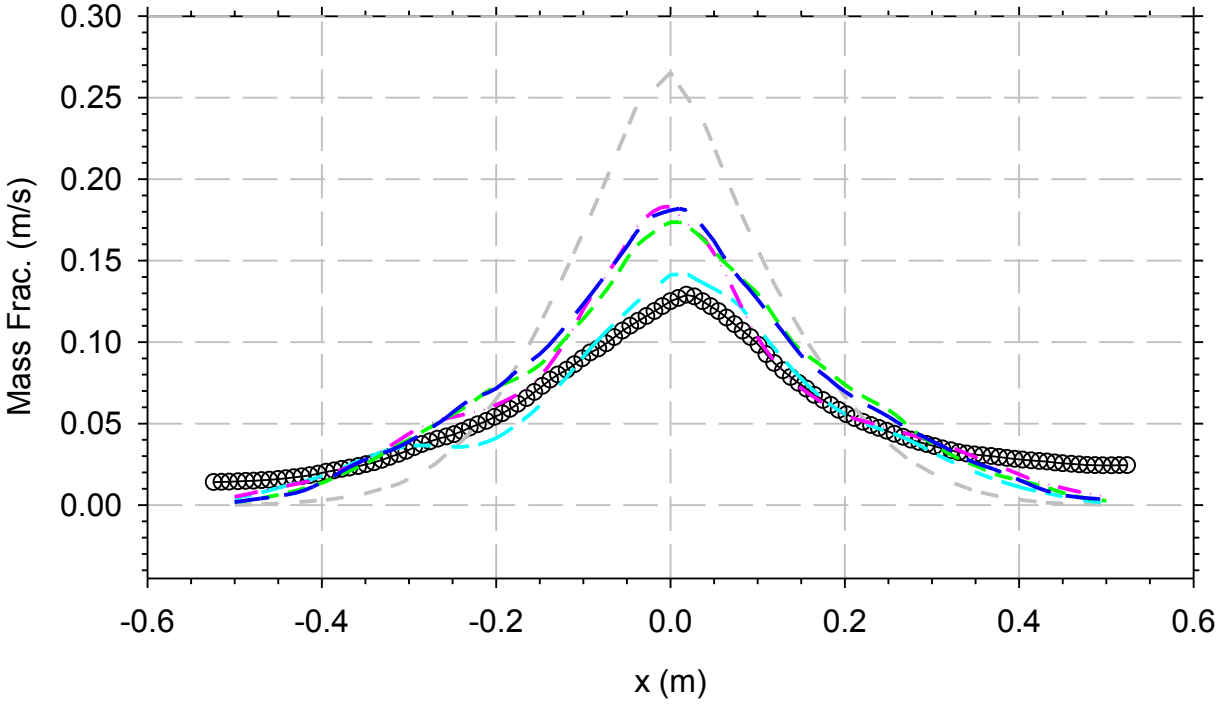

Figure 4-18. Mass fraction comparisons at 0.6 m above the diffuser

Root-mean-squared (RMS) fluctuating velocity was also provided by the tests and was extracted from the model predictions at three of the mesh resolutions. These were extracted based on 300-400 instances of the developed plume results, and post-processed from the domain extractions. The RMS is also equal to the standard deviation (STD) of the velocity. Figure 4-19 through Figure 4-21 shows vertical velocity (W-velocity) 0.2, 0.4, and 0.6 m elevation RMS predictions versus the data. In each case, there is a clear improvement of the model predictions from R4 to R8 in terms of the shape of the trends and the peak magnitudes. This provides evidence of improving predictions of the dynamic behavior of the plume as mesh resolution increases.

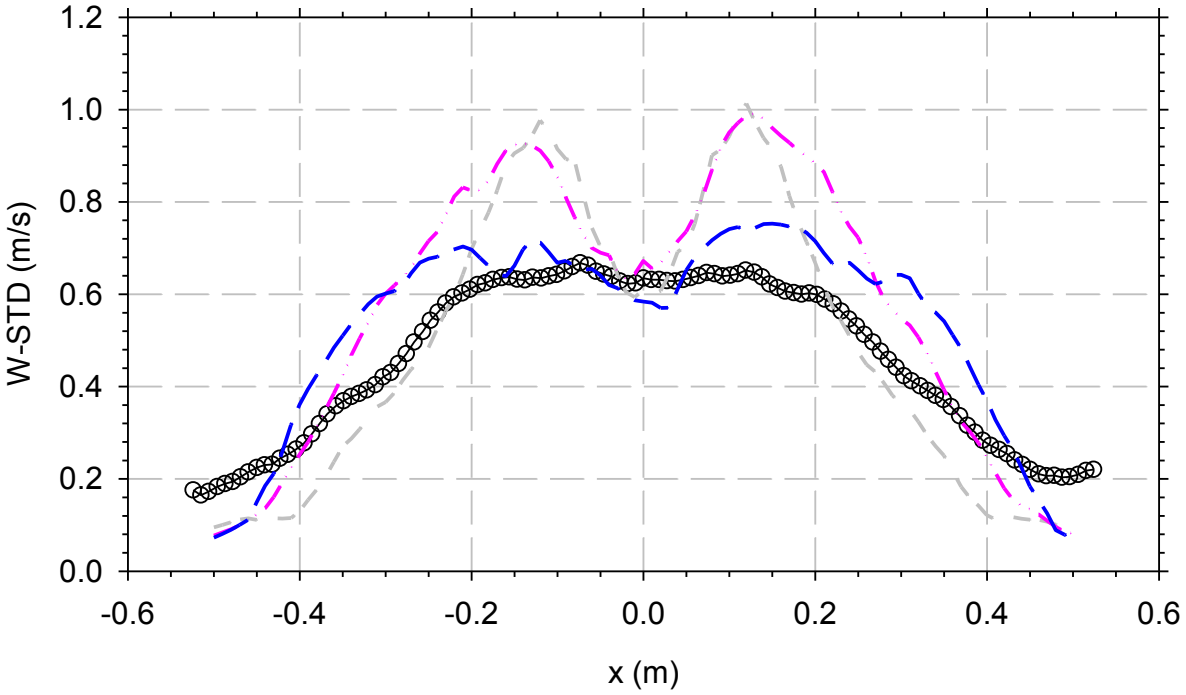

Figure 4-19. RMS W-Velocity comparisons at 0.2 m above the diffuser

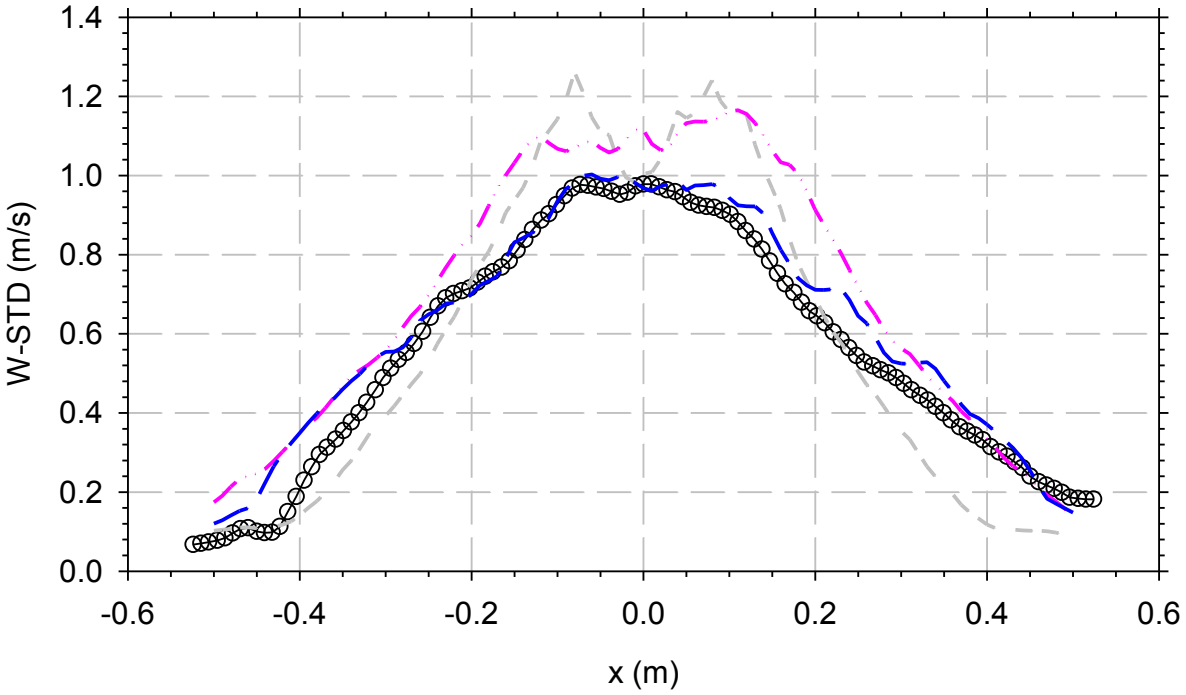

Figure 4-20. RMS W-Velocity comparisons at 0.4 m above the diffuser

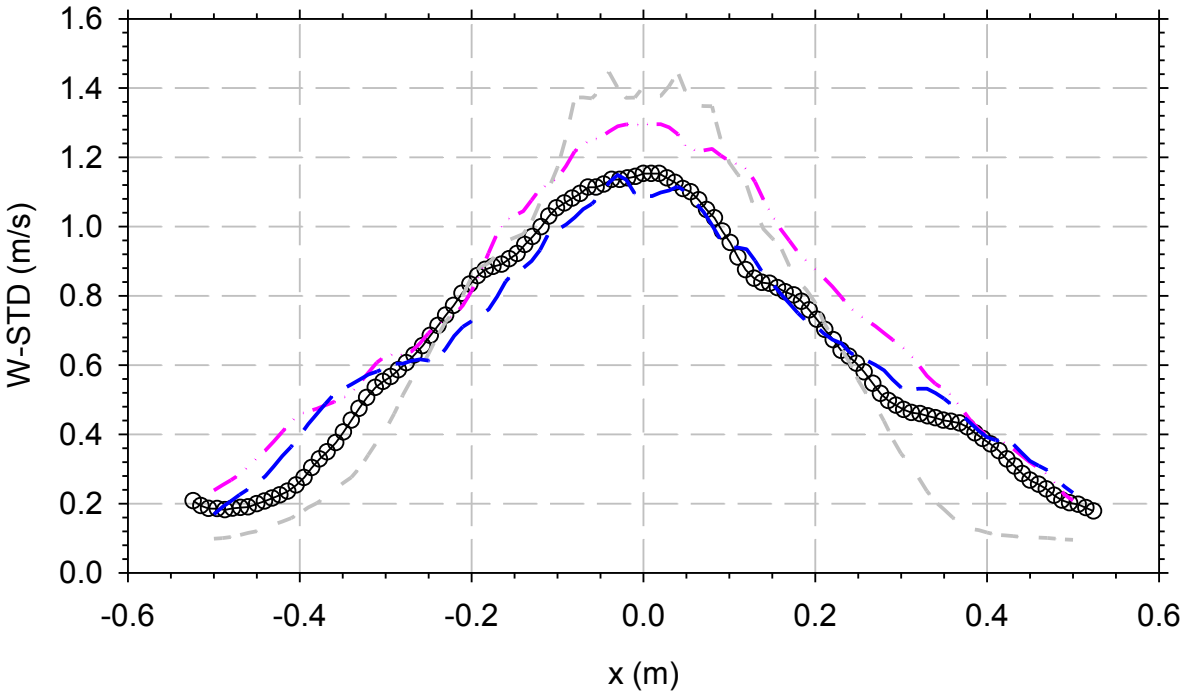

Figure 4-21. RMS W-Velocity comparisons at 0.6 m above the diffuser

Figure 4-22 through Figure 4-24 show U-Velocity RMS comparisons for the three simulations versus the data. In all cases, the R4 simulations are clearly poorer than the others compared to the data. The R6 and R8 simulations resolutions do much better and are mostly indistinguishable except at 0.2 m where R6 curiously appears better than R8. Note here as with the magnitude plots that the fluctuations in the radial velocity are much smaller in magnitude than the corresponding vertical velocity fluctuations. We note that increased resolution tends to lead to greater radial U-velocity fluctuations while increased resolution tends toward lower vertical W-velocity fluctuations. This suggests that increased isotropy in the turbulent kinetic energy results from resolution, or perhaps that the anisotropy associated with acceleration tends to remain in the vertical component when there is less resolution and less of a turbulent cascade.

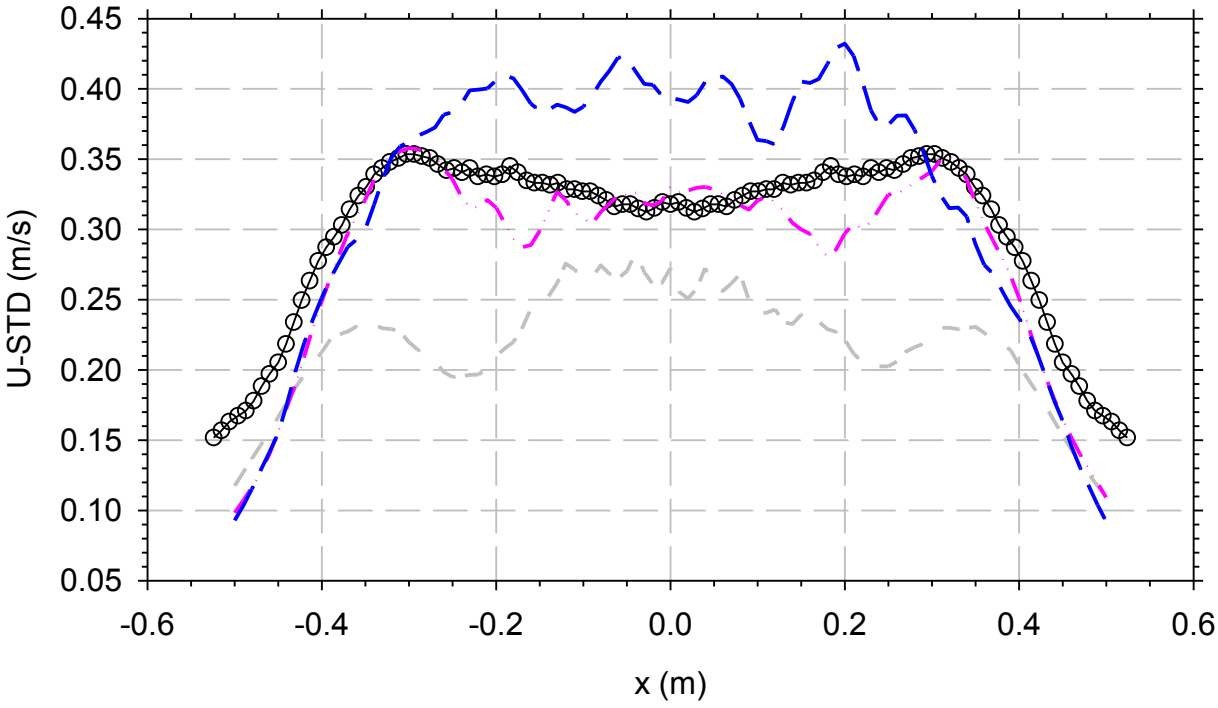

Figure 4-22. RMS U-Velocity comparisons at 0.2 m above the diffuser

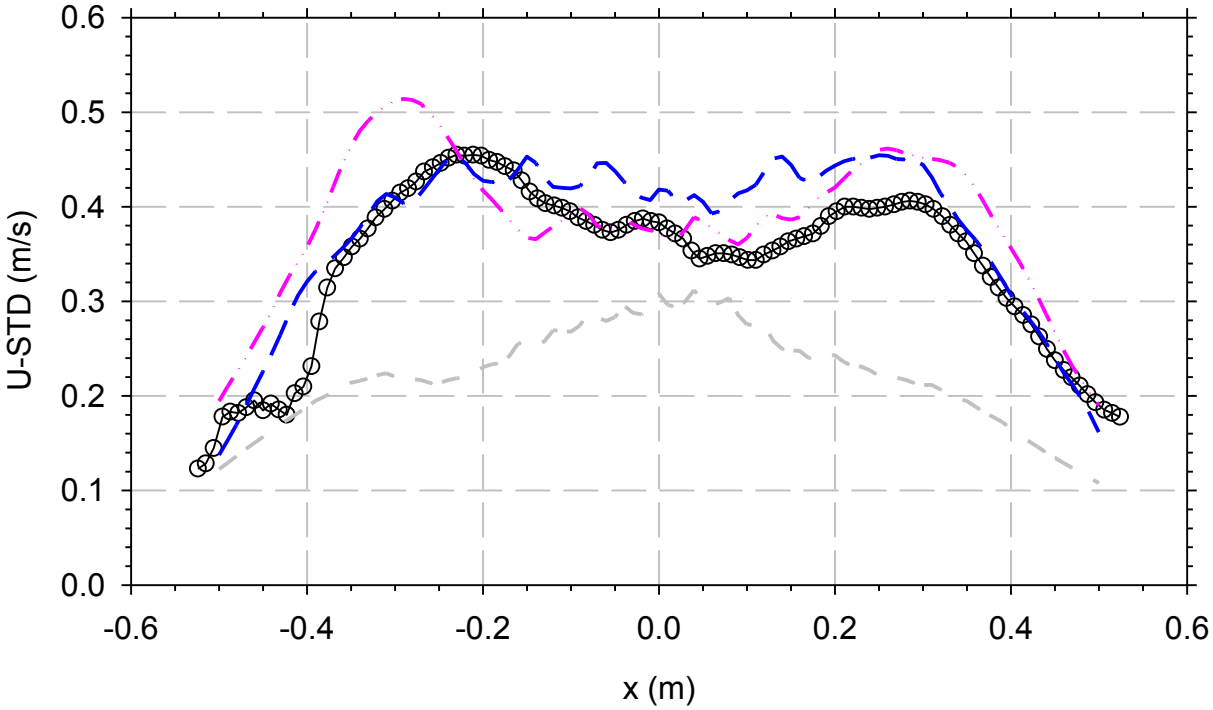

Figure 4-23. RMS U-Velocity comparisons at 0.4 m above the diffuser

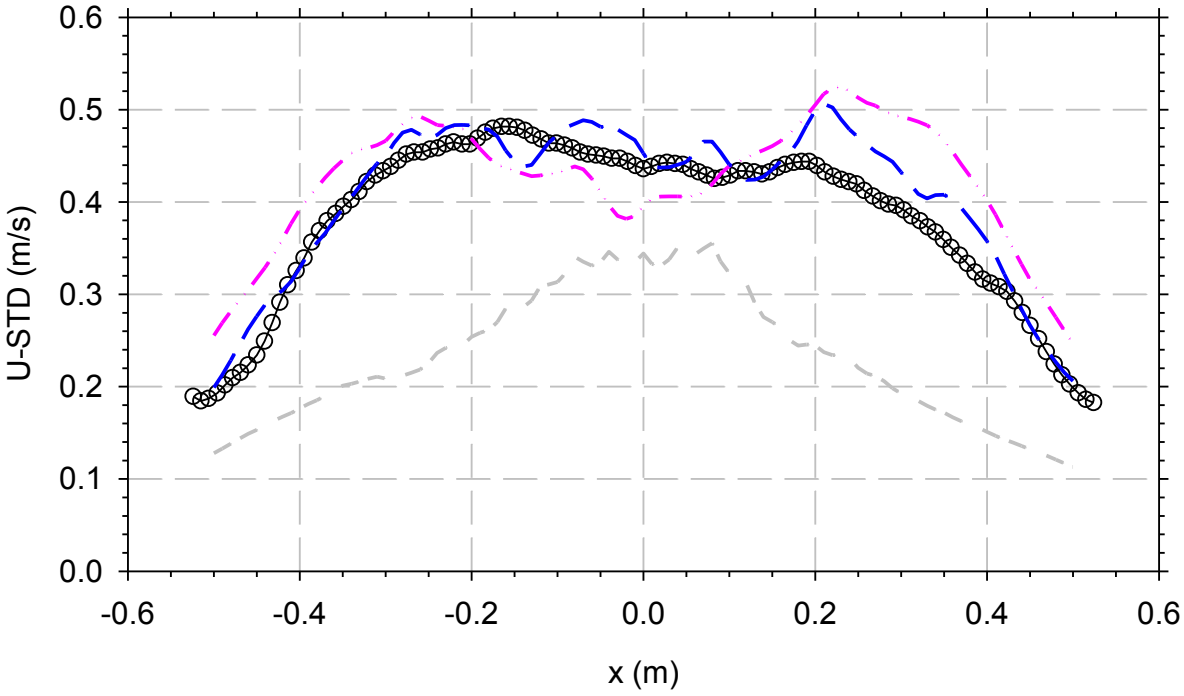

Figure 4-24. RMS U-Velocity comparisons at 0.6 m above the diffuser

Figure 4-25 through Figure 4-27 show the mass fraction RMS predictions compared with data. The simulations generally predict higher fluctuations than the data, and trending is good for the R6 and R8 mesh resolutions. Like the scalar data for mass fraction, there is an asymmetric skew to the RMS data that do not appear in the model predictions. It is curious that the mass fraction RMS is moderately lower than predictions given that the predicted velocity fluctuations were reasonably approximate to the data. This would seem to point to a diffusive error rather than an advective error, since the velocity fluctuations appear to converge towards the data.

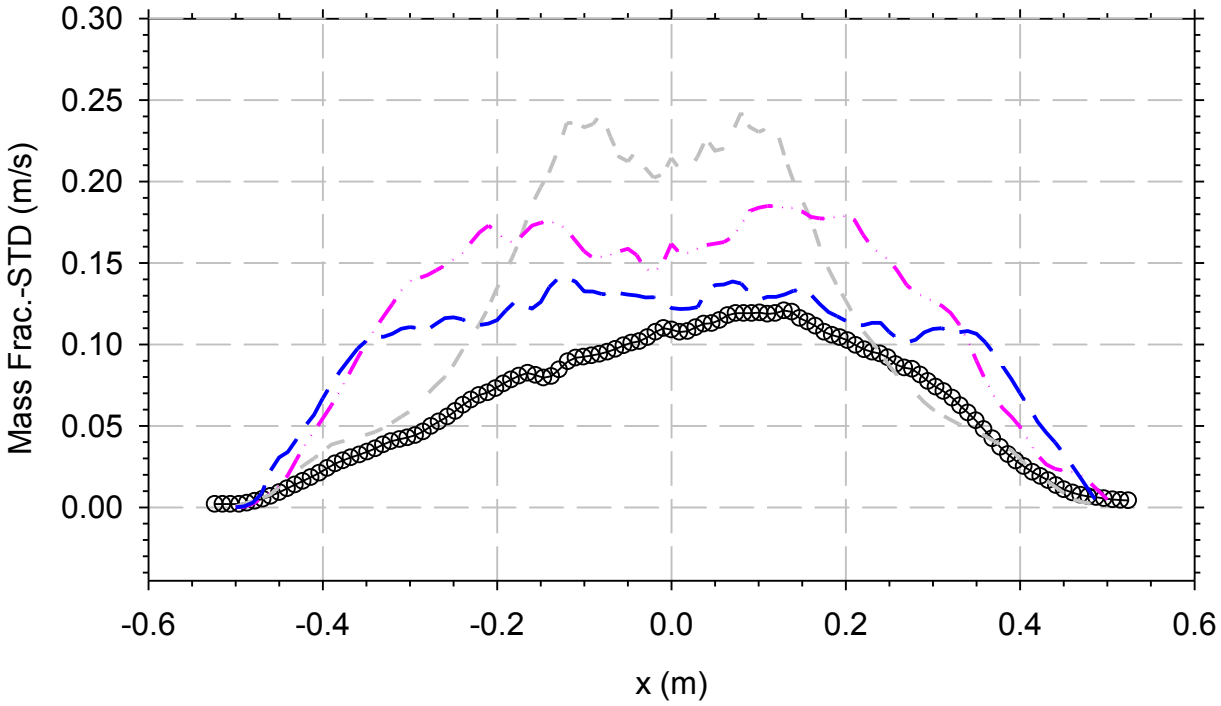

Figure 4-25. RMS mass fraction comparisons at 0.2 m above the diffuser

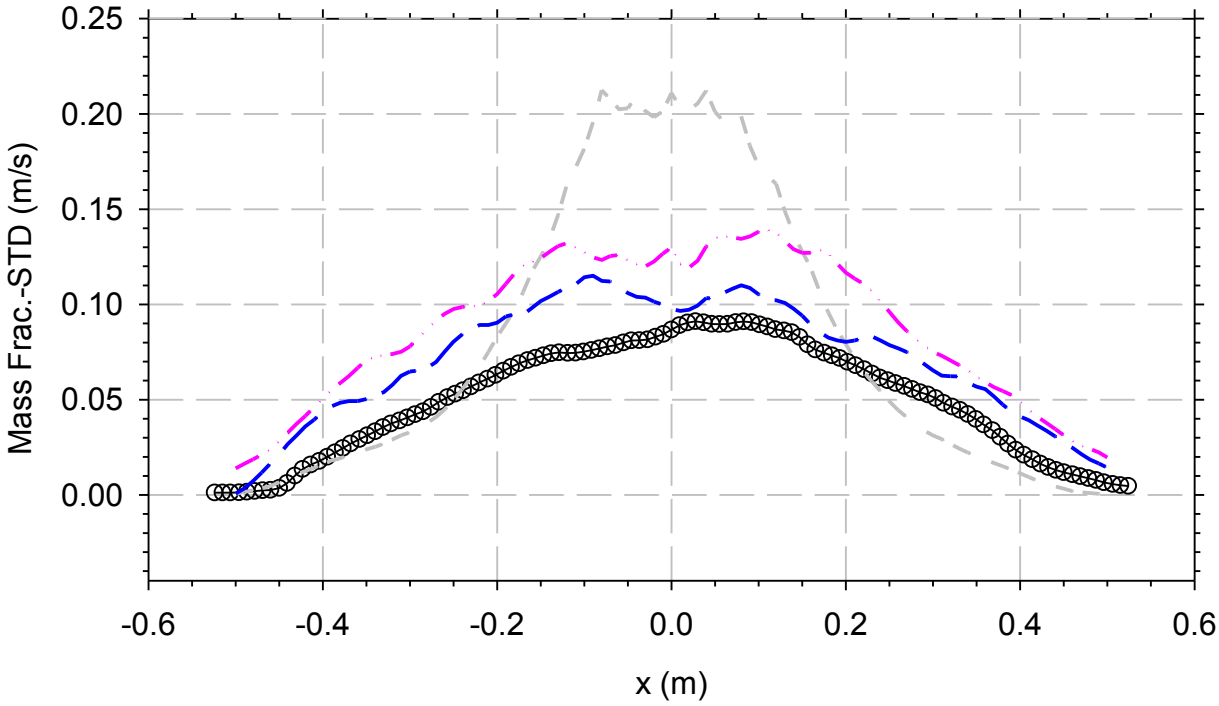

Figure 4-26. RMS mass fraction comparisons at 0.4 m above the diffuser

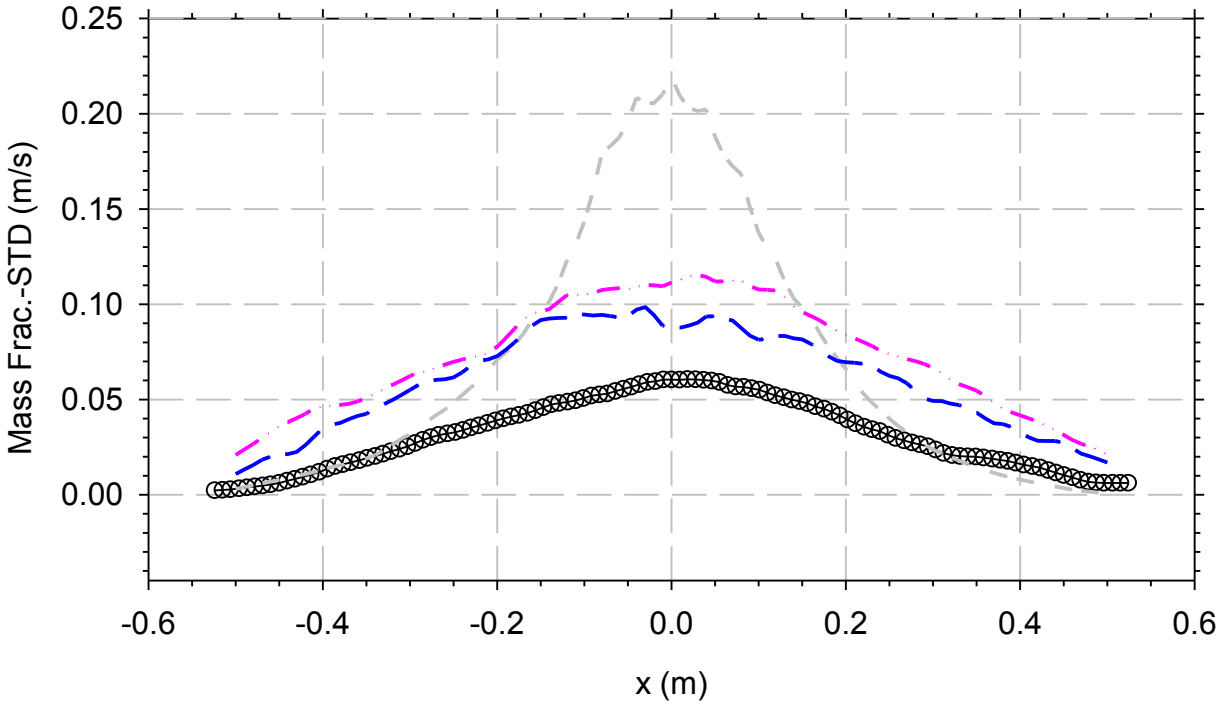

Figure 4-27. RMS mass fraction comparisons at 0.6 m above the diffuser

4.3.2. Quantitative Comparisons

It is instructive to make quantitative comparisons between the model and data in addition to the simple plotting of line results. The methods for quantitative comparison are numerous and can give a different picture of the accuracy of the model depending on the chosen approach. Here we elect to illustrate two methods that represent the accuracy of the three main variables and their RMS values. We have previously applied a variety of methods to an even more detailed CFD comparison (see Brown et al., 2021). From that work, the correlation analysis was found to be a preferred metric for comparison. Here we also evaluate the Euclidian Norm, a metric proposed by Peacock et al. (1999) for studying model accuracy for fire simulations.

Comparison methods require that the model and experiment be spatially coincident. The intervals of data and model output were different, so this needed rectification. The simulation results are first interpolated onto the data using a linear interpolation. With coincident data, detailed comparisons can be made on each variable. Here the coefficient of determination, or R^2 based on the correlation analysis, is used for assessing model accuracy. The correlation coefficient is calculated as follows:

$$R_{xy} = \frac{\sum_{i=1}^{n}(x_i - \bar{x})\,(y_i - \bar{y})}{\sqrt{\sum_{i=1}^{n}(x_i - \bar{x})^2}\sqrt{\sum_{i=1}^{n}(y_i - \bar{y})^2}}$$

The correlation analysis is an estimate of the linear fit between the model and experiment (x and y), which should ideally be linearly related with a slope of 45º.

The Euclidian Norm is also determined for the dataset. This parameter presumes the data and model are in a vector space of n dimensions involving n data points, and that the similarity between the model and data are represented by vector quantities. Vector magnitudes are typically the most interesting component of this analysis. The Euclidian norm E is the distance between the two vectors normalized by the experimental vector magnitude. This gives a sense of the similarity between the model and data in Euclidian terms.

$$E_{xy} = \sqrt{\frac{\sum_{i=1}^{n}(y_i - x_i)^2}{\sum_{i=1}^{n}(y_i)^2}}$$

In this case, the experimental result is the 'y' component. The correlation analysis is different in that it is agnostic to the data source component (i.e., which component is x and which is y).

Figure 4-28 shows the Euclidian Norm of the predictions for the three variables and their RMS values plotted against the spatial resolution of the finest scales in the simulations. There is a general trend towards improved results as the mesh refinement is increased. All variables should ideally decrease from right to left in this plot. Notably, the vertical or W velocity improves significantly, as does the Y RMS value. In some cases, a refinement results in a worse prediction, like the mass fraction (Y) and radial velocity (U) for the last two steps of refinement. These are generally small, perhaps reflective of the variable having reached a level above which further refinements are unlikely to resolve the data any better. While the direct variables don't always exhibit improvements with refinement, the RMS variables appear to improve significantly with the increased refinement. The Euclidian Norm is best with a value of zero. Prior experience with CFD comparisons with this metric suggests good comparisons are below 0.2 in magnitude, which is achieved for the W-velocity and the U- and W-velocity RMS variables for R8 and some of the other higher resolution meshes.

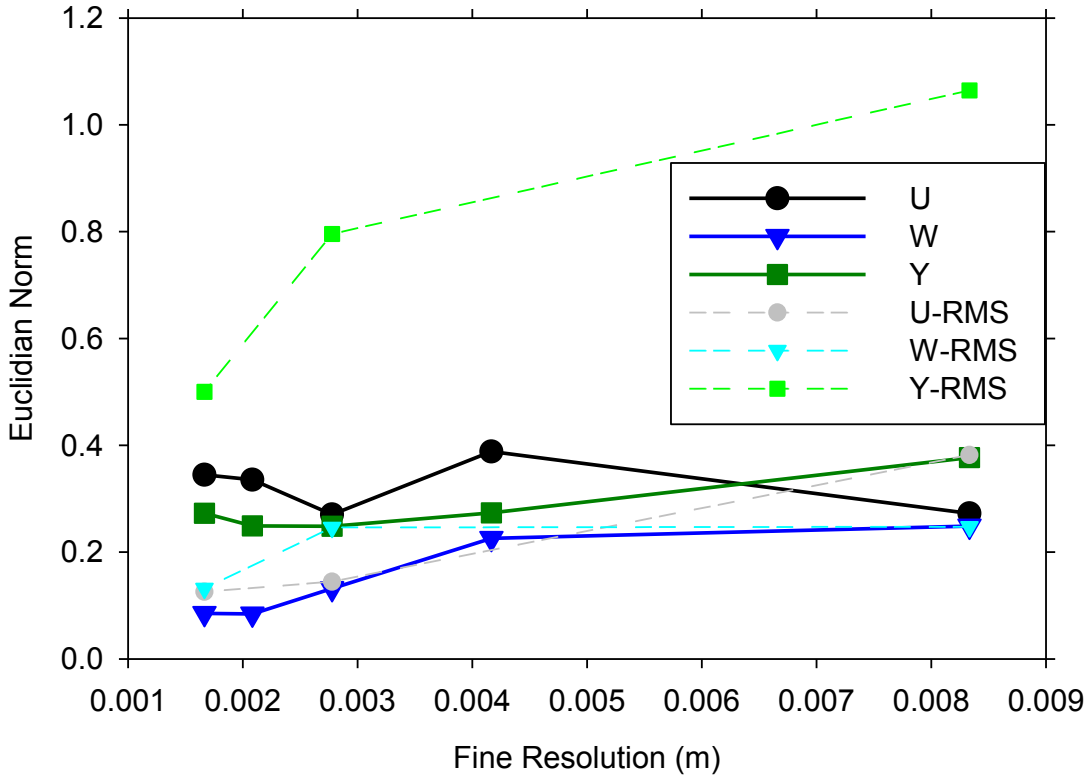

Figure 4-28. Euclidian norm for the comparisons as a function of resolution

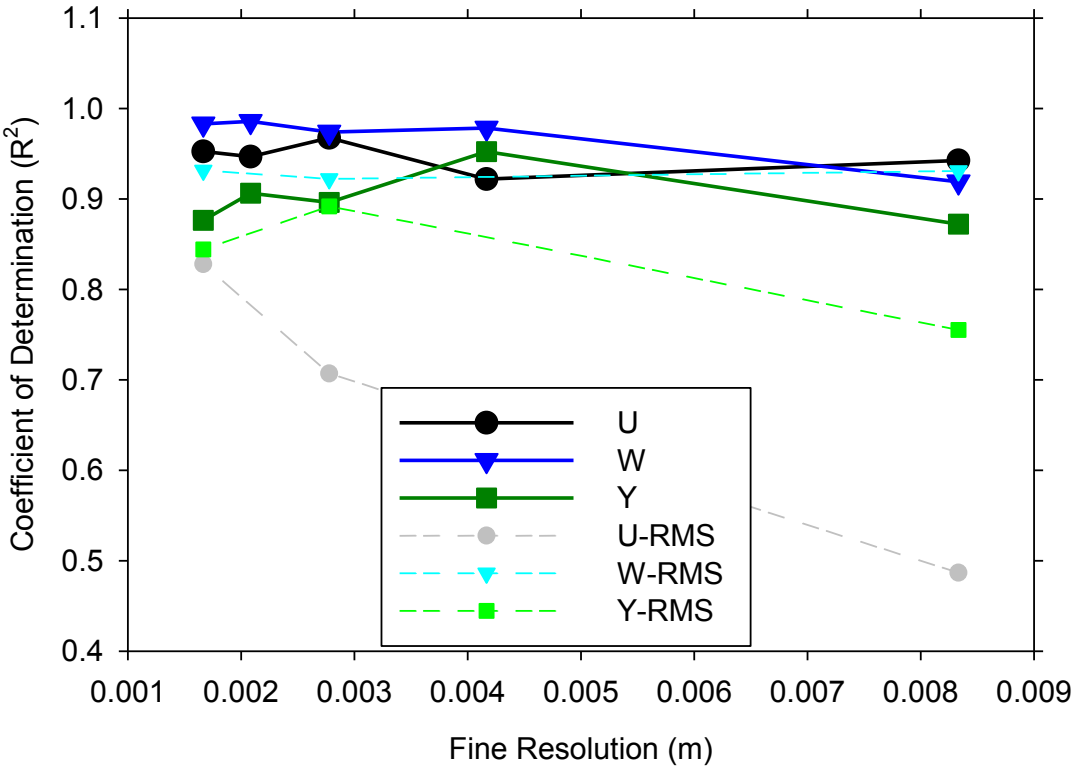

Figure 4-29. Coefficient of Determination (R^2) for the comparisons as a function of resolution

Figure 4-29 shows the coefficient of determination for the primary variables. This parameter has a maximum of 1.0, which is suggestive of a perfect fit. Good fits are in the 0.9 and above range, although prior experience suggests some secondary (gradient) and difficult parameters may be significantly below this value for scenarios with good visual similarity of planar contours. There is a general upward trend moving from right to left in this plot, suggesting improved convergence and improved comparisons with improved resolution. The primary variables do well, although the mass fraction appears to get worse with improved resolution after a point. The U-RMS variable (radial velocity) is particularly poor at the lowest resolution and improves significantly with increasing resolution. The W-RMS variable (vertical velocity) is about as good regardless of resolution. The W-velocity (vertical) comparisons for the highest two resolutions are excellent, approaching the ideal of 1.0.

The radial velocity component is generally much smaller than the vertical, and it seems to contribute greatly to the uncertainty in the system. Looking at the data from a vector angle and magnitude perspective suggests the velocity comparisons are actually quite good, as suggested by Figure 4-30. Transposed to magnitude, the R^2 values are all above 0.9, and converge towards 1.0. Three angle assumptions were used: A) a straight comparison for all data, B) comparing only where *experiment and simulation* were above *10%* of the maximum velocity, and C) comparing only where the *experimental* results were *8%* above the maximum. Assumption A suggests poor directional comparison, but after limiting the comparisons to where the velocity was reasonably high (B), the results significantly improve. The C assumption suggests a major increase in the correlation with improved mesh refinement. This suggests that the core of the plume is well predicted by all resolutions both in magnitude and direction. It also suggests that the improved resolution helps better resolve the details of the low average velocity regime to a point.

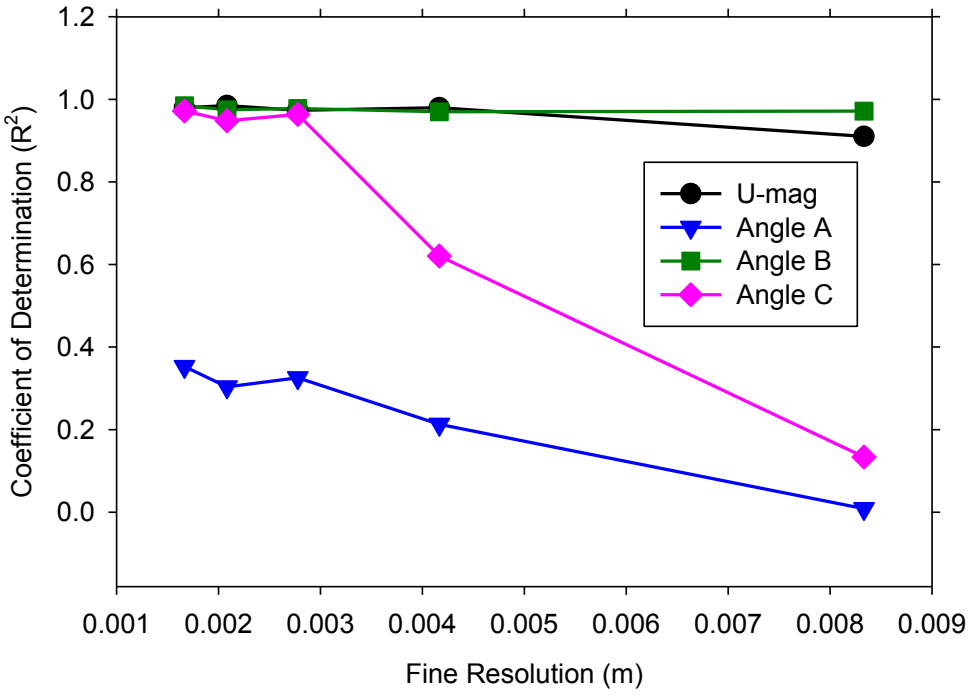

Figure 4-30. Coefficient of Determination for the velocity magnitude and angle comparisons as a function of resolution using three angle approximations

Data are ostensibly symmetric in this scenario, and the data consist of two sides of the centerline, which provides basis for making an estimate of the accuracy of the data. Using correlation, the data are folded back onto themselves, and an analysis is made. Table 4-2 shows how well the right and left sides are correlated based on the data, along with some coefficient of determination data from the prior analysis corresponding to results in Figure 4-29. If the correlation between the data left and right side is larger than that with the data, one can conclude that the simulations correlate to the data at least as well as the data accuracy permits. The plume mass fraction (Y He and Y He rms) falls clearly below the data accuracy level, but the velocity predictions are generally about the same as the data-to-data comparison, the U rms being the worst case in this regard. The simulation U data actually compare better to the data than it does to itself for all five refinements.

Table 4-2. Coefficient of determination (R^2) for five mesh results to the data and the data folded onto itself

	Data-Data	R4	R5	R6	R7	R8
Y He	0.974	0.872	0.952	0.896	0.906	0.876
Y He rms	0.934	0.755		0.892		0.844
U (m/s)	0.876	0.946	0.922	0.967	0.947	0.952
U rms (m/s)	0.935	0.487		0.707		0.828
W (m/s)	0.991	0.919	0.978	0.974	0.986	0.983
W rms (m/s)	0.968	0.931		0.922		0.931

4.3.3. Puffing Frequency

Figure 4-31 shows the W-velocity plotted versus time for the R6 mesh at a point above the pool. The puffing frequency is not obvious, as the peaks are not always clear. If the peak just after 55 seconds is taken as the start, and 18 peaks are assumed to 68 seconds, the puffing frequency is 1.38 Hz. This is reasonably consistent with the data as expressed in O'Hern et al. (2005).

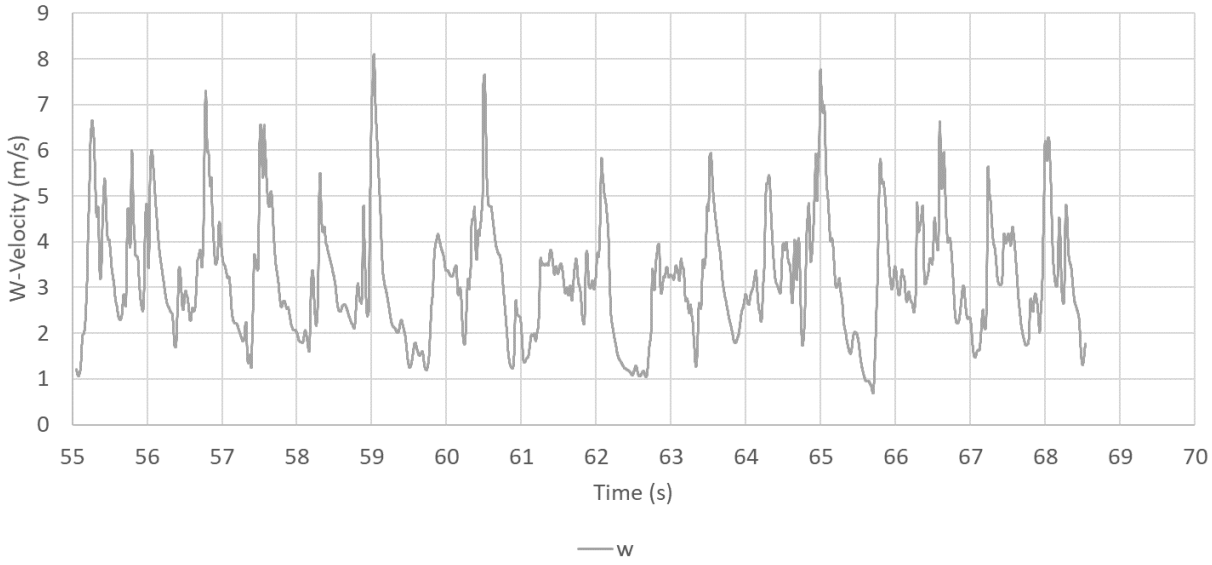

Figure 4-31. Point velocity extraction from which puffing frequency is estimated

4.4. Discussion

In this section the prediction sensitivity to the resolution and other factors is discussed in addition to addressing some challenges of making comparisons with large-scale measurements.

4.4.1. Inflow conditions

The inflow boundary condition required adjustments to achieve a representative field that matched the data. Here we explore the test set-up and ways to interpret the finding.

In Section 4.2.3 a simple model for the boundary condition corresponding to the plume-inflow diffuser was described. This boundary condition allows some degree of interaction of the plume with the porous diffuser. Results in Figure 4-4 show that the simulation results are sensitive to the porosity of the inflow region leading to the inlet porosity profile described in Figure 4-2. Here we analyze the experimental inflow characteristics, addressing the potential for pressure fluctuations that might be greater than the pressure drop across the diffuser and the possibility that molecular species diffusion in the diffuser might be a significant factor.

For the bulk inflow velocity of 0.325 m s^{-1} the flow through the honeycomb cells is laminar with a Reynolds number of approximately 10. We can estimate the pressure drop across the honeycomb using simpler laminar pipe flow relations, $C_f = 16/Re_d = \Delta P_{in} d/(2\rho W_0^2 L)$ where C_f is the coefficient of friction, Re_d is the Reynolds number based on the cell diameter, $d = 3$ mm, ΔP_{in} is the inlet pressure drop over the honeycomb length $L = 0.104$ m, $\rho_0 = 0.23$ kg m^{-3} is the source density and $W_0 = 0.325$ m s^{-1} is the bulk flow velocity. Using these values, we estimate the pressure drop across the honeycomb is 2 to 3 Pa. We can compare this to the approximate pressure change involved in slowing the radial entrainment flow to turn it upward. This can be estimated from Bernoulli's equation as $\Delta P_{rad} = \rho U_r^2/2$ where U_r is the mean radial inflow velocity. In Figure 4-3 the radial velocities peak around 0.7 m s^{-1}, and the pressure change in the radial direction is expected to be on the order of 0.07 Pa. Since this is more than an order of magnitude smaller than the estimated pressure drop across the honeycomb, we can estimate that the influences due to Bernoulli-equation changes in the pressure associated with velocity changes will be small. However, it is also true that local acceleration (associated with turbulent fluctuations) may be substantially greater than the pressure gradient associated with the mean acceleration.

To assess the importance of molecular diffusion in the diffuser, we consider the Peclet number. Upstream diffusion will be significant for length scales where the Peclet number, $Pe = W_0 z/D$, is of order unity. Here D is the molecular diffusivity that takes on values in the range of 10^{-5} to 10^{-4} m^2 s^{-1} for species in the plume. Setting $Pe = 1$ with the bulk velocity of 0.325 m s^{-1} the upstream diffusion distances are expected to be sub-millimeter scale even for helium.

These simple analyses suggest that neither upstream diffusion nor pressure fluctuations should have a significant effect on the flow dynamics at the plume source. However, the results in Figure 4-4 do indicate substantial sensitivity. Recirculation is noted in some of the predictions with different inflow conditions in Figure 4-4, and this changes as the inflow porosity changes. Recirculation arises from flow separation, which itself arises from the combination of shear stress and adverse pressure gradients, it is possible that the flow sensitivity arises by matching the appropriate shear stress over the plume source.

Other sources for the inlet discrepancy include the lack of completely planar surfaces surrounding the inlet, and the non-uniformity of the flow coming out of the diffuser. The pre-test flow characterization showed some variation in the flow across the diffuser (Blanchat, 2001). This was based on either manufacturing defects, or variations in the developed flow through the inlet. The diffuser and planar surface were not completely planar, as there were hex bolt heads and metal rings that rose above the base plane. The ring might have an effect much like the recession as modeled herein. The effects of the bolts and the non-uniformity of the inflow would need to be examined with additional explicit tests attempting to produce these effects on the simulation.

4.4.2. Prediction sensitivity to mesh resolution

The velocity and mass fraction measurement uncertainties are well-described in the journal article presenting the results (O'Hern et al. 2005). Uncertainties in the velocity means were reported to be ±20% and those for the fluctuations were ±30%. Uncertainties in the mass fraction means were estimated at ±18% plus some systematic offset of ±5%; those in the fluctuations were ±21%. These uncertainties are relatively large because of the challenges associated with these large-scale flows. The magnitude of these uncertainties can be compared with the Euclidean norms of the differences between measurements and predictions from Figure 4-28. Where the experimental uncertainties exceed the Euclidean norm differences, it might be reasonable to ascribe agreement between the predictions and measurements. However, a more careful comparison of the profiles as discussed here can provide insight into the prediction trends relative to experimental trends.

In general, referring to Figure 4-28 and Figure 4-29, the Euclidian norm and the coefficient of determination for the vertical mean velocity, W, are close enough to their optimal values that we can ascribe good agreement to this quantity for most resolutions, though there is a trend to improve predictions from mesh R5 to R6 and R7. For the vertical velocity profile, it is important to correctly predict both the magnitude of the velocities and the spreading of the plume since the plume spreading is indicative of mass entrainment while the velocity magnitude indicates buoyant acceleration. Considering the profiles in Figure 4-10 through Figure 4-12, visual agreement is good for meshes R6, R7 and R8, especially for the 0.4 m and 0.6 m heights. At the lowest height there are small deviations that reflect the challenges in modeling the development of turbulence at the plume base.

The vertical mass flux associated with buoyant plumes, i.e. $\int_0^\infty \pi\rho W r dr,$ increases with height. The radial velocity component, U, is important for describing the mean entrainment of the surroundings into the plume that is responsible for this increased mass flux. U-velocity profiles in Figure 4-13 through Figure 4-15 appear to have visibly greater differences between the predictions and measurements. However, the U-velocity magnitudes here are almost one order of magnitude smaller so that the absolute differences, on the order of 0.1 m s^{-1} for each of these figures, may be comparable. Of greater concern is the significant differences in the profile shape for the higher heights at 0.4 and 0.6 m and the fact that these differences are enhanced with increasing resolution. It is not clear whether the profile shape differences reflect experimental variability or prediction errors, through there is more right-left asymmetry in these measurements compared to other measurement sources (c.f. Table 4-2). The coefficient of determination comparisons suggest good agreement here while the Euclidean norm is generally greater than 0.3, which is larger than expected with the experimental uncertainties of 20%. This larger value for the Euclidian norm might reflect the similar differences (0.1 m s^{-1} for each component mentioned above) normalized by the relatively small magnitude of the entrainment velocities. Also the analysis of the coefficient of determination

in terms of the velocity magnitude and angle from Figure 4-30 suggests that small differences associated with the components of lower velocity samples significantly influence the comparisons.

The final mean quantity that was measured is the mean plume mass fraction, Y. As noted above in conjunction with Figure 4-16 through Figure 4-18, there is a systematic shift from underpredicting the near-center mass fractions at low heights to overpredicting the near-center mass fractions at higher heights, and this shift is amplified as the mesh resolution increases. This occurs despite the radial inflow velocities tending to predict greater values than measured, which would suggest the opposite behavior. It is expected that the integral vertical flux of the plume source, $\int_0^\infty \pi\rho WYrdr = \pi\rho_0 W_0 D^2/4$, should be conserved, and presumably species/mass conservation within the simulation forces the predictions to maintain a constant vertical flux. One item worth noting is that at the 0.6 m height the measurements suggest that the plume could have spread beyond the measured radii, and this could easily make up for the measured differences. The global measures of prediction accuracy in the Euclidean norm and the coefficient of determination have moderate values for Y, but interestingly the highest resolutions move slightly away from the optimal values. The centerline offset might be ascribed to errors in diffusion or the advective field. The advective field is well predicted and the diffusion is not thought to be so significantly erroneous. It is possible that the use of a mixture fraction to describe the plume gas is culprit. This assumption involves assuming the helium and the acetone (used to generate the experimental signal) were of equal proportion in the inlet and through the lower plume. The degree to which this is not the case may contribute to the centerline errors.

The velocity fluctuations provide the large-scale mixing between the plume and the surrounding. Velocity fluctuations drive the transfer of energy from buoyant vertical acceleration to more random turbulent motions that ultimately lead to viscous and diffusive transport. Because the flow energy is added in the vertical direction, the vertical fluctuation magnitudes are largest, but large coherent vortices are responsible for puffing that transfers the energy between the vertical and horizontal components. The predictions show a trend toward greater transfer of this energy from vertical to horizontal with increasing mesh resolution. This might arise from a greater dynamic range of eddies associated with the transfer. The initial coherent structures need to break down through the turbulent cascade to approach a more isotropic turbulent state. The flow here does not reach a point where velocity fluctuations are isotropic, and this is a part of the reason that large-eddy simulations perform significantly better for buoyant plumes than Reynolds-averaged simulations (which weren't the subject of this study). The Reynolds-averaged Navier-Stokes simulations are generally implemented with an assumption of isotropic velocity fluctuations, at least when solving for a single turbulent kinetic energy instead of the full Reynolds stress tensor. All comparison metrics suggest the velocity fluctuations are better predicted with higher mesh resolution.

The mass-fraction fluctuations presented in Figure 4-25 through Figure 4-27 show the predictions as having uniformly greater fluctuations than the measurements with a magnitude that exceeds the expected measurement uncertainties. Scalar fluctuations like this are relevant to the overall scalar transport through terms that (in RANS) would be of the form $\overline{U'Y'}$. While the correlation is a part of this quantity, overpredictions of the scalar fluctuations would be expected to lead to predictions of faster plume spreading in terms of the scalar profiles in Figure 4-16 through Figure 4-18. Faster spreading of the mean mass fraction is not generally observed in these figures, so that it is difficult to interpret the significance of the overprediction shown in the fluctuations. Scalar fluctuations in fires can be important measures of unmixedness, suggesting slower fuel-air mixing. If this is an issue it might be reflected in higher flame heights as fuel pockets mix with air more gradually in predictions. This can be assessed in separate flame height comparisons. For fires in enclosures,

flame height can be less of an issue, but the mixing of the plume with its surroundings is an important factor in assessing hazards associated with hydrogen releases.

4.4.3. Recommendations

While largely successful, this exercise comparing simulations to data is not without challenges. The data do not suggest a perfect comparison, and there are a number of ways this might be improved.

Already noted, the modeling effort could include an improved approach to propagation of the inlet uncertainties. The inlet was assumed to be uniform, while facility characterization tests provide a more variable indication of the true uniformity of the inlets. Irregularities at the surface may also play a role in the non-ideal nature of the plume and how this propagates to the experimental results.

The comparisons herein neglected the uncertainty in the experimental results, which were expressed by the test reports and as indicated above. The simulations have a nominal uncertainty as well, which could be expressed by applying a range of inlet or model parameter uncertainties and propagating them through the model. A joint statistical analysis would provide a better picture of the accuracy of the assessment. The methods for making a comparison of this nature are more commonly deployed on point or line data. These data were nominally planar, which presents a methods challenge. The velocity comparisons were understandably poor when mean velocities neared zero, which is possibly more a reflection of the inadequacy of the comparison technique than an inadequacy of the model. Where mean velocities approach zero, the direction becomes meaningless, and the direct comparisons of the relative magnitudes of the vector components are similarly unrevealing. Comparison methods need to take these into account, which does not have a straightforward solution.

Examining the data versus the model using the multiple techniques was insightful and should be considered for future comparisons of this nature. The correlation analysis and the Euclidian Norm method both gave similar indications for many of the comparisons but revealed different magnitudes of error depending on the quantity being evaluated. The RMS comparisons exhibited this strongly. The use of a magnitude/direction versus a Cartesian component expression of the velocity helped illustrate different sensitivity factors as well. The vector magnitudes were well predicted, and where these were sufficiently high with adequate resolution the directions were also well resolved.

The mass fraction predictions appear to skew at the centerline, possibly an indication of lack of mode fidelity. A potential source of this might be the mixture fraction employed, which did not allow for differential diffusion of the acetone and the helium. This effect might be further studied.

Application work is largely unable to evaluate as wide of a range of mesh sensitivities as were tested here. Depending on accuracy requirements, a plume would need to involve sufficient resolution across the diameter (≈80 elements) to resolve the dynamics. While predictions of the coarsest R4 mesh were generally poorer than refined simulations, the basic dynamics were reasonably well predicted. The RMS predictions were less reliable than the primary velocity and concentration magnitude variables.

4.5. Conclusions

The bulk vertical motion and spreading of the plume is predicted reasonably well to within the measurement uncertainties and with variation with mesh resolution for all but the coarsest of the mesh resolutions. This is observed especially for heights of 0.4 m and greater (relative to the 1 m plume source). At the lowest measured height, the predictions are more challenging because the

initial buoyant turbulence development must occur at small scales with a move toward larger scales coming from buoyant acceleration and nonlinear interactions.

The predictions improve to a maximum for the three most refined meshes, suggesting that plume resolutions with more than 75 elements across the plume source (pool diameter) provide good mixing predictions, while those simulations with roughly 50 elements across the source will provide reasonable bulk flow predictions for some purposes. Accurate predictions of more sophisticated quantities like the fluctuations will require the more refined meshes, but the results here show how the mesh density can vary to address the prediction needs. Indications are that further improvements are unlikely for additional refinement in part because there is an accuracy threshold to the data beyond which improved simulation resolution will not benefit the comparison.

Velocity fluctuations initially develop in the vertical direction because of buoyant forcing, and the turbulent mixing, including the large-scale coherent vortices, which redistribute these fluctuations to other components like the radial velocity fluctuations studied here. As the resolution is improved the energy transfer from the vertical to the radial velocity components increases, suggesting that having a greater range of scales facilitates this redistribution of the turbulent kinetic energy toward more isotropic flows. However, the flows do not approach isotropic turbulence in the region studied. The strongly anisotropic nature of the velocity fluctuations points to the value of going to a more sophisticated LES approach than a single turbulent kinetic energy with RANS assuming isotropic turbulence.

Predictions of both the radial inflow and the mean mass fractions did not always follow the measurements to within expected uncertainties. A careful analysis of the velocities suggests that magnitude predictions are reasonably good, but the angular alignment of velocity vectors is challenging in the regions where the velocity magnitudes are smallest.

It was also found that a model for the inlet diffuser flow that includes some porosity measurably affects the flow near the base of the plume. The behavior for a range of inlet diffuser parameters suggests that this affects the development of turbulent shear stresses in the near-plume-source region. When the inflow region can develop the right initial turbulent-mixing characteristics, the overall performance improves.

The overall results suggest that bulk behavior can be addressed at moderate resolutions using large-eddy simulations, though the required resolution will depend on the required fidelity, particularly in the near-source regions of the flow. Predictions of quantities beyond the bulk plume rise and spread require greater resolution.

This page left blank

5. ISO9705 FIRE SIMULATIONS

This section details results from a series of standard fire computations. This work was initially presented at the 12th US National Combustion Institute Meeting, and a paper was produced for this meeting (Brown et al., 2021). The results in this section will differ from the report to that conference in several ways. While the original simulation matrix was mostly completed for the conference report, after the results were finalized for the report there were a number of follow-up simulation activities that add to the results. These include:

1. The 'fine' simulation had not completed in time to make the final draft of the original report. The case was subsequently completed, and these results are included here.
2. Plotting of tabulated results would not fit within the paper length requirements for the original manuscript, the addition of which greatly augments the ability of the manuscript to highlight key trends in the results.
3. A number of follow-on quantifications and simulations have been proposed based on evaluation of the results from the initial matrix. The matrix is expanded to include an iteration on the parameter study based on evaluation of the results from the initial matrix. These are also included.
4. Some analysis of the results is added.

This Chapter provides an expanded result from the original simulation campaign.

5.1. Introduction

Of the isotopes of hydrogen, the most common, protium (^{1}H), is by far the most well studied for fire hazards. Because it is a useful and common gas, it is regularly bottled and sold. There are considerations for a hydrogen energy economy, which postulates hydrogen distribution much like natural gas or gasoline. Primary fire hazards are moderately different from many of the more typical hydrocarbon fuels, as hydrogen fires can be invisible to the eye yet just as intense in terms of gas temperatures. Hydrogen leaks can also result in explosive conditions when mixed with air (e.g. Rigas and Amyotte 2012, Najjar 2013).

Less common isotopes are deuterium (^{2}H, or D) and tritium (^{3}H, or T). Deuterium gas (D_2) is also bottled and sold, although not nearly on the same scale as protium. It has special applications in science, and can act as a chemical tracer, or be used to make materials with slightly varying properties to those composed of protium. Deuterium is twice as dense and has a moderately different reactivity. Little is found on deuterium safety, as it is generally considered similar enough to protium to not warrant any special additional considerations. Tritium, on the other hand, is a synthesized isotope that is not produced in large quantities. It has commercial application for self-powered lighting, can be used as a tracer, and has research applications for nuclear physics. As the only radioactive isotope of hydrogen, it is not regularly bottled and sold, and it is stored at special handling facilities, typically at much lower pressures and quantities compared to protium. It naturally decays, with a radioactive half-life of around 12 years. Tritium emits low energy β radiation (5.7 keV), which does not penetrate the skin. The greatest health risks therefore arise from tritium entering the body by absorption through the skin and inhalation. The hazard from inhalation of the diatomic gas (TH or T_2) form is relatively low compared to that of the oxidized form (T_2O or HTO) or otherwise reacted states (Mishima and Steel, 2002).

Despite the chemical similarity of isotopes, the differences in handling and storage make for completely different concerns between protium (H_2) and tritium (T_2) safety. T_2 quantities are often too low to merit serious consideration of the explosive potential, and low-pressure storage makes sustained, jetting flames improbable in many cases. A tritium release without a fire involves reduced risk; it is the combination of the two that is the highest risk because of the increased hazard associated with the oxidized form. In a worst-case scenario, one must have an external source of fuel for the fire or heat, except possibly in the manufacturing and synthesis facilities with the highest T_2 inventories where the quantities are sufficiently high to warrant consideration of flaming hydrogen.

The US Department of Energy (DOE) maintains safety documents for addressing facility safety concerns and prescribing assumptions for design basis work and defining hazards. DOE Handbook 3010 (2013), which is currently under revision, defines airborne release fractions (ARFs) and respirable fraction (RFs) for various radionuclides in a range of accident scenarios following a formula based mostly on particulate hazards. The product of ARF and RF is proportional to the radiological hazard. For tritium gas, the RF is 1.0, since all gas may be readily inhaled into the lungs. Unlike radioactive particle releases, the hazard with a tritium gas release is mostly determined by the fraction of gas that is released in the more hazardous oxidized form. The dynamics leading to this state are not particularly well addressed in the historical literature on tritium safety.

Radiological facilities that handle higher quantities of tritium can incur enormous increases in expense for operations if they are deemed to fall within a higher hazard category. Thus, it is important to improve the accuracy of prediction assessments and safety categorization to minimize unnecessary safety related costs while maintaining adequate safety.

The scarcity of tritium, the radiological hazards posed by tritium combustion products, and the costs of performing fire experiments with a radioactive material all contribute to a historical lack of data on tritium behavior in fires. This is an application area ideal for computational models, which when appropriately designed can provide the basis for safety in lieu of dangerous or unfeasible tests. Evidence from computational tools need to meet a high standard of accuracy and expected validity to be deemed decisional.

In this work we present a computational study surrounding a standard fire scenario including a representative release of tritium gas. The epistemic proof of validity for the calculations is a work in progress, with some of the evidence being exhibited in Chapter 3 and 4. Some input parameter uncertainties are dealt with through a parameter sensitivity evaluation. Other sources of potential uncertainty and error are quantified. The scenario shown here mimics an ISO-9705 test, a fire standard test relevant to a laboratory room developed by the International Organization for Standardization (ISO), and includes in addition the release of tritium away from the fire during the burn. The premise behind this arrangement of the test is to illustrate how a representative release of tritium *not* engulfed in a fire may exhibit a substantially lower oxidation conversion than the conservative safety assumption of 100% (typically considered due to a lack of data suggesting lower conversion fractions). The scenario is designed to illustrate how a dispersed tritium inventory under released conditions might result in significantly lower hazards than a concentrated release in a fire and how modeling parameters with varying levels of uncertainty affect the results.

5.2. Methods

Numerous challenges are present simulating tritium fires. First, a comprehensive set of data on the physical parameters for the reactant and product species is lacking. Deuterium properties may be

found in standard references, but less so for tritium. We have had to deduce what we could not find; this effort is the topic of Chapter 3. Second, there are few datasets for isotope fires with which to validate any modeling. There are numerous protium fire studies, but little on deuterium and nearly nothing on tritium. This is a gap currently being addressed with some tests at Sandia, which are subsequently described in Chapter 6. Leveraging the isotope trends may be the best way to assess tritium behavior, as data from protium and deuterium tests should be much more attainable. Third, it is difficult to postulate an accident scenario that is consistent with operations and handling since there are no known fire/tritium accidents at SNL or SRNL from which to deduce probable risk conditions. Hence, we elect to rely upon adaptation of a standard test not developed specifically to evaluate T_2 safety to be a representative hazard. The trace release of hydrogen isotope is considered the 'contaminant' in the remainder of this study, being distinctive from the hydrogen naturally occurring in a fire.

5.2.1. SIERRA/Fuego Simulations

SIERRA/Fuego (2019a, 2019b) is a low-Mach number code for simulating objects in fires and is extended to support a variety of problems of interest to Sandia and affiliates who use the code. A major differentiating factor is that the code is a control volume finite element mechanics (CVFEM) code rather than a more traditional control volume code. A variety of mesh elements are available to the unstructured solver; however, the mesh in this case is hexahedral and regular, which would be suited to a structured code solver as well. Fuego is massively parallel, and the resolved scale for simulations typically is in the 1-100 cm range. A variety of turbulence and reaction models exist, with this work electing to represent the fire with the Eddy Dissipation Concept (EDC) model for fluid (gas)-phase reactions (Magnussen and Hjertager 1977, Magnussen 1981) and the Temporally Filtered Navier-Stokes (TFNS) (Tieszen et al. 2005) model (a hybrid LES/RANS capability) for turbulence. The EDC model permits a single fuel. This effort simulates the fire with a methane gas release. Due to this limitation, the reaction of tritium to oxide is solved separately through a 1-step mechanism that is external to the EDC model. For protium, a separate species conservation equation for hydrogen is tracked to distinguish H_2 formed as part of the EDC model from that involved in the release.

Participating media radiation energy transport is simulated using Nalu coupling (SIERRA/Fuego 2019b), which mostly involves a heat loss from the fire to the surroundings. Nalu uses a Discrete Ordinates solver to solve the radiative transfer equation. Participating species include soot, CO_2, and H_2O using a gray approximation. The radiation contribution of released vapors is neglected and believed to be small due to the low concentrations. The walls and ceiling are simulated with a 1D conduction model and thermal properties consistent with the ISO standard (600 kg/m^3 density, 20 mm thick). Walls become heated over the duration of the burn, and provide thermal feedback.

All cases were run with version 4.56.4 of the SIERRA/Fuego code. Designed under the governance of DOE order O 414.1D, version control, nightly testing, and verification are inherent in the code design and maintenance practices that lend to the credibility of the results.

Validation involves benchmarking the solutions to datasets, which help establish the accuracy of the modeling. A campaign to validate the code resulted in numerous component validation results beginning approximately 20 years ago. More recent and relevant validation efforts include a comparison to a dispersion in an urban geometry (Brown et al. 2019, Brown et al 2020), and a comparison to a buoyant plume of He gas (Brown et al. 2018, see also Chapter 4). A validation test campaign specifically to test the accuracy of the simulations for hydrogen isotope oxidation modeling is underway involving flows of H_2 and D_2 through a heated tubular reactor. When

comparisons of the isotope behavior are complete this dataset may provide improved validation more directly relating to the cases under present consideration.

5.2.2. Simulation Properties

A global kinetic model for reaction of hydrogen is found in Marinov et al (1995), which provides a simple basis for a reaction scheme for hydrogen and oxygen to become water (H_2+1/2O_2->H_2O). The equation for the reaction mechanism is:

$$r_{global} = Aexp\left(-\frac{E}{RT}\right)[H_2]^{n_H}[O_2]^{n_O}$$

The rate constants are A=1.8x10^{13} $cm^{1.5}/mol^{0.5}/s$ and E/R = -17614 K with the concentrations in mol/cm^3. We infer units from an evaluation of the model and knowledge of the autoignition temperature being about 500 ºC. We have adapted the model for mol/m^3 as required by Fuego with new constants of A=1.77x10^{10} $m^{1.5}/mol^{0.5}/s$ and E/R = -17600 K, verifying these constants yield appropriately equivalent reaction rates to the original model in the original unit set. This mechanism is assumed for all isotopes. This was selected because it is a simple global mechanism. Other H_2 kinetic models exist, and were also considered, including for example, Fernandez-Galisteo et al., (2009), Konnov (2008, 2019), Li et al. (2004), Marinov et al. (1996), Miller and Kee (1997), Mueller et al (1999), Rogers and Chinitz (1983), Sekar and Mukunda (1990), Vargas et al (2015), and Westbrook and Dryer (1981).

It is normally not advisable to simulate fire scenarios with direct kinetic mechanisms such as this because flames are typically ~1 mm in scale and the resolution required to resolve this is not generally available for fire problems of practical interest. Besides the resolution problem, stiff reactions can also be challenging to solve with accuracy. The EDC model is designed to produce approximations to fires in under-resolved scenarios and is a mixing-limited approximation. The use of the global 1-step mechanism is thought to be reasonable for the contaminant reactions in this circumstance because:

1. The reactions are not expected to occur under flaming environments with the low-concentration leaked hydrogen as the primary fuel source
2. The reactions are very non-linear with temperature, and cell average temperatures provided by the EDC model are probably adequate to capture the bulk reaction behavior
3. There is a degree to which the reactions will be advection and/or diffusion controlled, this being the case the mechanism can be approximate and may still yield acceptable results

The previously described validation effort underway is expected to help qualify the accuracy of our methods and the validity of these assumptions. Because the fire is intended only as a heat source, simulating it with the EDC model is an acceptable approximation for a fire condition as it affects the reaction of the contaminant release of hydrogen. The EDC fuel is CH_4, and the inflow is selected to give a heat release rate for the reaction as specified in the ISO-9705 standard.

5.2.3. The ISO 9705 Scenario

Some descriptions of the ISO 9705 (2016) scenario have been detailed earlier. This standard prescribes a 3.6-m by 2.4-m room 2.4 m high with a doorway of 2.0 m height and 0.8 m length centered along one of the 2.4 m walls. A 170 mm square gas burner surface is prescribed, and this dimension is also used to locate a methane injection on the ground in the corner furthest from the doorway of the domain. The other corner is where the contaminant is released from a similarly

dimensioned boundary condition (see Figure 5-1 and Figure 5-2 for illustrations). The release was assumed 0.1 g over 6 seconds at a constant rate. The release is not part of the standard. The standard fire is prescribed as 100 kW, with the potential for increasing the output to 300 kW at 10 minutes and continuing the test for an additional 10 minutes.

To model the fire, an extended flow region outside the doorway is added to allow for natural ventilation conditions that would be more representative of the ISO-9705 tests. An open boundary is applied to the periphery of this extension of the domain. During tests, the door provides an escape path for hot products towards the top, and an inflow of fresh air towards the bottom as is naturally developing under these conditions. It simulates a scenario involving an open door to the lab space that is on fire.

5.2.4. Safety Scenarios

A parameter study is the context used in this paper for assessing potential variations in either variables with uncertainty, or model configuration parameters. This study took place in two main phases, with the first phase comprising cases 1-16, and the second phase being planned after analysis of the results from the first phase.

For phase 1, we selected a few variables of interest to vary so that we could begin to capture the sensitivity of the contaminant conversion. Two model parameters were varied that were suspected of having high uncertainty and at least moderate effect on the outcome of the simulations. The Schmidt number is used to assign the diffusivity based on the viscosity. This is common practice in this type of simulations. The Schmidt number (defined as the kinematic viscosity divided by the diffusivity) is normally 0.7-0.9 for air scenarios, but a wider range (as low as 0.2) is appropriate for hydrogen and/or helium scenarios (see Section 3.3.1). The kinetic mechanism used herein was previously introduced. This is a global 1-step mechanism for protium in air at 1 atm. We anticipate deuterium and tritium reactions to be slower. As far as physical parameters, the release location of the contaminant gas is considered a variable, and is adjusted along the same distance from the back wall, but to intervals approximately 75%, 50%, and 25% of the distance separation from the fire in the nominal case. Table 5-1 provides details of the scenarios illustrated in this report. The cases are designated by a number, and a code that helps easily identify the mesh, fire output power, and hydrogen isotope affiliated with the case as well as the other variations.

For phase 2, the release position was moved, the nominal fire size was varied in smaller increments, and the effects of an assumed HVAC system were captured. The new kinetic rates that are expected to be improved based on recent data derived in Chapter 6 are also assessed for a single scenario.

Table 5-1. The initial simulation matrix

Case	Mesh	Power	Contaminant	Other Variables
1-C3T	Coarse	300 kW	T_2	
2-M3T	Medium	300 kW	T_2	
3-F3T	Fine	300 kW	T_2	
4-M3D	Medium	300 kW	D_2	
5-M3H	Medium	300 kW	H_2	
6-M3TA1	Medium	300 kW	T_2	Kinetic pre-exponential (A) parameter reduced by a factor of 10
7-M3TA2	Medium	300 kW	T_2	Kinetic pre-exponential (A) parameter reduced by a factor of 3.16
8-M1H	Medium	100 kW	H_2	
9-M1D	Medium	100 kW	D_2	
10-M1T	Medium	100 kW	T_2	
11-M1DS1	Medium	100 kW	D_2	Schmidt number reduced from 0.7 to 0.475
12-M1DS2	Medium	100 kW	D_2	Schmidt number reduced from 0.7 to 0.2
13-M3T25	Medium	300 kW	T_2	Release inlet 25% of nominal distance from fire
14-M3T50	Medium	300 kW	T_2	Release inlet 50% of nominal distance from fire
15-M3T75	Medium	300 kW	T_2	Release inlet 75% of nominal distance from fire
16-M2T	Medium	200 kW	T_2	
17-M1.5T	Medium	150 kW	T_2	
18-M2.5T	Medium	250 kW	T_2	
19-M3T22.5	Medium	300 kW	T_2	Contaminant release position rotated 22.5º about fire
20-M3T45	Medium	300 kW	T_2	Contaminant release position rotated 45º about fire
21-M3T67.5	Medium	300 kW	T_2	Contaminant release position rotated 67.5º about fire
22-M3T90	Medium	300 kW	T_2	Contaminant release position rotated 90º about fire
23-M3T90I	Medium	300 kW	T_2	Case 22 with fire and plume source switched
24-M3THV	Medium	300 kW	T_2	Assumes HVAC flow
25-M4T	Medium	400 kW	T_2	
26-M3.5T	Medium	350 kW	T_2	
27-M5T	Medium	500 kW	T_2	
28-M3TK	Medium	300 kW	T_2	Kinetics based on tests

The original motivation behind the variations in the reaction power for the fire varying from 100-300 kW is based on the ISO-9705 standard. These are the two fire intensities prescribed in the

standard test parameters. The nominal heat release rate is 100 kW, which is prescribed in the standard for the first 10 minutes of the burn. This study evaluates 300 kW (a potential increase in the standard tests) since initial results with 100 kW exhibited negligible conversion. Using 300 kW yields more significant conversion of the hydrogen. It helps magnify the scenario differences compared to the 100-kW assumption. This increase may not make sense for the scenario at hand, as laboratories tend to include sprinklers that would severely reduce the probability of and inhibit the growth of the fire to this magnitude. It is therefore considered a conservative approximation made for convenience of reporting the dynamics of the results, and not a reasonable representation of a standard or expected fire. The original matrix included three power settings, but the results were non-monotonic, so in subsequent tests the power was varied increasingly to better capture the magnitude and trends of this effect.

Some of the scenarios involved variation in the location of the fire and the release. Figure 5-1 illustrates graphically from a top-down view how these varied by case.

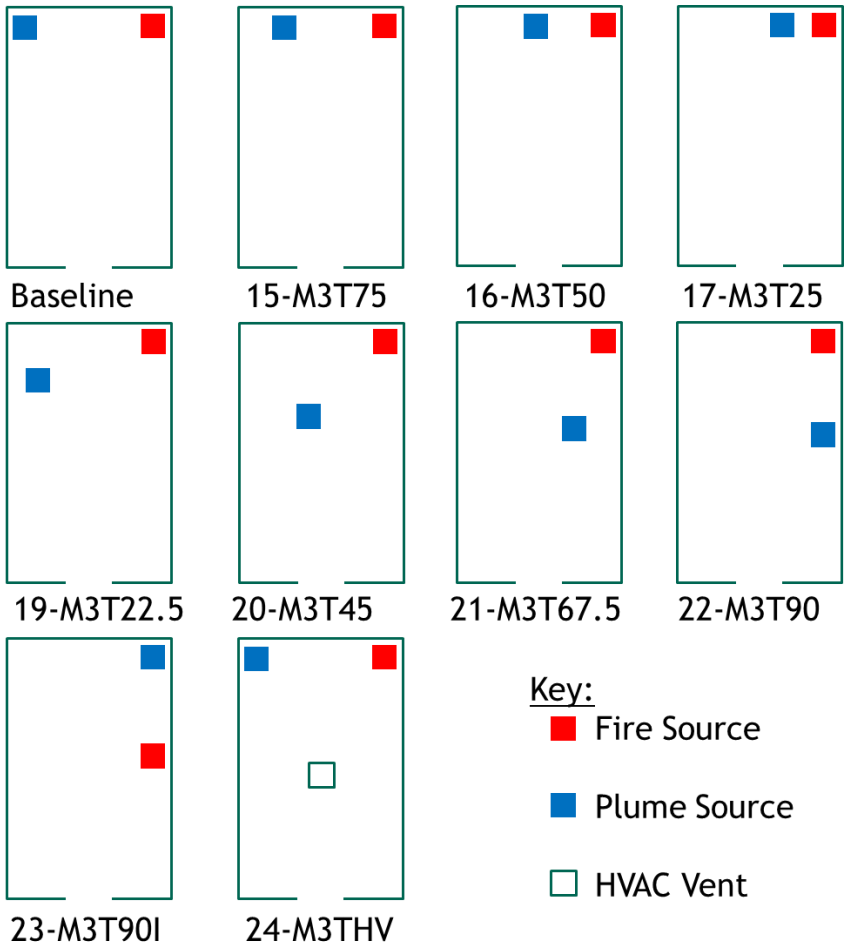

Figure 5-1. An illustration of the positional variations of the plume and fire sources

The idea behind simulating the various isotopes in release is to help understand what effect the variation in the properties of the isotope have on the predicted result (Cases 2, 4, 5, 8, 9, and 10). If there are negligible differences, one might in the future consider H_2 as an appropriate surrogate for

T_2 safety experimental studies. Properties changed for the different isotopes in the model include viscosity (and diffusivity via the Schmidt number), density (buoyancy), and specific heat. The mesh variations (Cases 1, 2, and 3) are to demonstrate the effect of mesh convergence on the answer to help justify using the medium results as a representative result. The kinetic mechanism is only characterized as accurate for protium, so the reaction rate was reduced by a factor of 10 to see if this has a significant role in the results with a step in-between (on a log scale) to assess linearity (Cases 6 and 7). Later after data indicated an even slower reaction rate, Case 28 was added to assess this effect. In a similar vein, the Schmidt number was varied to see how much of an effect it has on the resultant predictions (Cases 11 and 12). We postulate that in the future we might have narrower bounds for varying these parameters, as we are working to reduce the uncertainty in the parameters through validation and model characterization efforts.

The release inlet was in the opposite corner of the fire nominally. In a series of parameter variations, the location of the release was altered to be closer to the fire to assess the functionality of this relationship (Cases 13, 14, and 15).

The coarse mesh had a nominal 8.5 cm spacing. The medium and fine meshes had 4.2 cm and 2.5 cm spacing, respectively. The mesh spacing was predominantly uniform, with the most significant variation from uniform being the locations near the fire and injection sources due to spacing requirements to accommodate the geometry. A cut-away wireframe image of the coarse mesh is seen in Figure 5-2 with the cut through the doorway. Biasing is used away from the door to improve simulation turn-around. The fire release boundary condition is red, and the contaminant release is blue. The timestep was fixed and kept the Courant number below 1.0.

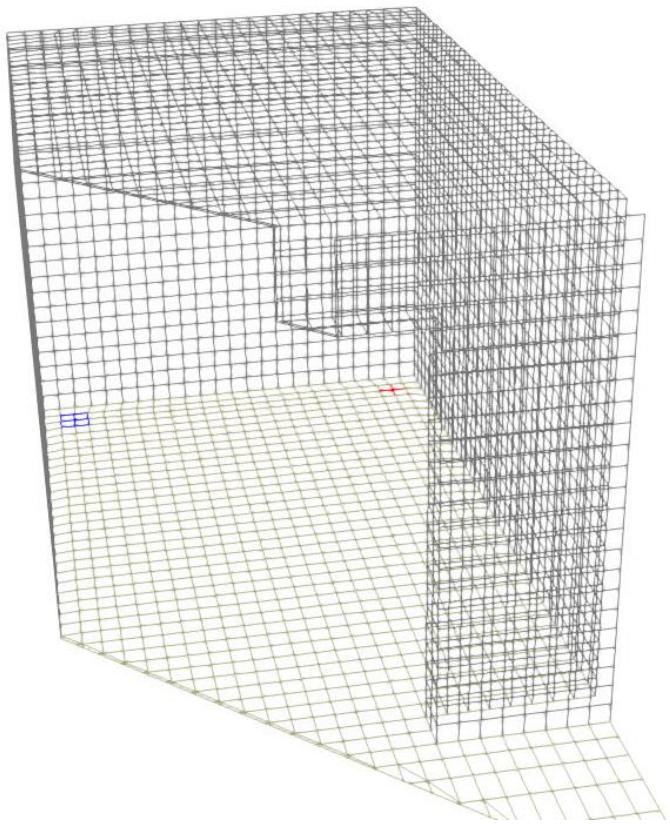

Figure 5-2. An illustration of the coarse mesh

5.3. Results

Typical time-series simulation results are shown here for the M3T case, which will be considered a nominal baseline case relative to most of the variants defined in the simulation matrix. In Figure 5-3 the normalized integrated volume fraction of T_2 and T_2O in the computational domain are plotted as a function of time. The cumulative out-flux of the same two variables is also shown, which comes from a time and space integration of the flux of contaminant. The injection from 10-16 seconds is followed by a dispersion period where the contaminant is relatively unchanged in concentration. It then begins to decrease by a combination of out-flow and conversion to T_2O. Outflow begins around 50 seconds and proceeds the fastest out to about 120 seconds. Figure 5-4 shows the cumulative T_2 and T_2O volume fraction, as well as their sum illustrating the slightly less than perfect mass balance closure due to the out-flux integration methods.

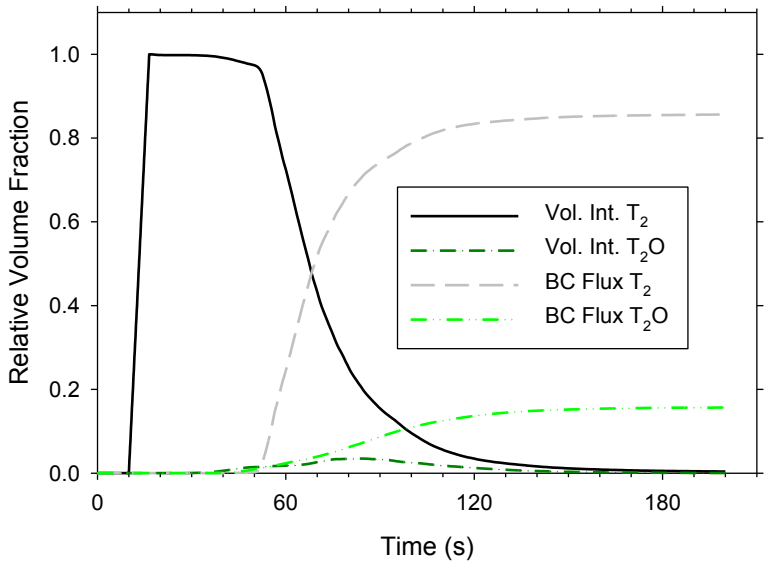

Figure 5-3. Relative volume fraction versus time for the baseline case 2-M3T

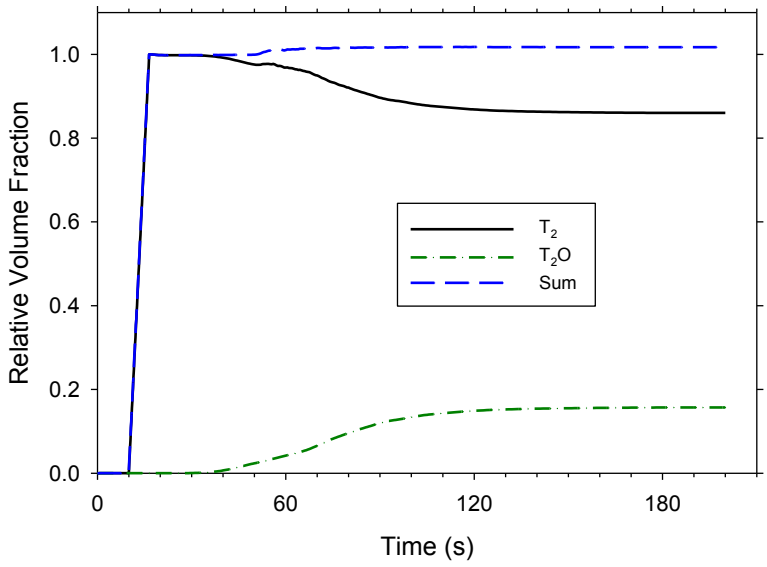

Figure 5-4. Total relative volume fraction versus time for case 2-M3T

Results are categorized by several variables. The maximum T_2O mole fraction divided by the maximum T_2 mole fraction gives an estimate of the maximum exposure in the simulation domain and is termed here C1. The time at which this maximum occurs, T1, is an indication of reactivity and the rate at which reactions are progressing. The total maximum conversion is estimated from the integration of the T_2O contaminant in the system added to an estimate of the flux out of the domain at time T2 seconds (the end of the simulation) divided similarly by the total injected T_2, and this parameter is denoted as C2. This is more reflective of the total conversion, but approximate since the system total was not conserved by a few percent due to imprecision in the surface flux integration. Estimates of the error can be made from the mass balance closure, which was typically within a few percent as previously illustrated in Figure 5-4. The total simulation time is reported as T2 in Table 5-2 with C2 being representative of the peak conversion. The C1 variable is the peak potential exposure (moles per mole released) to an individual in the room to the oxidized hydrogen. These result metrics are discussed above as if they are all for tritium, however the other isotopes should be viewed as simulants for tritium.

Table 5-2. Simulation results

CASE	C1	T1 (s)	C2	T2 (s)
1-C3T	0.0513	86	0.309	180
2-M3T	0.0348	84	0.1543	180
3-F3T	0.0595	85	0.2534	180
4-M3D	0.0447	74.5	0.195	180
5-M3H	0.0974	57.5	0.388	180
6-M3TA1	0.0397	81	0.1628	180
7-M3TA2	0.0384	82.5	0.1634	180
8-M1H	0.0067	70.0	0.0322	180
9-M1D	0.0054	121	0.0264	180
10-M1T	0.0087	113	0.0374	180
11-M1DS1	0.0052	125	0.0281	180
12-M1DS2	0.0051	116.5	0.0252	180
13-M3T25	0.9063	19.3	1.0	180
14-M3T50	0.3601	29.5	0.6159	180
15-M3T75	0.0520	82	0.2224	180
16-M2T	0.0463	62	0.2124	180
17-M1.5T	0.0223	66	0.1184	180
18-M2.5T	0.0514	93	0.3072	180
19-M3T22.5	0.0362	84	0.1777	180
20-M3T45	0.0111	88.5	0.0785	180
21-M3T67.5	0.0260	38.5	0.0661	180
22-M3T90	0.0790	33.5	0.3808	180
23-M3T90I	0.3071	47.5	0.7638	180
24-M3THV	0.0305	76	0.1426	180
25-M4T	0.0431	70.5	0.1465	180
26-M3.5T	0.0427	76.5	0.1580	180
27-M5T	0.0750	68.5	0.2646	180
28-M3TK	0.0084	97.5	0.0472	180

The simulation matrix permits assessment of a variety of factors. First, the mesh had a decreasing effect beyond the coarse simulation out to 50 seconds, illustrated comparing Case 1,

2, and 3. Figure A - 1 in the appendix shows a reasonable similarity between Cases 2 and 3 at early times, which suggests the appropriateness of using medium mesh cases for analysis.

The effect of isotope is evident in comparing results between Cases 2, 4, and 5 as shown in Figure 5-5. The protium isotope had the largest conversion, presumably due to an effect of buoyancy. A similar trend is not seen in the 100 MW cases (8, 9, and 10), with the highest conversion from the tritium and the lowest from deuterium (see Figure 5-6). These results are non-monotonic, but the isotope effect is not as significant with C1 parameters all below 1%, and C2 parameters all in the range of 2-4%. These simulations serve to indicate the degree to which the experimental results from one isotope can be used to predict the results of another. The isotope effect appears to be a bigger effect than most of the other parameters varied. In this particular case, the effect of assuming protium as a surrogate for tritium would result in a significant over-estimation of the tritium hazard with a 300-kW fire.

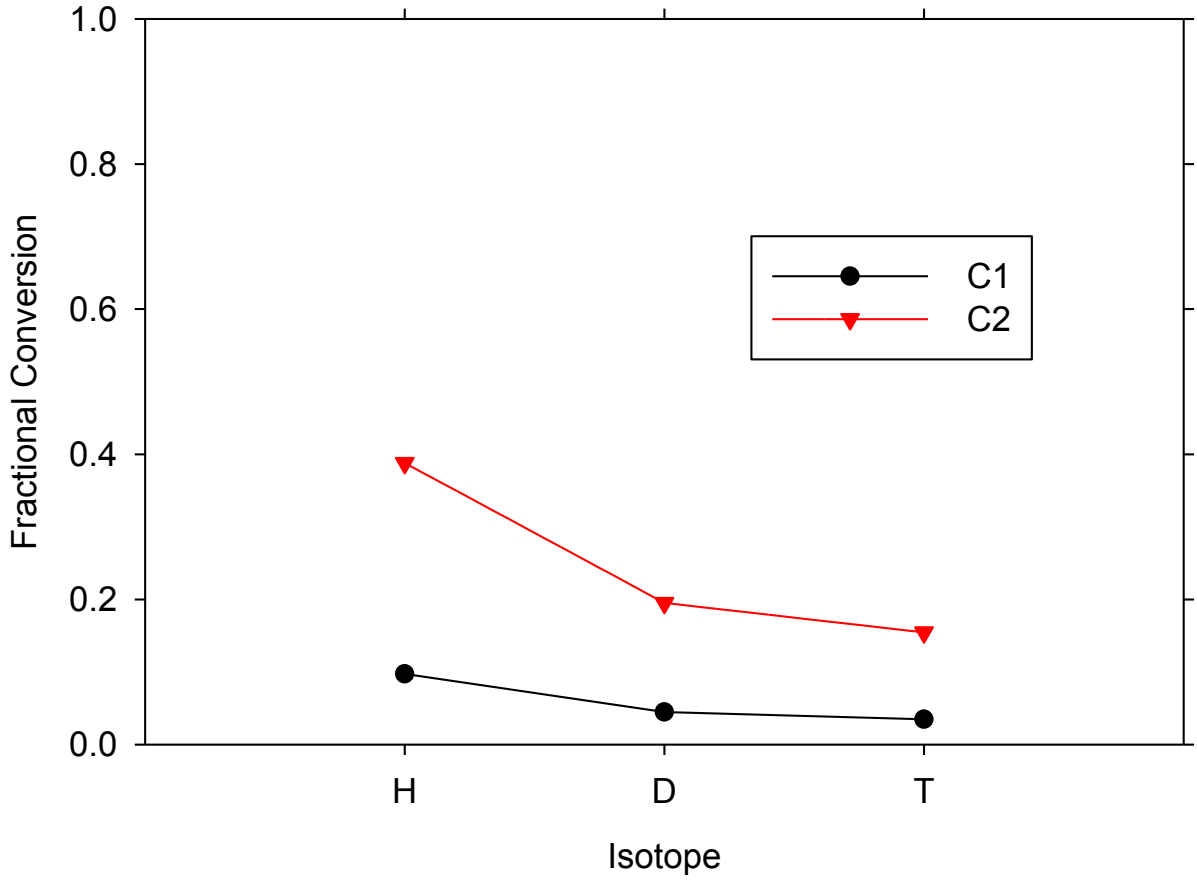

Figure 5-5. Isotope effect for the 300 kW scenarios

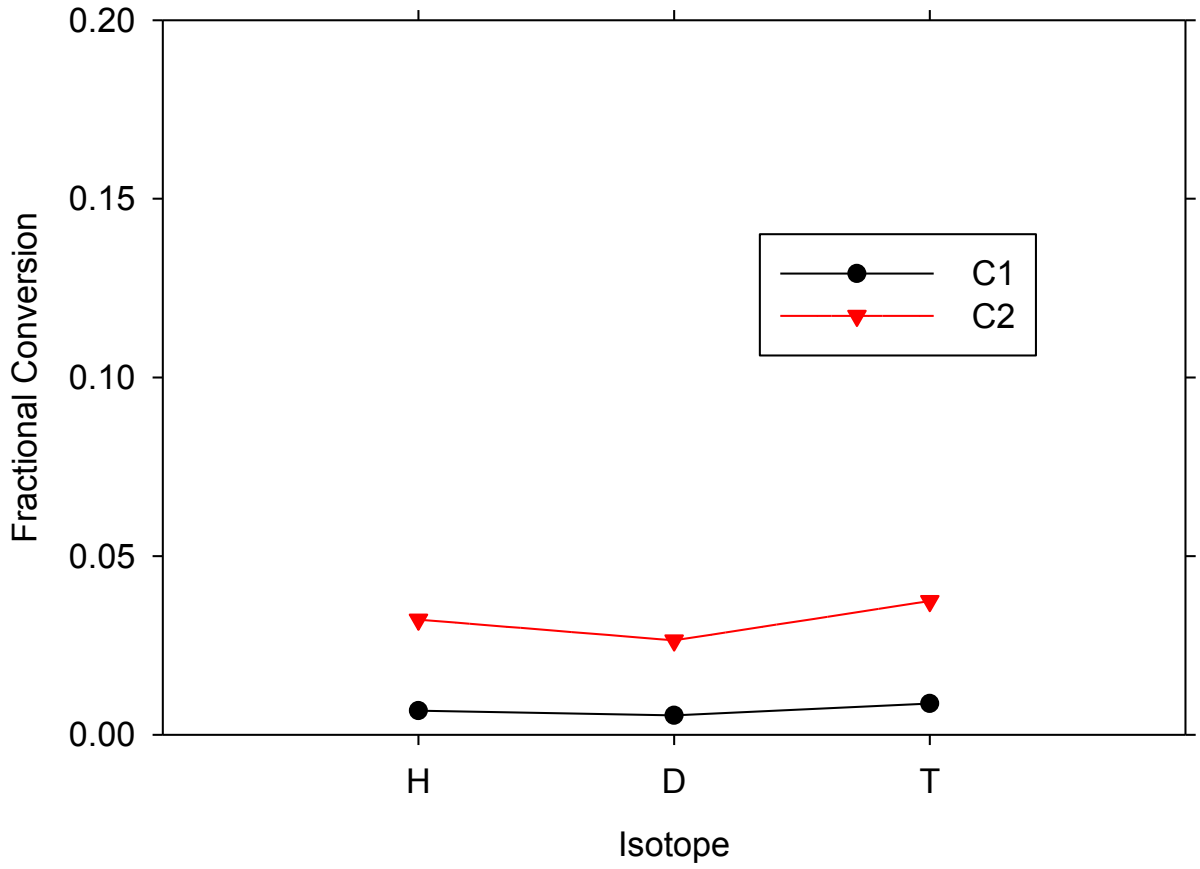

Figure 5-6. Isotope effect for the 100 kW scenarios

To explore the isotope trend in a little more detail, the centroid of the contaminant versus time for the three isotopes is plotted in the x (horizontal) and z (vertical) directions in Figure 5-7 and Figure 5-8. The x-position centroid suggests the protium is more mobile and gravitates to the centerline of the facility (x=0) the fastest. This is a presumed effect of the diffusion. Likewise, the protium is the fastest to reach the upper-layer and achieves the highest centroidal z-position. This includes diffusion but is aided also by buoyancy.

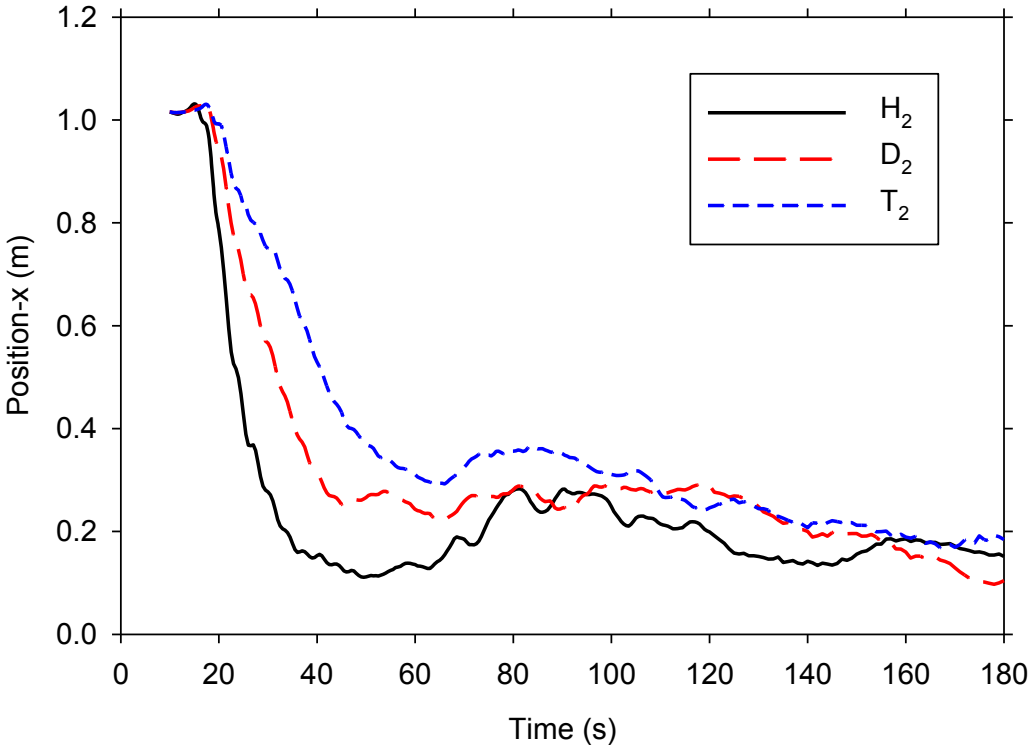

Figure 5-7. Contaminant x-centroids (horizontal) versus time for the 300 kW case

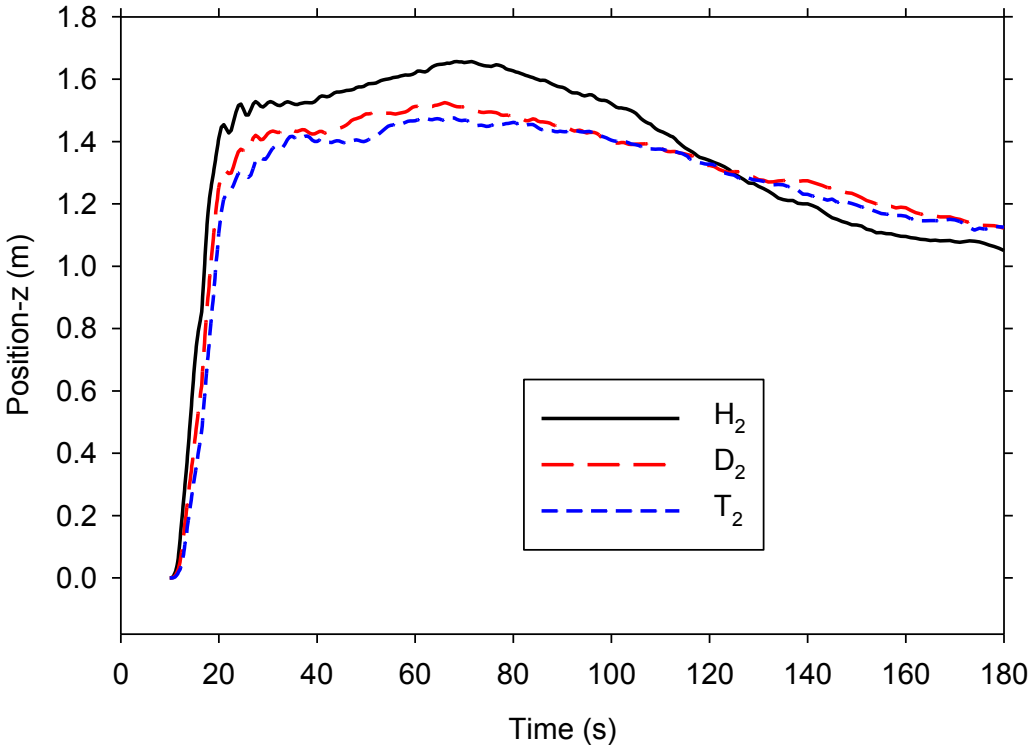

Figure 5-8. Contaminant z-centroids (vertical) versus time for the 300 kW case

The effect of varying the kinetic rate was small based on the initial variation, as can be seen comparing results from Cases 2, 6, and 7. This suggests that the kinetics are not a particularly strong factor in determining the hazard from these scenarios, provided that the assumption that the reaction rates are slower for the D and T reaction holds true. An order of magnitude slower rate expression resulted in changes to the answer that were relatively small. Trending appears somewhat non-monotonic, but this is probably in the noise of the simulations. After obtaining test data in the correct regime, a new expression based on data was used in Case 28, which results in much lower conversion, a factor of 3.27.

The effect of the Schmidt number is evident comparing simulations for case 9, 11, and 12. Lower Schmidt number increases the diffusivity, and has minimal effect on the conversion variables C1 and C2. Like with the kinetic expression changes, the results here are probably not different enough to assess any significance to the differences.

The effect of the location of the release relative to the fire had a significant effect on the conversion. Compare here the results for Cases 2 and 13-15. The case of 25% distance (about 0.5 m from the fire) resulted in full conversion (C2=1.0). The contaminant release was drawn into the fire and reacted completely. The case of 50% distance (about 1.0 m from the fire) still had high conversion, but not full conversion like the 25% case. Further away, the conversion drops significantly. This suggests that the advective draw of the fire is a primary factor in the conversion of the hydrogen when released close to the fire. It is exposure to the hot part of the fire where active burning is ensuing, with a smaller contribution by the heat of the upper smoke layer. Proximity to the fire has a significant effect on the amount that is drawn in and oxidized. This suggests a turbulence model and/or parameter study might prove more significant and could make sense for subsequent assessments.

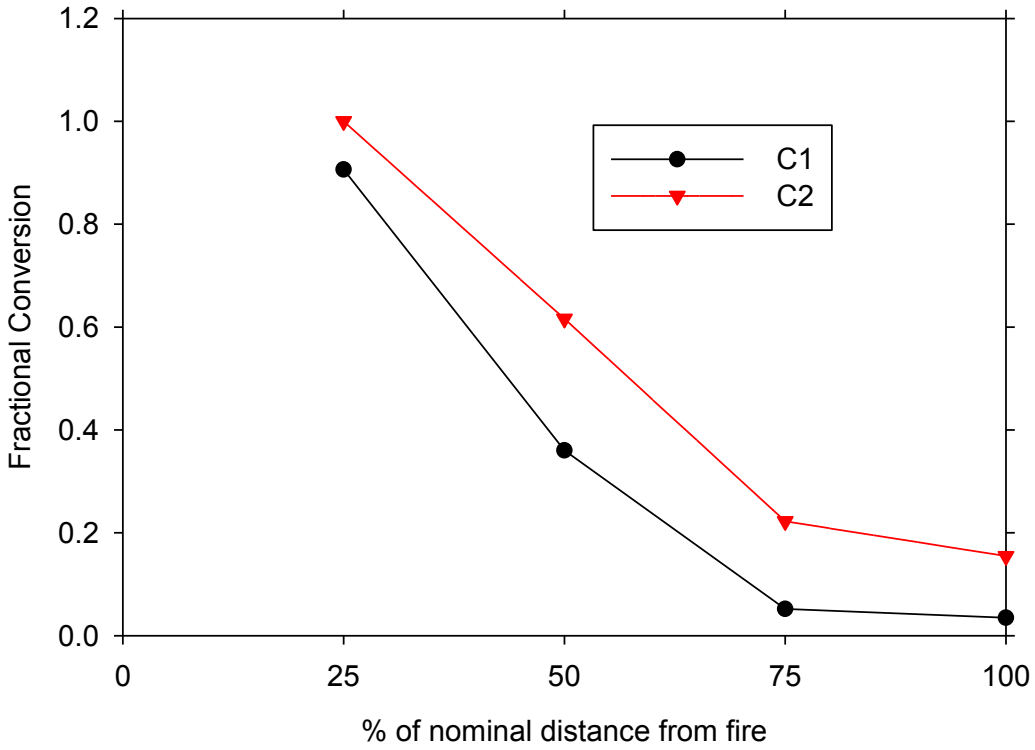

Figure 5-9. Conversion as a function of distance from the fire for the 300 kW fire

The fire intensity effect is illustrated in comparing results from Cases 2, 10, 16-18, and 25-27, and results are plotted in Figure 5-10. There is a non-monotonic behavior in the conversion results. The lowest conversion is with 100 kW, but surprisingly the highest was 250 kW. Simulation input files were confirmed for quality assurance to be identical other than the fuel release. It is suspected that the variation here is due to variations in the intensity of the ambient flows that set up during the fire. It is generally expected that the conversion will increase with increasing fire intensity. Higher intensity fires induce more flow through the opening, which augments the exhaust of the contaminant. They also induce a thicker hot layer near the ceiling, which factor seems to be reduced once the induced motion becomes a greater factor around 250-300 kW.

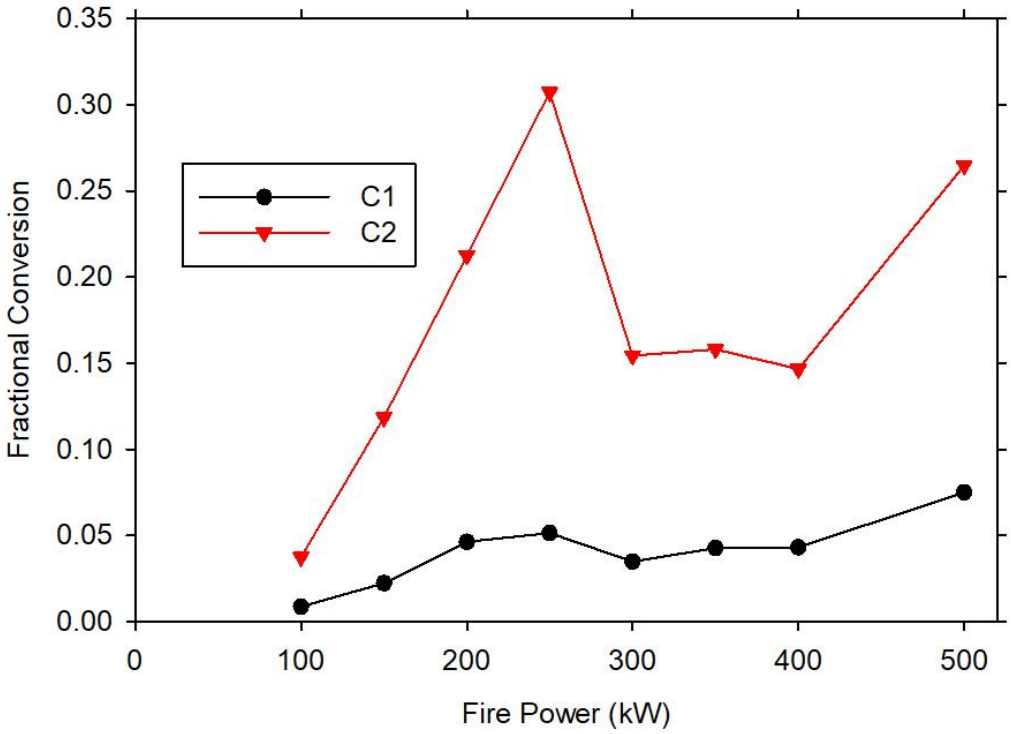

Figure 5-10. Conversion as a function fire power

Given that the kinetic and Schmidt number parameter variations had little effect on the conversion parameters (C1 and C2), the need for increased fidelity in these inputs is not clear. What is presumably happening is that the fire ignites and draws fresh air at the base to replace the buoyant reacted air. The doorway is rapidly established as the main source for the fresh air, which results in an insignificant draw from the other corner of the room where the release is located. When the release is closer to the fire (as in Case 13, 14), the release is close enough to be drawn into the base of the fire. When the release is further away, the draw is small, and the buoyancy of the isotope appears to be a more significant factor, as is the general motion of the ceiling layer towards the exit.

Case 3 with Cases 19-23 illustrate the effect of position of the fire relative to the release. Figure 5-11 shows a graphical representation of the results. In all these scenarios, the nominal baseline distance between the fire and release is maintained. Case 23-M3T90I is plotted at 270° since it is

best described as such relative to the fire position. The I was chosen to designate 'inverted', as the fire and plume sources were inadvertently inverted. The case still yields relevant data, and so it was included in the matrix (The I might also be for inadvertent). It was by far the most extreme result, which is not unexpected. The contaminant now has to pass the fire on its way out the door. This case suggests that a proximity to the fire hazard plot may be drop or star shaped, as the plumes to the side appear less likely to be drawn into the fire. Note the trend with angle. The 0-degree case results are moderate, then drop as the angle increases to 67.5, then go up again at 90 degrees. The initial drop is probably due to a faster escape with the increased proximity to the door initially, and then as the release is more likely to get entrained back into the fire with the incoming air, causing the results to rise again.

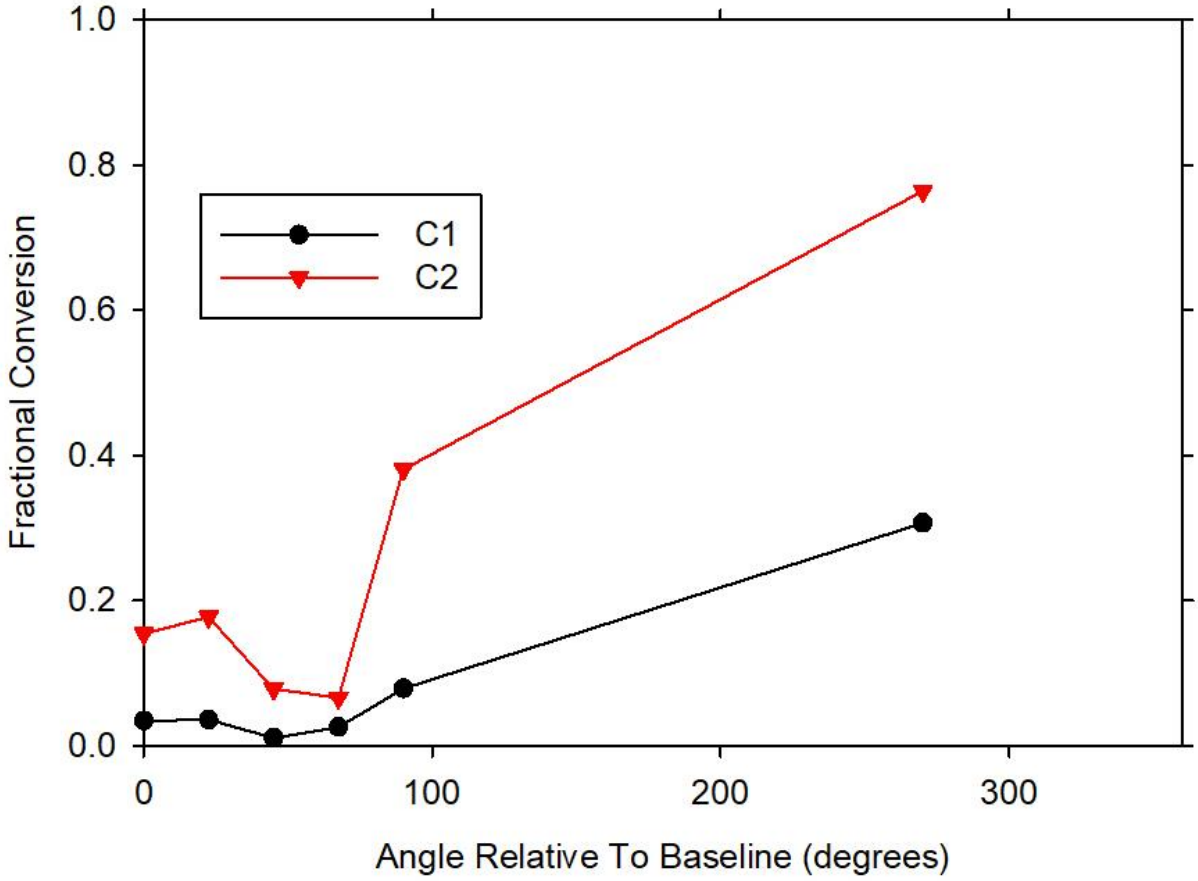

Figure 5-11. Conversion as a function angular position of the release

5.4. Discussion and Analysis

A value of having performed this simulation study is in the ability to observe the results of a variety of scenarios in terms of hazard. A general lack in experimental data of this nature is not expected to be improved upon in the near future, so the simulations help develop an understanding of how an accident scenario might transpire where otherwise this would be difficult to measure. The use of a standard fire as a scenario helps assure the results are in a realistic setting. The validation and attention to the relative importance of model parameters helps support the credibility of the qualitative and quantitative accuracy of the predictions. We intend to continue working on developing the credibility of the simulation methods to help guide safety planning. Planned work

includes additional model validation efforts to demonstrate the isotope models are accurate, and that predictions from scenarios of this type are consistent with experimental data.

It is instructive to list ways that this assessment is perceived as conservative versus non-conservative. This is an important exercise, because it helps articulate where the model might be lacking and how reality might differ from this simulation exercise. It also is reflective of some comments from tritium operations personnel, who perceive some attempts at regulating the tritium hazard as over-conservative. The study was not intended to be anything but a best estimate study of a tritium release. Some parameters with uncertainty were explored as part of the simulation matrix. These results help to understand the role of these factors. Despite this, it is nearly impossible to proceed without assumptions that have a degree of uncertainty that are not reflected in the study. These following two lists help address our perception of the study in this regard.

Conservatisms:

1. We have assumed 100% release of a container for the simulation. In reality, this could be off by 100%. The release of the contaminant is contingent on failure of the container, as well as full escape. A more detailed analysis could significantly reduce this parameter, but since data are lacking the 100% conservative approximation will be used.
2. The majority of our fires in this study are 300 kW fires, which based on the ISO-9705 standard is conservative by a factor of 3.
3. We neglect the potential presence of a mitigating factor like a glove box or a storage cabinet (which would further reduce the release potential and fire exposure) as well as the possibility of the container being in an inert storage area like a glove box.
4. Many lab spaces are equipped with suppression systems, which we have neglected.
5. Fires might be more likely with people present, who may respond by suppressing the fire. No response was assumed.
6. The notion of an ARF/RF is often used for studying particle contaminants. It is applied to tritium fires, but it is questionable whether this is the right approach given the differences between the contaminant types.
7. The primary reaction mechanism used in this study will be shown by the data in the next chapter (as well as Case 29) to vastly over-predict the conversion compared with recent datasets at the low molar fraction range of interest to this problem.
8. The emission was assumed into a mature fire. Fires tend to be more transient and increase and decrease in intensity with time. This assumption of a release into a mature fire constitutes a conservative approximation.
9. The ISO-9705 scenario is relatively small, representative of a minimally sized room. A more realistically sized lab space might be significantly larger, which could result in significantly lower conversion fractions.
10. There might not be a reasonable possibility of fire at all. Many of the lab spaces involving tritium lack significant combustible materials, which makes the assumed fire condition conservative. Laboratory management practices can reduce available fuel and eliminate the possibility of propagating fires.

Non-conservativisms:

1. We have omitted furniture from our room. Laboratory furnishings will obstruct flows, reduce air volume, and as a fire burns will induce turbulence with could enhance mixing and therefore conversion.
2. There is a potential for the contaminant to further react outside the bounds of the present computational domain. These simulations cut short this domain, possibly inhibiting further reactions in the corridor or hallway outside the room. This was not included because it was not part of the standard test. Exhausting gases and smoke are significantly cooler than the fire, probably lacking flames except in the largest of fires. This effect is likely minimal except for the largest fires.
3. We have assumed one mole of T_2 makes one mole of T_2O in our mechanism. Due to the possibility of forming other contaminants like HTO, the true ratio is probably a little different, with a maximum difference of a factor of 2 due to this approximation.
4. The use of the ISO9705 geometry and test conditions was intended to simulate a representative fire, not a worst-case fire.
5. All releases were ground releases, possibly resulting in longer rise times than would be for a release at desk or table height (although there is a possibility a higher release will be more likely to exhaust faster, resulting in the opposite trend).

We plot some summary plots here to help illustrate potential use of these model results for safety guidelines. Figure 5-12 shows 100 kW results, which show a peak fractional conversion of less than 0.04 for all cases simulated. The kinetic rate is too fast for these cases, so when reducing the rate by the rate reduction factor earlier presented, 1% is about the largest expected conversion based on existing scenarios.

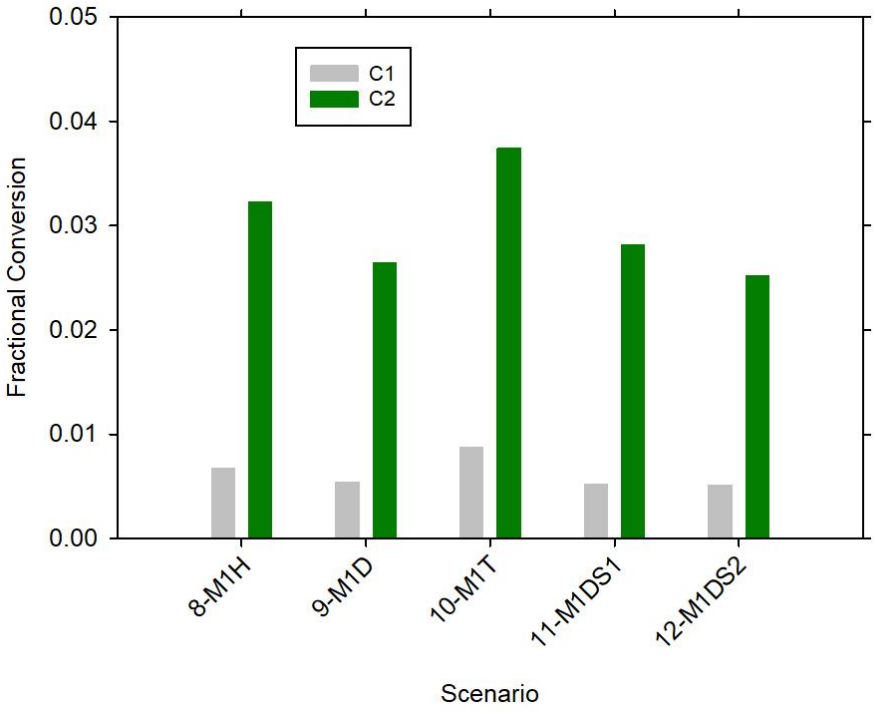

Figure 5-12. 100 kW scenario conversion

Most of the parameter study was done at 300 kW, which is three times larger than the baseline standard fire. These results are more instructive, suggesting that the orientation of the baseline 100 kW cases was not the worst case. Full results from the 300 kW scenarios are found in Figure 5-13. Case 13 is the worst, with full conversion. But the release in this case is only about 50 cm out of the fire, which constitutes consideration of it being in the fire. Most use facilities have low quantities of distributed inventory, and this study was aiming at assessing the impact on releases not in the fire. Neglecting case 13, the worst case is 23. But the reaction rate for all but case 28 was significantly faster than data suggest. When projecting the 300 kW data by the scaling factor based on Case 28, results in Figure 5-14 suggest peak conversion is below 30% for all scenarios, with the average being well below 10%.

The 300 kW scenarios are conservative based on the ISO-9705 standard and were used because the nominal 100 kW scenarios did not yield results high enough to assess the effects of model variations. Figure 5-15 takes the smallest conversion factor available for converting between 100-300 kW scenarios and applies it to the 300 kW results to project them to 100 kW case results. Note the change in the vertical scale. Peak conversion is well below 10%. The scenario involves non-linear physics, and using linear projections is approximate. This is, however, a reasonable and possibly the best available approach given the lack of improved data in this regard. More simulations would be required for a better approximation

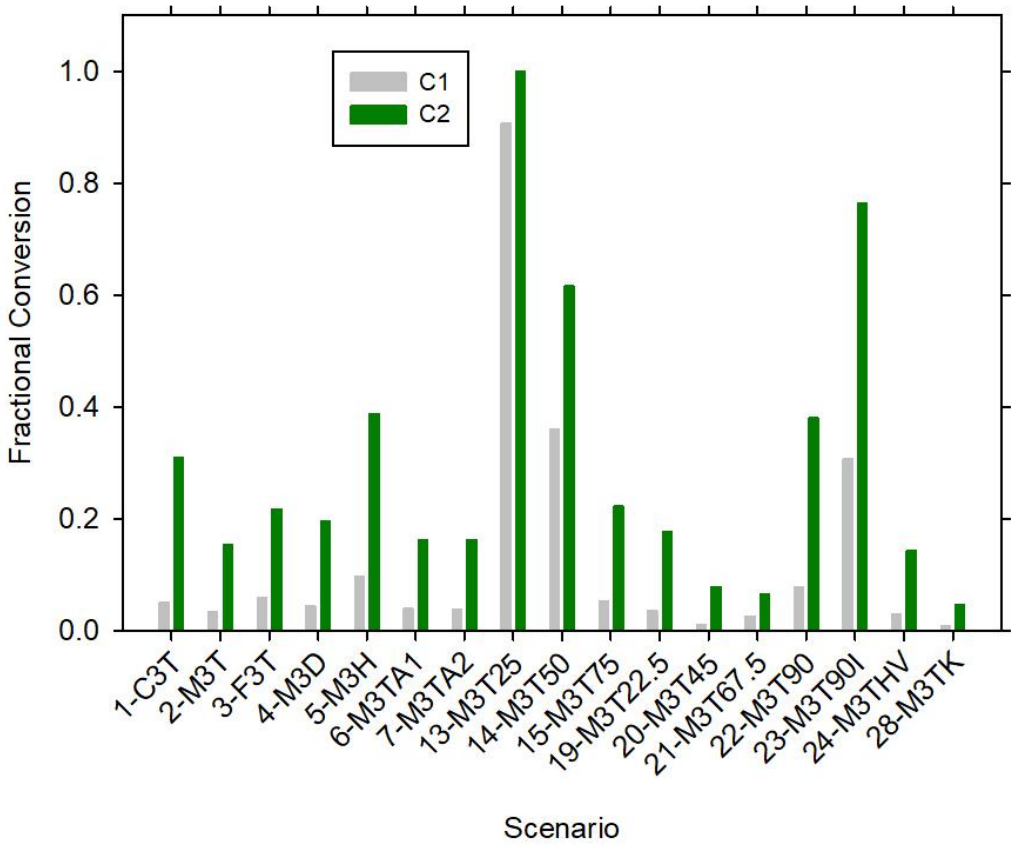

Figure 5-13. 300 kW scenario conversion

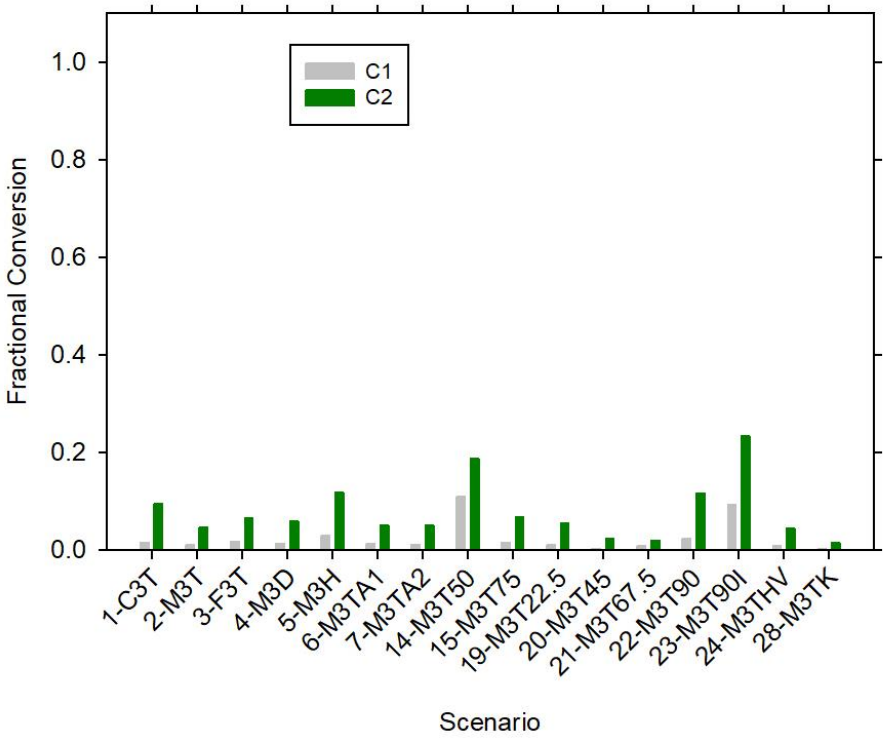

Figure 5-14. 300 kW scenario conversion adjusted for a more realistic kinetic reaction rate

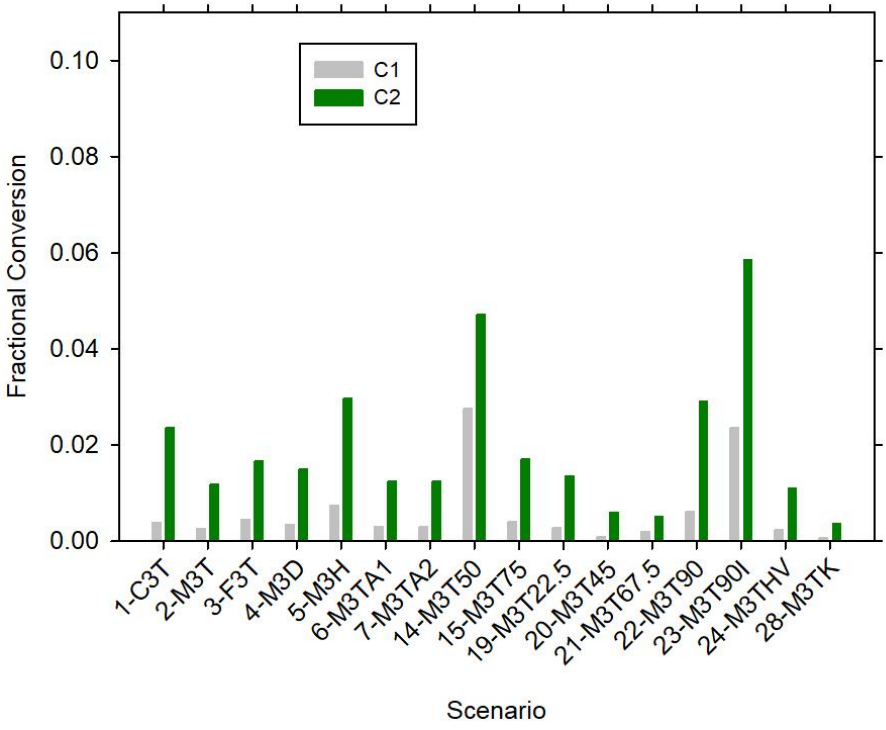

Figure 5-15. 300 kW scenario results adjusted to 100 kW and for a more realistic kinetic reaction rate

The linearity or lack thereof of the projection of data between the two kinetic rates is explored via an analysis of the fire simulation results at 180 seconds as a function of fire power. The reaction rate used for most of the studies initiated reactions around 550 K. The experiments detailed in Chapter 6 suggest reactions do not begin until about 800 K. Iso-contours of the fire with temperatures greater than these two thresholds suggest the volume of the domain where oxidation reactions may occur. These are found plotted in Figure 5-16. These show that the 800 K iso-contour is generally increasing with fire magnitude. The 550 K iso-contour increases quickly to about 200 kW, after which it increases more slowly. This is because the hot gas volume is limited by the exhaust, and the limit begins to have a more significant factor in the reaction volume. This is notably about where the first inflection in the 300 kW conversion versus power plot (Figure 5-10) shows deviation from a monotonically increasing trend.

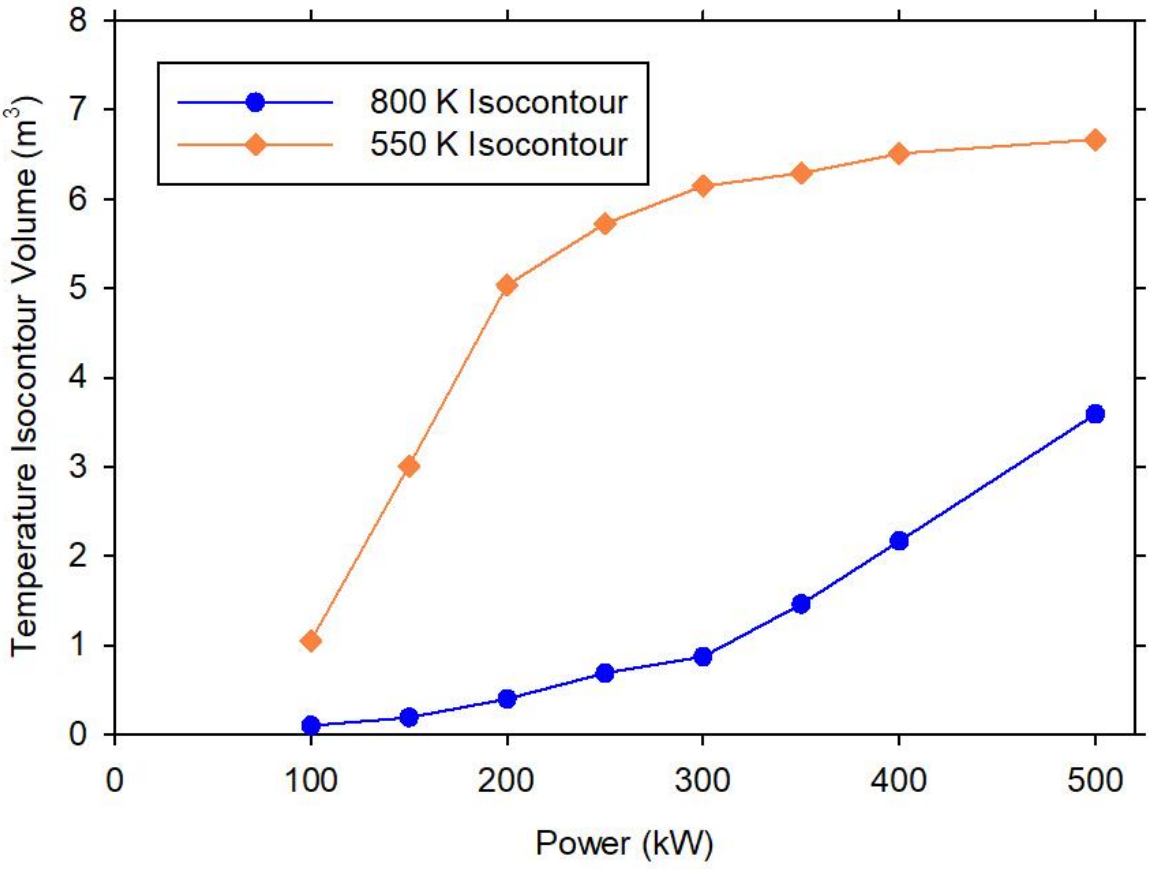

Figure 5-16. Predicted isocontour volumes for two temperatures at 180 seconds as a function of power

5.5. Conclusions

A variety of release scenarios for hydrogen isotopes were simulated for an ISO-9705 standard fire to assess the conversion of H_2 to H_2O, which for tritium (^3H) is the main hazard factor. The isotope effect was seen to be a large factor in the conversion, which suggests a need for T_2 specific studies. The proximity of the release to the fire was also a significant factor. The intensity of the fire has a significant effect on the resultant conversion; however, conversion was low for nominal standard testing conditions. Schmidt number and kinetic parameter sensitivities were assessed. The kinetic rate based on recently obtained data suggests low conversion in representative fires. Schmidt number was a minor factor within the range of parameter variability studied, and advection is probably the main factor in conversion of a release at the test conditions. Various orientations of the plume release relative to the fire were tested. Projecting results to the standard test, less than 10% conversion for releases outside the fire (50-100 cm away) are deemed reasonably conservative. Simulations of this nature are helpful towards understanding the risks associated with handling tritium and are looked to as surrogate data for scenarios that are unlikely to be tested due to the risk and costs associated with the contaminant source. There are a number of open questions regarding the accuracy of the predictions, and estimates can be further improved by greater focus on these contributing assumptions.

New data described in Chapter 6 became available towards the end of this study. The kinetic rate used for most scenarios is expected to result in extremely conservative conversion, as actual tests of hydrogen isotope reactions under low (sub-flammable) conditions suggest a much slower progression of the reactions. Current results were linearly projected to the expected results given this change. A linear behavior is not expected to be an adequate method for high-consequence safety studies. The simulation campaign would need to be re-run to fully express the true expected conversion of tritium under these representative hazard conditions.

6. REACTION KINETICS EVALUATION

This chapter describes an experimental and modeling study to quantify oxidation rates of hydrogen isotopes at sub-flammable concentrations. This work was submitted for presentation at the 7th Thermal and Fluids Engineering Conference; the content of this chapter is from a paper that was produced for this meeting (Shurtz et al., 2022).

6.1. Introduction

Tritium is a radioisotope of hydrogen that produces a low-energy beta particle upon decay and has applications in self-luminous phosphors, fusion energy production, and nuclear weapons. At U.S. Department of Energy tritium facilities, tritium is stored primarily as a diatomic gas (T_2) or as a solid hydride that can be heated to release T_2 gas. At smaller (i.e. radiological) tritium facilities, the potential flame or explosion hazard is not a major safety concern since the T_2 inventories are insufficient to sustain a flame, and gases are frequently stored at sub-atmospheric pressures. Nevertheless, T_2 to water conversion in fire environments remains a major safety concern due to radiological hazard considerations; tritiated water vapor is readily absorbed by the human body, making it 10^4 times more hazardous than the same amount of tritium uptake as T_2 gas (DOE-STD-1129-2015).

Due to the relatively high dose consequence for tritiated water on the human body, the fraction of T_2 that can convert to water vapor is an important factor in tritium safety evaluations. A report reviewing tritium safety (Mishima and Steel, 2002) has noted that T_2 to T_2O conversions lower than 100% could (in principle) be applied for regulatory safety compliance in specific scenarios with adequate technical support. It is the aim of this report to provide such technical support. Although extensive literature exists that examines H_2 gas combustion with high starting pressures and volumes, specific information such as molecular conversion fractions and oxidation rates under low pressures and volumes of typical concern for laboratories with tritium inventories are virtually non-existent. Even less information exists for T_2 oxidation rates due to the inherent difficulties of performing combustion experiments that generate radiologically hazardous reaction products. To address these critical knowledge gaps, this paper examines the non-radioactive isotopologues of diatomic hydrogen (H_2, D_2) over a range of temperature conditions in a tube reactor and their conversion to water under low concentrations in air. The experimental data from the tube reactor experiments are used to gauge how readily these isotopes react to form water vapor and determine isotopic trends. These trends are then extrapolated to produce kinetic rate parameters appropriate for tritium oxidation at low concentrations of relevance to radiological tritium facilities.

Measured flame speeds for D_2 are slower than measured for H_2 (Gray and Smith 1967; Gray, Holland and Smith 1970; Koroll and Kumar 1991), consistent with early observations of slower reaction rates for heavier isotopes (Hinshelwood, Williamson, and Wolfenden 1934). In principle, these measurements could be used to estimate even slower flames speeds for T_2 that would be applicable to releases above the lower flammability limit. However, leaks of T_2 from a container at sub-atmospheric pressure (as is common in a radiological tritium facility) are likely to result in concentrations below the lower flammability limit, which is the regime of focus for this report; the calculations in Chapter 2 demonstrate the low likelihood of flammable concentrations arising from tritium stored at sub-atmospheric pressures. To our knowledge, no existing literature consider oxidation rates of hydrogen isotopes in this low-concentration regime (where the non-radioactive isotopologues pose no safety hazard), especially in terms of simplified global kinetics suitable for large-scale simulations. There are a few studies of initial elementary steps in the oxidation process for H_2 and D_2 (Westenberg and de Haas, 1967; Pamidimukkala and Skinner, 1982; Michael, 1989;

Marshall and Fontijn, 1987), but inferring global oxidations rates applicable at very low concentrations from these is not necessarily straightforward.

6.2. Experimental Methods

Hydrogen gas (99.999%), deuterium gas (99.999%) and synthetic air (ultra-zero grade) were acquired from Matheson TriGas and used without purification. Gas flow rates were controlled using mass flow controllers (MFCs, Brooks). The MFCs were calibrated using a bubble-meter, and flows are reported at standard temperature and pressure.

Hydrogen isotope oxidation tests were carried out within a quartz glass cylindrical tube (internal diameter 13.5 mm, length 420 mm) in a tube furnace under a range of H_2 (D_2): air ratios, gas flow rates, and temperatures. The gas composition was monitored downstream of the quartz tube using a gas chromatograph (GC, Agilent 3000A). A cold finger was installed downstream of the quartz tube to condense out most of the water product and thereby prevent flooding of the separation column in the GC.

Figure 6-1 shows a schematic representation of the tube reactor setup. Note that the hydrogen inlet was 2.5 cm inside the quartz glass tube, whereas the air flow entered the system further upstream. The hydrogen inlet tube was a piece of stainless-steel tubing (outer diameter 3.175 mm or 1/8", inner diameter 1.75 mm), centered within the quartz. The gas within the quartz tube was maintained at atmospheric pressure, which in Albuquerque is typically 635 Torr.

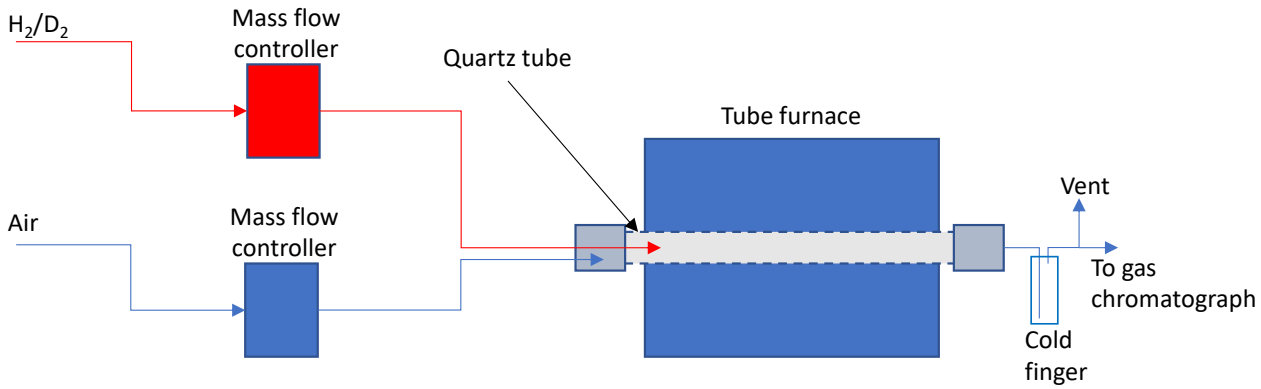

Figure 6-1. Schematic representation of tube furnace reactor setup.

Once stable gas flows were achieved (as determined by GC output, typically within 10-15 mins of initiating gas flow) and the GC had been calibrated, the tube furnace was heated rapidly (stepwise) to 500°C and allowed to stabilize. No hydrogen isotope oxidation was observed at 500°C under any of the conditions used in this study, and this was used as the calibration point for the GC. The downstream cold finger was immersed in ice, and the furnace was programmed to heat at a rate of 1°C/min from 500°C to 750 or 800°C, hold for 15 minutes, and then cool at 1°C/min to 500°C. The GC drew a sample of the gas exiting the quartz tube approximately every three minutes throughout the entire experiment.

Due to differing degrees of condensation in the outlet tubing for different furnace temperatures, the experimental measurement of outlet water concentration was insufficiently reliable to use for meaningful conversion calculations. Hence, experimental conversion was calculated from residual H_2 alone (or D_2) using Equation 6-1:

$$X_{H_2,exp} = \frac{y_{H_2,c} - y_{H_2,f}}{y_{H_2,c}} \quad 6\text{-}1$$

where X is fractional conversion of H_2 to H_2O and y is a gas-phase outlet mole fraction. The subscript "f" refers to the final or outlet concentration measurement at a given temperature and the subscript "i" specifies a concentration of H_2 or D_2 measured at the cold (500°C) furnace condition used to calibrate the GC for each set of flow conditions immediately before the oxidation experiment.

Early exploratory experiments consisted of outlet concentration measurements with several fixed temperature profiles, so temperatures at these conditions were measured along the interior wall of the quartz tube (see Figure 6-2). This was done by inserting a 1/8" diameter K-type thermocouple probe through the outlet with only air flowing. Hydrogen concentrations in the oxidation experiments were low enough for thermal effects of hydrogen oxidation to be neglected for the purpose of boundary conditions (BCs). Temperatures near the ends of the tube were less accessible using this approach but were sufficiently low to be considered non-critical for the purpose of modeling the reaction rates. The shape of the temperature profiles shown in Figure 6-2 near the ends of the quartz tube varies with flow rate due to the velocity dependence of convective heat transfer. Conditions with higher inlet airflow are expected to cool the inlet upstream of the heat source more efficiently, so the lower measured wall temperatures near the H_2 inlet shown in Figure 6-2b at 1000 standard cubic centimeters per minute (SCCM) with respect Figure 6-2a at 100 SCCM are reasonable.

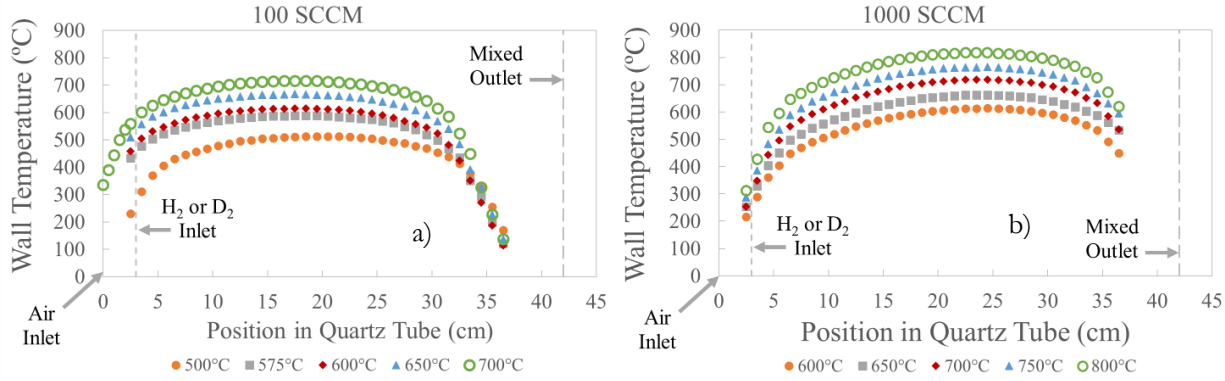

Figure 6-2. Temperature profile measurements used to interpolate boundary conditions for the quartz wall.

6.3. Computational Approach

6.3.1. Computational fluid dynamics modeling in SIERRA/Fuego

SIERRA/Fuego (2019a, 2019b) is a low-Mach number computational fluid dynamics (CFD) code for simulating objects in fires and is extended to support a variety of problems of interest to Sandia National Laboratories and affiliates who use the code. A major differentiating factor is that the code is a control volume finite element mechanics (CVFEM) code rather than a more traditional control volume code. A variety of mesh elements are available to the unstructured solver. This work employed tetrahedral elements for 3-dimensional (3-D) simulations and triangular elements of comparable size for 2-D simulations; this choice facilitated meshing cylinders of different sizes present in the experimental geometry.

The Reynolds number for the quartz tube with airflow at 100 SCCM is 10,000 at 300 K (27°C) and 44,000 at 1000 K (727°C). At 1000 SCCM the Reynolds numbers increase an order of magnitude to 100,000 at 300 K and 440,000 at 1000 K. These Reynolds numbers are all well above 2300, which indicates that the experiments were all above the expected transition from the laminar to turbulent regime for interior pipe flow. Turbulence was modeled using settings for a hybrid LES/RANS technique as described in Chapter 5 in both 3-D and 2-D. These simulations are likely under-resolved in terms of turbulence. However, this simple geometry with low concentrations closely approximates a 1-D plug flow reactor (PFR), so the kinetics are most strongly influenced by the temperature profile and the residence time; turbulence is not expected to strongly impact the measurements and simulations of kinetic rates in this configuration. If anything, turbulence improves the PFR approximation and hence the kinetic measurements by ensuring radially uniform heating of the gas mixture and efficient mixing of H_2 or D_2 with air prior to achieving temperatures high enough for oxidation to occur. The gas temperatures also cool more uniformly under the influence of turbulence at the end of the heated zone. The main reasons for pursuing a CFD simulation for these kinetic studies rather than a simpler 1-D PFR simulation (in a software package such as Cantera) were (1) to get a pre-test indication of whether good mixing could be expected before the hydrogen encountered high temperatures and (2) to prepare for the simulations described in Chapter 5 by implementing the kinetics from this chapter with the properties documented in Chapter 3 in a comparable but simplified simulation scenario.

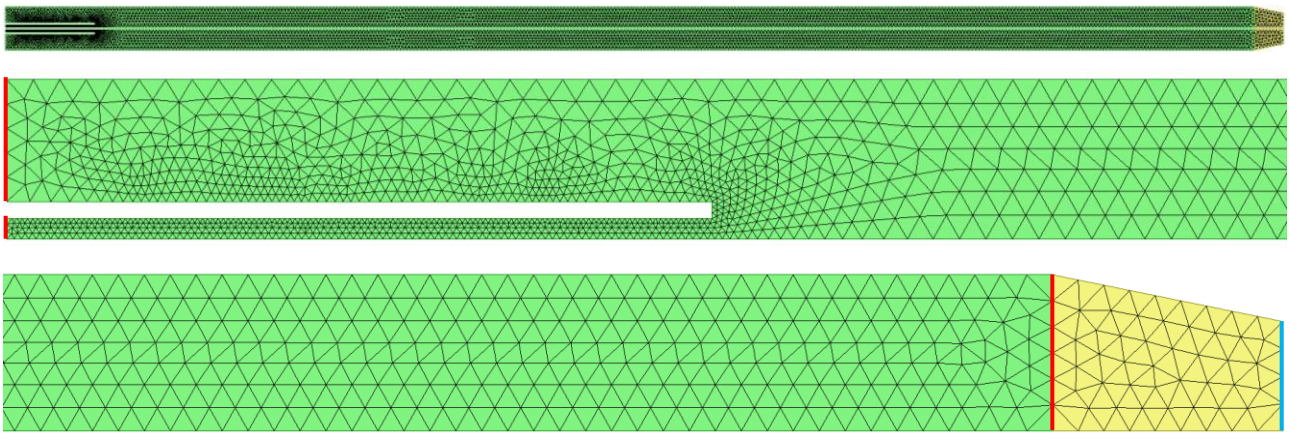

Figure 6-3. Mesh used to model the hydrogen and deuterium oxidation experiments. Top view: full 2-D mesh. Middle view: inlet mesh with central hydrogen inlet and annular air inlet at left. Bottom view: outlet mesh with artificial contraction to 70% diameter over 1 cm excess length.

The top view in Figure 6-3 includes normal and mirrored perspectives of the 2-D axisymmetric mesh used for the bulk of simulations shown in this chapter to illustrate the entire domain with the axis of symmetry. The magnified view of the inlet in the middle panel of Figure 6-3 has two vertical red edges of different sizes on the far left; the tall edge on top is the BC for the annular air inlet and the short edge below the gap representing the fuel tube wall is the BC for the central hydrogen inlet tube. Both inlet BCs are specified in terms of velocity vectors, temperature (300 K or 27°C) and composition. The yellow artificial contraction in Figure 6-3 was appended to the green representation of the experimental geometry. This yellow conical region was adopted to ensure that outlet concentrations of the experimental geometry (averaged over the red line on the far-right edge of the green region) were not influenced by spurious turbulent backflow from the simulated domain outlet (blue line on the far right of the yellow region). The simulated domain outlet (blue line) was

defined as an open or outflow boundary condition. Any backflow occurring at this outlet BC was defined to be air at 300 K (27°C).

Pre-test simulations like the one illustrated in Figure 6-4 were conducted on a 3-D tetrahedral mesh (with a shorter hydrogen inlet tube and mesh size parameters equivalent to Figure 6-3) to verify that adequate mixing of hydrogen isotopes with air could be expected to occur upstream of the hot zone where oxidation rates become significant. Figure 6-4 indicates that the simulated mixing became very uniform between 5 and 10 cm of the hydrogen injection point, which was sufficient to prevent oxidation reactions in the inlet region with higher concentrations using the pre-test kinetic parameters (conservatively fast based on the flammable regime, as described in the next subsection).

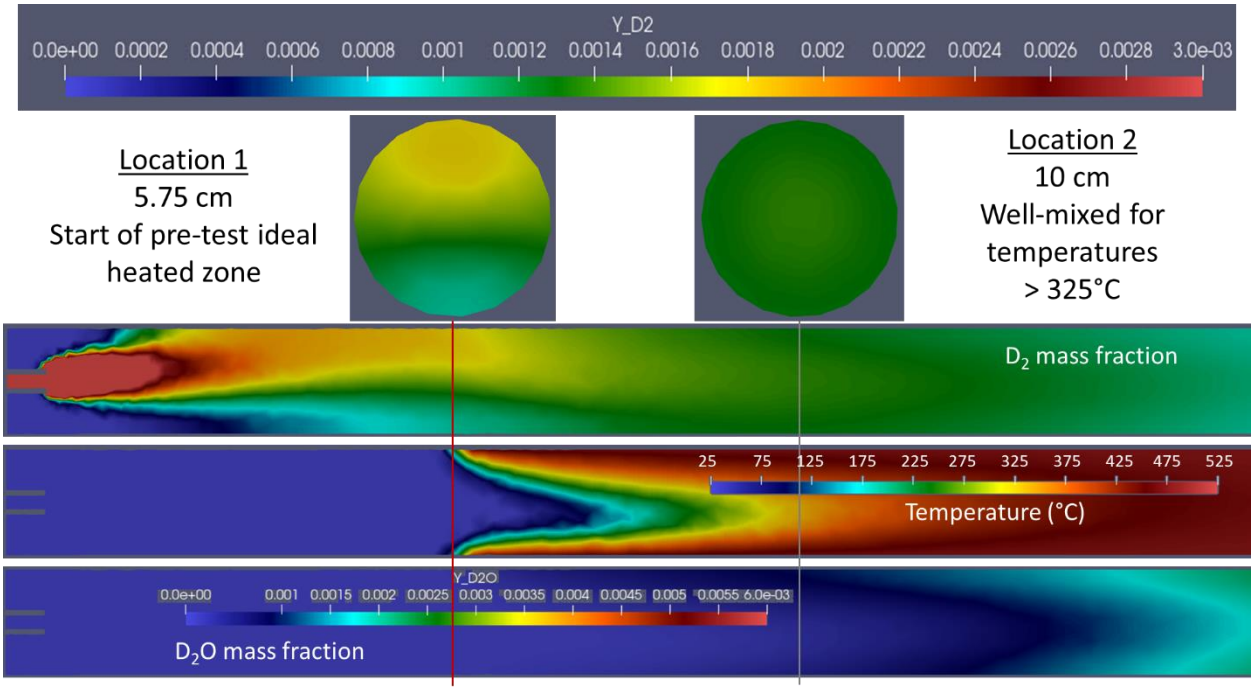

Figure 6-4. Pre-test simulation on 3-D mesh used to verify adequate mixing of hydrogen isotopes prior to the onset of temperatures high enough to cause oxidation.

When post-test kinetic analysis began, the 2-D axisymmetric mesh shown in Figure 6-3 was created to expedite iteration of parameter values (the axisymmetric simulations neglected gravity). Figure 6-5 shows that with equivalent (optimized) kinetic parameters and operating conditions, the 2-D simulations yielded nearly the same conversion results as 3-D simulations when averaged at the fully developed outlet (within 2% hydrogen conversion in Figure 6-5). The computational expense for the 2-D base mesh was reduced by a factor of 40 with respect to the 3-D base mesh. The 3-D mesh refinement study on the right of Figure 6-5 likewise exhibits only minor variations in final H_2 conversion. A more detailed version of this comparison is described in the following paragraphs.

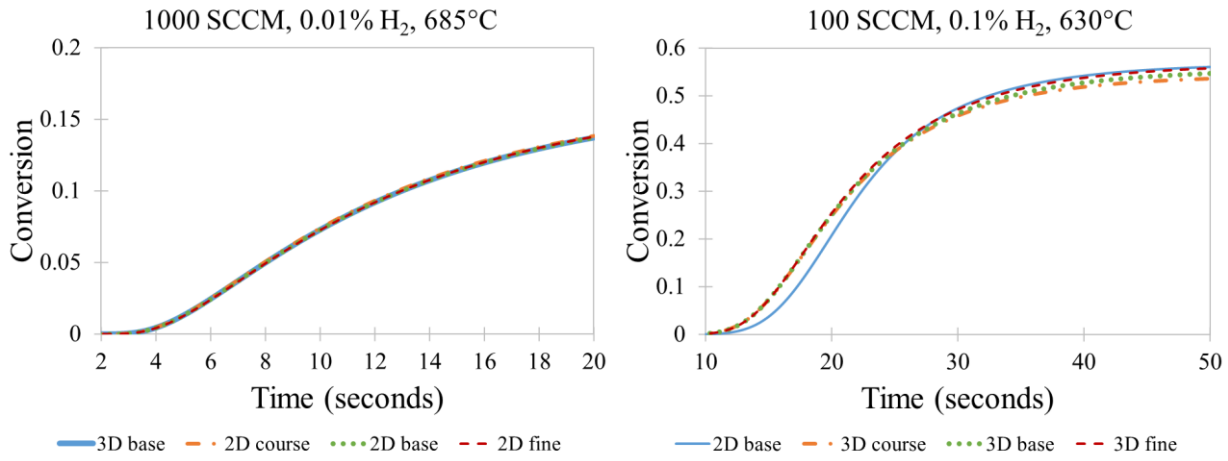

Figure 6-5. H_2 conversion profiles averaged over domain outlet (red line in bottom panel of Figure 6-3) with different mesh types and refinements.

Comparisons were made to different resolutions of 2-D and 3-D meshes on two selected cases from the post-test simulation campaign to show that the mesh resolution chosen was sufficient to yield solutions with low sensitivity to element size. The first condition chosen was 1000 SCCM with 0.01% H_2 and a furnace setpoint of 685°C. This condition was used to compare various resolutions of the 2-D mesh to the baseline 3-D mesh. The second condition chosen was 100 SCCM with 0.1% H_2 and a furnace setpoint of 630°C. This condition was used to compare the baseline 2-D mesh to various resolutions of the 3-D mesh. Parameters for these meshes and simulations are listed in Table 6-1, and the two chosen simulation conditions are circled in Figure 6-12 in Section 6.4.2, which compares the simulations to the experimental data. A shorter simulation time was used for the condition with a higher flow rate.

Table 6-1. Conditions used for mesh resolution study

Mesh	Conversion	Max Courant #	Elements
1000 SCCM, 0.01% H_2, 630°C, 20 seconds			
2-D course	0.138	0.680	1479
2-D base	0.137	0.901	6934
2-D fine	0.138	0.790	24896
3-D base	0.137	0.701	98452
100 SCCM, 0.1% H_2, 630°C, 50 seconds			
2-D base	0.561	0.627	6934
3-D course	0.536	0.796	32465
3-D base	0.547	0.835	98452
3-D fine	0.558	0.964	696846

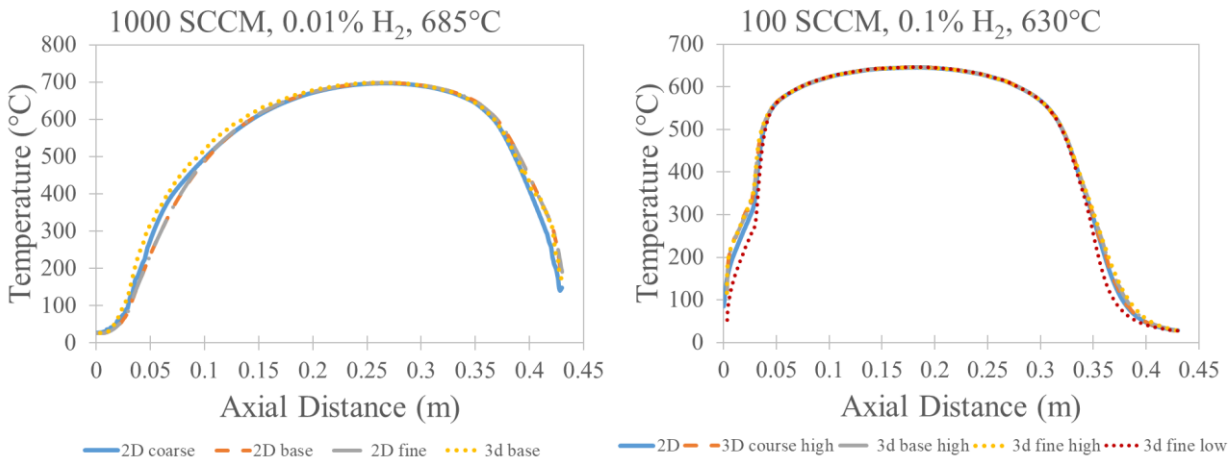

Figure 6-6. Simulated temperature profiles at 50% radius and final timestep with different mesh types and refinements.

A line above the fuel injection tube at 50% radius was chosen as a basis of comparison for the figures in this section. For the cases with the lower flow rates on the right panels, a second comparison from 50% radius below the fuel injection tube is also included. Figure 6-6 shows that the temperature profiles at 50% radius are very similar for all the cases considered in Table 6-1, with greater agreement between base and fine mesh resolutions in all cases. However, the temperatures near the inlet and outlet are slightly higher above the fuel injector compared to the same radius below the fuel injector, which indicates that some buoyancy effects occur when entering and exiting the heated zone with a 3-D mesh.

The trends for axial velocity are more interesting, especially for the right panel of Figure 6-7. The 3-D cases exhibit higher velocities above the fuel injector at locations with high temperature gradients (as seen by comparing to Figure 6-6). Lower velocities occur below the fuel injector and some recirculation effects are evident (negative axial velocities). This is a further demonstration of buoyancy effects that cannot be modeled in the 2-D axisymmetric case (where gravity was not modeled). The 2-D case is a good approximation of the 3-D simulations averaged at the upper and lower 50% radius. The 3-D coarse mesh solution on the right of Figure 6-7 is very noisy, but the two cases with higher resolution are smoother and consistent with each other. The panel on the left in Figure 6-7 exhibits less of these effects for the single 3-D case shown because the higher-momentum flow has less residence time in the regions with temperature gradients where buoyancy effects occur.

The concentration profile plots in Figure 6-8 show that the simulated oxidation reaction with optimized parameters slows to almost zero rate as soon as the temperature begins to drop. The various meshes are all in reasonable agreement, and the 2-D base mesh compares quite well with the 3-D fine mesh on the right of Figure 6-8, especially at the outlet. The disagreements between the 2-D and 3-D cases on the top left panel of Figure 6-8 are indicative of the buoyancy-driven mixing near the inlet noted in the previous plots. In any case, sufficient mixing occurs by the time the temperature becomes elevated to produce conditions that are practically identical in the hot region where water is produced.

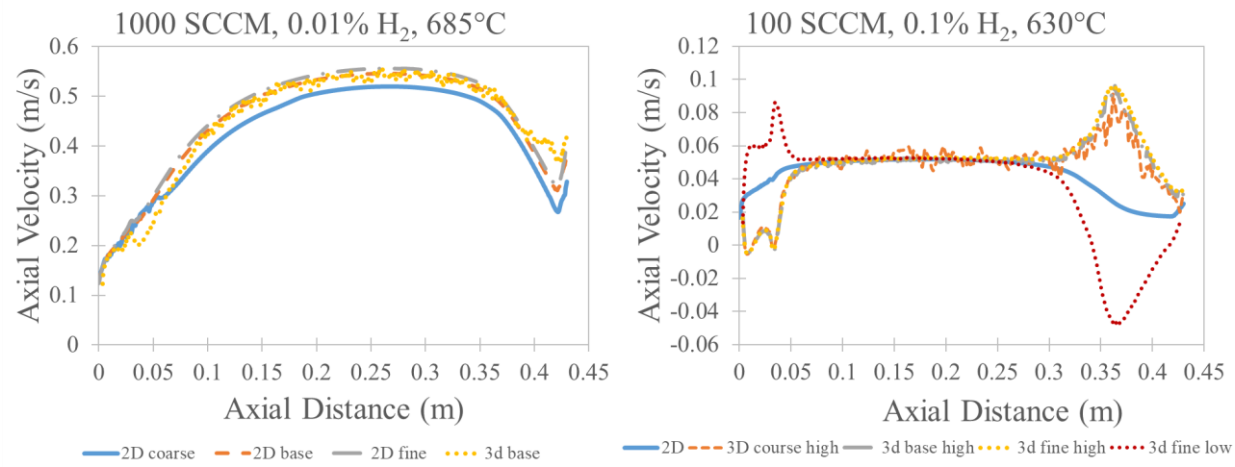

Figure 6-7. Simulated axial velocities profiles at 50% radius and final timestep with different mesh types and refinements.

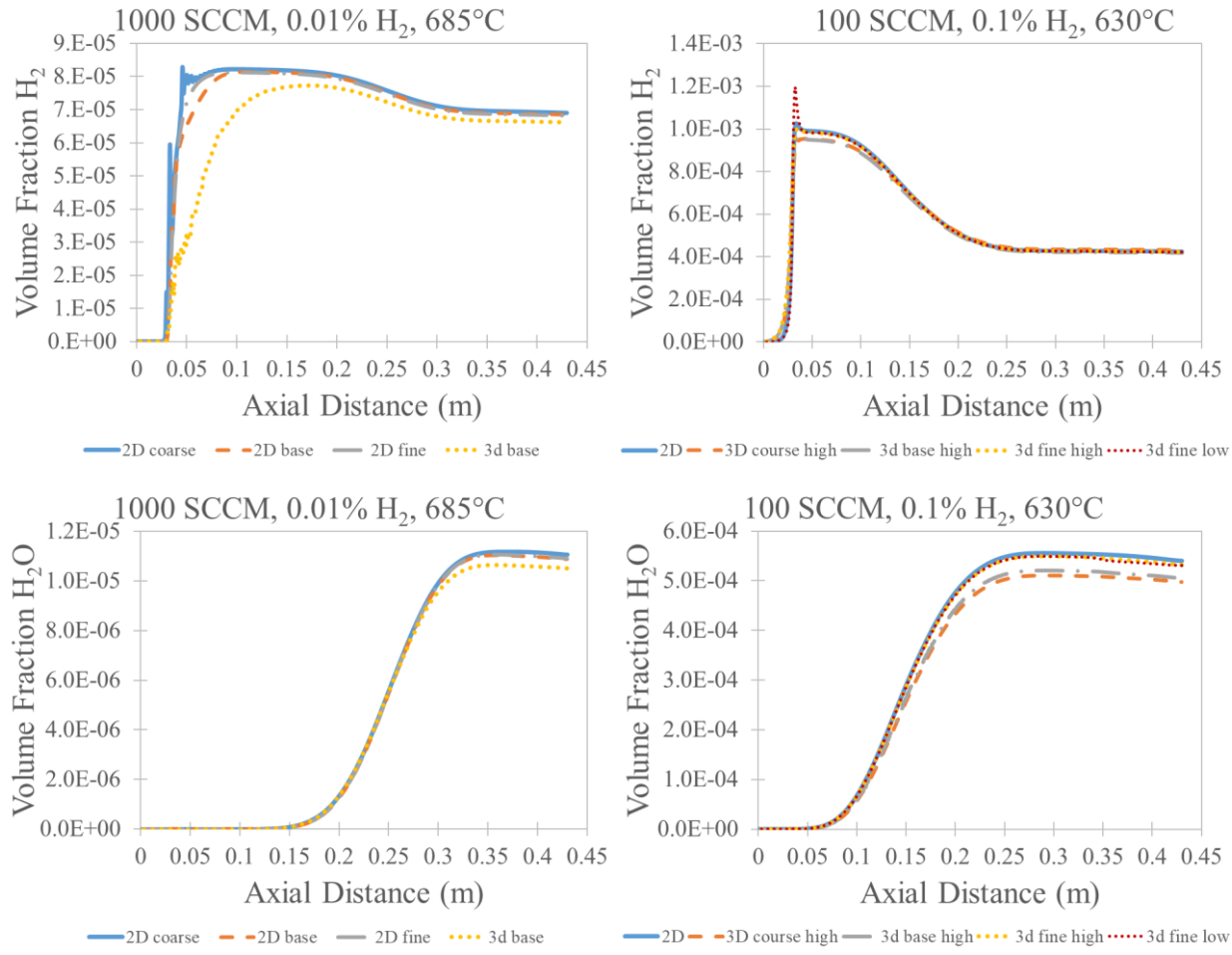

Figure 6-8. Simulated axial concentration profiles at 50% radius and final timestep with different mesh types and refinements.

6.3.2. Kinetic modeling in SIERRA/Fuego

SIERRA/Fuego includes a capability to model user-defined reactions. Hence, Fuego simulations with the geometry in Figure 6-3 accounted for flow, mixing, heating, reaction (water formation) and cooling. Temperature-dependent properties of hydrogen isotopes selected for this work are described in Chapter 3. The modeling parameters for kinetic rates were manually optimized within the CFD code. A global hydrogen oxidation mechanism from Marinov et al. (1995) was initially selected for this work, as specified in Chapter 5:

$$r_{global} = Aexp\left(-\frac{E}{RT}\right)[H_2]^{n_H}[O_2]^{n_O} \qquad 6\text{-}2$$

The default reaction orders of $n_H = 1.0$ and $n_O = 0.5$ specified in this equation are consistent with the stoichiometry of the global oxidation reaction ($H_2 + ½\ O_2 \rightarrow H_2O$). We have adapted the originally reported rate constants for this reaction to units required by Fuego with concentrations in mol/m^3 (indicated by square brackets). The originally reported Arrhenius parameters and reaction orders for Equation 6-2 were calibrated to flame speed data (Marinov 1995), but the regime of interest for this work corresponds to sub-flammable hydrogen concentrations (far below 4% in air at atmospheric pressure) (Hertzberg 1981, Benz et al. 1981).

The pre-test simulations are not shown in this work, but the exercise revealed that the initial kinetic parameters (Marinov 1995, see also Chapter 5) caused simulated oxidation of hydrogen to occur at temperatures ~250°C lower than the measurements. The pre-test simulation results also indicated that a small mixing benefit could be expected from centering the hydrogen injection tube radially within the quartz reaction tube. The global reaction model represented by Equation 6-2 does not apply directly to all regimes because it omits intermediate species from elementary reaction steps. Therefore, it was necessary to adjust the hydrogen reaction order and the Arrhenius parameters to match our measurements of hydrogen and deuterium oxidation at low concentrations as described in the Results and Discussion (Section 6.4).

Wall temperature profile BCs were taken directly from the measurements in Figure 6-2. In some cases, these temperature profiles were linearly interpolated to achieve convenient spacing in terms of the measured conversion. Different extrapolation methods were selected to yield physically reasonable behavior near the ends of the quartz tube with different flow rates based on careful consideration of the measurements shown in Figure 6-2. Temperatures near the outlet of the quartz tube with an inlet air flowrate of 100 SCCM were extrapolated using exponential decay from the semi-logarithmic slope of the last two measured points towards an asymptotic limit of 25°C. Measurements for the temperature profile at 700°C were taken close to the inlet (upstream of the heated zone) at an air flowrate of 100 SCCM, as shown Figure 6-9a. A linear slope of temperature versus position was defined from these measurements and applied to extrapolate the wall temperature towards the quartz inlet for the other profiles having the same flow rate. The left panel of Figure 6-2 shows that the first measurement was taken at 2.5 cm for profiles other than 700°C at 100 SCCM. For conditions with an air inlet flowrate of 1000 SCCM the measured slopes from the two points nearest the inlet were used to extrapolate the inlet temperatures for the same profile, as shown in Figure 6-9b. The same inlet slope was multiplied by -1 and used to extrapolate the outlet, with a limiter to prevent extrapolations below 25°C from occurring.

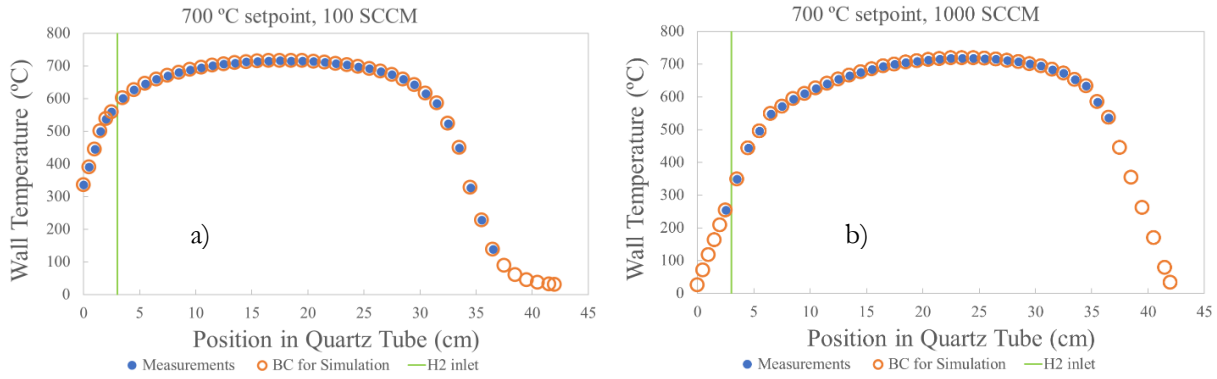

Figure 6-9. Representative temperature profile measurements with boundary condition (BC) extrapolations.

The furnace control temperatures are near the plateau temperatures shown in Figure 6-2 at the center of the quartz tube; these control temperatures are used to compare fractional hydrogen conversions from the simulations with respect to the measurements. This choice of reference temperatures for the non-isothermal reaction tube is consistent with the furnace temperatures supplied with the concentration measurements, which exhibited only minimal hysteresis. The conversion from the simulations is derived from both the hydrogen (H_2 or D_2) and water (H_2O or D_2O) concentrations at the simulated domain outlet (before the artificial conical contraction on the bottom right of Figure 6-3) using Equation 6-3:

$$X_{H_2,sim} = \frac{y_{H_2O,f}}{y_{H_2,f} + y_{H_2O,f}} \qquad 6\text{-}3$$

where y is an outlet mole fraction at the final simulation time, which was typically 50 seconds at 100 SCCM and 20 seconds at 1000 SCCM to achieve a steady-state condition.

6.4. Results and Discussion

6.4.1. Experimental Results

The increasing and decreasing temperature scans yielded only minor hysteresis in the measured conversion of hydrogen isotopes shown in Figure 6-10. This indicates that the temperature scan rate was slow enough to approximate thermal equilibrium, comparable to the static conditions measured in Figure 6-2. Figure 6-10a shows that the H_2 detection limit for the gas chromatograph (GC) was reached for 0.025% H_2 with 1000 SCCM air at about 95% conversion and again for 0.01% H_2 with 1000 SCCM air at about 75% conversion. As the H_2 detection limit is reached, the apparent conversion jumps to 100%. It is not surprising that these two series of measurements operating near the detection limit have the worst hysteresis, as illustrated by the arrows in Figure 6-10a.

Figure 6-10 shows that oxidation usually occurs at lower temperatures for H_2 than it does for D_2 with the same molar inlet concentration, which is consistent with theoretical expectations and historical observations of faster reaction rates for lighter isotopologues (Melander and Saunders 1980). The exception to this trend shown in Figure 6-10c and Figure 6-10d occurs with both airflow rates for the lowest hydrogen or deuterium flow rates. The calibrations of the mass flow controllers and the GC are expected to be applicable for these data, but uncertainties for both flow and concentration measurements are expected to be maximized at the lowest flow rates. At this point, experimental factors cannot be ruled out as a cause for apparent H_2 oxidation rates that are similar

to or lower than D_2 oxidation rates at the lowest flow rate; follow-up investigations of this effect at low concentrations are recommended.

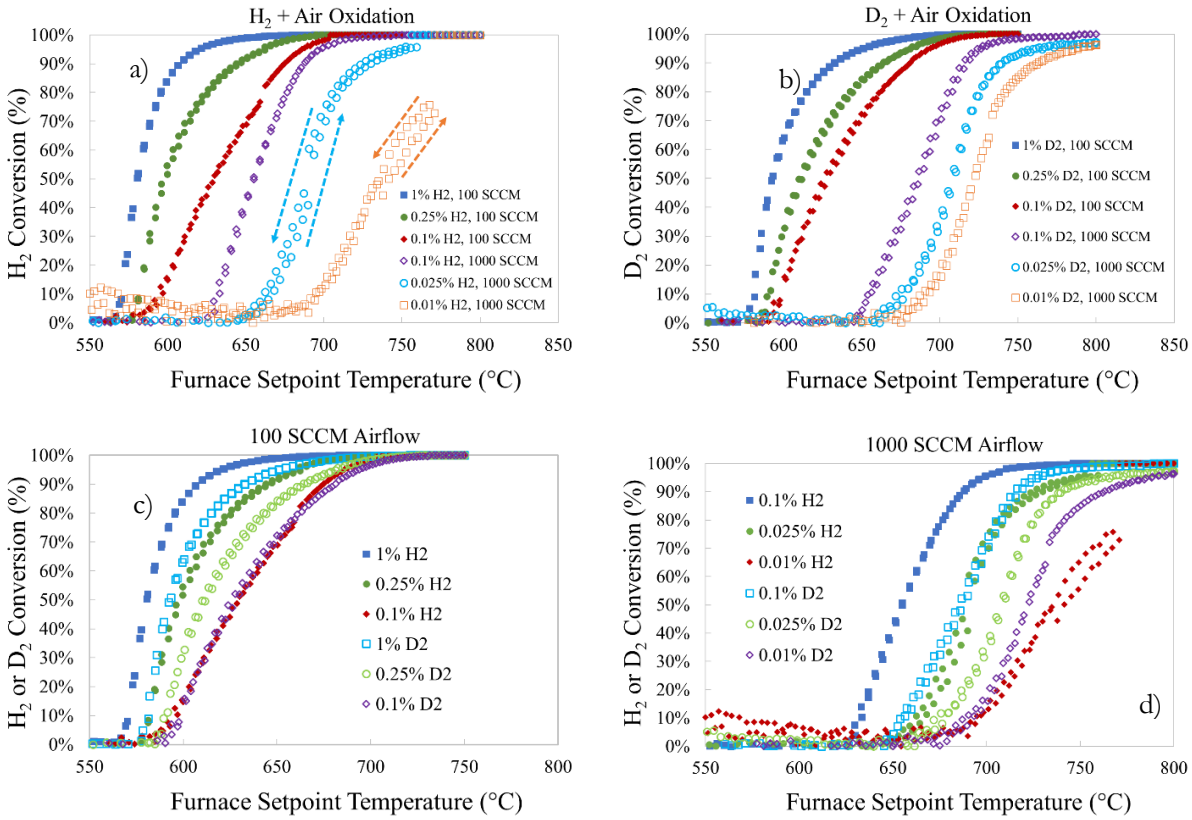

Figure 6-10. Conversion of H_2 and D_2 in the tube furnace reactor; a) H_2 oxidation, b) D_2 oxidation, and both isotopes with c) 100 SCCM airflow (long residence time), and d) 1000 SCCM airflow (short residence time).

6.4.2. Kinetic Modeling Results Compared to Experiments

Several parameter adjustments were required for the kinetic model in Equation 6-2 to represent the data in Figure 6-10. The kinetic parameter adjustments for this work were done manually, so the recommended parameters constitute a "visual fit" of the data rather than a statistical fit. This approach was taken to simplify the workflow, as automated optimization of parameters is tedious to set up and prone to errors when the objective function depends on the output of CFD simulations. The manual approach was deemed sufficiently accurate for the intended safety assessment applications, especially given the simplicity of the global reaction model in Equation 6-2 and the noise in the measurements. Equation 6-2 is a global mechanism that omits details inherent in the underlying elementary reaction steps. Therefore, it is too simple to predict all features in the conversion profiles over the full range of possible experimental conditions.

It was found that manual parameter adjustment was most efficient with the following order of operations. First, the activation energy E was adjusted, followed by the hydrogen reaction order n_H, with intermediate and final updates to the pre-exponential factor A as needed to ensure a good match of the target data. The default oxygen reaction order of $n_O = 0.5$ was not changed because no measurements with varying oxygen concentration were made. Oxygen concentration is not expected to vary much in applications of interest for this kinetic study, so the default oxygen reaction order is

probably adequate. For brevity, the figures in this section only show simulation results with the finalized parameters, which are listed below the original values (Marinov 1995) in Table 6-2.

Table 6-2. Kinetic parameters for Equation 6-2 for oxidation of trace concentrations of molecular hydrogen. Tritium pre-exponential factor is extrapolated from the other isotopes via Equation 6-4.

Isotope	Molecular Mass (g/mol)	A	E/R (K)	n_H
H_2 (protium, Marinov 1995)	2.016	1.77×10^{10} $m^{1.5}/mol^{0.5}/s$	17,600	1.0
H_2 (protium, this work)	2.016	8.0×10^{24} $m^{4.5}/mol^{1.5}/s$	50,000	2.0
D_2 (deuterium, this work)	4.028	4.0×10^{24} $m^{4.5}/mol^{1.5}/s$	50,000	2.0
T_2 (tritium, extrapolated)	6.032	2.9×10^{24} $m^{4.5}/mol^{1.5}/s$	50,000	2.0

Figure 6-11 highlights measurements with hydrogen and deuterium concentrations of 0.1% with two rates of airflow. The differences in residence time are expected to be the principal cause of this behavior, and the activation energy E is the single parameter in Equation 6-2 that scales residence time effects. Increasing the activation energy for the simulation of the tube reactor increases the effect of residence time (greater temperature differences for onset of oxidation) and makes conversion happen more rapidly after onset (steeper conversion versus temperature). It was also apparent from the slopes of the conversion curves that activation energies much larger than the published value of 17,600 K (Marinov 1995, see also Chapter 5) would be required. It is not surprising that the activation energies would differ, because the published value was derived from a flaming regime with much higher fuel concentrations. The activation energy and pre-exponential factors were adjusted manually until the simulated conversions were all in agreement with measured conversions in the range of 5% and 20%; this was the definition used to match the onset behavior.

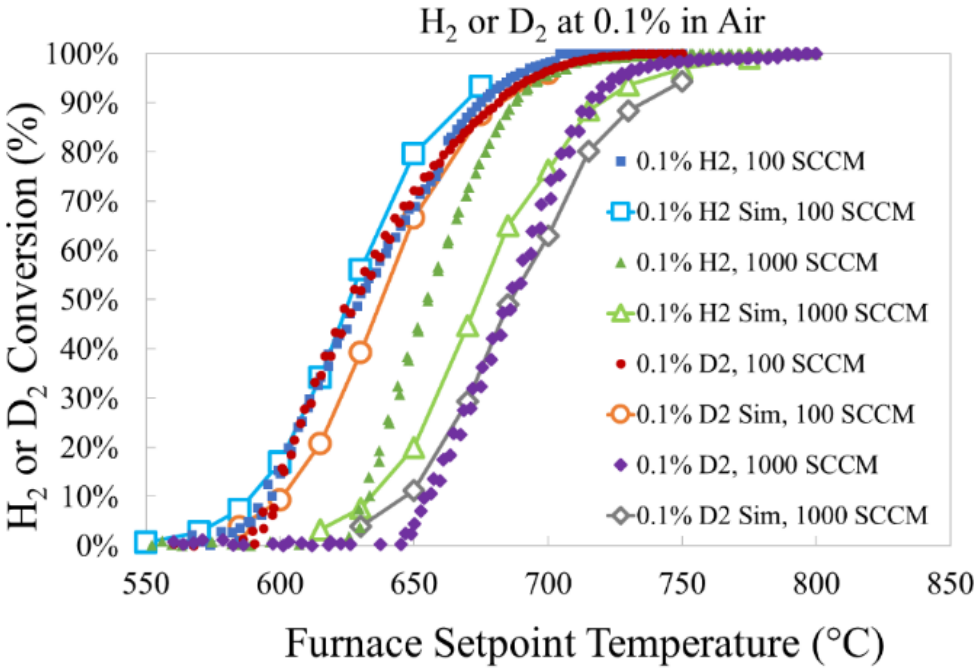

Figure 6-11. Simulated and experimental conversion of H_2 and D_2 at 0.1% in air

Figure 6-11 includes simulation results assuming E/R is 50,000 K, suggesting that increasing E/R with respect to the literature value provides an acceptable match of oxidation onset in the H_2 and D_2 conversion data at 0.1% inlet concentration in air with different residence times. Figure 6-11 and Figure 6-12 show that the simulations and measurements are in better agreement for D_2 compared to H_2. Literature suggests that in cases where differences in activation energy exist for different isotopes, higher activation energies should be expected for the heavier isotopologues (Melander and Saunders 1980). However, inspection of Figure 6-11 and Figure 6-12 (a and b) indicates that using a lower activation energy for H_2 in Equation 6-2 would make the kinetic model representation of the measurements worse because the simulated conversion curves for H_2 would become less steep and the separation in terms of temperature between the two residence times would be reduced. Likewise, it does not appear that a significant benefit would be gained by modeling D_2 with a higher activation energy, as the simulated steepness for most conditions and temperature separation of the conversion curves with different residence times are already comparable to the measurements. Therefore, the same activation energy was applied for the global oxidation reaction of all hydrogen isotopes at low concentrations (see Table 6-2).

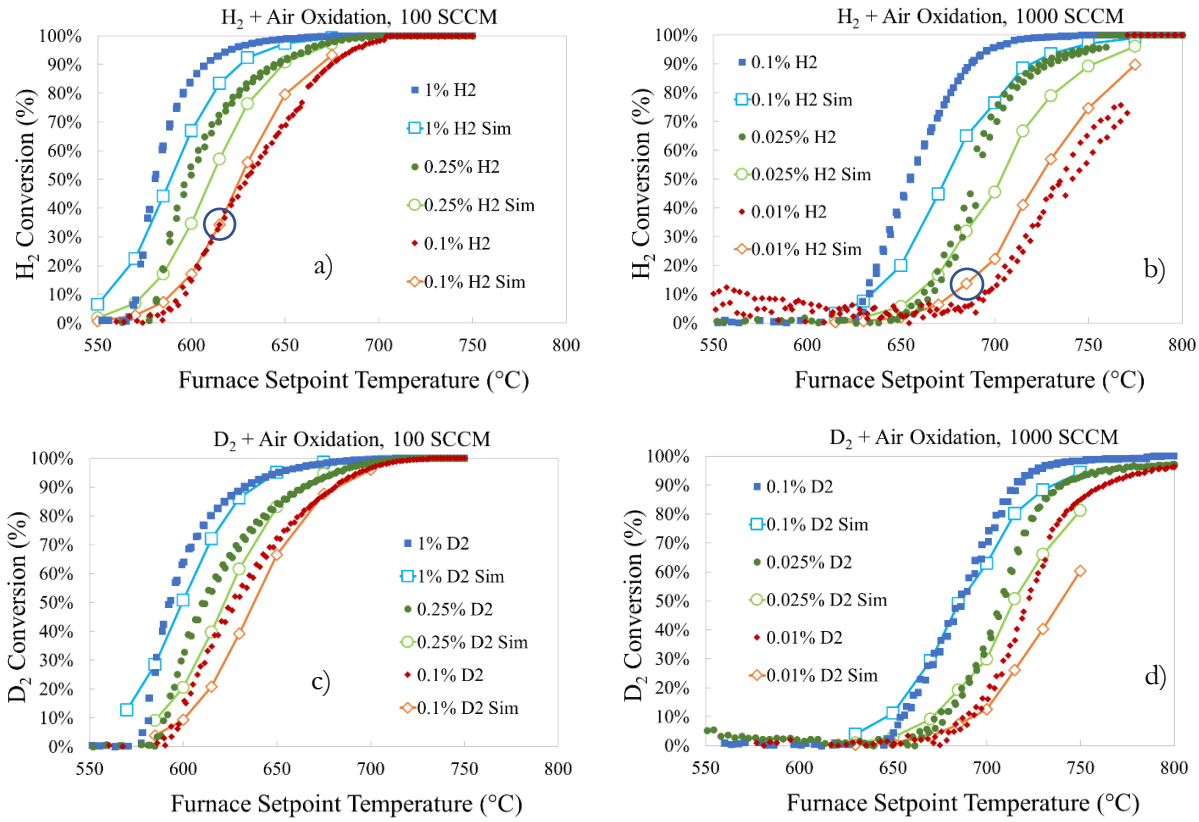

Figure 6-12. Simulated and experimental conversion of H_2 and D_2 with two residence times (airflow). Circled open diamonds in parts a) and b) were used for the resolution study in Section 6.3.1.

As noted with respect to the raw measurements in connection with Figure 6-10, the conversion curves for 0.1% H_2 with 100 SCCM and 0.01 H_2 with 1000 SCCM (with the lowest flow rate) could be expected to occur at slightly lower temperatures based on the comparison to the analogous D_2 oxidation measurements. If the pre-exponential factor for H_2 were increased to produce such an effect (shifting the open orange diamonds in Figure 6-12 to the left), the simulations with higher

concentrations in panels a and b of Figure 6-12 (open blue squares and green circles) would also shift to the left. Several replicates and/or different measurement approaches would be required to demonstrate the presence of an error for the measurements represented by the solid red diamonds in panels a and b of Figure 6-12. Despite the potential improvement compared to experiments at moderate levels of conversion, the current lack of corroborating data precludes justifying an increase in the modeled H_2 rates at present.

Figure 6-12 shows that the simulations compare favorably to the measurements from D_2 and H_2, especially in terms of the fundamental trends. Attempts to model oxidation with the default hydrogen reaction order of $n_H = 1.0$ disallowed any differences between the three simulations shown within each panel of Figure 6-12 (open blue squares, green circles, and orange diamonds). This makes sense for a first-order reaction because increasing the flow rate of the limiting reactant by an arbitrary factor with an identical temperature history will cause the reaction rate to increase by the same factor; the higher average reaction rates cancel with the higher initial reactant concentration when the data are normalized as fractional conversions. Parameter scoping exercises indicate that the optimal reaction order should be near $n_H = 2.0$ for both D_2 and H_2. Values of n_H closer to 3.0 yield too much separation between conversion curves. An integer value for n_H is preferred, as it produces simpler units for the pre-exponential factor, and the measurement uncertainty combined with the oversimplified form of Equation 6-2 with respect to the constituent elementary reaction steps preclude achieving a fit much better than shown in Figure 6-12 with non-integer values of n_H. The optimal value for the reaction order is dependent on the choice of the activation energy, so simulated curves with imperfect conversion slopes can only exhibit accurate concentration scaling in a narrow range of temperatures. The reaction order of $n_H = 2.0$ performs best at the temperature in each panel of Figure 6-12 where the lowest conversions (open orange diamonds) are 10% or lower.

Appendix B includes comparisons of the data and models shown in Figure 6-12 (parts a and c) to earlier measurements from the same tube furnace using slightly different experimental techniques. These comparisons indicate that the model parameters recommended in Table 6-2 fit within the combined uncertainty of the full set of available experimental measurements. Appendix B recommends a systematic investigation of factors such as the axial position of the quartz tube within the furnace once additional funds become available for more experiments and/or modeling.

6.4.3. Kinetic Modeling of Tritium Oxidation

The pre-exponential factor shifts the simulated conversion curves left and right in terms of the plots shown in this paper without much change in the shape or spacing between the various curves (in terms of either the temperature or conversion axes). With the same activation energy and reaction order, increasing the rate of H_2 oxidation by a factor of 2 with respect to the optimized D_2 parameters yielded the best simulated results in Figure 6-11 and Figure 6-12. This approach simplifies scaling the kinetic rates for T_2, which is the objective driving this work.

Arrhenius rate constants are defined as $k = A\exp(-E/RT)$. A relationship for isotopic pairs of Arrhenius rate constants may be derived from kinetic (collision) theory of gases, where molecular velocities are inversely related to the square root of molecular weight. This relationship is given by (Melander and Saunders 1980, Swain et al. 1958):

$$\left(\frac{k_H}{k_T}\right) = \left(\frac{k_H}{k_D}\right)^{1.44} \qquad 6\text{-}4$$

where the subscripts H, D and T refer to normal hydrogen (protium), deuterium, and tritium. The exponent of 1.44 is defined using the following function of atomic masses (Melander and Saunders 1980, Swain et al. 1958):

$$\frac{1-\sqrt{\frac{m_H}{m_T}}}{1-\sqrt{\frac{m_H}{m_D}}} = 1.44 \qquad 6\text{-}5$$

Equation 6-4 neglects quantum effects such as tunneling, which may become non-negligible at the high temperatures investigated in this work. However, Equation 6-4 has been successful in describing experimental trends over a very broad range of conditions (Melander and Saunders 1980, Lewis and Robinson 1968, Stern and Weston 1974). Equation 6-4 is expected to capture the most important aspects of the isotopic trend in reaction rates and is recommended as the best available method to scale the experimentally-derived pre-exponential factors in Table 6-2 from protium and deuterium to produce the recommended value for the tritium pre-exponential factor.

If future measurements indicate higher H_2 oxidation rates are appropriate at low concentrations, as discussed in connection with Figure 6-12, then the tritium pre-exponential factor in Table 6-2 would be reduced in accordance with Equation 6-4. In other words, the most probable bias direction for experimentally derived oxidation rate parameters for H_2 and D_2 would cause modeled tritium oxidation rates to be higher than reality. If the currently recommended parameters in Table 6-2 result in modeling excess conversion of tritium to water, this would result in a degree of conservatism when modeling hazards associated with a tritium leak scenario. With or without a small experimental bias, such modeling assessments are expected to be more realistic than the current assumption of 100% conversion (DOE-STD-1129-2015).

6.5. Conclusions

This work reports oxidation measurements for H_2 and D_2 at sub-flammable concentrations in a tube furnace, with five concentrations from 0.01% to 1% by volume in air. Oxidation to the water form (H_2O or D_2O, respectively) occurred between 550°C and 800°C, and the rates of protium conversion exceeded the deuterium oxidation rates for most experimental conditions. These experimental trends indicate that tritium should have oxidation rates lower than the measured deuterium rates reported in this study. Furthermore, the hydrogen oxidation rates reported in this work were significantly slower than predicted by a global 1-step reaction model that was originally developed from high-concentration measurements in the flammable regime (Marinov 1995); H_2 in pre-test simulations of the experiments oxidized between 350°C and 500°C.

These results have safety implications for tritium, as the hazard level for a release scenario is largely determined by the fraction of released tritium that is converted to the more hazardous water form (T_2O or THO). The low measured oxidation rates for H_2 and D_2 and the expected reduction in oxidation rates for T_2 with respect to the lighter hydrogen isotopes both imply that a substantial fraction of tritium released in a credible low-concentration scenario is likely to remain unoxidized in the vicinity of a heat source such as a fire (see Chapter 5).

Rate parameters for a global 1-step hydrogen oxidation reaction (Marinov 1995) were adapted in this work to model the experimentally measured conversions, using a common apparent reaction order and activation energy for H_2 and D_2 in the low-concentration regime. The same reaction order and activation energy are recommended for T_2 oxidation, while the tritium pre-exponential factor was

extrapolated from the experimentally derived trends of protium and deuterium oxidation. The global rate expression with the parameters recommended in this study are intended to facilitate comparisons to other data sources and to provide an alternative means to evaluate the hazards of tritium release scenarios with respect to the typical regulatory assumption of 100% oxidation (DOE-STD-1129-2015).

7. SUMMARY AND CONCLUSIONS

This work is a significant expansion of the body of work on tritium fire safety. Tritium safety is not an aspect of many prior studies, and the proclivity to model tritium safety after the hydrogen safety community is illustrated to be questionable due to a number of significant differences in the quantities, processes, and hazards associated with the different isotopes.

The second chapter employs equilibrium modeling and helps identify the safety space for the need to consider tritium as an explosive hazard and indicates that facilities with low quantities of inventory might be reasonably excluded from such consideration. HC2 and HC3 facilities lack sufficient quantities of tritium to merit concern for an explosive scenario under conventional use scenarios.

The third chapter details property information newly derived from theory that enables transport and reactive simulations using CFD and provides a source for future computations of this nature. Properties are derived from existing protium and deuterium data, employing assumptions regarding the isotopic trend.

The fourth chapter illustrates a validation study that helps quantify the expected accuracy of CFD simulations for scenarios with lighter-than-air gases under turbulent conditions. Good accuracy is found for the 1-meter diameter He release, and model accuracy is generally well within the limits of the experimental uncertainty. The effect of mesh resolution is exhibited through a significant range of simulation resolutions. Coarse simulations are found to largely predict the main variables with accuracy, but fluctuations and statistical behavior benefits from improved spatial resolution. Results are illustrated here for SIERRA/Fuego, however, the work was coordinated with the fire science community that is producing comparable results for the same scenario with a variety of other contemporary fire science CFD codes. These broader results may be forthcoming in other publications.

The fifth chapter illustrates a number of simulations that are designed to be representative of a facility fire and release. The simulation study helps illustrate how a release outside a fire in a facility may not contribute significantly to a sizeable respirable fraction of the tritium in its most hazardous form. Assuming 100% conversion of the release appears to be highly conservative except for a release directly inside the fire, very close to the fire, or in a room engulfed in fire (a very extreme event). The results utilize a standard fire scenario, which helps address the problem of a near infinite range of potential fire scenarios.

The sixth chapter presents some hydrogen isotope measurements of reaction kinetics at low hydrogen concentrations. The protium (^{1}H) and deuterium (^{2}H) rates at low concentrations are much slower than the global mechanism used for most of the Chapter 5 effort, suggesting the main results of the simulation study are heavily conservative without revisiting the computed scenarios with the improved rate models.

So long as tritium inventories are limited, dispersed, and unpressurized, the safety of tritium is differentiated from typical hydrogen storage and handling safety concerns. For tritium, fire is the main concern, as it converts T_2 to water. This has much higher risk for ingestion and human health. Because tritium is scarce, inventories scaled and managed like standard protium are much less

common. Low inventories of tritium will not sustain a fire themselves, and the fire consequently needs to be external to the tritium inventory in question. Explosives hazards are negligible except for the highest inventories and might be regulated as such by thresholds as suggested in this study. Dispersed inventories will likely only result in fractional releases, as facility-engulfing fires have reduced credibility as a threat (this may need to be confirmed site-by-site taking into consideration scenario particulars). The modeling is approached with rigorous methods, as should be the case when direct validation data are limited or lacking. The validation and parameter determination methods help provide credibility to the analysis performed. Allowing safety to be guided by the best available models and data helps strike a reasonable balance between providing the assurance of quality safety operations while not over-burdening operational requirements with extreme and burdensome measures that may contribute little to the overall safety.

REFERENCES

ANSI/AIHA Z9.5: Laboratory Ventilation and Decommissioning Package

Assael, M. J., S. Mixafendi and W. A. Wakeham (1986). "The Viscosity and Thermal Conductivity of Normal Hydrogen in the Limit of Zero Density." *Journal of Physical and Chemical Reference Data* 15(4): 1315-1322.

Assael, M. J., S. Mixafendi and W. A. Wakeham (1987). "The Viscosity of Normal Deuterium in the Limit of Zero Density." *Journal of Physical and Chemical Reference Data* 16(2): 189-192.

Baker, W. E., Cox, P. A., Westine P. S., Kulesz J. J., and Strehlow R. A. (1992), *Explosion Hazards and Evaluation*, in Fundamental Studies in Engineering 5, Elsevier Scientific Publishing Company, Fourth Impression, New York, page 290.

Benz, F. J. and P. L. Boucher (1981). Flammability characteristics of hydrogen/oxygen/nitrogen mixtures at reduced pressures. *Workshop on the Impact of Hydrogen Water Reactor Safety*. Albuquerque, NM, United States: 137-169, NUREG/CR--2017-Vol3.

Bird, R. B., W. E. Stewart and E. N. Lightfoot (1960). Transport Phenomena. New York, Wiley.

Bird, R. B., W. E. Stewart and E. N. Lightfoot (2002). Transport Phenomena, 2nd Ed. New York, Wiley.

Blanchat, T.K. (2001), "Characterization of the Air Source and the Plume Source at FLAME," Sandia Report SAND 2001-2227.

Brown, A.L., M.D. Clemenson, M.J. Benson, C.J. Elkins, S.T. Jones (2021), "An Urban Dispersion Inspired Scenario for CFD Model Validation," *Fire Safety Journal*, Vol. 120: 103130. https://doi.org/10.1016/j.firesaf.2020.103130

Brown, A.L., D. Glaze, F. Pierce (2014), "Sensitivity Analysis and Verification of a 1-D Surface Solid Combustion Model for a Fire CFD Boundary Condition," in the *2014 ASME/AIAA Summer Conference*, Atlanta, Georgia, June 16-20, 2014.

Brown, A.L., Lance, B.W., Grieb, N.P., Clemenson, M., Benson, M., Elkins, C. (2020), "Dispersion Validation for Urban Flow in Downtown Oklahoma City," SAND2020-10131, Sandia National Laboratories.

Brown, A.L., Bruns, M., Gollner, M., Hewson, J., Maragkos, G., Marshall, A., McDermott, R., Merci, B., Rogaume, T., Stoliarov, S., Torero, J., Trouve, A., Wang, Y., Weckman, E. (2018), "Proceedings of the first workshop organized by the IAFSS working group on measurement and computation of fire phenomena (MaCFP)," *Fire Safety Journal*, 101: 1-17. https://doi.org/10.1016/j.firesaf.2018.08.009.

Brown, A. L., R. C. Shurtz, L. K. Takahashi, M. R. Kesterson and J. E. Laurinat (2021). "A Computational Scenario Based Assessment of Hydrogen Isotope (^{3}H) Fire Safety." *12th US National Combustion Institute Meeting*. Virtual Meeting Hosted by Texas A&M and CSSCI, Central States Section of the Combustion Institute (CSSCI). Paper 128FR-0216.

Buddenberg, J. W. and C. R. Wilke (1949). "Calculation of Gas Mixture Viscosities." *Industrial & Engineering Chemistry* 41(7): 1345-1347.

Cadwallader, L. C., Petti, D. A. (2002). Deuterium and Tritium Safety Issues in IFE Target Fabrication. *Fusion Science and Technology*, 41(3P2), 635-641.

Chase, M. W. (1998). "NIST-JANAF Thermochemical Tables." *Journal of Physical and Chemical Reference Data Monograph 9*: 1-1951. See also https://janaf.nist.gov/ (accessed 2020).

DIPPR Project 801 (2010), "Evaluated Standard Thermophysical Property Values," Design Institute for Physical Properties, AIChE. https://dippr.aiche.org/

DOE-STD-1129-2015 (2015), "Tritium Handling and Safe Storage." Washington, D.C., United States Department of Energy, Office of Environmental Management.

DOE-STD-1027 (1997), "Hazard Categorization and Accident Analysis Techniques for Compliance with DOE Order 5480.23," Nuclear Safety Analysis Reports, Washington, D.C., United States Department of Energy, Office of Scientific and Technical Information.

DOE-HDBK-3010 (2013), "Airborne Release Fractions/Rates and Respirable Fractions for Nonreactor Nuclear Facilities," December 1994, Reaffirmed 2013.

Fairbanks, D. F. and C. R. Wilke (1950). "Diffusion Coefficients in Multicomponent Gas Mixtures." *Industrial & Engineering Chemistry* 42(3): 471-475.

Fernández-Galisteo, D., Sánchez, A.L., Liñán, A. and Williams, F.A. (2009), "One-step reduced kinetics for lean hydrogen–air deflagration." *Combustion and Flame*, 156(5), pp.985-996.

Goodwin, D. G., R. L. Speth, H. K. Moffat and B. W. Weber (2021), "Cantera: An object-oriented software toolkit for chemical kinetics, thermodynamics, and transport processes," Version 2.5.1. doi: 10.5281/zenodo.4527812. Available: https://www.cantera.org (accessed 2021).

Gray, P. and D. B. Smith (1967), "Isotope effects on flame speeds for hydrogen and deuterium," *Chemical Communications (London)*, 4: 146-148. https://doi.org/10.1039/C19670000146.

Gray, P., S. Holland, and D. B. Smith (1970), "The effect of isotopic substitution on the flame speeds of hydrogen-oxygen and hydrogen-nitrous oxide flames," *Combustion and Flame*, 14(3): 361-374. https://doi.org/10.1016/S0010-2180(70)80050-5.

Greenwood, N. N. and A. Earnshaw (1997). Chemistry of the Elements. Boston, Butterworth-Heinemann.

Fickett W., and Davis, W. C. (1979), Detonation, U. of California Press.

Hertzberg, M. (1981), "Flammability limits and pressure development in H_2-air mixtures," *Workshop on the Impact of Hydrogen on Water Reactor Safety*. Albuquerque, NM, United States: 13-67, NUREG/CR--2017-Vol3.

Hinshelwood, C. N., A. T. Williamson, and J. H. Wolfenden (1934), "The Reaction Between Oxygen and the Heavier Isotope of Hydrogen," *Proceedings of the Royal Society of London. Series A, Mathematical and Physical Sciences*, 147(860): 48-57. http://www.jstor.org/stable/2935460.

Hobbs, M. L., Brundage, A. L., Yarrington, C. D. (2014), "JCZS2i: An Improved JCZ Database for EOS Calculations at High Temperature and Pressure," *15th International Detonation Symposium*, Office of Naval Research, ONR-43-280-15, San Francisco, CA, 804.

Hobbs, M. L., Schmitt, R. G., Moffat, H. K., Lawless, Z. (2018), "JCZS3—An Improved Database for EOS Calculations," *16th International Detonation Symposium*, Cambridge, MD, Office of Naval Research, Arlington Virginia 22217-5660, pp 651-660.

ICRP Publication 119 vol. 41, supplement 1, 2012

ISO 9705-1 (2016), "Reaction to fire tests - Room corner test for wall and ceiling lining products - Part 1: Test method for a small room configuration," Vernier, Geneva, Switzerland, Swedish Institute for Standards.

Jensen, G., and J. Martin, J. (April 1988), "Investigation of Fire at Council, Alaska: A Release of Approximately 3000 Curies of Tritium." PNL 6523, Pacific Northwest Laboratory, Richland, WA.

Kee, R. J., G. Dixon-Lewis, J. Warnatz, M. E. Coltrin and J. A. Miller (1986), "A FORTRAN Computer Code Package for the Evaluation of Gas-Phase, Multicomponent Transport Properties," Livermore, California, Sandia National Laboratories, SAND86-8246.

Kerstein, A.R., M.A. Cremer, and P.A. McMurtry (1995), "Scaling Properties of Differential Molecular Diffusion Effects in Turbulence," *Phys. Fluids*, **7**(8): 1999-2007.

Kinney GF and Graham KJ, Explosives Shocks in Air, 2nd Edition, Springer-Verlag, New York (1985).

Konnov, A.A. (2008), "Remaining uncertainties in the kinetic mechanism of hydrogen combustion," *Combustion and flame*, *152*(4): 507-528.

Konnov, A.A. (2019), "Yet another kinetic mechanism for hydrogen combustion," *Combustion and Flame*, *203*: 14-22.

Koroll, G. W. and R. K. Kumar (1991), "Isotope effects on the combustion properties of deuterium and hydrogen," *Combustion and Flame*, 84(1): 154-159. https://doi.org/10.1016/0010-2180(91)90044-C.

Lefebvre, A. H. and Ballal, D. R. (2010), Gas Turbine Combustion 3E, Alternative Fuels and Emissions. Boca Raton, FL: CRC Press, Taylor and Francis Group.

Lewis, E. S. and J. K. Robinson (1968). "The influence of tunneling on the relation between tritium and deuterium isotope effects. The exchange of 2-nitropropane-2-t," *Journal of the American Chemical Society* 90(16): 4337-4344.

Li, J., Zhao, Z., Kazakov, A. and Dryer, F.L. (2004), "An updated comprehensive kinetic model of hydrogen combustion," *International Journal of Chemical Kinetics*, 36(10): 566-575.

Magnussen, B.F., and Hjertager, B.H. (1977), "On mathematical modeling of turbulent combustion with special emphasis on soot formation and combustion," *16th Symposium on Combustion*, The Combustion Institute, 719-729.

Magnussen, B.F. (1981), "On the structure of turbulence and a generalized eddy dissipation concept for chemical reactions in turbulent flow," *9th AIAA Sc. Meeting*, St. Louis, MO, USA.

Marshall, P. and A. Fontijn (1987), "HTP kinetics studies of the reactions of O(2 3PJ) atoms with H_2 and D_2 over wide temperature ranges," *The Journal of Chemical Physics*, 87(12): 6988-6994. https://doi.org/10.1063/1.453395

Marinov, N. M., C. K. Westbrook and W. J. Pitz (1995), "Detailed and Global Chemical Kinetics Model for Hydrogen." *8th International Symposium on Transport Properties*. San Francisco, California, United States, Lawrence Livermore National Laboratory.

Marinov, N.M., Westbrook, C.K. and Pitz, W.J. (1996), "Detailed and global chemical kinetics model for hydrogen." *Transport phenomena in combustion*, 1(118-129): 80.

Matsunaga, N. and A. Nagashima (1983), "Prediction of the transport properties of gaseous water and its isotopes at high temperatures." *The Journal of Physical Chemistry* 87(25): 5268-5279.

McBride, B. J., S. Gordon and M. A. Reno (1993). "Coefficients for calculating thermodynamic and transport properties of individual species," John H. Glenn Research Center, NASA TM-4513. Available: https://ntrs.nasa.gov/citations/19940013151 (accessed 2020).

McBride, B. J., M. J. Zehe and S. Gordon (2002), "NASA Glenn Coefficients for Calculating Thermodynamic Properties of Individual Species," John H. Glenn Research Center, NASA TP-2002-211556, John H. Glenn Research Center, NASA TP-2002-211556. Available: https://www.grc.nasa.gov/WWW/CEAWeb/TP-2002-21556.htm (accessed 2020).

Melander, L. and W. H. Saunders (1980). Reaction rates of isotopic molecules. New York, Wiley.

Michael, J. V. (1989), "Rate constants for the reaction $O+D_2 \rightarrow OD+D$ by the flash photolysis–shock tube technique over the temperature range 825–2487 K: The H_2 to D_2 isotope effect," *The Journal of Chemical Physics*, 90(1): 189-198. https://doi.org/10.1063/1.456513

Miller, J.A. and Kee, R.J. (1977), "Chemical nonequilibrium effects in hydrogen-air laminar jet diffusion flames," *The Journal of Physical Chemistry*, *81*(25): 2534-2542.

Mishima, J. and Steele, C.M. (2002), "Oxidation of Tritium Gas under Accident and Transport Conditions," Report to DOE, LA-UR-02-3803.

Mitchell, R. E. (1980), "Theoretical model of chemically reacting recirculating flows. Livermore, California, Sandia National Laboratories, SAND79-8236.

Monchick, L. and E. A. Mason (1961), "Transport Properties of Polar Gases," *The Journal of Chemical Physics* 35(5): 1676-1697.

Mueller, M.A., Kim, T.J., Yetter, R.A. and Dryer, F.L., (1999), "Flow reactor studies and kinetic modeling of the H_2/O_2 reaction," *International journal of chemical kinetic*s, 31(2): 113-125.

National Oceanic and Atmospheric Administration. (2013, August 13). Flammable Levels of Concern. Flammable Levels of Concern. Retrieved January 19, 2022, from https://response.restoration.noaa.gov/oil-and-chemical-spills/chemical-spills/resources/flammable-levels-concern.html

Najjar, Y.S. (2013), "Hydrogen safety: The road toward green technology," *International Journal of Hydrogen Energy*, 38(25): 10716-10728.

Ndubizu, C.C., Ananth, R. and Tatem, P.A. (2005), "Transient burning rate of a noncharring plate under a forced flow boundary layer flame." *Combustion and flame*, 141(1-2): 131-148.

NFPA 45: Standard on Fire Protection for Laboratories Using Chemicals

NFPA 91: Standard for Exhaust Systems for Air Conveying of Vapors, Gases, Mists, and Particulate Solids

O'Hern, T.J., Weckman, E.J., Gerhart, A.L., Tieszen, S.R. and Schefer, R.W. (2005), "Experimental study of a turbulent buoyant helium plume," *Journal of Fluid Mechanics*, *544*: 143-171.

Pamidimukkala, K. M. and Skinner, G. B., (1982), "Resonance absorption measurements of atom concentrations in reacting gas mixtures. VIII. Rate constants for $O+H_2 \rightarrow OH+H$ and $O+D_2 \rightarrow OD+D$ from measurements of O atoms in oxidation of H_2 and D_2 by N_2O," *The Journal of Chemical Physics*, 76(1): 311-315. https://doi.org/10.1063/1.442779.

Peacock, R.D., Reneke, P.A., Davis, W.D. and Jones, W.W. (1999), "Quantifying fire model evaluation using functional analysis," *Fire Safety Journal*, 33(3): 167-184.

Rigas, F. and Amyotte, P., (2012), Hydrogen safety, CRC Press.

Rogers, R.C. and Chinitz, W. (1983), "Using a global hydrogen-air combustion model in turbulent reacting flow calculations," *AIAA journal*, 21(4), pp.586-592.

Sekar, B. and Mukunda, H.S. (January 1991), "A computational study of direct simulation of high speed mixing layers without and with chemical heat release," In *Symposium (International) on Combustion,* 23(1): 707-713, Elsevier.

Shapiro, Z. M. and Moffette, T. R. (September 1957), "Hydrogen Flammability Data And Application To Pwr Loss-Of-Coolant Accident," Westinghouse Electric Corp., Pittsburgh, PA, USA, WAPD-SC-545. https://doi.org/10.2172/4327402

Shurtz, R. C., A. L. Brown, L. K. Takahashi, M. R. Kesterson, and J. E. Laurinat (2021), "A Suite of Thermodynamic and Transport Properties for Computational Simulations with Hydrogen Isotopes," presented at the *12th US National Combustion Institute Meeting*, Virtual Meeting Hosted by Texas A&M and CSSCI, May 24-26, 2021. Paper 128FR-0224.

Shurtz, R. C., E. N. Coker, A. L. Brown and L. K. Takahashi (2022). An Experimental and Modeling Study of Oxidation of Hydrogen Isotpes at Trace Concentrations. *7th Thermal and Fluids Engineering Conference (TFEC)*. Las Vegas, NV, USA, American Society of Thermal and Fluids Engineers (ASTFE). May 16-18, 2022, Paper TFEC-2022-40826.

Sierra Thermal Fluids Development Team (2019a), "Sierra Low Mach Module: Fuego Theory Manual – Version 4.54," Sandia National Laboratories, SAND2019-12289.

Sierra Thermal Fluids Development Team (2019b), "Sierra Low Mach Module: Fuego User Manual – Version 4.54," Sandia National Laboratories, SAND2019-12291.

Stern, M. J. and R. E. Weston (1974). "Phenomenological manifestations of quantum-mechanical tunneling. III. Effect on relative tritium-deuterium kinetic isotope effects." *The Journal of Chemical Physics* 60(7): 2815-2821.

Swain, C. G., E. C. Stivers, J. F. Reuwer and L. J. Schaad (1958), "Use of Hydrogen Isotope Effects to Identify the Attacking Nucleophile in the Enolization of Ketones Catalyzed by Acetic Acid1-3." *Journal of the American Chemical Society* 80(21): 5885-5893.

Svehla, R. A. (1995), "Transport Coefficients for the NASA Lewis Chemical Equilibrium Program," Cleveland, Ohio, NASA Lewis Research Center, NASA Technical Memorandum 4647.

Tieszen, S.R., Domino, S.P., and Black, A.R. (June 2005), "Validation of a simple turbulence model suitable for closure of temporally-filtered Navier-Stokes equations using a helium plume," SAND2005-3210, Sandia National Laboratories.

Thompson, R. T., Torok, R. C., Randall, D. S., Sullivan, J. S., Thompson, L. B. and Haugh, J. J. (1988) "Large-scale hydrogen combustion experiments: Volume 1, Methodology and results: Final report," Electric Power Research Institute, EG&G Energy Measurements, ASTRON Research and Engineering, United States, EPRI-NP-3878-Vol.1. https://www.osti.gov/biblio/6751527-large-scale-hydrogen-combustion-experiments-volume-methodology-results-final-report

Turns, S. R. (2000), An Introduction to Combustion: Concepts and Applications, 2nd Edition. New York, NY: McGraw-Hill Higher Education.

Varga, T., Nagy, T., Olm, C., Zsély, I.G., Pálvölgyi, R., Valkó, É., Vincze, G., Cserháti, M., Curran, H.J. and Turányi, T. (2015), "Optimization of a hydrogen combustion mechanism using both direct and indirect measurements," *Proceedings of the Combustion Institute*, *35*(1): 589-596.

Walker, William C. (ORNL) Hazard Categorization Threshold Quantities for Tritium, Tritium Focus Group Presentation, May 16, 2018. https://www.energy.gov/sites/prod/files/2018/06/f52/Hazard Categorization Threshold Quantities for Tritium.pdf

Westenberg, A. A. and de Haas, N. (1967), "Atom—Molecule Kinetics Using ESR Detection. III. Results for O+D2→OD+D and Theoretical Comparison with O+H2→OH+H," *The Journal of Chemical Physics*, 47(10): 4241-4246. https://doi.org/10.1063/1.1701606.

Westbrook, C.K. and Dryer, F.L. (1981), "Simplified reaction mechanisms for the oxidation of hydrocarbon fuels in flames" *Combustion Science and Technology*, *27*(1-2): 31-43.

Wilke, C. R. (1950), "A Viscosity Equation for Gas Mixtures," *The Journal of Chemical Physics* 18(4): 517-519.

APPENDIX A. ADDITIONAL ANALYSIS OF ISO9705 SIMULATIONS

Figure A - 1 shows an indication of mesh convergence comparing coarse, medium, and fine simulation integrated volume fraction results for the first 90+ seconds of simulation. The coarse results diverge faster from trends of the other two cases. The mesh resolution exhibits greatest dependency on the drop rate of the T_2 volume fraction suggesting a faster exit of the contaminant from the domain with decreased resolution.

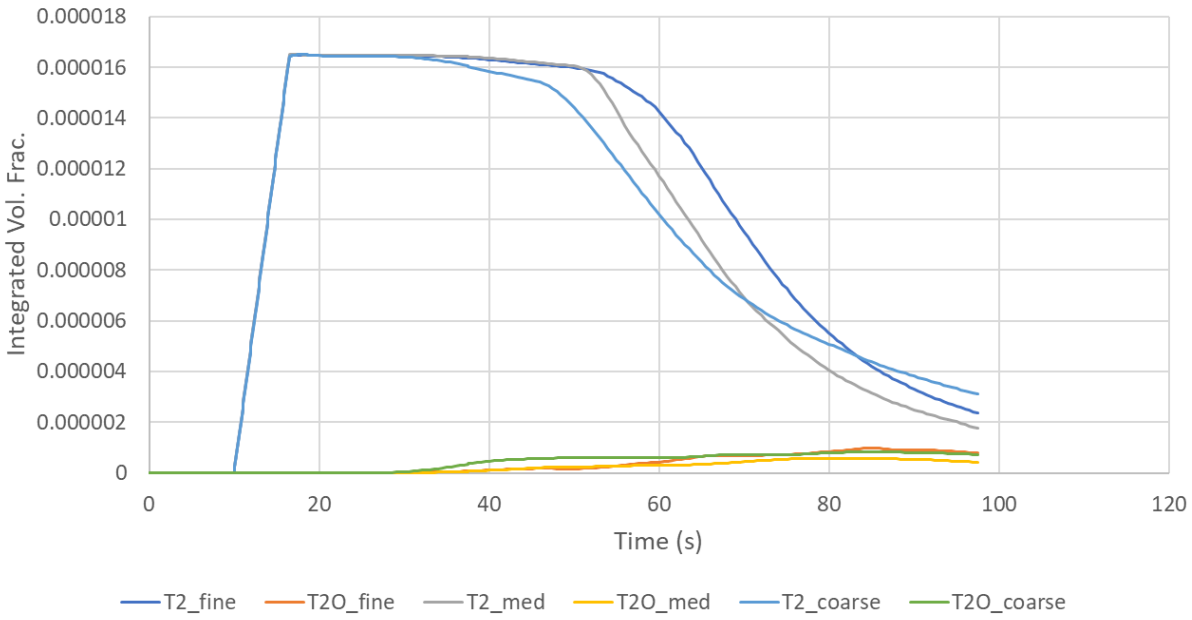

Figure A - 1. Integrated volume fraction for T_2 and T_2O for the coarse, medium and fine cases

Because part of the reporting here is abstract and lacks some of the detailed information provided by the simulations, some 3D visualization frames are included here for the baseline case, 2-M3T. In all the subsequent images, the left and right frames are identical except the left frame shows T_2 molar fraction iso-contours, and the right frame shows T_2O molar fraction iso-contours at the same magnitude. The steady-state fire is observed in Figure A - 2 at 10 seconds. Figure A - 3 shows 20 second results, illustrating the initial distribution of the injected hydrogen rising and beginning to interact with the upper smoke layer. Figure A - 4 shows results at 40 seconds. The T_2 is predominantly spreading towards the door beneath the smoke layer. The T_2O is greatest in the smoke layer at the top of the room. Figure A - 5 shows predictions at 60 seconds near the peak of the T_2O. High concentration T_2 can be seen exhausting beneath the smoke layer. Figure A - 6 shows 120 second results. By this point in time, the high concentration of T_2 exhibited by the red contour is mostly gone. The T_2O continues to exhaust, and the blue T_2 contour is exhibiting significant dynamic in the contour shapes presumably caused by turbulent and diffusive mixing.

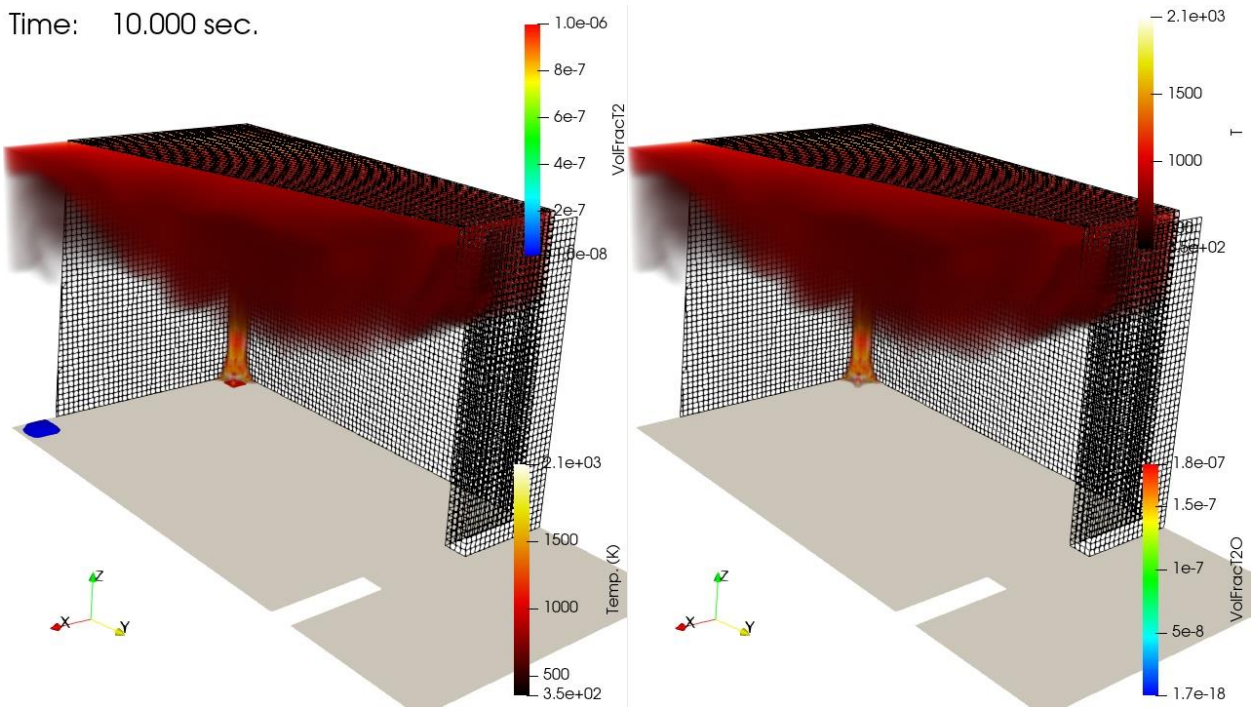

Figure A - 2. 2-M3T simulation visualization at 10 seconds

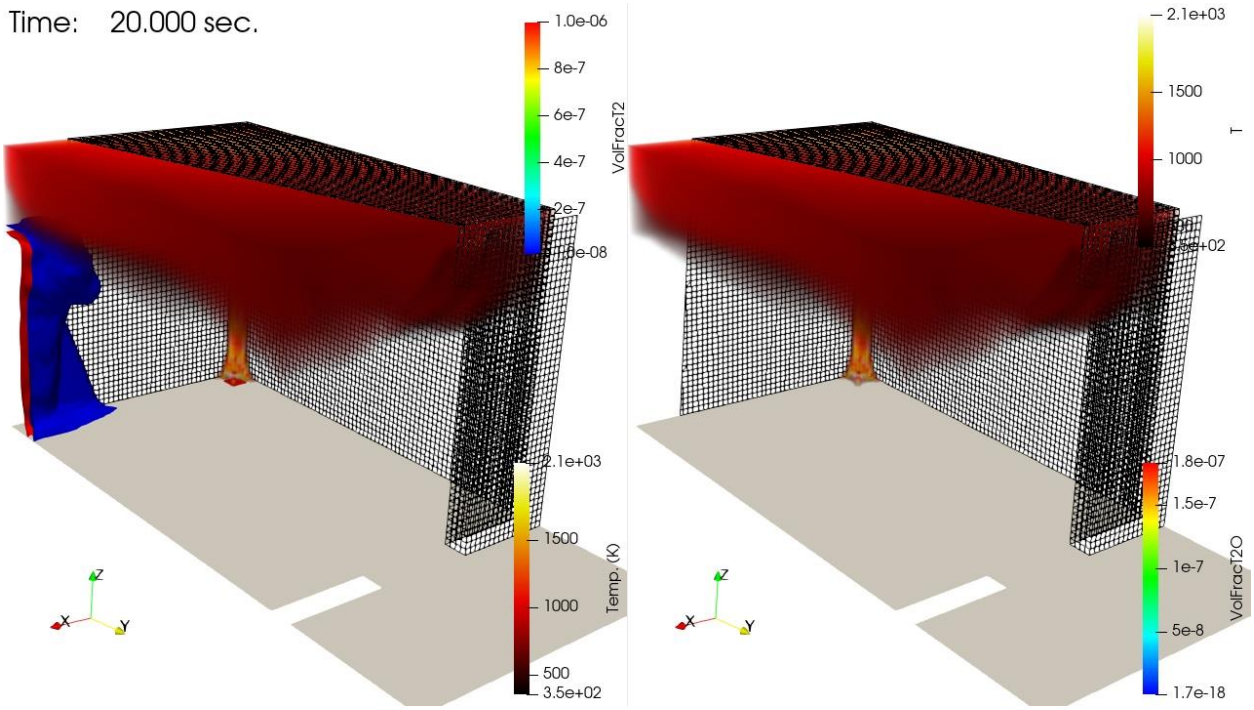

Figure A - 3. 2-M3T simulation visualization at 20 seconds

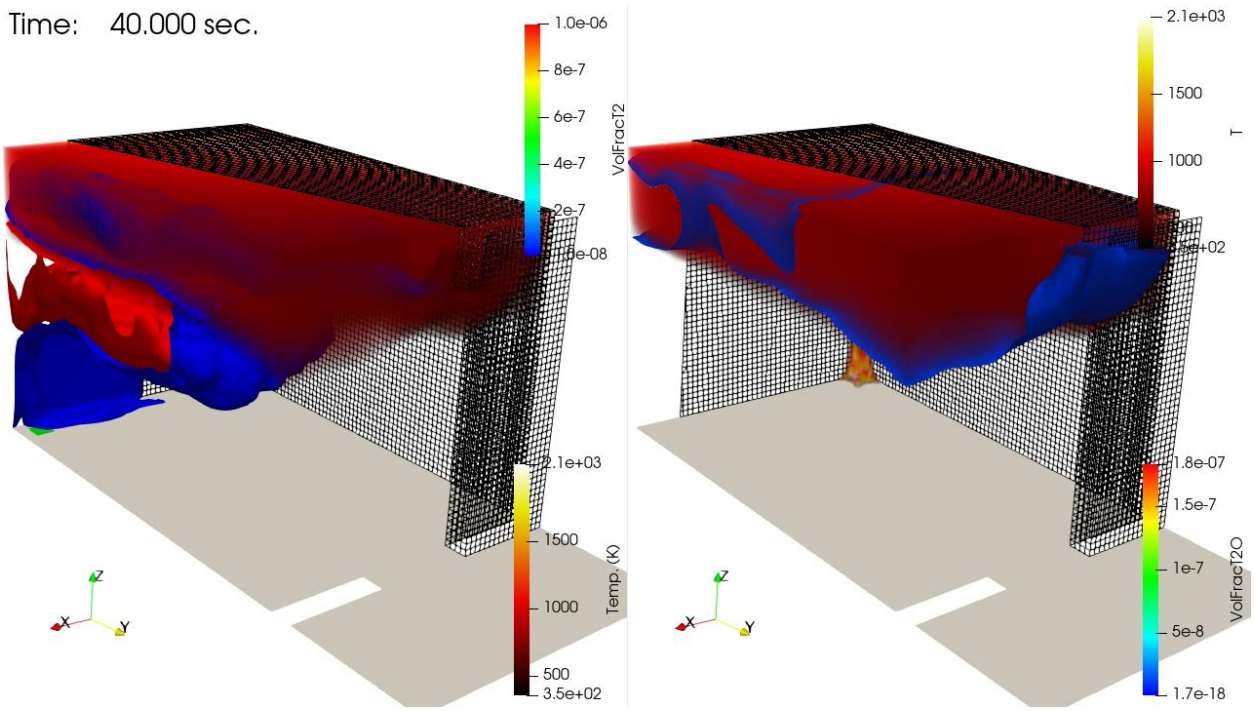

Figure A - 4. 2-M3T simulation visualization at 40 seconds

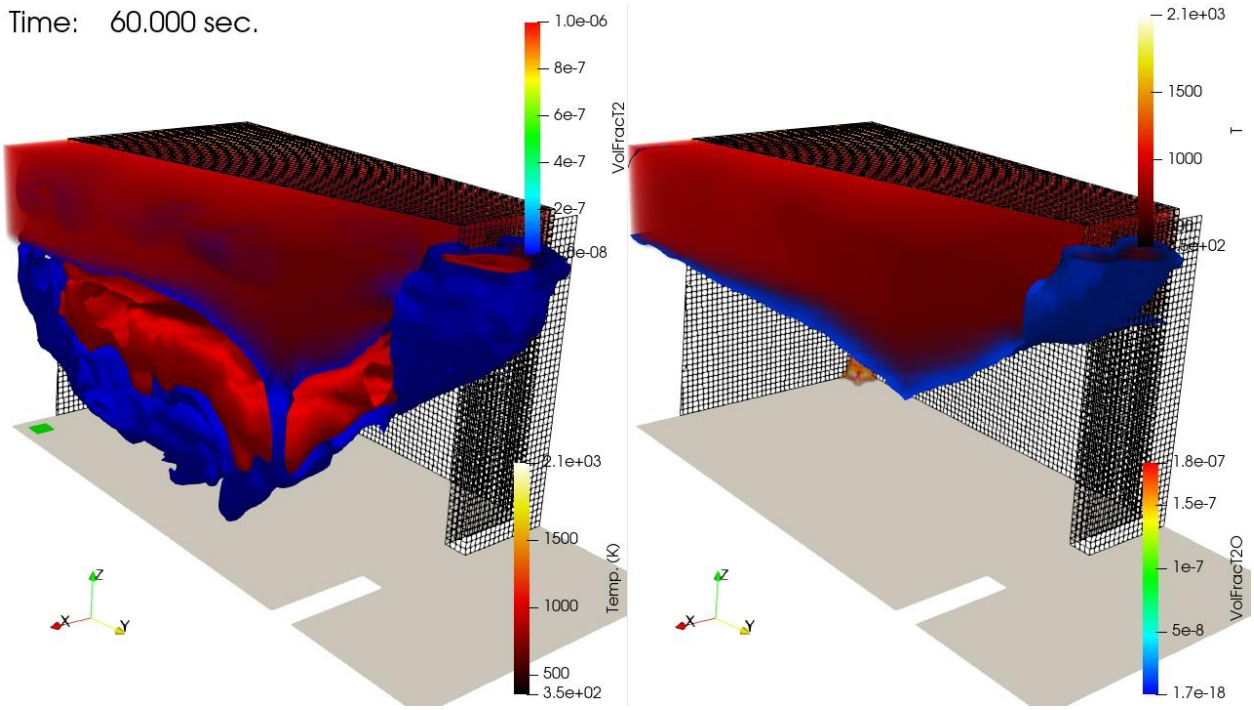

Figure A - 5. 2-M3T simulation visualization at 60 seconds

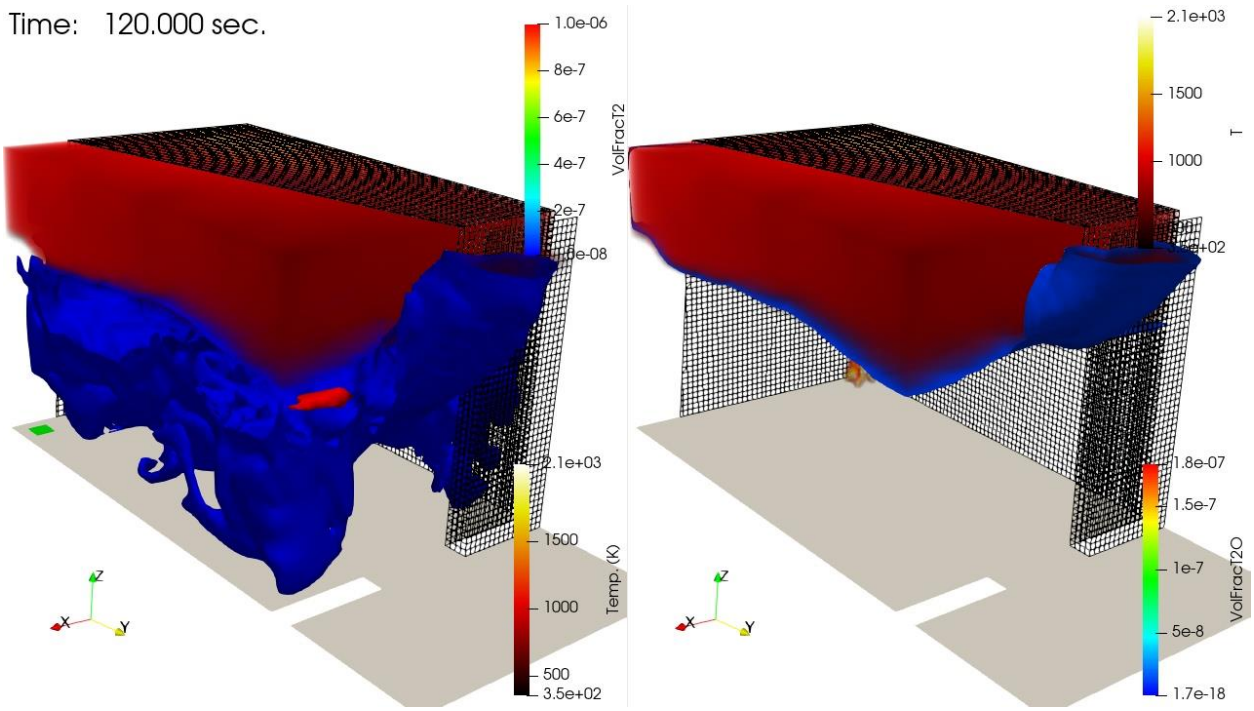

Figure A - 6. 2-M3T simulation visualization at 120 seconds

APPENDIX B. ADDITIONAL H_2 AND D_2 OXIDATION MEASUREMENTS

Two kinds of measurements were acquired for oxidation of H_2 and D_2 in a tube furnace. The figures in Chapter 6 correspond to the more recent data, where the furnace temperature was ramped up and down at 1°C/min while measuring outlet concentrations of of H_2 or D_2. Earlier measurements were made while holding the furnace temperature constant, which was less efficient in terms of the quantity of measurements obtained. These earlier, sparser measurements are presented in this appendix because they were not central to the conclusions in Chapter 6 and had some behavior that was considered anomalous with respect to the more recent measurements.

Figure B - 1 shows the early H_2 oxidation measurements compared to the subsequent ramped data with the same level of airflow (100 SCCM). Figure B - 2 presents a similar comparison for D_2 oxidation. Solid symbols with black outlines labeled "No Ramp" correspond the earlier measurements with stable temperatures in these plots. Kinetic simulations from the parameters recommended in Chapter 6 are also included for comparison.

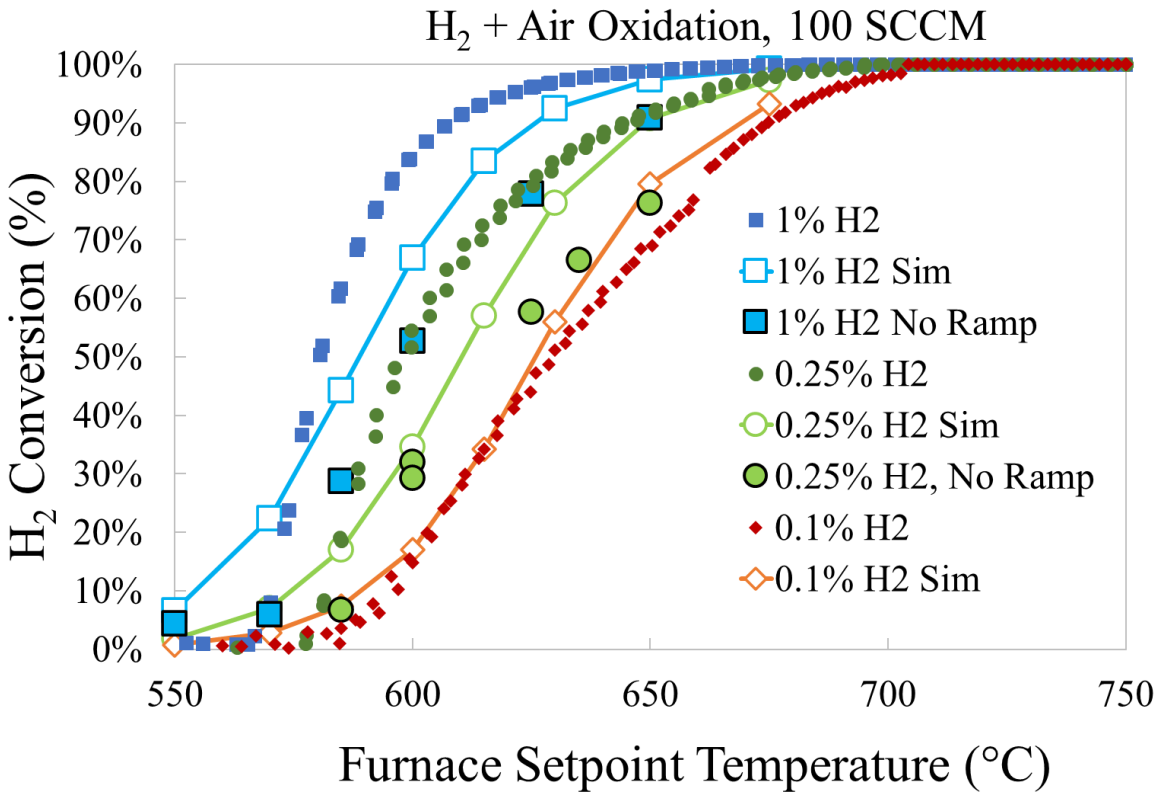

Figure B - 1. Comparison of different H_2 oxidation experiments with kinetic simulations

From the four groups of early measurements with steady temperatures, only the series with D_2 at 1% matched the corresponding measurements with ramped temperatures (Figure B - 2). The other three series with stabilized temperatures were less reactive than the corresponding cases with ramped temperatures. The difference in oxidation rates between the two H_2 concentrations was similar using both experimental methods (Figure B - 1), but the differences between concentrations for D_2 were larger for the earlier measurements without the temperature ramp (Figure B - 2).

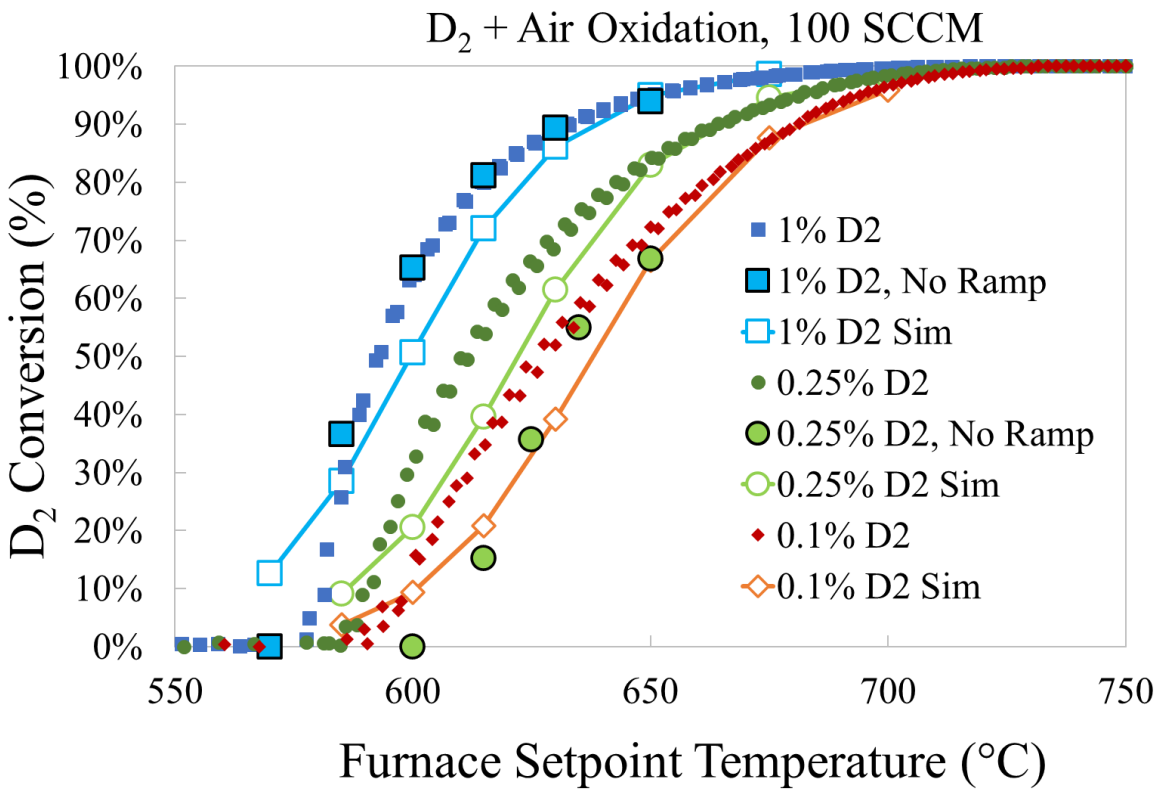

Figure B - 2. Comparison of different D_2 oxidation experiments with kinetic simulations

No explanation has been conclusively identified as of this writing for these observed differences between experimental techniques. For the three conditions where the early oxidation measurements occurred at higher temperatures compared to the measurements with ramped temperatures, the two types of experimental measurements bound the conversion curves produced from the recommended kinetic parameters developed in Section 6.4.2, even though the kinetic models are based exclusively on the data with ramped temperatures. This means that the kinetic parameters from this study represent all the oxidation data with similar uncertainty while capturing the onset behavior occurring at the lowest temperatures.

The observed anomalies with the smallest H_2/D_2 flow rates identified in Section 6.4.1 suggest experimental uncertainties of magnitudes comparable to the differences between experimental techniques noted in this appendix. This may indicate that small differences in the experimental setup result in experimental uncertainties such that the oxidation temperatures for a given level of conversion shift by 15°C to 30°C. This is roughly half the temperature range required after the onset of oxidation to achieve >90% conversion for a given residence time.

The tube furnace was moved and/or disassembled on a few occasions for temperature profile measurements and other purposes. It is possible that the location of the air and fuel inlets varied by as much as 1 to 3 centimeters with respect to the edge of the furnace for some groups of experiments, which could change the length of the preheating zone. Allocation of additional resources is recommended to conduct a systematic investigation of whether axial position variations of 1 to 3 centimeters cause conversion to occur at different temperatures. The variation between experiments shown in Figure B - 1 and Figure B - 2 may be explained if studies with different axial positions yield shifts on the order of 15°C to 30°C for a given level of conversion.

DISTRIBUTION

Email—Internal

Name	Org.	Sandia Email Address
Jeff Brewer	00531	jdbrewe@sandia.gov
Jeff Engerer	01532	jengere@sandia.gov
William W. Erikson	01516	wweriks@sandia.gov
Russell Jarek	07576	rljarek@sandia.gov
Richard Karnesky	08341	rakarne@sandia.gov
Carlos Lopez	01532	carlope@sandia.gov
Clark Snow	07585	cssnow@sandia.gov
Rajan Tandon	07576	rtandon@sandia.gov
Ben Zeidman	00531	bdzeidm@sandia.gov
Technical Library	01977	sanddocs@sandia.gov

Email—External [redacted]

Name	Company Email Address	Company Name
Brandon Chung	chung7@llnl.gov	LLNL
Nanette Founds	nanette.founds@nnsa.doe.gov	US/DOE/NNSA
Matthew Kesterson	Matthew.Kesterson@srs.gov	SRS/SRNL
James Klein	james.klein@srnl.doe.gov	SRNL
James Laurinat	james.laurinat@srnl.doe.gov	SRNL
Chandra Marsden	chandra@lanl.gov	LANL
Adrian Mistreanu	adrian.mistreanu@srnl.doe.gov	SRNL
Marlene Moore	marlene.moore@srs.gov	SRS/SRNL
David Pinkston	pinkston1@llnl.gov	LLNL
Jorge Sanchez	sanchez3@llnl.gov	LLNL
Jacob Tuia	jacob.tuia@nnsa.doe.gov	US/DOE/NNSA
Bill Weaver	bill.weaver@em.doe.gov	US/DOE

Sandia National Laboratories is a multimission laboratory managed and operated by National Technology & Engineering Solutions of Sandia LLC, a wholly owned subsidiary of Honeywell International Inc. for the U.S. Department of Energy's National Nuclear Security Administration under contract DE-NA0003525.